SERDP

FINAL REPORT

Resilience of Boreal Ecosystems Assessed Using High-frequency Records of Dissolved Organic Matter and Nitrate in Streams

Tamara Harms
University of Alaska Fairbanks

Thomas Douglas
Cold Regions Research and Engineering Laboratory

February 2023

SERDP Project RC-2507

DISTRIBUTION STATEMENT A
This document has been cleared for public release.

This report was prepared under contract to the Department of Defense Strategic Environmental Research and Development Program (SERDP). The publication of this report does not indicate endorsement by the Department of Defense, nor should the contents be construed as reflecting the official policy or position of the Department of Defense. Reference herein to any specific commercial product, process, or service by trade name, trademark, manufacturer, or otherwise, does not necessarily constitute or imply its endorsement, recommendation, or favoring by the Department of Defense.

REPORT DOCUMENTATION PAGE

Form Approved
OMB No. 0704-0188

The public reporting burden for this collection of information is estimated to average 1 hour per response, including the time for reviewing instructions, searching existing data sources, gathering and maintaining the data needed, and completing and reviewing the collection of information. Send comments regarding this burden estimate or any other aspect of this collection of information, including suggestions for reducing the burden, to Department of Defense, Washington Headquarters Services, Directorate for Information Operations and Reports (0704-0188), 1215 Jefferson Davis Highway, Suite 1204, Arlington, VA 22202-4302. Respondents should be aware that notwithstanding any other provision of law, no person shall be subject to any penalty for failing to comply with a collection of information if it does not display a currently valid OMB control number.
PLEASE DO NOT RETURN YOUR FORM TO THE ABOVE ADDRESS.

1. REPORT DATE *(DD-MM-YYYY)*	**2. REPORT TYPE**	**3. DATES COVERED** *(From - To)*
25/02/2023	SERDP Final Report	9/28/2018 - 5/24/2023

4. TITLE AND SUBTITLE

Resilience of Boreal Ecosystems Assessed Using High-frequency Records of Dissolved Organic Matter and Nitrate in Streams

5a. CONTRACT NUMBER
18-C-0082

5b. GRANT NUMBER

5c. PROGRAM ELEMENT NUMBER

6. AUTHOR(S)
Tamara Harms
University of Alaska Fairbanks

Thomas Douglas
Cold Regions Research and Engineering Laboratory

5d. PROJECT NUMBER
RC-2507

5e. TASK NUMBER

5f. WORK UNIT NUMBER

7. PERFORMING ORGANIZATION NAME(S) AND ADDRESS(ES)
University of Alaska Fairbanks
Institute of Arctic Biology
902 N Koyukuk Dr, PO Box 757000
Fairbanks, AK 99775-7000

8. PERFORMING ORGANIZATION REPORT NUMBER
RC-2507

9. SPONSORING/MONITORING AGENCY NAME(S) AND ADDRESS(ES)
Office of the Deputy Assistant Secretary of Defense (Energy Resilience & Optimization)
3500 Defense Pentagon, RM 5C646
Washington, DC 20301-3500

10. SPONSOR/MONITOR'S ACRONYM(S)
SERDP

11. SPONSOR/MONITOR'S REPORT NUMBER(S)
RC-2507

12. DISTRIBUTION/AVAILABILITY STATEMENT
DISTRIBUTION STATEMENT A. Approved for public release: distribution unlimited.

13. SUPPLEMENTARY NOTES

14. ABSTRACT
This SERDP project assessed whether stream biogeochemistry can indicate the ecological state of the contributing area, assess ecosystem resilience, and/or provide early warning of regime shifts caused by fire and permafrost thaw. The Department of Defense maintains extensive lands in the boreal forest that are managed to provide both suitable training grounds and ecosystem services including carbon storage and wildlife habitat. These lands are vulnerable to thawing permafrost and changing fire regime, which can replace the previously dominant black spruce forests with deciduous forests that do not insulate permafrost. Stream chemistry integrates signals originating from throughout the contributing area and could therefore assess ecosystem state at larger scales than ground-based measures.

15. SUBJECT TERMS
Boreal Ecosystems, High-frequency Records, Dissolved Organic Matter, Nitrate, Streams. Monitoring, arctic, infrastructure

16. SECURITY CLASSIFICATION OF:			**17. LIMITATION OF ABSTRACT**	**18. NUMBER OF PAGES**	**19a. NAME OF RESPONSIBLE PERSON**
a. REPORT	**b. ABSTRACT**	**c. THIS PAGE**			Tamara Harms
UNCLASS	UNCLASS	UNCLASS	UNCLASS	175	**19b. TELEPHONE NUMBER** *(Include area code)* 907-474-6117

Table of Contents

List of Figures ..... **iii**
List of Tables ..... **vi**
List of Acronyms ..... **vii**
ABSTRACT **10**
EXECUTIVE SUMMARY **11**
INTRODUCTION **18**
BACKGROUND **19**
OBJECTIVES **20**
TECHNICAL APPROACH & FINDINGS **21**
..... **22**
Task 1: Select sites and secure permissions **23**
Task 2: Install infrastructure **27**
Task 3: Establish data relay system **28**
Task 4: Initial sensor calibrations **30**
Task 5: Install sensors and collect high-frequency data **31**
5.1 Data collection 31
5.2 Weather & hydrologic conditions during monitoring 34
Task 6: Statistical approaches for quality control **36**
Task 7: Model instream metabolism & N uptake **38**
Task 8: Determine sources of water and nitrate to streams **44**
8.1 Sources of water contributing to streamflow 44
8.2 Sources of NO_3^- in streamwater 48
Task 9: Time series models to estimate effects of disturbance on C and N fluxes **52**
9.1 Overview 52
9.2 Demonstration of time series statistical approaches to a single season 52
9.3 Concentration-discharge relationships during storms, 2018-2022 64
9.4 Daily-scale variation in stream chemistry 83
9.5 Multi-scale temporal variation in stream chemistry 87
9.6 Decadal-scale effects of fire history on stream solute chemistry 97
Task 10: Quantify leading indicators of regime change **103**
10.1 Overview 103
10.2 Effectiveness of leading indicators in detecting state changes from stream chemistry and discharge 104
10.3 Baseline values of leading indicators for boreal catchments varying in disturbance history 107
CONCLUSIONS AND IMPLICATIONS FOR FUTURE RESEARCH/IMPLEMENTATION **114**
ACKNOWLEDGEMENTS ..... **ix**
LITERATURE CITED **116**
APPENDIX A: Supporting Data **126**

Temporal patterns in instream gross primary production 126
..... 130
Wavelet transform and wavelet coherence plots 131
..... 167
APPENDIX B: Scientific & Technical Publications 171
APPENDIX C: Responses to Comments on the Final In-Progress Report 172

List of Figures

Figure 1. Conceptual model of alternative stable states in high-latitude, boreal forests (adapted from Johnstone et al. [2010]). 18
Figure 2. Locations of study sites in Interior Alaska. 25
Figure 3. Sensors were installed in five streams, with data collection generally extended from snowmelt until freeze-up. 26
Figure 4. Infrastructure installed to secure sensors and provide routine access for maintenance. 27
Figure 5. Data telemetry network on the Yukon Training Area. 29
Figure 6. Example of relationships between fDOM and colored DOM (indexed by absorbance at 254 nm), temperature (°C) and turbidity (FNU). 30
Figure 7. Discharge and stream chemistry in boreal streams measured at 15-min intervals. 33
Figure 8. Long-term variation in precipitation of Interior Alaska. 34
Figure 9. Cumulative precipitation during each of the study years. 35
Figure 10. Total number of storm events and average storm size varied across the study years. 35
Figure 11. Cumulative discharge for each site and study year. 36
Figure 12. Example of raw data from the EXO sensor (top panels) and values after automated QA/QC (bottom panels). 37
Figure 13. Modeled rates of gross primary production (GPP) and stream discharge in Moose Creek. 41
Figure 14. Modeled daily rates of gross primary production (GPP) in the study streams. 42
Figure 15. Modeled daily rates of ecosystem respiration (ER) in the study streams. 43
Figure 16. Mixing plots depicting concentrations of the two conservative solutes used in mixing models (magnesium and chloride), and prospective end members 45
Figure 17. Mean proportions and 95% credible intervals of water source contributions by site and year. 46
Figure 18. Estimates of source water contributions to streams as a function of julian day. 47
Figure 19. Variation in mean proportion of precipitation and groundwater contributions to streamflow across all years relative to disturbance history of the catchments. 48
Figure 20. δ^{15}N-NO_3^- in stream water and potential source waters. 50
Figure 21. δ^{18}O-NO_3^- in stream water and potential source waters. 50
Figure 22. Dual isotope plot of NO_3^- in stream water and potential source waters. 51
Figure 23. Headwater catchments monitored in 2017. 53
Figure 24. High-frequency (15-min) data collected by sensors installed in headwater streams that drain catchments of varying spatial extent of permafrost and burn history. 57
Figure 25. Covariate effects on daily NO_3^- (a–b) and fDOM (c-f) concentrations in headwater catchments estimated by MARSS models. 59
Figure 26. Concentration-discharge relationships during storms in headwater catchments. 60
Figure 27. Wavelet coherence of nitrate (NO_3^-) concentration with discharge (a–b) and gross primary productivity (GPP) (c–d) in streams draining catchments with 54% permafrost (PF) (a, c) and <4% permafrost (b, d). 62
Figure 28. Daily mean NO_3^- concentration for each catchment and year of the study (35-142 days after peak snowmelt runoff in the Chena River). 67
Figure 29. Daily mean fDOM concentration for each catchment and year of the study. 68
Figure 30. Daily mean SPC for each catchment and year of the study. 69

Figure 31. Daily turbidity concentration within each year of the study 70
Figure 32. Hysteresis index versus β during all delineated storms for fDOM (A), NO_3^- (B), SPC (C), and turbidity (D). 72
Figure 33. Hysteresis index across all storms for fDOM (A), NO_3^- (B), SPC (C), and turbidity (D). 73
Figure 34. Slope of the concentration-discharge relationship on the rising limb of each storm (β), across all storms for fDOM (A), NO_3^- (B), SPC (C), and turbidity (D). 74
Figure 35. Standard deviation of HI across all storms for fDOM (A), NO_3^- (B), SPC (C), and turbidity (D). 75
Figure 36. Standard deviation of β across all storms for fDOM (A), NO_3^- (B), SPC (C), and turbidity (D). 76
Figure 37. Catchment attributes explaining variation in concentration-discharge dynamics of fDOM summarized across all storms observed within each catchment across all study years. ... 78
Figure 38. Catchment attributes explaining variation in concentration-discharge dynamics of NO_3^- summarized across all storms observed within each catchment across all study years.. 79
Figure 39. Standardized effects of storm size, antecedent precipitation, and seasonality on HI estimated by linear regression on all storms observed within each catchment across all study years. 81
Figure 40. Standardized effects of storm size, antecedent precipitation, and seasonality on β estimated by linear regression on all storms observed within each catchment across all study years. 82
Figure 41. Standardized effects of covariates on mean daily fDOM concentration (ln-transformed) estimated by MARSS models. 84
Figure 42. Standardized effects of covariates on mean daily NO_3^- concentration (ln-transformed) estimated by MARSS models. 85
Figure 43. Seasonal trends in fDOM (top) and NO_3^- concentrations for each catchment and year of the study. 86
Figure 44. Rate of reversion of mean daily fDOM (top) and NO_3^- (bottom) concentration to the mean of the time series for each catchment and year. 87
Figure 45. Wavelet decomposition of fDOM concentration in 2020. 90
Figure 46. Wavelet decomposition of fDOM concentration in 2022. 91
Figure 47. Wavelet decomposition of NO_3^- concentration in 2020, the wettest monitoring period during the study. 92
Figure 48. Wavelet decomposition of NO_3^- concentration in 2022, the driest monitoring period during the study. 93
Figure 49. Wavelet coherence of fDOM concentration and discharge in 2019. 95
Figure 50. Wavelet coherence of NO_3^- concentration and discharge in 2019. 96
Figure 51. A synoptic survey of streams in Interior Alaska included variation in catchment slope, permafrost, and burn history. 99
Figure 52. Observed solute concentrations in streams of Interior Alaska during baseflow. 100
Figure 53. Coefficients from multiple regression models estimating effects of catchment attributes on ln-transformed solute concentrations in streams. 101
Figure 54. Model-predicted yields of solutes from boreal catchments at baseflow across a gradient of burn extent. 102
Figure 55. Conceptual model integrating resilience theory with catchment biogeochemistry... 103

Figure 56. Leading indicators of regime change were applied to long-term observations of monthly stream nitrate concentration from reference and clearcut catchments in the experimental forests of Coweeta, NC (left column) and Hubbard Brook, NH (right column). 106
Figure 57. Leading indicators of regime change estimated from seasonal time series of nitrate concentration measured at 15-min resolution. 109
Figure 58. Leading indicators of regime change estimated from seasonal time series of absorbance at 254 nm (a proxy for DOM concentration) measured at 15-min resolution. 110
Figure 59. Leading indicators of regime change estimated from seasonal time series of fDOM concentration measured at 15-min resolution. 111
Figure 60. Leading indicators of regime change estimated from seasonal time series of specific conductivity measured at 15-min resolution. 112
Figure 61. Leading indicators of regime change estimated from seasonal time series of turbidity measured at 15-min resolution. 113

List of Tables

Table 1. Project timeline. 21
Table 2. Research questions, hypotheses, and associated tasks. 22
Table 3. Attributes of boreal catchments included in the study. 24
Table 4. Sensor deployment dates and missing data (as percent of deployment days). 32

List of Acronyms

abs254	absorbance of light at a wavelength of 254 nm
AR	autoregressive
CRREL	Cold Regions Research and Engineering Laboratory
C	carbon
C-Q	concentration-discharge
DLM	dynamic linear model
DO	dissolved oxygen
DOC	dissolved organic carbon
DoD	Department of Defense
DOM	dissolved organic matter
ER	ecosystem respiration
EXO	multi-parameter sonde (proprietary)
fDOM	fluorescent dissolved organic matter
GDU	growing degree units
GPP	gross primary production
HI	hysteresis index
K	gas evasion rate
MARSS	multivariate autoregressive state space
N	nitrogen
NEON	National Ecological Observatory Network
NH_4^+	ammonium
NO_3^-	nitrate
OM	organic matter
O	oxygen
PAR	photosynthetically-active radiation
PF	permafrost
PPFD	photon flux density
Q	discharge
QA/QC	quality assurance/quality control
RMSE	root mean square error
SD	standard deviation
SPC	specific conductance
SUNA	Submersible Ultra-violet Nitrate Analyzer (proprietary)
TDN	total dissolved nitrogen
TDP	total dissolved phosphorus
Z	water depth

Keywords

alternative stable states
boreal forest
carbon
catchment
fire
groundwater
nitrogen
optical sensors
organic matter
permafrost
resilience
streams
time series
watershed

Acknowledgements

A host of scientists and technicians contributed to collecting and analyzing the data presented in this final report. Jacob Adams, Jake Cavaiani, Karen Jorgenson, and Alex Webster led aspects of modeling, data analysis, and data collection. Jessica Czarnecki and Rachel Willis contributed to developing and testing the sensor network, collected field data, and performed laboratory analyses. Amanda Barker, Albin Bjärhall, Lauren Bosche, Melanie Burnett, Adela Contreras, Reiner Giesler, Margaret Haney, Justin Hill, Laura Knutsen, Kate Liddle-Broberg, Patricia Nielsen, Gerard Rocher-Ros, Steph Saari, Deanna Strohm-Klobucar, Maria Väisänen and Dragos Vas assisted with data collection. Neal Pastick contributed remotely sensed attributes and modeled permafrost extent. Colin Edgar, Jason Downing, Jamie Hollingsworth, and Karl Olson contributed to project logistics including deployment and maintenance of the telemetry system, site maintenance, and access to long-term climate data collected by the Bonanza Creek Long-Term Ecological Research Program.

ABSTRACT

Introduction & Objectives: This SERDP project assessed whether stream biogeochemistry can indicate the ecological state of the contributing area, assess ecosystem resilience, and/or provide early warning of regime shifts caused by fire and permafrost thaw. The Department of Defense maintains extensive lands in the boreal forest that are managed to provide both suitable training grounds and ecosystem services including carbon storage and wildlife habitat. These lands are vulnerable to thawing permafrost and changing fire regime, which can replace the previously dominant black spruce forests with deciduous forests that do not insulate permafrost. Stream chemistry integrates signals originating from throughout the contributing area and could therefore assess ecosystem state at larger scales than ground-based measures.

Technical Approach: High-frequency (15-min) observations of stream chemistry were collected by instream sensors in a space-for-time design that included five catchments arrayed across orthogonal contrasts in spatial extent of permafrost and fire history within Interior Alaska. Statistical approaches were applied to deconvolute resulting temporal patterns at diel, storm, and seasonal time scales. A synoptic survey of stream chemistry across Interior Alaska provided context for the high-frequency data. Finally, analysis of multi-decadal datasets from experimentally harvested catchments in the temperate zone assessed the utility of long-term records of stream chemistry in detecting ecological regime shifts.

Results: Spatial and temporal patterns contrasted among catchments varying in fire history and spatial extent of permafrost. Greatest temporal variation at all time scales occurred in an unburned, high-permafrost catchment, and therefore flashiness in discharge and stream chemistry provides an indicator of permafrost integrity. Storms were the dominant source of variation in all catchments, and larger burned areas resulted in stronger source-limitation of nitrate export from catchments during storms. Catchments draining less extensive permafrost delivered nitrate to streams at a constant rate through each storm, whereas nitrate was diluted during storms in spatially extensive permafrost. Daily mean nitrate concentration was negatively correlated with temperature in burned catchments, which could result from nutrient uptake by regrowing vegetation. A broad-scale survey demonstrated that extensive fires also reduced export of dissolved organic matter from catchments to streams. Finally, leading indicators of regime change applied to multi-decadal observations of stream chemistry in experimentally harvested and reference catchments in the temperate zone demonstrated the utility of stream monitoring in detecting regime changes.

Benefits: Monitoring stream chemistry on boreal lands managed by the Department of Defense could aid in management by identifying catchments vulnerable to or currently undergoing loss of permafrost and carbon stores. High-frequency monitoring to quantify temporal variation and concentration-discharge relationships during storms could identify catchments subject to permafrost thaw and training or construction activities could be mitigated or redirected to less vulnerable locations. Decadal-scale change in storm dynamics could signal loss of resilience and lands within such catchments might be then used less intensively. Similarly, lower-frequency (e.g., monthly) monitoring over multiple decades could provide early warnings of regime change when temporal variance exceeds a pre-disturbance baseline. Finally, surveys of dissolved organic matter concentration conducted every several years could indicate recovery of soil organic matter pools, a key contributor to resilience of boreal ecosystems, and distinguish catchments that are unlikely returning to a spruce-dominated state that insulates permafrost.

EXECUTIVE SUMMARY

Introduction

This SERDP project assessed how stream chemistry reflects ecological states of boreal forest ecosystems, describes ecosystem resilience, and/or predicts ecological regime changes. Rapid climate warming at high latitudes causes more frequent fires, thaws permafrost, and results in a more temporally variable precipitation regime. The Department of Defense manages extensive lands in the boreal forest that provide training grounds as well as ecosystem services such as carbon storage and wildlife habitat. These lands are vulnerable to increasing intensity and frequency of fire and thawing permafrost. However, uncertainty about the resilience of boreal ecosystems to climate change constrains efforts to anticipate change and manage lands to maintain training and stewardship missions.

Mature forest ecosystems of Interior Alaska occupy one of two alternative states that are maintained by stabilizing feedbacks. Black spruce forests are resilient to infrequent fires of low intensity. Resilience of black spruce stands results from accumulation of a thick organic layer on the forest floor that insulates permafrost and fosters slow rates of decomposition and nutrient cycling. Deciduous forests follow frequent or intense fires that consume the soil organic layer. Changes between these two alternative stable states have consequences for integrity of permafrost, long-term storage of carbon in ecosystems, and water quality of receiving streams and groundwater, but changes are difficult to detect and predict at large spatial scales.

Hydrologic flowpaths contributing to streamflow integrate catchment-level spatial heterogeneity in ecosystem processes and could provide signals of ecosystem state at the catchment scale. In boreal ecosystems of Interior Alaska, the thick organic layer that accumulates in spruce forests provides a source of dissolved organic matter to streams. Wildfires might impart biogeochemical signals by removing vegetation and soil organic matter as sources of dissolved organic matter to streams. Removal of vegetation by fire also reduces the terrestrial sink for nitrogen during early succession and more rapid cycling of nitrogen in deciduous-dominated stands could result in increased nitrogen available for hydrologic export. Permafrost thaw also imparts signals in stream chemistry by activating flowpaths through deeper soils and fractured bedrock that generate mineral-rich runoff characterized by increased concentrations of nitrate and specific conductivity, and less dissolved organic matter. In addition to characterizing the current state of boreal ecosystems, temporal patterns in stream chemistry, including increased temporal variation, could signal loss of resilience in catchments and impending state changes.

Objective

The primary objective of this SERDP project was to determine whether stream chemistry contains signals of ecosystem state, resilience, and impending regime shifts resulting from disturbances in the contributing area.

Technical Approach

We assessed signals of ecosystem state in stream chemistry at multiple temporal scales, from diurnal oscillations to multi-decadal trends. We collected high-frequency observations (15 min) from five boreal streams draining catchments that vary in fire history and spatial extent of permafrost. We also surveyed streams across Interior Alaska spanning a gradient in fire history from 1 to greater than 70 years post-fire to provide context for the high-frequency data. Finally, we used multi-decadal datasets from experimentally harvested catchments in the temperate zone to demonstrate how long-term observations of stream chemistry could provide indicators of regime shifts.

High-frequency (15-min) observations of stream chemistry were collected by instream

sensors in a space-for-time design that included five boreal catchments arrayed across orthogonal contrasts in spatial extent of permafrost and fire history within Interior Alaska. Three of the catchments were within the Army's Yukon Training Area. We monitored concentrations of nitrate, dissolved organic matter, dissolved oxygen, turbidity, and specific conductivity as well as water temperature and stream discharge. We also measured concentrations of major anions and cations in grab samples collected at daily to biweekly frequency. Monitoring focused on the open-water period (~May-Oct) of 2019-2022.

High-frequency data were analyzed using statistical approaches for time series. We applied wavelet decomposition and coherence analysis to quantify patterns at daily to monthly frequencies. We examined concentration-discharge dynamics of individual storms to test hypotheses regarding material stores and hydrologic flowpaths resulting from presence of permafrost and fire history. Finally, we tested hypotheses at a seasonal scale using autoregressive state-space models that quantified trends; temporal stability in chemistry; and effects of temperature, antecedent precipitation, and instream production.

We conducted a single synoptic survey of >70 streams that drained catchments varying in fire history, vegetation, and permafrost extent. Analysis of stream chemistry included concentrations of dissolved organic carbon, total dissolved nitrogen, ammonium, nitrate, total dissolved phosphorus, and major anions and cations. We then attributed spatial patterns in stream chemistry using multiple regression analysis.

Finally, attributes of ecosystems can become more temporally variable as resilience is lost. Increased temporal variation occurs due to greater displacement of the ecosystem from a basin of attraction when perturbed or longer recovery times following perturbations. Analysis of resilience from temporal variation requires observations of duration encompassing disturbance and recovery. To demonstrate potential for stream chemistry to indicate regime changes, we analyzed multi-decadal records collected in paired catchment studies in the temperate zone that included experimental forest harvest.

Results and Discussion

Disturbance of terrestrial ecosystems by fire and permafrost thaw yielded spatial and temporal variation in stream chemistry. Signals of catchment state captured by stream chemistry included:

- Greatest temporal variation at all time scales occurred in an unburned, high-permafrost catchment (Fig. ES1). Flashiness in discharge and stream chemistry might therefore provide an indicator of permafrost integrity.
- Storms were the dominant source of variation in all catchments (Fig. ES1).
- Significant diel oscillations in dissolved organic matter concentration occurred under baseflow conditions in burned catchments (Fig. ES1). Oscillations on a daily time scale might reflect diurnal fluctuations in the depth of flowpaths due to evapotranspiration contributed by burned soils and regrowing vegetation. It might also reflect patchy distribution of organic matter on the forest floor of burned catchments.

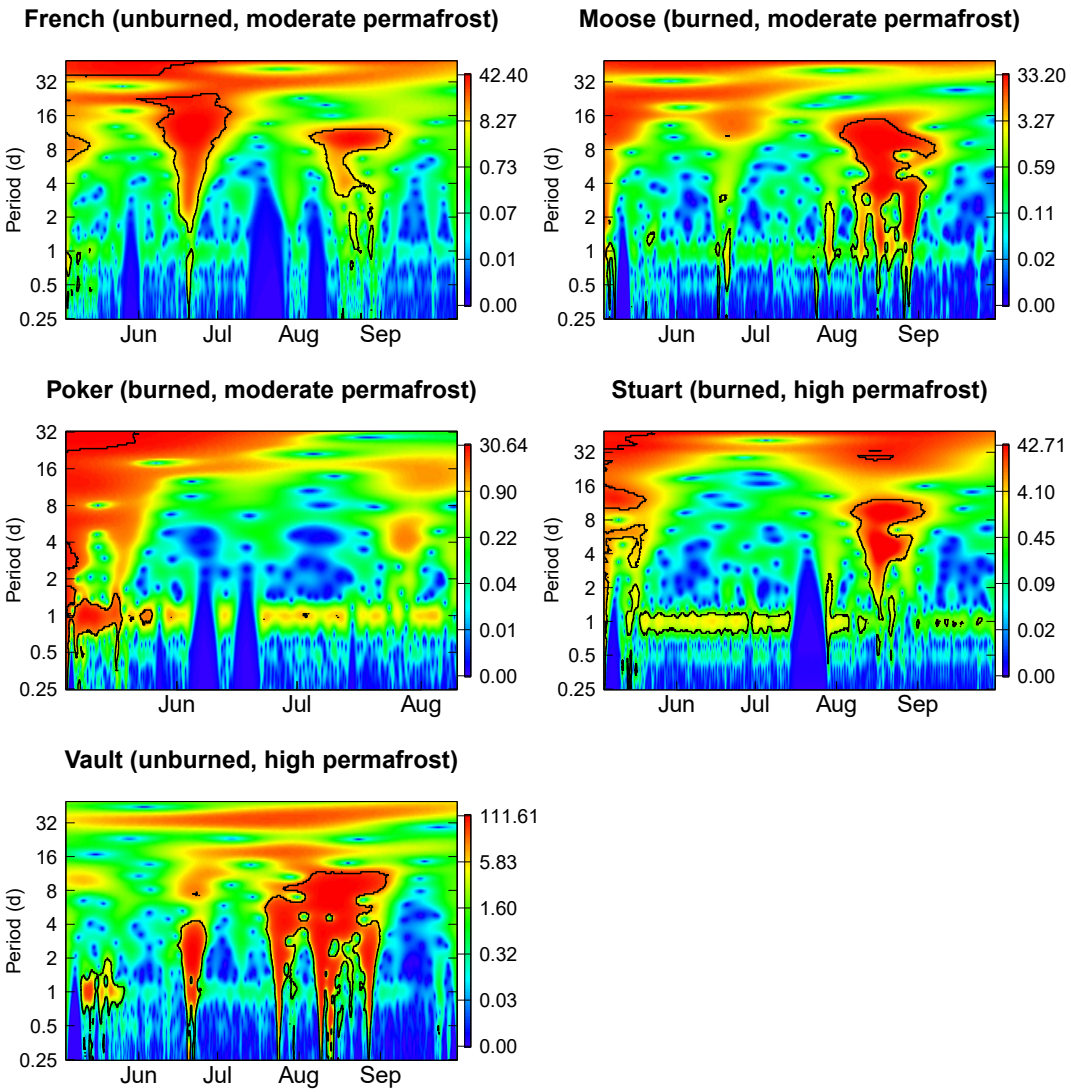


Figure ES1. Wavelet decomposition of fDOM concentration in 2022. Observations were made at 15-min frequency. The vertical axis displays frequencies and the scale bar indicates wavelet power (square of amplitude), with warmer colors associated with greater variation. Black outlines designate variation that is significantly greater ($\alpha = 0.05$) than expected from an autoregressive time series. The shaded cone indicates values with little data support. Note that the temporal extent varies slightly across the streams. Total precipitation for Jun-Aug was 125 mm in 2022, less than the long-term mean. Significant temporal variation at multiple frequencies is typically associated with storms in all catchments. Significant oscillations in fDOM concentration occur more often and over a wider range of frequencies at Vault Creek, which drains an unburned catchment of high permafrost extent. Note also significant diurnal oscillations not associated with storms in Poker and Stuart, which drain burned catchments.

- Concentration-discharge dynamics during storms varied along gradients of fire and permafrost extent. Larger burned areas resulted in stronger source-limitation of nitrate export during storms (Fig. ES2a). Catchments draining less extensive permafrost delivered nitrate to streams at a constant rate through each storm, whereas nitrate was diluted during storms in spatially extensive permafrost (Fig. ES2b).

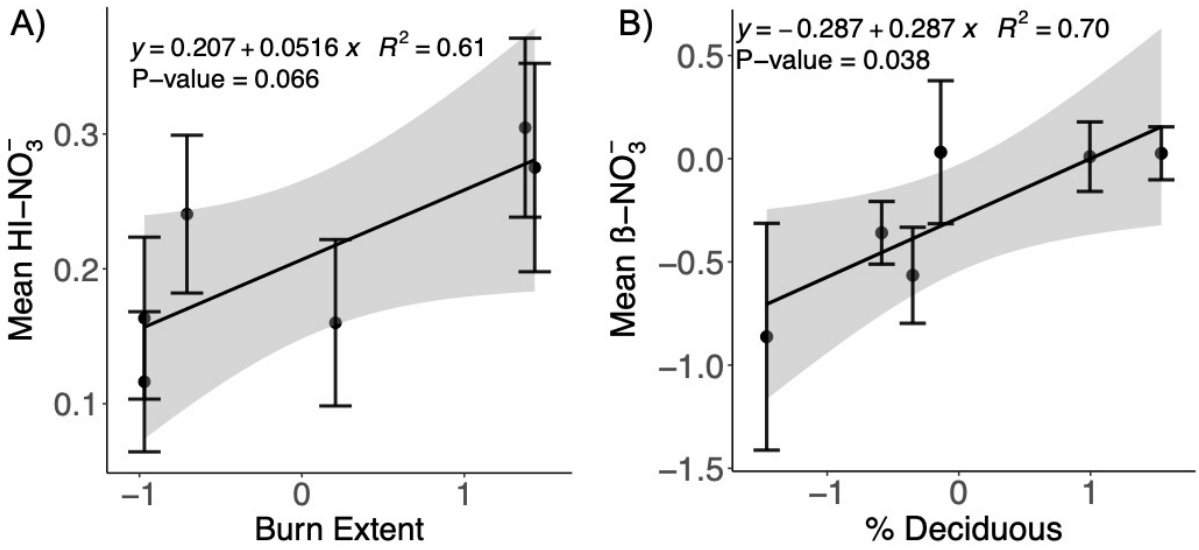


Figure ES2. Spatial extent of fire and permafrost were correlated with concentration-discharge dynamics during storms. Points are means across all storms observed in each catchment (~50 storms/catchment observed over 4-5 years). Error bars represent standard error across all storms observed in each catchment. Shading represents 95% confidence band of the regression relationship. Predictor variables reflect standardized values. A) Mean hysteresis index (HI) of nitrate (NO_3^-) as a function of burn extent in the catchment. HI describes differences in concentration relative to stream discharge on the rising and falling limb of each storm. Larger HI is associated with source limitation, whereby insufficient NO_3^- is available to supply the stream on the falling limb relative to the rising limb of the storm. Greater source limitation might occur in burned catchments if shallow flowpaths characterized by lower concentration of NO_3^- are rapidly activated during storms. B) Flushing/dilution dynamics (β) as a function deciduous cover in the catchment. Greater deciduous cover is associated with less extensive permafrost. Catchments of less extensive permafrost cover maintain NO_3^- export to streams during storms, whereas NO_3^- is diluted in the presence of permafrost. This pattern supports the hypothesis that deciduous stands, which occur in the absence of permafrost, contain greater supplies of inorganic nitrogen that are subject to hydrologic export.

- Daily mean nitrate concentration was negatively correlated with temperature in burned catchments (Fig. ES3). Variation in nitrate concentration with temperature in burned catchments likely reflects influence of nitrogen uptake by biota. Regrowing vegetation and/or soil microbes likely cycle nitrogen rapidly following fire.

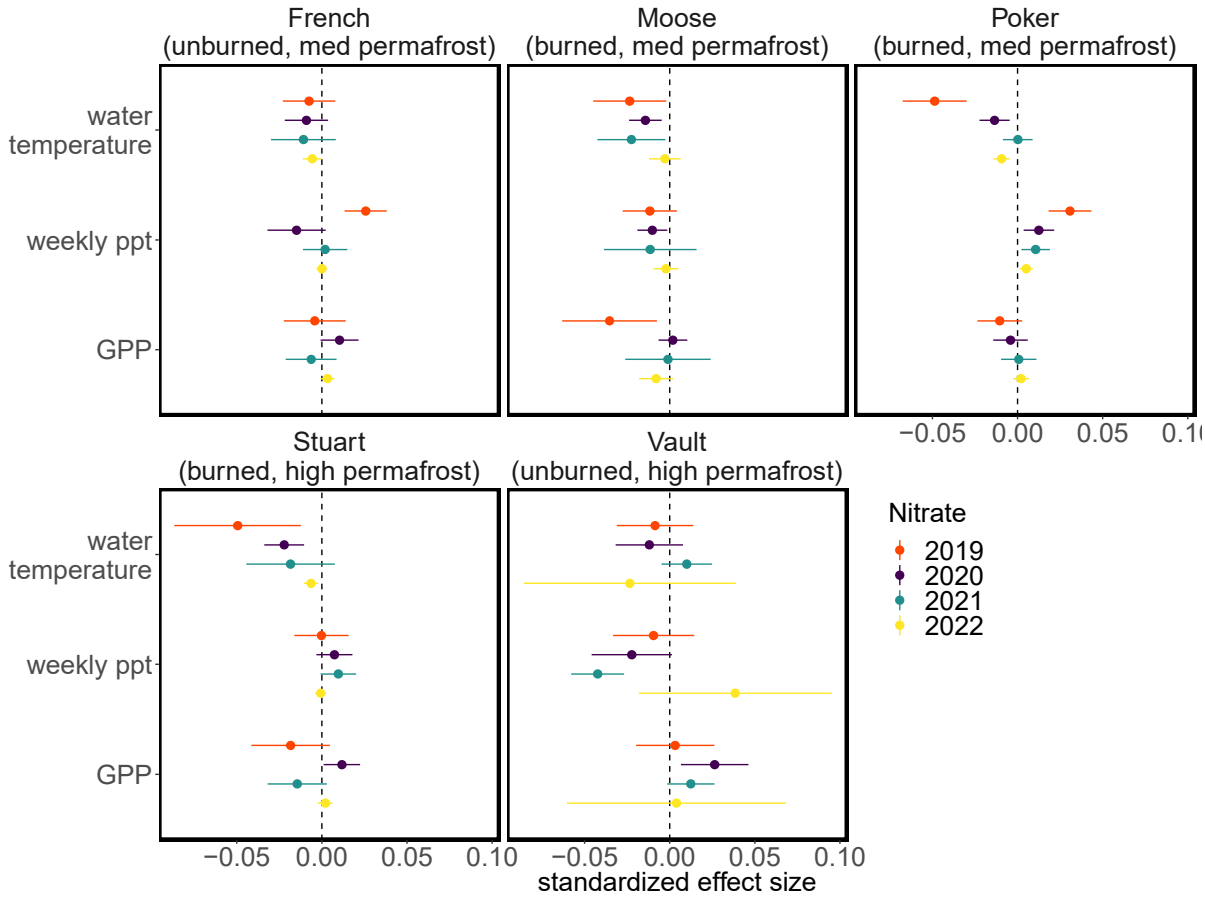
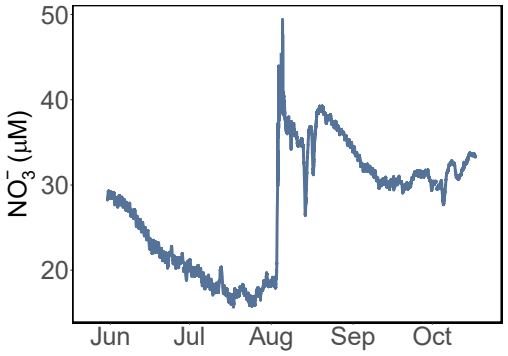


Figure ES3. Standardized effects of temperature, antecedent precipitation, and instream gross primary production (GPP) on mean daily nitrate concentration. Effects were estimated using multivariate autoregressive state-space models on ln-transformed concentration. Points reflect standardized estimates and error bars are 95% confidence intervals. Significant, negative effects of temperature on nitrate concentration occurred only in burned catchments. Instream GPP had significant effects on nitrate concentration sporadically, and these effects were both positive and negative, possibly suggesting a correlative, rather than causal relationship. Therefore, stream chemistry in these boreal streams is likely reflective of catchment processes, and signals are minimally modified by instream processes.

- Abrupt, non-linear increases in solute concentration, particularly of nitrate, were associated with precipitation in August or thereafter (Fig. ES4). Rain contributes to permafrost thaw and abrupt thaw of ice wedges could reroute flowpaths, exposing new sources of nitrate within catchments to hydrologic export.

Figure ES4. Non-linear increases in nitrate (NO_3^-) concentration were associated with precipitation in August or thereafter. Data from Poker Creek (burned, moderate permafrost catchment), 2019. Sustained, elevated nitrate concentration after return to baseflow suggests rerouting of hydrologic flowpaths that exposed new sources of nitrate to hydrologic export.



- Spatially extensive fires reduced export of dissolved organic matter from catchments to streams. The effect of fire on stream chemistry persisted over 1– > 70 years since fire, reflective of organic matter export on decadal or longer timescales, consistent with recovery trajectories of forests. Reduced fluvial export of DOM from burned catchments persists on a decadal timescale (Fig. ES5).

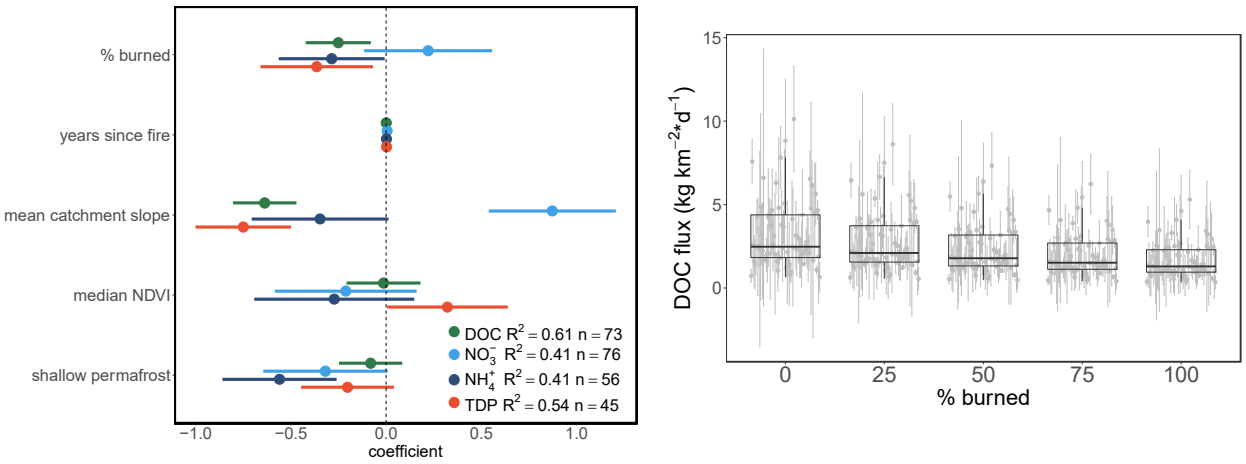


Figure ES5. Stream chemistry measured in a broad-scale synoptic survey of Interior Alaska was related to spatial extent of fire and permafrost in the catchment. Left: Standardized effects of catchment attributes on ln-transformed solute concentrations estimated by multiple regression models. Significant effects of fire on solute concentrations and no effect of time since fire (0– > 70 years) implies that recovery of solute pools occurs on decadal time scales and/or heterogeneous recovery trajectories among catchments. Right: Model-estimated fluvial yields of DOC decrease by 52%, on average, between unburned and completely burned catchments.

Implications for Future Research and Benefits

Stream chemistry and discharge contain signals relevant to diagnosing the effects of disturbance at catchment scales. Monitoring stream chemistry on lands managed by the Department of Defense could aid in identifying catchments vulnerable to or currently undergoing loss of permafrost, shifting vegetation cover, and changing patterns in carbon storage. High-frequency monitoring of a single season could characterize concentration-discharge dynamics during storms that reflect contrasts in fire history and permafrost extent. This short-term monitoring would therefore identify the present ecological state of whole catchments. Modifications to training or construction activities could then prevent further degradation of the soil organic layer and/or permafrost in catchments where permafrost is vulnerable to thaw or where the organic layer is reaccumulating post-fire.

Decadal-scale monitoring that captures dynamic responses to warming climate and changing fire regime could indicate catchments vulnerable to state changes caused by climate warming. Over multiple years, directional changes in concentration-discharge dynamics during storms or increased variance in these dynamics, including shifts toward chemostasis of inorganic solutes, could signal changing resilience due to degrading permafrost. Catchments exhibiting declining resilience might then be used less intensively to prevent a regime shift. Additional low-frequency (annual to every several years) monitoring of dissolved organic matter concentration in streams could indicate recovery of soil organic matter pools following fire. The soil organic layer is a key contributor to resilience of boreal ecosystems though difficult to detect remotely. Organic matter concentration in streams is a low-cost and easy-to-measure proxy for organic matter storage in the forest floor and could distinguish catchments that are recovering from fire and returning to a spruce-dominated state from those transitioning to a deciduous-dominated state. Therefore, low-frequency monitoring of dissolved organic matter in streams could contribute to identifying ecosystem services provided by expansive, but heterogeneous lands managed by the Department of Defense, including wildlife habitat and carbon storage.

Finally, analysis of multi-decadal records from the temperate zone demonstrated that longer-term observations of stream chemistry can detect loss of resilience in terrestrial ecosystems. Evaluating utility of stream chemistry for characterizing resilience of boreal ecosystems to climate warming will require monitoring over longer duration than the four years available from this project. The space-for-time approach used in this project documented contrasting temporal patterns among catchments exemplifying two alternative stable states. Longer-term records that encompass successional processes in the boreal forest are needed to observe whether patterns in stream chemistry shift through time reflecting change in catchment state.

Overall, monitoring stream chemistry to detect the ecological state of lands managed by the Department of Defense provides a complementary approach to ground-based or remote sensing methods for detecting landscape change in the boreal forest. Forest inventories and monitoring permafrost temperature track change in small areas and single point locations. Remote sensing can capture change in vegetation, but cannot yet track gradual permafrost thaw or dynamics of the organic layer over large areas. Temporal patterns in stream chemistry complement these traditional approaches to monitoring boreal change by integrating multiple physical and ecological processes at catchment scales. Stream sensors provide rapid access to data, such that management decisions regarding the timing and locations of military training activities might respond to indicators of reduced stability and resilience of ecosystems.

INTRODUCTION

Rapid climate warming at high latitudes results in more frequent fires, thawing permafrost, and a more temporally variable precipitation regime (Bintanja et al., 2020; Chapin et al., 2010; Jorgenson et al., 2010; Osterkamp, 2007; Wolken et al., 2011). Ecosystem responses to climate warming in northern, boreal forests might include changes in seasonality or rate of primary production, reduced carbon (C) storage, and degrading water quality due to increased turbidity or nutrient release. However, uncertainty about the resilience (cf. Holling, 1973) of boreal ecosystems to climate change constrains efforts to project change and manage lands to maintain the training and stewardship missions of the Department of Defense (DoD).

Presence of permafrost underlying ~40% of Interior Alaska strongly shapes the state of boreal ecosystems, but is expected to mostly disappear from the near surface (upper 1 m) by 2100 (Pastick et al., 2015). Mean annual air temperature in the region (currently –1°C) is projected to increase by at least 2°C and 5°C by 2050 and 2100, respectively (Lader et al., 2017). Permafrost in Interior Alaska is "ecosystem protected" by an insulating layer of organic matter (OM) over the ground surface (Jorgenson et al., 2010). Disturbance to this insulating layer from climate warming, infrastructure development, or wildfire increases ground heat flux and promotes top-down and lateral permafrost thaw (Farquharson et al., 2022; Smith et al., 2022). Thawing permafrost permits deeper infiltration of soils, which can cause increased export of nitrate (NO_3^-) to streams and reduced leaching of dissolved organic matter (DOM; Harms et al. 2016). Elevated turbidity in streams additionally occurs when abrupt thaw of ice-rich permafrost causes erosion (Beel et al., 2020).

Boreal forest ecosystems of Interior Alaska exhibit two alternative stable states that are maintained by stabilizing feedbacks, but can undergo state changes initiated by intense or frequently recurring fire. Deciduous forests dominate under a short return interval of fire or in response to high-intensity fires that combust most of the organic layer on the forest floor (Fig. 1; Johnstone et al., 2010). Black spruce forests are resilient to infrequent fires of low intensity. Resilience of black spruce stands to fire is contributed by accumulation of a thick organic layer on the forest floor that insulates permafrost and results in cold soils supporting slower rates of decomposition and nutrient cycling. Changes between these two alternative stable states have consequences for long-term storage of C in ecosystems (Mack et al., 2021), as well as for water quality of receiving streams and groundwater.

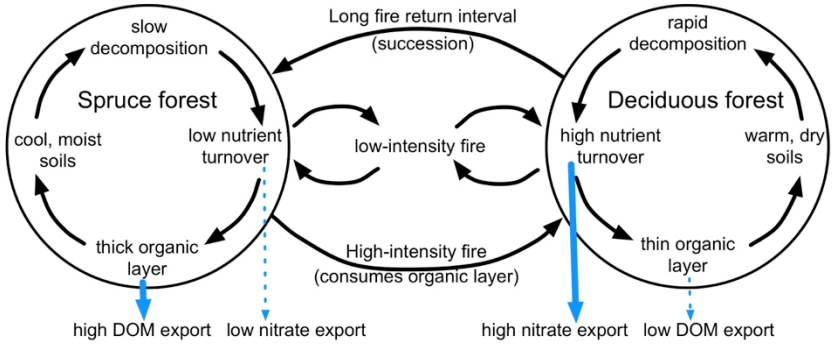


Figure 1. Conceptual model of alternative stable states in high-latitude, boreal forests (adapted from Johnstone et al. [2010]). We investigated the utility of fluxes of DOM and NO_3^- in streams (blue arrows indicating relative magnitude) as indicators of spruce and deciduous-dominated regimes.

This SERDP project assessed whether stream biogeochemistry can indicate the ecological state of the contributing area and potentially provide early warning of a regime shift between the spruce- and deciduous-dominated states. Attributes of ecosystems can become more temporally variable as resilience is lost, resulting from greater displacement

of the ecosystem from a basin of attraction when the ecosystem is perturbed or longer recovery time following perturbations (Scheffer et al., 2015). Bimodality and increasing skew also characterize loss of resilience, when perturbations cause oscillations between two alternative stable states (Wang et al., 2012).

Research established the use of stream chemistry as an indicator of the ecological state of whole catchments and to determine the susceptibility of boreal ecosystems to a changing disturbance regime. We collected high-frequency (15-min) observations of stream chemistry using instream sensors deployed in boreal catchments arrayed among orthogonal contrasts in spatial extent of permafrost and fire history. We then applied statistical approaches to characterize ecosystem states from time series of stream chemistry. Sensors provide rapid access to data, such that management decisions regarding the timing and locations of military training activities might respond to indicators of reduced stability and resilience of ecosystems. Stream chemistry integrates signals originating from throughout the contributing area, providing assessment of ecosystem state at larger scales than ground-based measures.

BACKGROUND

Stream chemistry reflects integrated signals resulting from the hydrological and ecological state of whole catchments (Likens, 2004). Temporal patterns including seasonal or longer-term trends, storm dynamics, and diel oscillations result from the spatial distribution of hydrologic flowpaths and stores of materials, including C and nitrogen (N) in the catchment, as well as biotic processes in receiving streams (Bernhardt et al., 2022; Burns et al., 2019; Kirchner et al., 2004). Changes in characteristic temporal patterns in stream chemistry might therefore indicate ecosystem responses to changing climate and disturbance regimes (e.g., Fork et al., 2020; C. S. Jones et al., 2017; Keller et al., 2010).

In the boreal forest of Alaska, stream chemistry reflects the thermal, hydrologic, and vegetation attributes associated with spatially discontinuous permafrost (ground that remains frozen for ≥2 years). Permafrost maintains cool, moist soils that slow decomposition resulting in accumulation a thick organic layer that insulates permafrost, promotes establishment of spruce forests, and provides a source of DOM to streams (Fig. 1; Johnstone et al., 2010; Jorgenson et al., 2010; Tank et al., 2016; Wickland et al., 2007). Deciduous forests occur in the absence of permafrost where warmer, drier soils foster more rapid nutrient turnover and limit accumulation of soil organic matter (OM; Johnstone et al., 2010; Melvin et al., 2015). As a result, a greater proportion of OM is stored in aboveground biomass, which could limit leaching and transport of DOM to streams in permafrost-free zones (Alexander & Mack, 2016).

Ice-rich permafrost prevents infiltration, confining hydrologic flowpaths through shallow, organic-rich soils (Carey & Woo, 1999; Hinzman et al., 2005). Permafrost thaw then activates flowpaths through deeper soils and fractured bedrock that generate more mineral-rich runoff (Jorgenson & Osterkamp, 2005; Koch et al., 2013). Instream signals of permafrost thaw can therefore include higher concentrations of inorganic solutes, such NO_3^- and specific conductivity (SPC; Balcarczyk et al., 2009; Connon et al., 2014; Harms et al., 2016; Koch et al., 2013). Permafrost thaw can also cause physical perturbations such as thermokarst that deliver sediment to streams (Kokelj et al., 2013).

Wildfires might also impart biogeochemical signals that are hydrologically transported to streams. Combustion of vegetation and the soil organic layer reduces export of DOM to streams (Betts & Jones, 2009; Rhoades et al., 2019; Zolkos et al., 2022). Removal of vegetation can also reduce the terrestrial sink for N, increasing export of inorganic N to streams (Rodríguez-Cardona

et al., 2020). Combustion of trees and soil OM limits evapotranspiration and can reduce capacity for water storage within the catchment, resulting in increased runoff and flashier responses of stream discharge to precipitation (Pimentel & Arheimer, 2021). Finally, wildfire contributes to permafrost degradation (Brown et al., 2015), which could deepen hydrologic flowpaths and yield greater export of mineral ions to streams (Petrone et al., 2007).

OBJECTIVES

The primary objective of this SERDP project was to determine whether signals of ecosystem state and responses to disturbance were present in temporal patterns of stream chemistry. Signals of permafrost loss or changing ecosystem structure could inform planning of training activities and construction projects to minimize further disturbance to vulnerable lands. We assessed signals of ecosystem state in high-frequency observations collected from five streams draining catchments that vary in fire history and spatial extent of permafrost. We also surveyed streams across Interior Alaska to provide context for the high-frequency data and used multi-decadal datasets from experimentally harvested catchments in the temperate zone to assess long-term patterns. From these data, we:

1) Assessed whether biotic processes in streams modify biogeochemical signals delivered from catchments
2) Estimated the flowpaths by which water traverses catchments and determined how disturbances alter the delivery of water and solutes to streams
3) Compared catchments varying in permafrost extent and fire history to assess how these disturbances are reflected in stream hydrology and biogeochemistry
4) Quantified “leading indicators” of ecological regime change to assess utility of stream chemistry in assessing resilience of catchments and the relative vulnerability of boreal ecosystems to multiple modes of disturbance

TECHNICAL APPROACH & FINDINGS

Schedule

This project was initiated October 2018, which was a delay relative to the timeline included in the project proposal due to delivery of the research contract. Field seasons for stream work in Interior Alaska are approximately May-October, so the first year of data collection occurred in 2019. An 8-month no-cost extension allowed a fourth field season of data collection, as originally proposed (Table 1; Task 5). The project incurred delays due to the COVID-19 pandemic related to access to laboratory facilities. Findings related to project objectives (Table 2) are detailed in the subsequent sections.

Table 1. Project timeline. F: field season, May-Oct. W: off-season, Nov-Apr. Note Year 1 of the project began W 2018, rather than F 2018 as proposed and an 8-month no-cost extension was granted.

	Year 1 2019		Year 2 2019		Year 3 2020		Year 4 2021		Year 5 2022	
Task	F	W	F	W	F	W	F	W	F	W
1: Select & characterize sites	■	■								
2: Install infrastructure	■									
3: Establish data relay system	■									
4: Initial sensor calibrations	■	■		■		■				
5: Collect high-frequency data	■		■		■		■		■	
6: Automate quality control		■		■						
7: Model instream processes		■		■		■		■		■
8: Mixing models		■		■		■		■		■
9: Time series models				■		■		■		■
10: Quantify leading indicators				■		■		■		■

Table 2. Research questions, hypotheses, and associated tasks.

Research question 1: How does resilience of biogeochemical cycles vary in response to the modes of disturbance typical of high-latitude, boreal ecosystems?	
	Task 1: Select sites and secure permissions
	Task 2: Install infrastructure
	Task 3: Establish data relay system
	Task 4: Initial sensor calibrations
	Task 5: Install sensors and collect high-frequency data
	Task 6: Statistical approaches for quality control
	Task 10: Quantify leading indicators of regime change
Research question 2: How do high-latitude catchments maintain resilience of biogeochemical cycles?	
	Hypothesis 2.1: Biota in streams take up NO_3^-, maintaining an ecosystem state characterized by low export of NO_3^-.
	Task 7: Model instream metabolism & N uptake
	Hypothesis 2.1: Shallow flowpaths route water through organic soils that leach DOM and support retention of NO_3^-, maintaining a state of high DOM and low NO_3^- export.
	Hypothesis 2.2: Capacity for denitrification within catchments contributes to a state of low NO_3^- export.
	Task 8: Determine sources of water and nitrate to streams
	Hypothesis 2.4: Strong coupling between cycles of C and N promotes ecosystem resilience because N constrains primary productivity and accumulation of organic matter in catchments (source of DOM), and plants and microbes retain N in biomass and remove NO_3^- by heterotrophic denitrification.
Research question 3: How do antecedent temperature and moisture conditions influence susceptibility of boreal ecosystems to regime changes?	
	Hypothesis 3.1: Drought and high temperatures increase potential for a state change by deepening flowpaths through catchments, disconnecting sources of DOM from streams and routing NO_3^- beneath the rooting zone.
	Hypothesis 3.2: Anomalously wet conditions can mitigate the effects of fire and permafrost degradation by activating flowpaths that connect shallow soils, which are sources of DOM and sinks for NO_3^-, to streams.
	Hypothesis 3.3: Oscillating wet and dry periods degrade ecosystem resilience due to build-up of N and soluble DOM within the catchment, followed by rapid depletion of these pools due to hydrologic export during floods, which results in loss of the nutrient limiting productivity of forests and decreased capacity to store C in terrestrial ecosystems.
	Task 9: Time series models to estimate effects of disturbance on C and N fluxes

Task 1: Select sites and secure permissions

The project applied a space-for-time approach to study effects of fire and permafrost thaw, by contrasting burned and unburned catchments of contrasting aspect, which influences spatial extent of permafrost. The study included five focal catchments that contrasted in fire history and permafrost extent (Table 3, Figs. 2 & 3). Three of the sites were located on the Army's Yukon Training Area (French, Moose, and Stuart Creeks). The sites were selected with input from the Natural Resources Office at Fort Wainwright. Two sites were monitored in 2018. The remaining sites were established in May 2019. Sites were located within the Yukon-Tanana uplands of Interior Alaska and were road-accessible.

Regional climate is continental and classified as semi-arid, with ~327 mm of precipitation per year, of which ~38% falls as snow. Long-term mean annual temperature is –1°C. The study catchments are underlain by spatially discontinuous to nearly continuous permafrost, defined as ground that remains frozen for two or more years. South-facing slopes, where permafrost is typically absent, are vegetated by hardwood forests (*Betula neoalaskana, Populus tremuloides*). Permafrost is typically present on north-facing slopes, which are vegetated by black spruce (*Picea mariana*), and in riparian zones, vegetated by shrubs including dwarf birch (*Betula glandulosa*), cranberry (*Vaccinium vitis-idaea*), blueberry (*V. uliginosum*), and tussock-forming grasses and sedges (*Eriophorum spp.* and *Calamagrostis canadensis.* Hardwoods (birch [*Betula neoalaskana*], balsam poplar [*Populus balsamifera*], and aspen [*P. tremuloides*]) colonize well-drained soils lacking permafrost and occur at intermediate successional stages. Black (*Picea mariana*) and white spruce (*P. glauca*) stands typically co-occur with permafrost on north- and east-facing slopes.

Table 3. Attributes of boreal catchments included in the study.

Site	Catchment area (km^2)	Slope (%)	Aspect	Permafrost extent (estimated)	Shallow (within 1 m of surface) permafrost extent (%)[#]	Substrate[‡]	% deciduous cover[†]	Year of most recent fire[§]	% burned, most recent fire	% high-intensity burn, most recent fire[^]	Year of largest fire	% burned, largest fire
Caribou*	43	11.3	east	moderate	38.9	Rocky upland	18.3	NA	NA	NA	NA	NA
French	44	12.3	west	moderate	32.3	Silty upland	22.7	2013	<0.1%	0	1997	7.3
Moose	111	10.2	west	moderate	28.2	Silty upland	22.5	2018	0.24	33.1	2013	65.7
Poker	62	11.5	west	moderate	36.9	Rocky upland	21.6	2016	0.15	25.6	2004	33.0
Stuart	125	13.7	north	high	28.7	Silty upland	18.8	2019	2.5	21.5	2013	67.4
Vault	35	9.4	north	continuous	40.7	Silty upland, yedoma soils	19.9	NA	NA	NA	NA	NA

[‡]Following Jorgenson et al. (2013)
[§]Fire history and burn extent summarized from the Alaska Interagency Coordination Center, with records of burn extent to 1940
[#]Estimated following Pastick et al. (2015)
[†]National Land Cover Dataset 2016
[^]Monitoring Trends in Burn Severity, https://www.mtbs.gov
*Discharge and chemistry data for Caribou Creek from the National Ecological Observatory Network

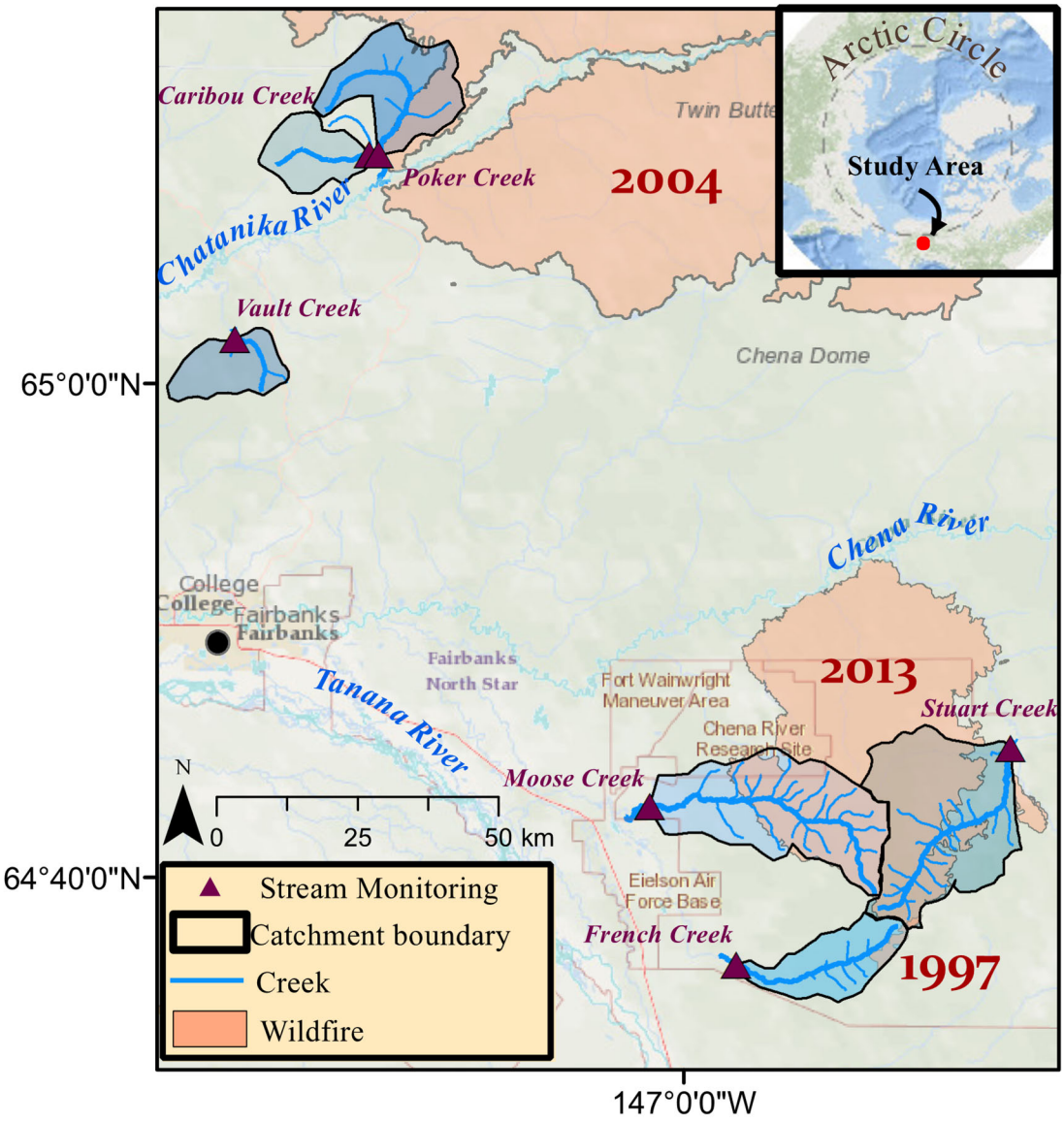


Figure 2. Locations of study sites in Interior Alaska. Boundaries of contributing areas are indicated to the point of instream monitoring. French, Moose, and Stuart Creeks are located on the Army's Yukon Training Area. In addition to the five sites monitored by this project, data from a site monitored by the National Ecological Observatory Network (Caribou Creek) using similar approaches are incorporated into analyses where possible.



Figure 3. Sensors were installed in five streams, with data collection generally extended from snowmelt until freeze-up.

Task 2: Install infrastructure

All five sites were equipped with infrastructure for housing instream sensors and telemetry equipment in May-June 2019. Infrastructure included an aluminum mesh housing that protects the sensors and is mounted on an I-beam with a winch to facilitate access to equipment for servicing. I-beams were variously attached to trees, a poured concrete pylon, and a bridge (e.g., Fig. 4).

Equipment was typically installed during ice-out in May and retrieved when ice cover formed in late September or October. In 2020, equipment installation was delayed until June, due to restrictions on research at the University of Alaska Fairbanks and Cold Regions Research and Engineering Laboratory, and restricted access to sites located on the Yukon Training Area due to COVID-19. Once equipment was installed, data collection proceeded as planned in the 2020 season.



Figure 4. Infrastructure installed to secure sensors and provide routine access for maintenance. Left: An I-beam anchored to a bridge. Right: Sensors were housed in an aluminum mesh cage (upper right) accessed using a winch (bottom right).

Task 3: Establish data relay system

Many statistical models for time series that are central to the approach for detecting biogeochemical signals in streams are not amenable to gaps > 24 h and we therefore aimed to maintin gapless datasets from the stream sensors. We established a telemetry system to allow remote monitoring of the data. Sites were visited in addition to regular, biweekly maintenance visits when measured parameters suggested impending interruptions to data acquisition or to data quality.

The telemetry system consisted of CRX-1000 dataloggers from Campbell Scientific, cellular transmitters, and radio repeaters and transmitters. The Vault and Moose Creek sites were relayed via reliable cellular service. The Poker Creek site was telemetered via radio transmission to a node maintained by the Bonanza Creek Long-Term Ecological Research Program. Configuration of the telemetry network for three most remote sites, located on the Yukon Training Area, is shown in Fig. 5. Data from French Creek were relayed via multiple radio transmission nodes to a datalogger at the Moose Creek site and provided intermittent connectivity due to obstructing terrain and vegetation. We were unable to establish a reliable connection with Stuart Creek, the most remote site, due to difficult terrain and limited access to the site and locations of radio repeaters due to Army training activities. Overall, the telemetry system provided consistent real-time monitoring of three sites and intermittent monitoring of a fourth site.

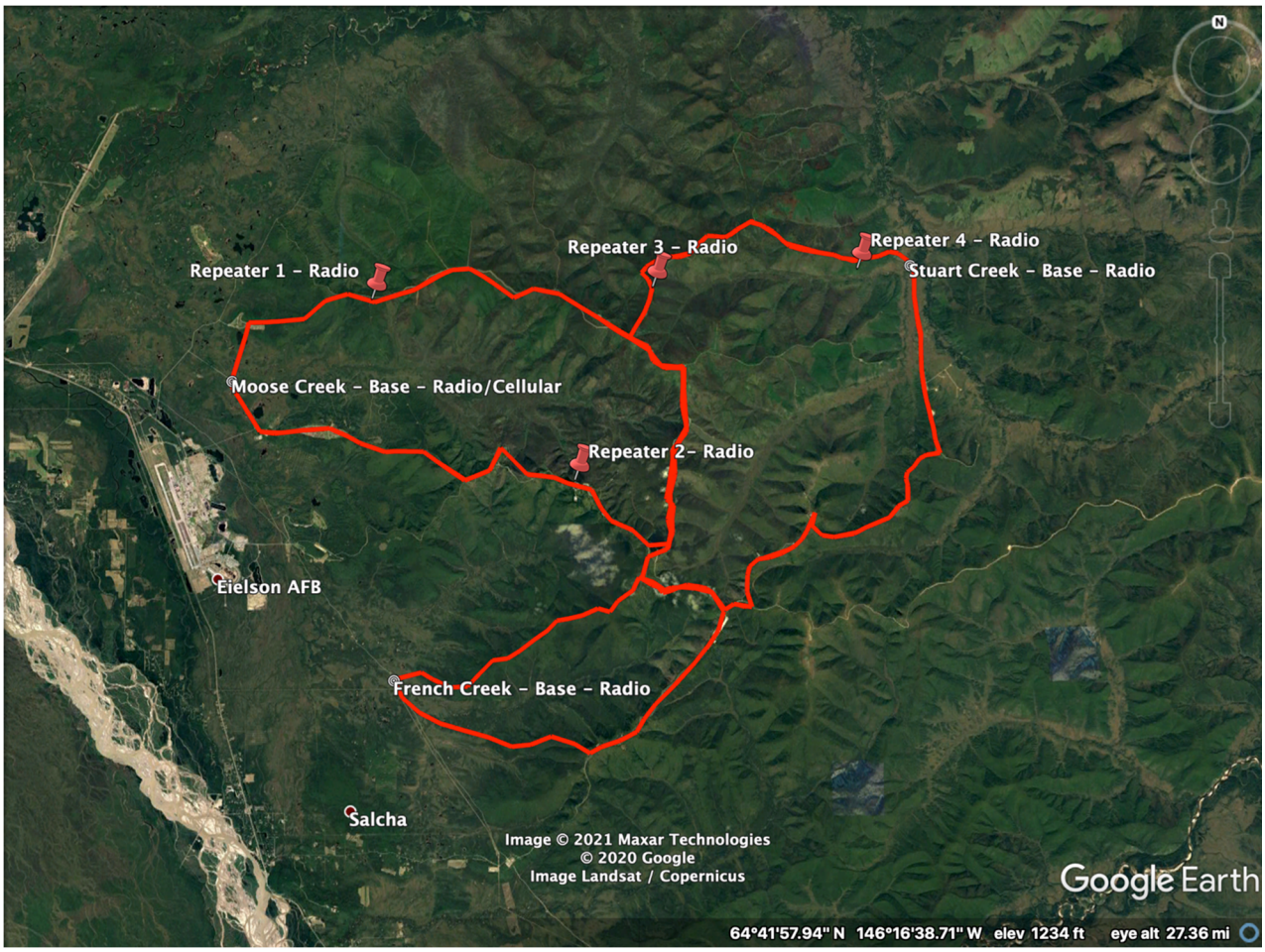


Figure 5. Data telemetry network on the Yukon Training Area. The network consisted of instream sensors linked to dataloggers with radio transmission and intervening radio repeater stations. Data from all three sites were collected by a datalogger located at the Moose Creek site and transmitted via the cellular network.

Task 4: Initial sensor calibrations

Sensor-collected data require several calibration steps to ensure accuracy and consistency. Sensors were calibrated to certified standards in the laboratory prior to deployment each season. Sensor-collected data were checked for drift and biofouling in deionized water approximately every two weeks during deployment and data were corrected for these effects when present. Sensor-collected observations of nitrate concentration were corrected to laboratory measures by a regression relationship with grab samples collected biweekly and analyzed by ion chromatography. Though dissolved organic carbon (DOC) is a more desirable output than fDOM because it can be used in carbon budgets, the fDOM-DOC relationship varied through the monitoring period each year, likely due to changing composition of DOC in the stream, and we report concentrations of fDOM as measured by the sensor.

Measures of fDOM collected by the fluorescence-based sensor additionally require adjustment for effects of temperature on performance of the sensor, and for interference by turbidity and colored DOM (Fig. 6). These correction factors require laboratory tests to produce correction factors that are potentially sensor- and site-specific (Downing et al., 2012; Watras et al., 2011). We used the following relationship to calculate corrected fDOM (Downing et al. 2012):

$$fDOM_{corr} = fDOM_{raw} + \rho(T_{meas} - 25) / r_p \times r_d$$

where T_{meas} is water temperature in °C, ρ is the temperature-specific fluorescence coefficient ($°C^{-1}$), and r_d and r_p are the instrument-specific correction functions for colored DOM and turbidity. We calculated functions for ρ and r_d for each instrument, and r_p for each instrument and site of deployment.

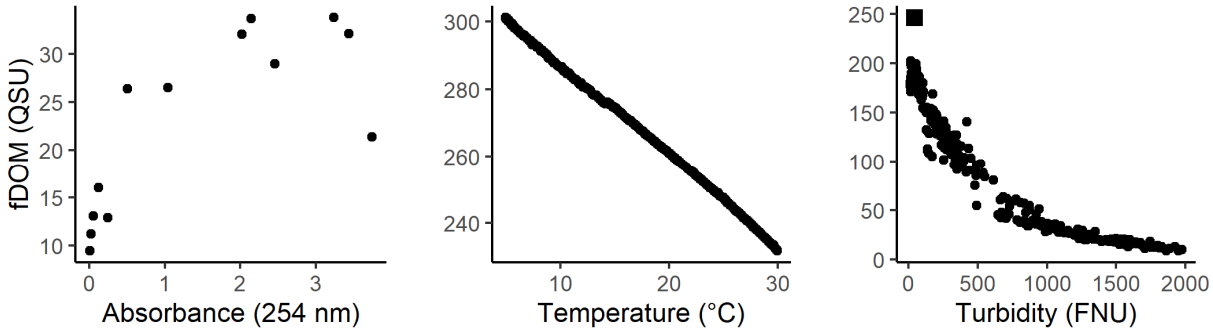


Figure 6. Example of relationships between fDOM and colored DOM (indexed by absorbance at 254 nm), temperature (°C) and turbidity (FNU). Calibration curves established in the laboratory were applied to correct field-measured fDOM concentration for these interferences. The black square on the turbidity plot represents filtered stream water.

A correction function for temperature effects on fDOM was generated by incubating sensors in a temperature-controlled cabinet while logging concentration of a constantly stirred sample of stream water. Temperature in the cabinet was raised from -0.1 to 30°C. We used the following relationship to calculate ρ (Watras et al. 2011):

$$fDOM_r = fDOM_m / [1 + \rho(T_m - T_r)]$$

where T is temperature (°C), $fDOM_r$ is the reference value and $fDOM_m$ is the measured value.

To calculate a correction function for colored DOM, we measured the absorbance at 254 nm (abs254) using a spectrophotometer and fDOM using the EXO sensor on a series of stream water

samples diluted with DI water. The correction factors for colored DOM (r_d) were calculated using the following relationship (Downing et al. 2012):

$$r_d = fDOM_{raw}/fDOM_{filtered}$$

To correct fDOM for interference by turbidity, turbidity (FNU: Formazin Nephelometric Units) and fDOM were measured on stream water samples with decreasing concentration of suspended sediment. Sediment were collected from each monitored stream. Filtered stream water and sediment were combined to reach turbidity exceeding that observed in the study sites. Sediment was suspended using a stir bar and serial dilutions were performed by filtering aliquots and returning filtered water to the measuring vessel. fDOM concentration of the initial, filtered stream water provided the value of $fDOM_{filtered}$. The resulting relationships between turbidity and fDOM readings were used to calculate correction functions for turbidity (r_p) using the following relationship (Downing et al. 2012):

$$r_p = fDOM_{raw}/fDOM_{filtered}$$

Task 5: Install sensors and collect high-frequency data

5.1 Data collection

Five streams were instrumented during the open-water period (~May-Oct) 2019-2022 (Table 4). A late June start occurred in 2020 due to COVID-19 restrictions on travel and research activities and gear was pulled in mid-Sept of 2021 due to freezing conditions. Instrumentation monitoring water chemistry and temperature included an EXO multi-parameter sonde (Yellow Springs Inc.) and a Submersible Ultraviolet Nitrate Analyzer (SUNA; Seabird Inc.). Sensors were equipped with a brush that cleaned read windows before each measurement. Each EXO sonde was equipped with sensors measuring specific conductivity and temperature, and optical sensors measuring concentrations of dissolved oxygen, turbidity, and fDOM. The SUNA measured absorbance at ~200 wavelengths of emitted light and is calibrated to compute NO_3^- concentration from the resulting absorbance spectrum. Nitrate concentration measured by the SUNA has a limit of quantitation (LOQ) = 0.014 mg N L^{-1} and short-term precision = 0.004 mg N L^{-1}). We also analyzed abs254 measured by the SUNA. Like fDOM, abs254 is also typically correlated with concentration of DOC, but likely reflects a different set of organic molecules characterized by aromaticity. These measures therefore provide complementary information about a complex organic pool. All water quality sensors recorded parameters every 15 minutes, collecting a "burst" of repeated measurements within a 30-s window. Sensor-collected records of water quality parameters are shown in Fig. 7.

Before deployment, we verified that SUNAs met the manufacturer specification of ±0.028 mg N L^{-1} in nanopore water and we calibrated SPC, fDOM, and turbidity sensors to externally-verified standards. Following manufacturer's specifications, we calibrated DO sensors in moist air. Once deployed, we made biweekly site visits to check EXO and SUNA sensors against nanopure water for drift and biofouling, clean optical read windows, and recalibrate EXO sensors as indicated based on drift and fouling. SUNAs also received maintenance by the manufacturer approximately every other year that included lamp replacement and recalibration of the spectrophotometer.

An ISCO autosampler was deployed to collect a daily grab sample from each stream for at least two weeks during each month of sampling, complementing manual grab samples collected during biweekly site visits. Water samples were retrieved approximately biweekly from autosamplers. Manual grab samples were filtered in the field and autosampler-collected samples were filtered in the laboratory (0.7 μm glass fiber filters for both) after transport on ice to the

Table 4. Sensor deployment dates and missing data (as percent of deployment days).

Site	Data collected	NO_3^-	fDOM	SPC	Turbidity
		2018			
Caribou	6/6-10/11	28.9	13.1	13.1	11.2
Moose	5/30-10/26	10.8	13.1	10.8	10.8
French	5/30/-10/12	37.8	1.5	1.5	1.5
		2019			
Caribou	5/7-9/24	3.7	0	0	0
Moose	5/9-10/21	1.8	0	0	0
French	4/29-10/10	0	0	0	0
Poker	5/11-10/16	0	0	0	0
Vault	5/10-10/16	0.6	2.5	2.5	2.5
Stuart	5/7-10/16	16.1	8.6	8.6	8.6
		2020			
Caribou	6/16-9/8	19.6	24.3	19.6	19.6
Moose	6/11-10/15	0	0	0	0
French	6/11-10/15	0	0	0	0
Poker	6/5-10/14	0	0	0	0
Vault	6/5-10/14	1.5	0	0	0
Stuart	6/17-10/12	0	0	0	0
		2021			
Caribou	5/7-10/18	6.5	0	0	0
Moose	5/5-9/28	47.9	0	0	0
French	5/5-9/27	0	15.9	15.9	15.9
Poker	5/6-9/29	34	17.8	17.8	17.8
Vault	5/11-9/27	32.4	10.1	10.1	10.1
Stuart	5/7-9/30	26	10.3	10.3	10.3
		2022			
Caribou	5/9-10/11	0	0	0	0
Moose	5/10-10/10	3.9	0	0	0
French	5/11-10/10	0	7.2	7.2	7.2
Poker	5/9-10/7	0	1.3	1.3	28.5
Vault	5/17-10/11	2.3	58.3	58.3	58.3
Stuart	6/2-10/8	0	0	0	0

laboratory. Samples were frozen or acidified to pH 2 and acidified until analysis, depending on the analyte. Solute concentrations and absorbance of the grab samples were used in calibration of the SUNA (Task 4) and in mixing models to estimate sources of water and solutes to each stream (Task 8).

Two pressure transducers (HOBO) monitored water pressure in each stream, and a pressure transducer monitoring atmospheric pressure was installed at a subset of the sites. These air pressure data, as well as air pressure monitored by nearby weather stations maintained by Eielson Air Force Base and the National Ecological Observatory Network were used to correct water pressure for changes in atmospheric pressure. Stream discharge was then estimated from corrected water pressure using site-specific rating curves. Stream discharge was measured by salt slug dilution and the velocity-area method using a flowmeter and wading rod approximately biweekly. Measured discharge was then regressed on water pressure to generate a rating curve, which was then applied to the time series of water pressure to produce a continuous record of stream discharge (Fig. 7). We also derived water level from hydrologic monitoring data and shared these with the Natural Resources Office at Fort Wainwright.

A tipping bucket rain gauge (both manufactured by HOBO) was installed at a subset of sites. These data complemented datasets collected by weather stations maintained by the National Ecological Observatory Network and the Bonanza Creek Long-Term Ecological Research Program, which were also used in analyses.

Finally, a sensor measuring photosynthetically-active radiation (PAR; Odyssey, Christchurch, New Zealand) was installed above the stream surface at each site. PAR drives

gross primary production (GPP) in streams, and these data were used in estimating daily rates of GPP (Task 7).

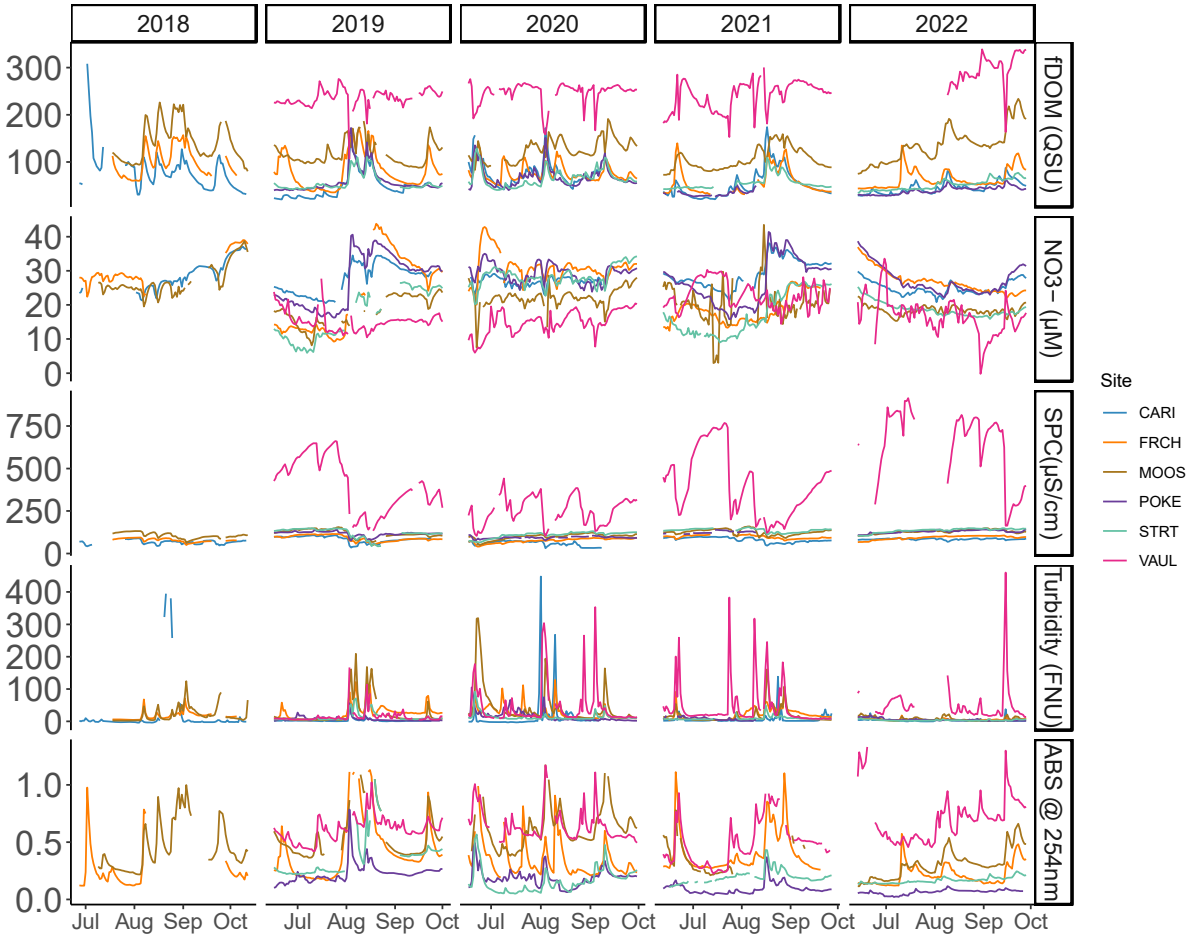


Figure 7. Discharge and stream chemistry in boreal streams measured at 15-min intervals. Data from CARI were collected by the National Ecological Observatory Network.

5.2 Weather & hydrologic conditions during monitoring

Mean annual air temperature in the study region (1992-2022) is -3.4°C with the lowest mean monthly temperature typically in January (-23.0°C) and the highest mean monthly temperature in July (15.1°C). During the study period (2018-2022), temperatures recorded in the Caribou-Poker Creek Research Watershed were similar to the long-term average, with exceptions of winter low temperatures ~3°C colder than average in 2018 and 2019, and summer high temperature ~1°C warmer than average in 2019.

Mean annual precipitation is 327 mm with 234 mm falling between June and August (Fig. 8). Summer precipitation was greater than average in 2019 (244 mm), 2020 (333 mm), and 2021 (260 mm), less than average in 2022 (125 mm), and similar to the long-term mean in 2018 (236 mm; Fig. 8). Seasonal variation in precipitation and storm size also varied across the study years (Fig. 9). The wettest year (2020) included frequent small storms (Figs. 9 & 10). Though cumulative precipitation was similar in 2019 and 2021, storms occurred earlier in 2019 and were slightly more frequent (Fig. 10). Discharge was influenced by patterns in summer rain as well as by the size of the snowpack (Figs. 8, 11).

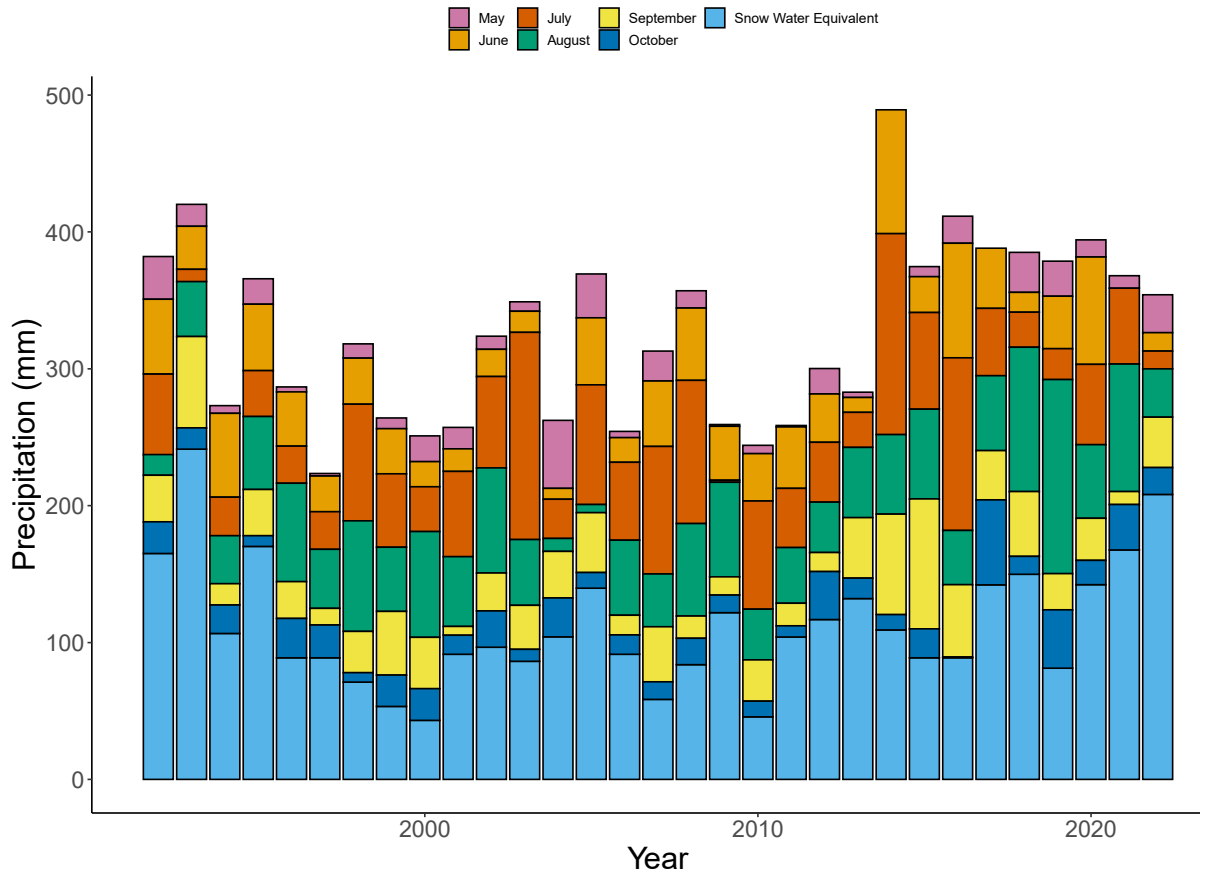


Figure 8. Long-term variation in precipitation of Interior Alaska. Rain measured by the Bonanza Creek Long-Term Ecological Research Program and snow-water equivalent from USDA Snotel Program, Fairbanks station *(*https://wcc.sc.egov.usda.gov/nwcc/site?sitenum=1174*).*

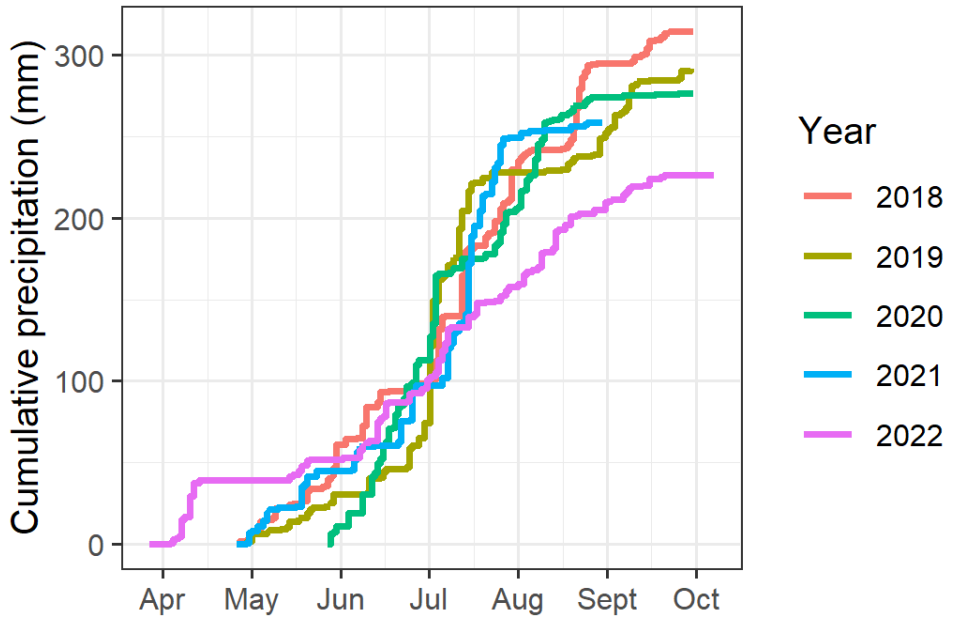


Figure 9. Cumulative precipitation during each of the study years. Observations made near the Poker Creek stream monitoring station by the Bonanza Creek Long-Term Ecological Research Program.

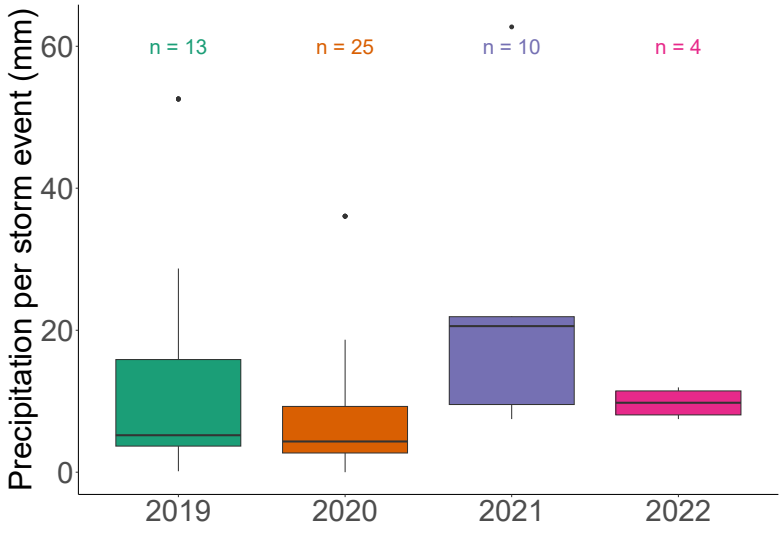


Figure 10. Total number of storm events and average storm size varied across the study years. Center line is drawn at the median storm size, box extent represents 25th and 75th quartiles, whiskers are drawn to whiskers are 1.5x the interquartile ranges, and points are values beyond this range.

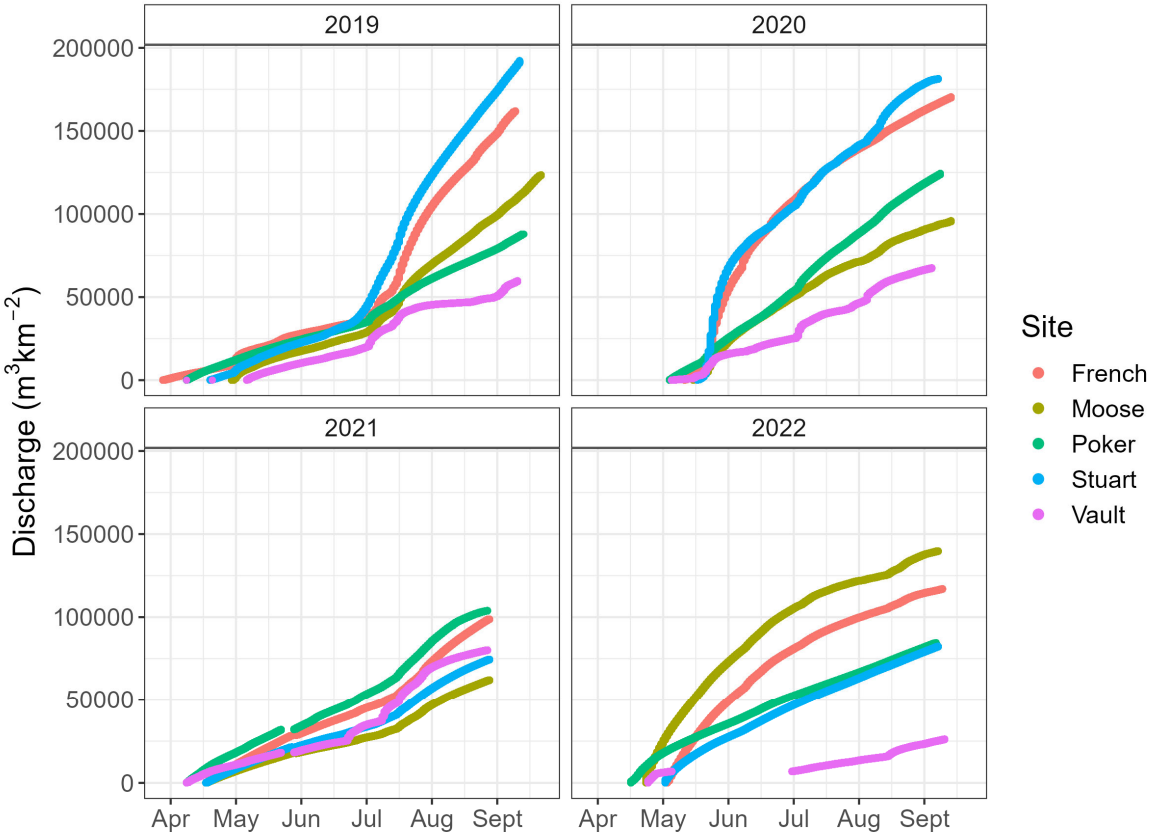


Figure 11. Cumulative discharge for each site and study year.

Task 6: Statistical approaches for quality control

We developed automated approaches for data quality assurance/control (QA/QC) of sensor-collected data. Routines for QA/QC of the SUNA and EXO-collected data entail steps for removing out-of-water points, values beyond the calibrated ranges of the sensors, and data collected during periods of poor sensor performance and reproducibility (Snyder et al., 2018).

The variance of the "burst" of measurements collected within a 30-s window was used to identify and remove outliers caused by poor reproducibility. Observations were removed when the standard deviation (SD) of a burst was greater than five times the average SD for a particular sensor and year of deployment. Thresholds based on observed instream values (e.g., water temperature) were applied to identify data collected when sensors were out of the water for servicing or due to hydrologic conditions. Examples of the results of these automated procedures are shown in Fig. 12.

Data collected by the SUNA were additionally checked for parameters associated with calculation of NO_3^- concentration based on spectral data. The statistical parameters (e.g., RMSE) of the wavelength vs. absorption relationship used by the sensor to calculate nitrate were evaluated and points associated with poor fit (RMSE > 0.04) were discarded. Nitrate measurements made by the SUNA are also unreliable when the background absorption of water is high, and observations associated with abs254 > 1.2 were removed from the record.

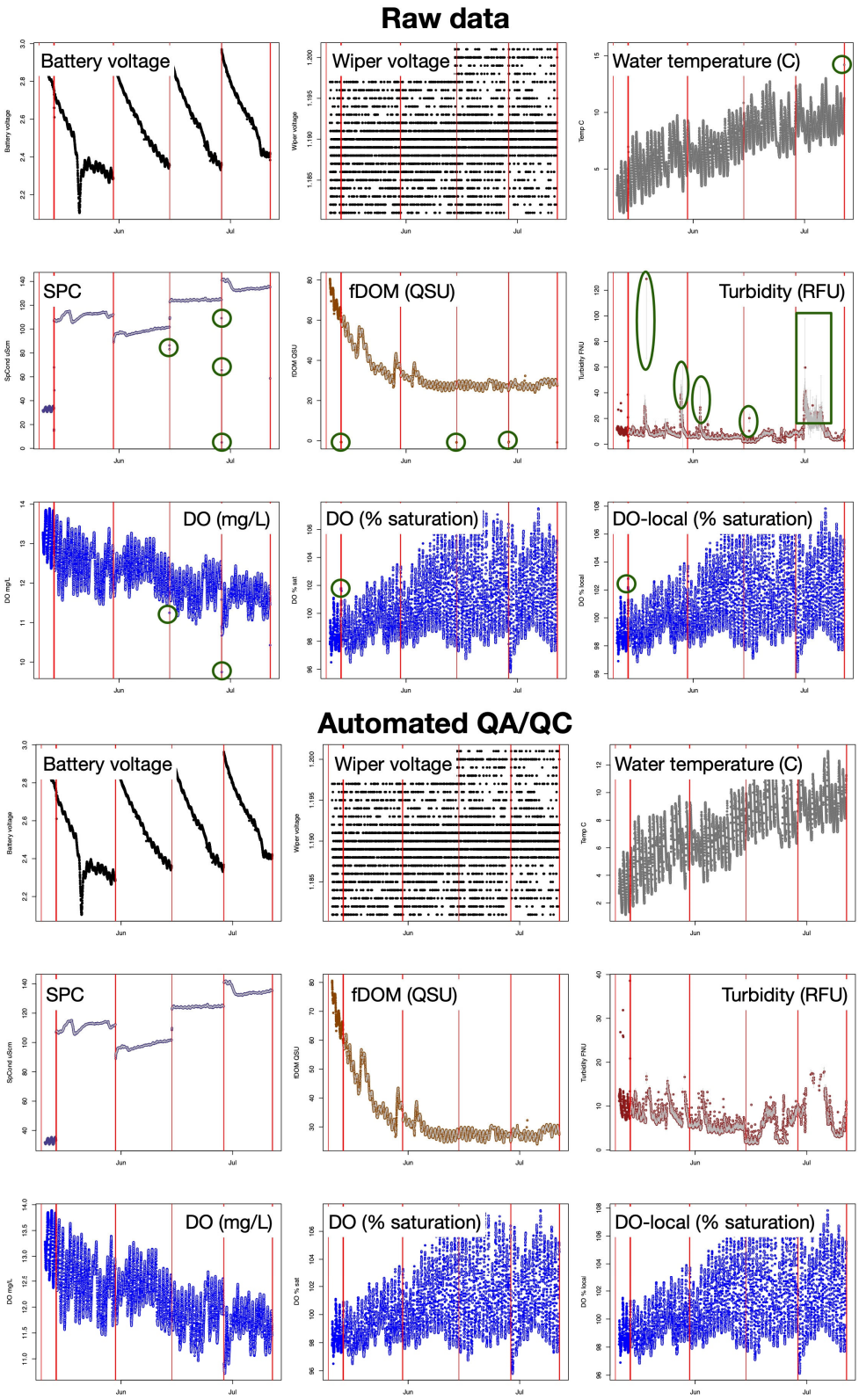


Figure 12. Example of raw data from the EXO sensor (top panels) and values after automated QA/QC (bottom panels). Data are shown as colored points, with gray error bars depicting one standard deviation calculated from a burst of observations collected within a 30-s window. Green outlines identify errant points in the raw data that were removed from the record by automated routines. Red vertical lines show dates of sensor maintenance.

Task 7: Model instream metabolism & N uptake

7.1 Rationale

Use of stream chemistry to infer the state of terrestrial ecosystems draining to the stream rests on the assumption that stream chemistry provides a faithful signal of processes occurring within the contributing area. However, instream processes might augment or diminish chemical signals by retaining or producing measured constituents, particularly fDOM and NO_3^-. We modeled rates of gross primary production (GPP) in each stream because primary producers, including benthic algae, can take up NO_3^- and produce DOM. Subsequent statistical modeling (Task 9) assessed correlations between fDOM or NO_3^- concentration and daily rates of GPP.

7.2 Methods

Estimates of instream metabolism quantify the inputs and outputs of carbon from the stream due to photosynthesis and ecosystem respiration (autotrophic + heterotrophic respiration; ER). We modeled rates of GPP and ER from diurnal variation in concentration of dissolved oxygen (DO). Estimates of GPP, ER, and gas evasion (K) were modeled from diurnal patterns in DO, light, and water temperature. This model is based on the DO budget summarized by Eq. 1 (Odum, 1956):

(1) $\frac{dO_t}{dt} = P_t + R_t + D_t$

where the rate of change in dissolved oxygen concentration is determined by the rate of productivity (P_t) at time t, rate of oxygen removal by respiration (R_t), and the rate of air-water oxygen exchange (D_t). We applied a Bayesian inverse model to determine rates of these processes, implemented in the R package *StreamMetabolizer* (Appling et al., 2018). The inverse model uses multi-day time series of measured DO concentration, water temperature, discharge, and light incident to the stream surface. Light was modeled from latitude, longitude, and date. The inverse model fits the parameters GPP (g O_2 m^{-2} d^{-1}), ER (g O_2 m^{-2} d^{-1}), and gas exchange rate (K_2; g O_2 m^{-2} d^{-1}) in Eqns 2-4. The areal rate of productivity, P_t is estimated by Eq. 2:

(2) $P_t = \frac{GPP}{z} \times \frac{(t_1 - t_0)\, PPFD_t}{\int_{u=t_0}^{t_1} PPFD_u du}$

as a function of depth (z)-normalized GPP and the photon flux density in the photosynthetic range (PPFD, µmol m^{-2} d^{-1}). Areal rate of respiration is given by (Eq. 3):

(3) $R_t = \frac{ER}{z}$

The instantaneous gas exchange rate D_t (g O_2 m^{-3} d^{-1}), is described by Eq. 4:

(4) $D_t = K_{2,t} \times (O\ sat_{t-\Delta t} - O\ mod_{t-\Delta t})$

where $K_{2,t}$ (day^{-1}) is the O_2-specific gas exchange coefficient, O_{sat} is the equilibrium concentration of dissolved oxygen at saturation, and O_{mod} is the modeled oxygen concentration. The model fits a daily value of K_{600}, the gas exchange coefficient for oxygen normalized to a Schmidt number of 600, reflecting oxygen concentration at 17.5 °C.

To avoid equifinality in parameter estimates, we used a Bayesian state-space statistical approach, separately estimating process and observation errors. Differences between observed and modeled oxygen concentrations are attributed to observation error as Eq. 5:

(5) $O_{obs,t} = O_{mod,t} + \varepsilon_{obs,t}$

where $O_{obs,t}$ is the observed concentration of dissolved oxygen at time, t, $O_{mod,t}$ is the corresponding modeled concentration and $\varepsilon_{obs,t}$ is observation error. Modeled oxygen at time *t* is a function of the change in oxygen concentration between timesteps and process error (Eq. 6):

(6) $O_{mod,t} = O_{mod,t-\Delta t} + \int_{u=t-\Delta t}^{t} (\frac{dO_{mod,u}}{du} + \varepsilon_{proc,u}) du$

where $\varepsilon_{proc,u}$ is process error at time, *u*.

We used a partial pooling approach to estimate K_{600}, relating daily values of K_{600} to discharge (*Q*). The gas-evasion rate is determined by turbulence at the air-water interface, which is related to river discharge (Raymond et al. 2012). Partial pooling is effective by attributing error in K to processes in addition to variation in *Q*. We allowed each daily estimate of K_{600} to deviate from the pooling prediction by an error term with standard deviation σ_{K600}.

We applied the default, normally-distributed priors recommended by Appling et al. (2018), as derived from estimates of metabolism compiled by Hall et al. (2016), with modifications described as follows:

(7) $GPP \sim \mathcal{N}(3.1, 6.0)$

(8) $ER \sim \mathcal{N}(-7.1, 7.1)$

(9) $K_{600} \sim \mathcal{N}(K_{600,pred}(Q_d), \sigma_{K600})$

where σ_{K600} describes deviation of K_{600} from the pooling prediction and the distributions for GPP and ER were truncated at zero. We report rates of GPP and ER following the convention of positive values for production and negative values for respiration.

We ran the model separately for each site and year of observations. For each model run, we used four MCMC chains run on four cores in parallel for 9,000 warmup steps and 1,500 saved steps. Models were fit in R (version: 4.2.2) using Stan (*rstan* version 2.26.13). We visually inspected trace plots of MCMC samples for mixing and assessed convergence of parameter estimates with the $\hat{R}$ metric, which compares within- and between-chain variance, and applied an upper threshold of 1.1 to establish convergence.

7.3 Results

Gross primary production was strongly seasonal (example shown in Fig. 13, all sites and years shown in Appendix 1), with negligible production during ice-out and spring freshet, and a seasonal maximum typically occurring in late June or early July. Gross primary production declined following storms. Rates of GPP increased again when storms occurred prior to August, but GPP typically did not return to pre-storm conditions following storms later in the season after water temperature began cooling. In the absence of storms, GPP typically began to decline in early August, and reached a minimum of about 0.5 g O_2 m^{-2} d^{-1} by the end of monitoring in late Sept/early Oct.

Mean rate of GPP measured in the five boreal streams were greater than rates measured in Arctic and boreal streams of Sweden and northern Alaska and were comparable to summertime rates in temperate streams. Gross primary production averaged 1.32 g O_2 m^{-2} d^{-1} (range: 0.003 to 13.1 g O_2 m^{-2} d^{-1}) across all daily observations made in the present study. By comparison, mean GPP was less than 1 g O_2 m^{-2} d^{-1} in Arctic tundra of Alaska and boreal and Arctic streams in Sweden (Myrstener et al., 2021; Rocher-Ros et al., 2020, 2021). Temperate streams in the US receiving high light input and stable discharge support peak rates of GPP of 2 g O_2 m^{-2} d^{-1} (Bernhardt et al., 2022), slightly greater than the mean rate observed in the boreal Alaskan streams.

Rates of ER observed in the boreal streams of this study were similar to rates observed elsewhere in Arctic and boreal zones and greater than rates in temperate streams. The focal boreal streams had a mean ER of -6.50 O_2 m^{-2} $d^{-}1$ (range: -3.15 to -9.47 g O_2 m^{-2} $d^{-}1$). This was similar to rates in high-latitude streams in Sweden and Arctic streams in Alaska (Rocher-Ros et al., 2020, 2021). Rates of ER in temperate streams are lower, on average, than in high-latitude streams, with mean of ~-4.0 g O_2 m^{-2} d^{-1} (Bernhardt et al. 2022). Overall, high-latitude streams support low rates of GPP relative to ER due to limitation of GPP by low temperature; light limitation by shading, turbidity, or colored DOM; and low nutrient availability. Higher rates of ER in high-latitude compared to temperate streams are likely supported by relatively large loads of DOM delivered to streams.

Mean rates of GPP and ER tended to be greatest at French and Stuart Creeks, though shorter periods of high productivity also occurred during most years at Moose Creek (Figs. 14 & 15). These patterns do not correspond to contrasts in fire or permafrost extent in the catchments. Instead, variation in stream metabolism across the monitored streams likely results from interactions among channel substrate, temperature, and light and nutrient inputs to the streams.

7.4 Implications

- Rates of GPP and ER in streams did not contrast among streams of varying fire or permafrost extent. Patterns in stream chemistry observed along these gradients (Tasks 8-10) are therefore unlikely due to instream processes.
- Modeled rates of GPP are used in subsequent models to evaluate potential for instream processes to contribute to production of fDOM or uptake of NO_3^-.

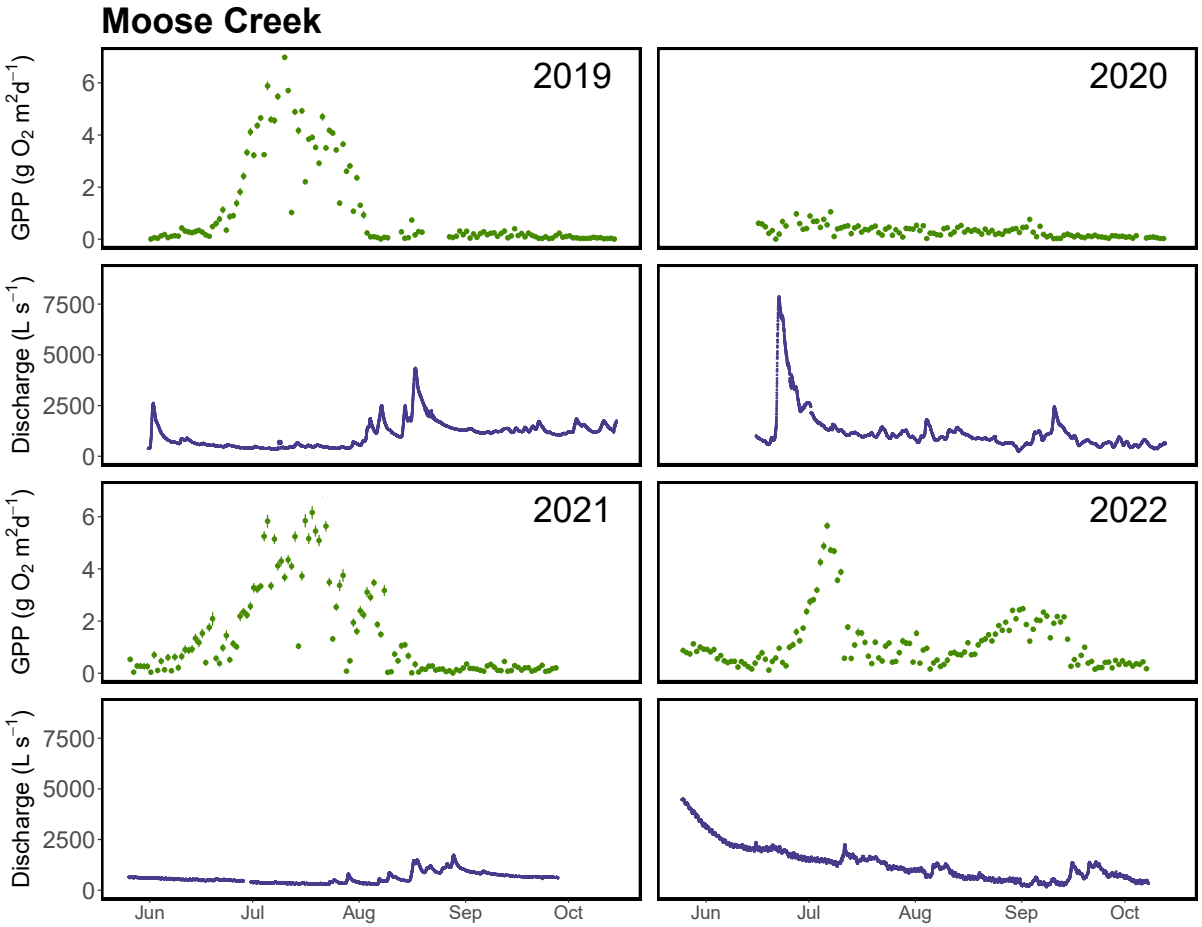


Figure 13. Modeled rates of gross primary production (GPP) and stream discharge in Moose Creek. Storms often curtailed GPP and production did not resume following storms occurring in August or thereafter. Note increased production in autumn of 2022, the driest year in the dataset. Modeled rates of GPP for all sites are in Appendix 1.

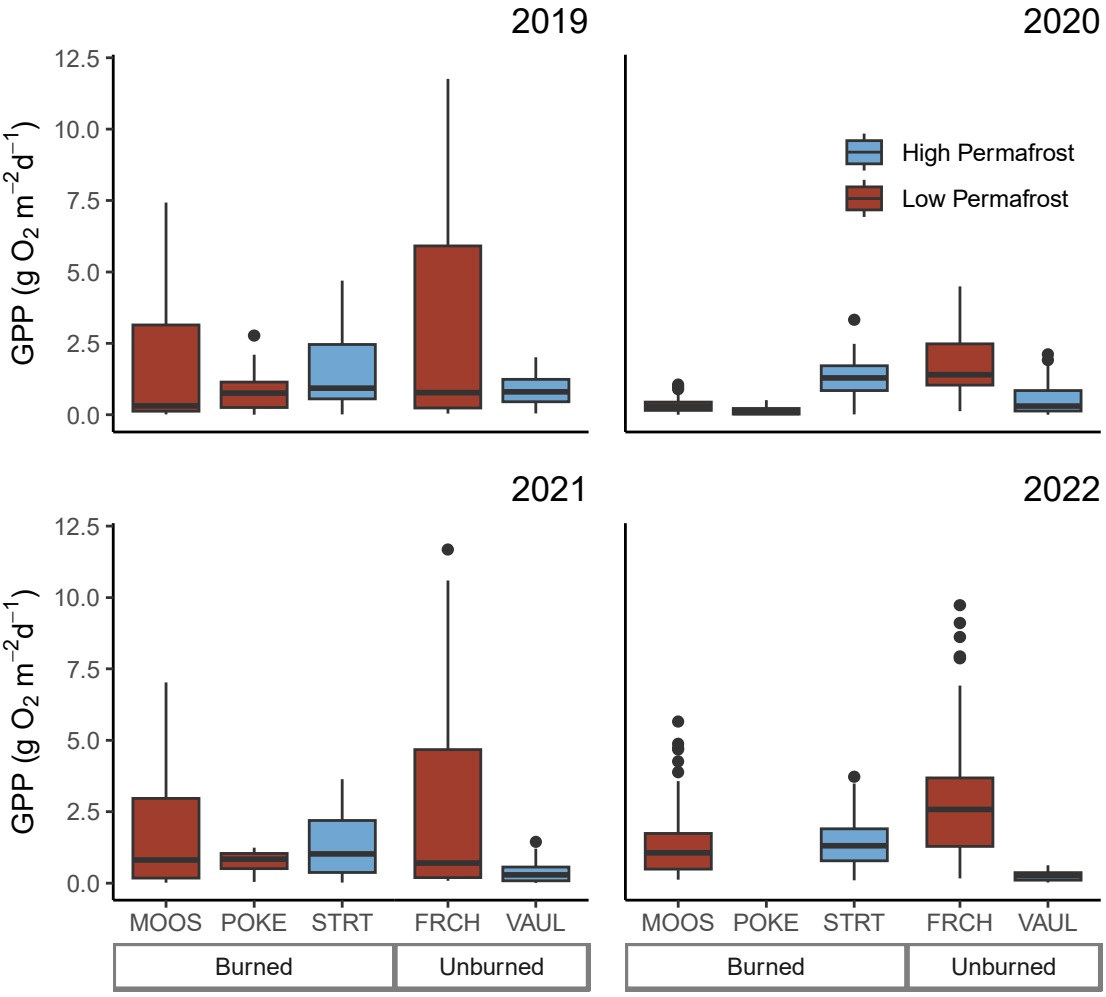


Figure 14. Modeled daily rates of gross primary production (GPP) in the study streams. Center line indicates median daily rate, boxes encompass 25th and 75th percentiles, whiskers are 1.5x the interquartile ranges, and points reflect values beyond this range. Data are summarized within a common time window for all sites and years.

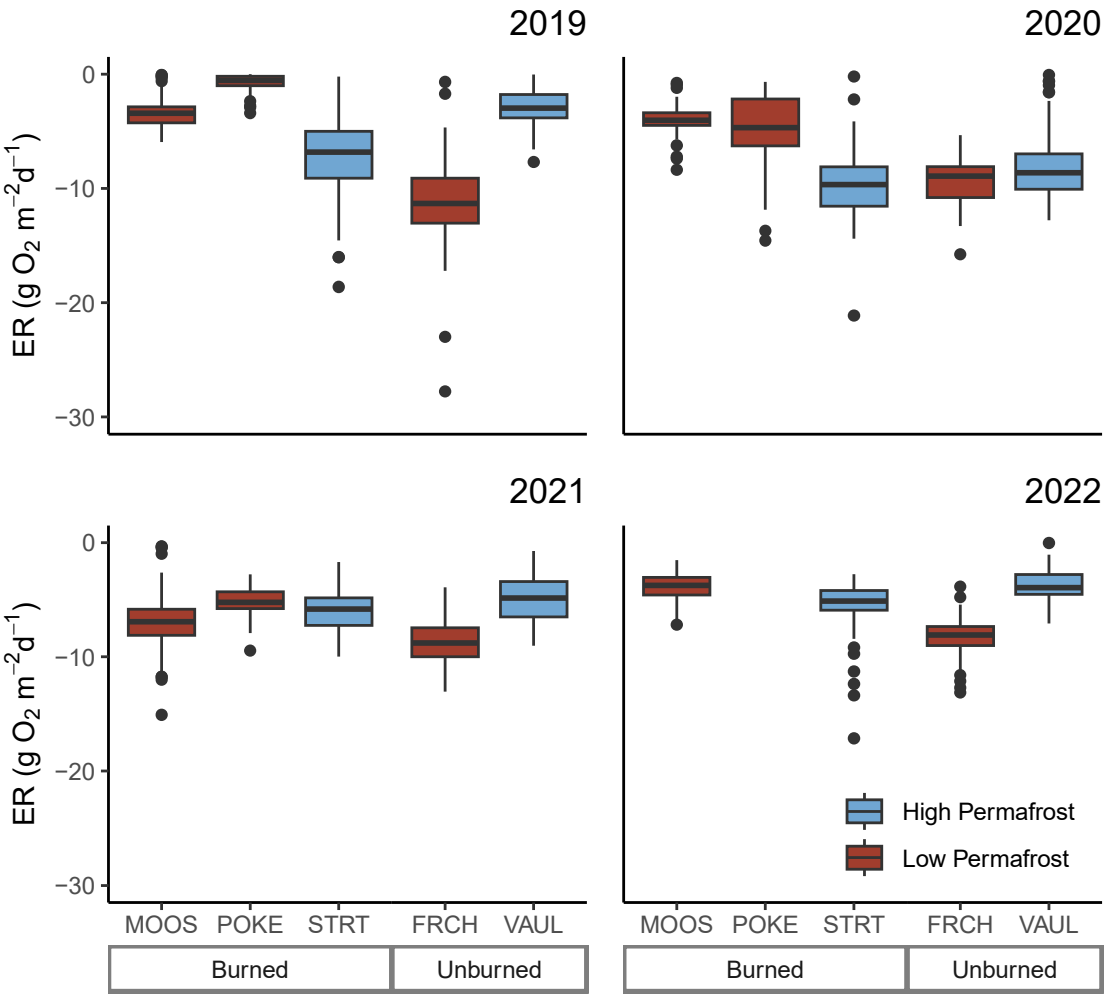


Figure 15. Modeled daily rates of ecosystem respiration (ER) in the study streams. Symbology as defined in Fig. 14.

Task 8: Determine sources of water and nitrate to streams

8.1 Sources of water contributing to streamflow

8.1.1 Overview & context

The flowpaths by which water traverses catchments have implications for export and storage of water and accompanying dissolved and suspended materials. Physical attributes of catchments including soils, geology, and topography determine flowpaths. In Interior Alaska, permafrost additionally influences flowpaths, confining flows to the active layer, the shallow soils above permafrost that freeze and thaw annually (Carey & Woo, 2001; Quinton & Marsh, 1999). These shallow flowpaths result in relatively low concentrations of inorganic ions in streams, low water residence time, and flashy storm responses (Carey et al., 2013; Jones & Rinehart, 2010; Petrone et al., 2007).

Permafrost thaw, more variable precipitation, wildfire, and shifts in vegetation cover can alter the flowpaths draining high-latitude catchments. Increasing thaw depth caused by warming climate will increase water storage in northern catchments (Tetzlaff et al., 2015), which could dampen responsiveness of stream discharge to precipitation (Jones & Rinehart, 2010). Climate models predict a shift to increased precipitation as rain, rather than snow, and a more variable precipitation regime (Bintanja et al., 2020; Wolken et al., 2011). Increased precipitation in summer could counteract the effects of deepening thaw, by rapidly routing water to streams. Observed and projected increases in frequency and intensity of wildfires in Interior Alaska could thaw permafrost, resulting in deepening of flowpaths (Brown et al., 2015; Flannigan et al., 2009; de Groot et al., 2013; Kasischke & Turetsky, 2006). In contrast, fire reduces evapotranspiration and can result in hydrophobicity of soils, causing decreased water residence time, reduced infiltration, and increased overland flow (Bond-Lamberty et al., 2009; Ebel & Moody, 2013). Finally, increased cover of deciduous forest caused by changing climate and fire regimes could cause increased evapotranspiration (Mekonnen et al., 2019; Park et al., 2016; Peralta-Tapia et al., 2015; Yuan et al., 2010). Interactions among these myriad changes to the hydrologic cycle will ultimately organize flowpaths draining catchments, but the net effects remain uncertain.

Many of the projected changes to high-latitude climate and ecosystems are predicted to cause deepening of hydrologic flowpaths and increased discharge of groundwater to streams (Walvoord & Kurylyk, 2016). However, few empirical studies have documented these predicted patterns. We used an end-member mixing model to estimate the flowpaths contributing to streamflow in catchments varying in permafrost extent and fire history. We evaluated how flowpaths changed as thaw deepened over summer as an analog of longer-term permafrost degradation. Flowpaths contributing to streamflow influence how the hypothesized biogeochemical signals of ecosystem state are transported to and expressed in streams.

8.1.2 Methods

Sample collection and analysis— We sampled water from six streams in Interior Alaska during the open-water period of 2019-2021 as described in Task 5. We also collected samples from waters potentially contributing to streamflow, including precipitation, soil water, and groundwater. Soil water was collected from saturated zones following precipitation in each of the catchments. Precipitation was collected as snow from the Stuart, Poker, and Vault catchments and rain was collected from nearly all storms occurring near Fairbanks in May-Sept 2019. Groundwater was collected from springs and upwellings, and from wells maintained by NEON, CRREL, and USGS, in addition to municipal wells. Most wells were not located within the contributing areas of the study catchments, but were considered representative of regional groundwater. All water samples were analyzed for concentrations of major anions and cations on

an ion chromatograph (ICS-2100, Thermo Scientific) equipped with AC-11 and CS-16 columns for analysis of anions and cations, respectively. Limits of quantitation for analytes ultimately used in mixing models were 0.21 µM for magnesium and 0.29 µM for chloride.

End-member mixing model— We used an end-member mixing model to estimate the proportion of precipitation, groundwater, and soil water contributing to streamflow. We selected chloride and magnesium as tracers because they are conservative and sufficiently bounded chemistry of the stream samples (Fig. 16). Models for all sites included the same group of source samples for precipitation and groundwater. Groundwater samples that had concentrations distant from the stream water sample concentrations were excluded. A single group of soil water samples were used for four sites, whereas water from an upwelling replaced soil water at the Vault site, which drains yedoma soils rich in solutes.

We implemented a Bayesian mixing-model using the *MixSIAR* package for R (Stock et al., 2018) to analyze source water contributions to streamflow. A separate model was parameterized for each site. Models included a random effect of year, and fixed effect of julian day to quantify variation in contribution of source waters among years and through seasonal time. We included residual error in the models to incorporate variation not explained by differences in source proportions (i.e., measurement error). The models were run for 100,000 iterations, and model convergence was assessed using the Gelman, Heidelberger and Welch, and Geweke diagnostics.

8.1.3 Results

Chemistry of stream water was bounded by chemistry of soil water, groundwater, precipitation, and in the Vault catchment, an upwelling (Fig. 16). Mixing models reached convergence and uncertainty around the mean was low. Precipitation comprised the largest proportion of source water at all sites except for Vault, which had large contributions of water

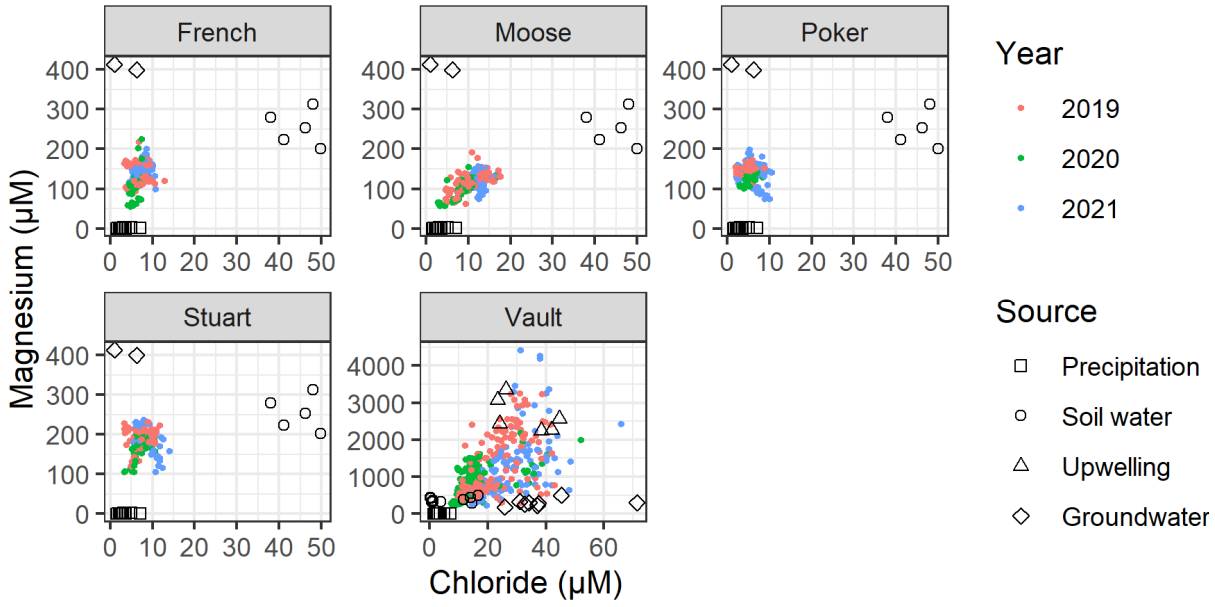


Figure 16. Mixing plots depicting concentrations of the two conservative solutes used in mixing models (magnesium and chloride), and prospective end members. Sources reflect the same groups of samples in all catchments, except for Vault Creek, which includes groundwater from additional sources as well as water expressed at the surface from a large upwelling.

that were chemically similar to an upwelling source (Fig. 17). This pattern indicates a strong influence of shallow flowpaths in all catchments, as water retaining the chemical composition of precipitation is routed to streams via flowpaths of short water residence time that likely flow overland or through shallow, organic soils.

The contribution of precipitation was significantly greater during 2020 (Fig. 17; 95% credible intervals did not overlap), the year of greatest total summer precipitation, than in the other two years for the three smallest catchments (French, Poker, and Vault). Precipitation was a larger contributor in 2020 than 2021 (the driest year) at the larger catchments (Moose and Stuart; Fig. 17). Greater sensitivity of flowpaths to inter-annual variation in precipitation in the smaller catchments compared to the larger catchments aligns with previous research demonstrating longer water residence time in larger catchments, due to groundwater storage (Wolock et al., 1997). Overall, variation in the proportion of precipitation in stream water in response to precipitation underscores the sensitivity of high-latitude hydrology to the precipitation regime.

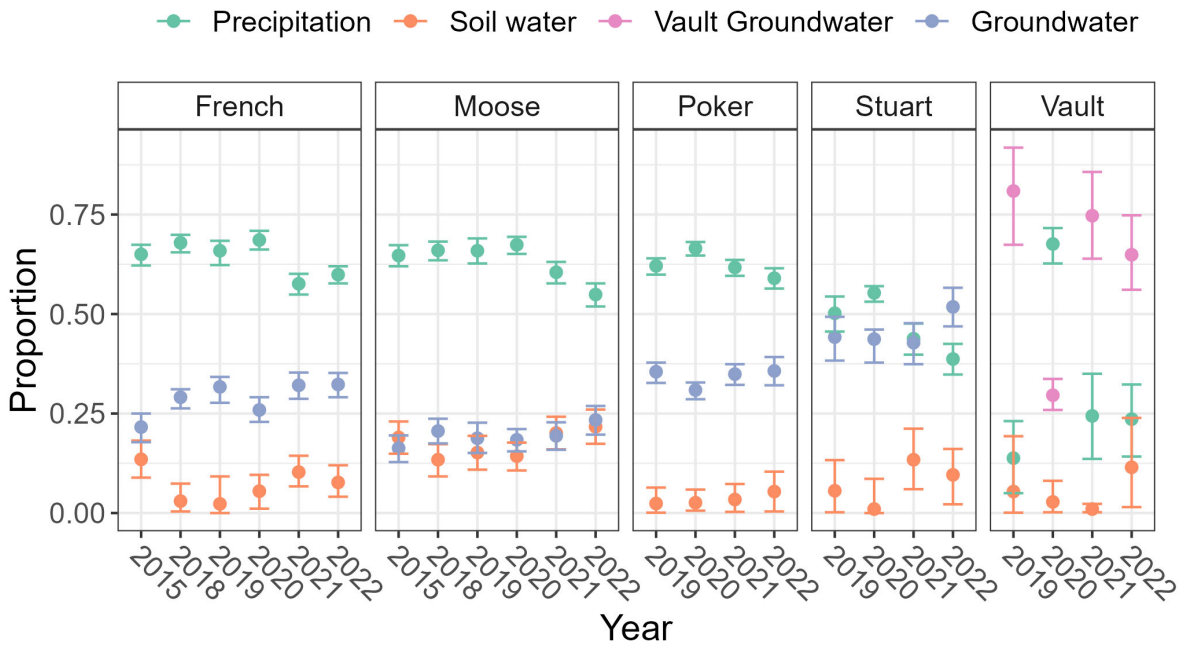


Figure 17. Mean proportions and 95% credible intervals of water source contributions by site and year.

Increasing variation in precipitation will influence solute concentrations due to shifting depth of dominant flowpaths draining catchments.

Deep groundwater contributed 15-49% to stream water, on average, across all sites and years. Contribution of groundwater was greatest to Poker and Stuart Creeks, both of which drain burned catchments (Fig. 17). Groundwater contributed less to runoff at French, Moose, and Vault, though the depth of the flowpath expressed in upwelling at Vault is unclear.

The contributions of source waters to streams changed seasonally, with increasing contributions from deep groundwater over the open-water period in all sites except French Creek (Fig. 18). Frozen soils restrict deeper infiltration and increasing contribution of groundwater over the thaw period is consistent with deepening of the dominant flowpaths draining catchments. At French Creek, decreasing contribution of precipitation was replaced by increased contribution of soil water over the thaw season, which could indicate shallower flowpaths in the French catchment compared to the other sites. Flow contributions varied most within and across years at

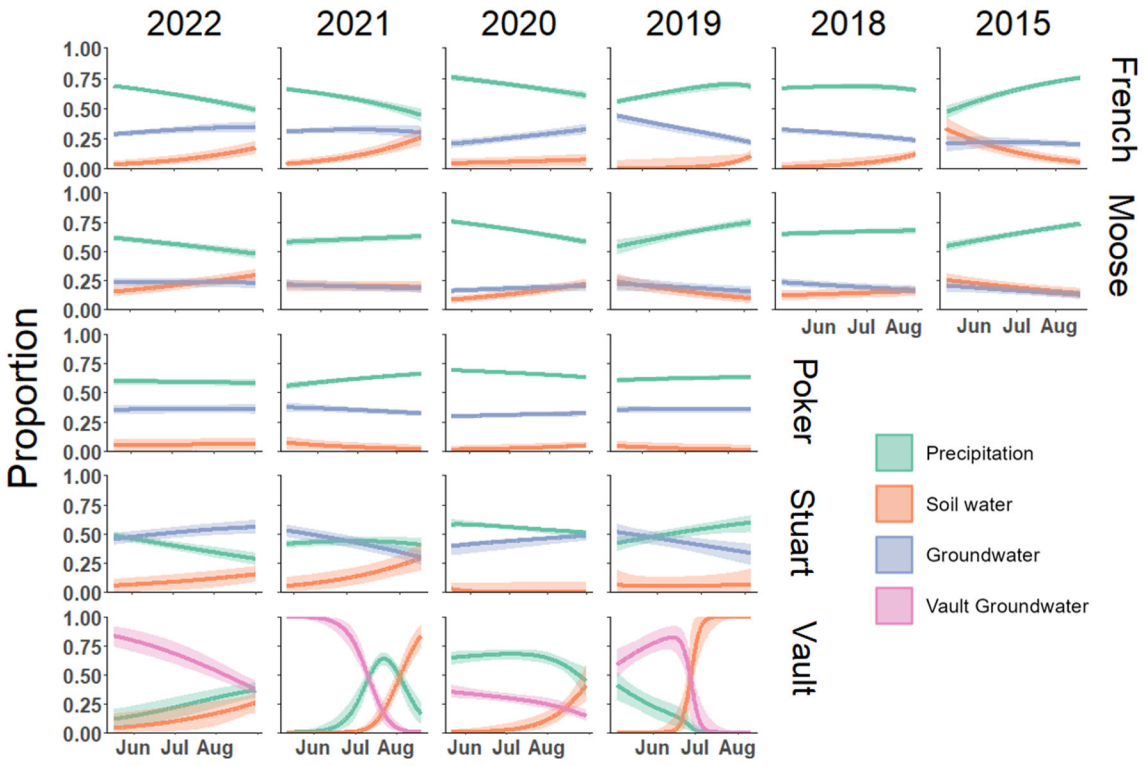


Figure 18. Estimates of source water contributions to streams through the open-water period of each study year. Dark lines depict median of the posterior distribution and shading reflects 95% credible intervals.

Vault Creek, the high-permafrost catchment. Temporal variation in flowpaths in this catchment and other catchments draining high spatial extent of permafrost could result from rapid routing of stormwater via shallow, suprapermafrost flowpaths and to spatial or temporal variation in ground thaw.

We visually assessed relationships between average contributions of precipitation and groundwater across gradients of deciduous forest cover and burn extent (Fig. 19). These patterns were heterogeneous which might imply that interactions among catchment topography, substrate, and disturbance history influence the relative depths of dominant flowpaths. Such interactions are too complex to evaluate with observations from just five catchments. However, we can draw conclusions about regional patterns in catchment hydrology from seasonal and inter-annual patterns. Consistent seasonal increases in soil water and/or groundwater contributions observed across all catchments confirmed that seasonal ground thaw results in seasonal deepening of flowpaths. Responses to inter-annual variation in precipitation indicated that shallow flowpaths of low residence time are activated by precipitation. Further, sensitivity of catchment hydrology to precipitation depends on catchment size and permafrost extent.

8.1.4 Implications

- Mixing analysis confirmed that dominant flowpaths draining catchments deepen over the thaw season. Responsiveness of flowpaths to thaw dynamics is an important component of hypothesized mechanisms relating permafrost thaw to biogeochemical signals in streams.
- Contribution of precipitation to streamflow was sensitive to inter-annual variation in rain during the open-water period. Catchment flowpaths, and therefore solute delivery, is influenced by variation in the precipitation regime.
- Monitoring the rate of seasonal thaw as expressed by flowpath depths contributing to streamflow (i.e., the slope of groundwater contribution over seasonal time) could identify catchments where permafrost thaw is resulting in significant change to catchment hydrology and biogeochemistry. This approach integrates over whole catchments, offering a metric of ground thaw that could complement monitoring permafrost temperature at a point scale.

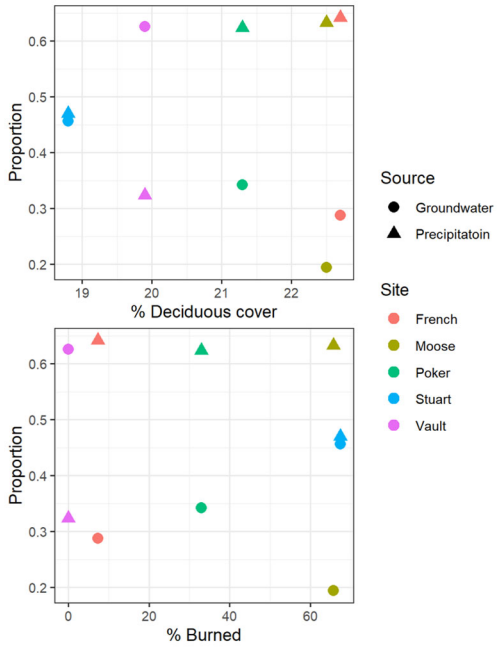


Figure 19. Variation in mean proportion of precipitation and groundwater contributions to streamflow across all years relative to disturbance history of the catchments. Deciduous forests are typically permafrost-free.

8.2 Sources of NO_3^- in streamwater

8.2.1 Rationale

In addition to water sources, we proposed to detect sources and transformations of NO_3^- using stable isotopes of NO_3^-. Nitrate enters the boreal catchments in this study from: 1) atmospheric deposition resulting primarily from fossil fuel combustion, 2) fixation of nitrogen gas by microbes, and 3) microbial transformation of other forms of N already present in ecosystems, such as from rock. Biological processing of NO_3^- (e.g., denitrification, nitrification)

in catchments can vary due to temperature and water table elevation, which are in turn influenced by presence of permafrost and fire. Additionally, one of our sites (Stuart Creek) is located downstream of an active firing range, which could contribute NO_3^- from energetics to the stream.

Each of the steps in the nitrogen cycle leaves an imprint on the stable isotope ratios of N and oxygen (O) of NO_3^- due to differences in isotopic fractionation by the reactions that produce and remove it. Atmospherically-deposited NO_3^- is detectable by elevated $^{18}\delta O$ (~15-70‰) imparted by reactions with ozone that produce NO_3^- in the atmosphere (Kendall, 1998). However, rates of atmospheric deposition of NO_3^- are low in the sparsely populated, high-latitude region of this study (National Atmospheric Deposition Program; https://nadp.slh.wisc.edu/networks/national-trends-network/). Input of synthetic NO_3^- from energetics would also contain elevated $^{18}\delta O$ (>20‰; Degnan et al., 2016; Hendry et al., 2018). Finally, inputs of N to ecosystems by biological N fixation carry a $^{15}\delta N$ of 0‰ due to atmospheric N_2 as the source of fixed N. This isotope ratio is then modified when the products of N-fixation are transformed to NO_3^-.

Nitrate is generated within ecosystems by nitrification (NH_4^+ oxidation + nitrite oxidation), a microbial metabolic pathway entailing oxidation of NH_4^+ to form NO_3^-. Decomposition of organic matter generates the NH_4^+ fueling microbial nitrification in many ecosystems. In addition, some types of rock contain organic N (sedimentary rocks) or NH_4^+ (silicate minerals) that become available to microbes as the rocks weather (Holloway & Dahlgren, 2002). Nitrate produced by microbial nitrification incorporates oxygen from the atmosphere as well as from available water (H_2O), resulting in ^{18}O-NO_3^- that reflects a mixture of these sources, but typically fully equilibrates with ^{18}O-H_2O of local water over time (Boshers & Granger, 2019). Nitrate produced from nitrification also retains the ^{15}N of available N sources (e.g., organic matter, rock).

Once formed, NO_3^- can be permanently removed from ecosystems by microbial denitrifiers, producing gaseous N that is emitted from ecosystems. Denitrification strongly fractionates against the heavy isotopes, removing lighter isotopes to gaseous products and leaving a smaller pool of NO_3^- that is enriched in both ^{15}N and ^{18}O (Kendall 1998).

8.2.2 Methods

Grab samples of stream water were collected approximately biweekly from the five focal streams during the open-water period of each year. We also analyzed a subset of the end members (e.g., precipitation, groundwater) described in Section 8.1 for NO_3^- isotopes. Samples were filtered and shipped frozen to the University of California Davis Stable Isotope Facility for analysis. The $^{15}\delta N$ and $^{18}\delta O$ of NO_3^- were analyzed by the denitrifier method (Sigman et al., 2001). Briefly, NO_3^- is converted to N_2O by bacterial denitrifiers and analyzed by mass spectrometry against VSMOW and atmospheric standards for ^{18}O and ^{15}N, respectively. Few laboratories are equipped to undertake this analysis and the COVID-19 pandemic has slowed availability of data on NO_3^- isotopes. We report on a partial dataset available for 2019-2021.

8.2.3 Results

Temporal patterns in isotopic content of NO_3^- generally showed increasing isotope ratios through the thaw season, particularly for N (Figs. 20 & 21). Heavier isotope ratios result from microbial processing of NO_3^-, particularly denitrification. Rates of microbial transformations could increase in response to warmer temperatures during the thaw season. In contrast, a shift in the source of NO_3^- delivered to streams could result in delivery of NO_3^- from more processed pools, such as from flowpaths with longer residence time in the catchment. Although upward trends in isotope ratios were observed in many catchments, these patterns were accompanied by temporal variation that could be due to precipitation inputs that result in shallower drainage

(Section 8.1) or non-linear changes in thaw depth and deeper flow contributions. Isotopic ratios were most temporally variable in Vault Creek, a high-permafrost catchment that also showed greatest temporal variation in sources of water contributing to streamflow (Section 8.1).

Comparison of NO_3^- isotopes in streamwater to isotope ratios in potential source waters showed concordance with groundwater and snow. A groundwater well sampled repeatedly showed temporally invariant isotope ratios relative to the streams, and the NO_3^- in many streams was isotopically similar to it, particularly for ^{18}O (Figs. 20 & 21). Samples of an upwelling at Vault Creek were isotopically similar to stream samples from many catchments collected near the same date (late July; Figs. 20 & 21). Similarity of streamwater with subsurface sources of NO_3^- suggest that NO_3^- is likely delivered to streams in similar proportions to sources of water. We found no evidence for the presence of synthetic NO_3^- from energetics in Stuart Creek, as $^{18}\delta$O-NO_3^- was always negative.

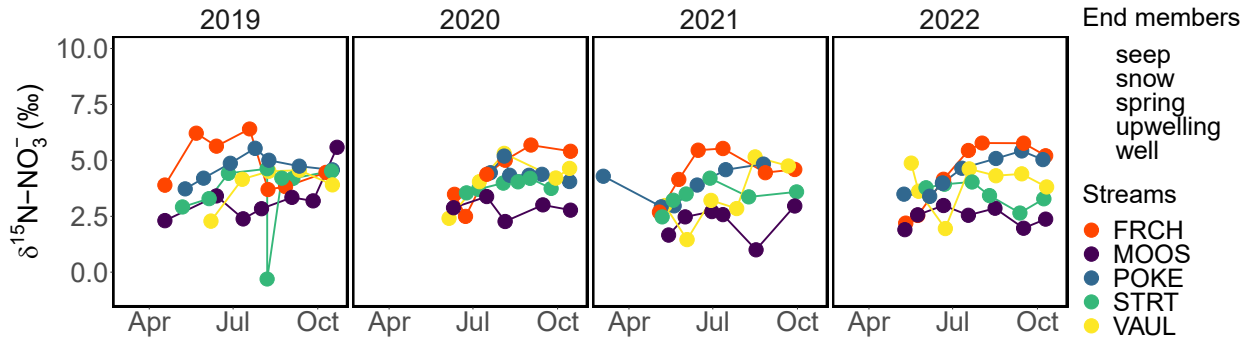


Figure 21. δ^{15}N-NO_3^- in stream water and potential source waters.

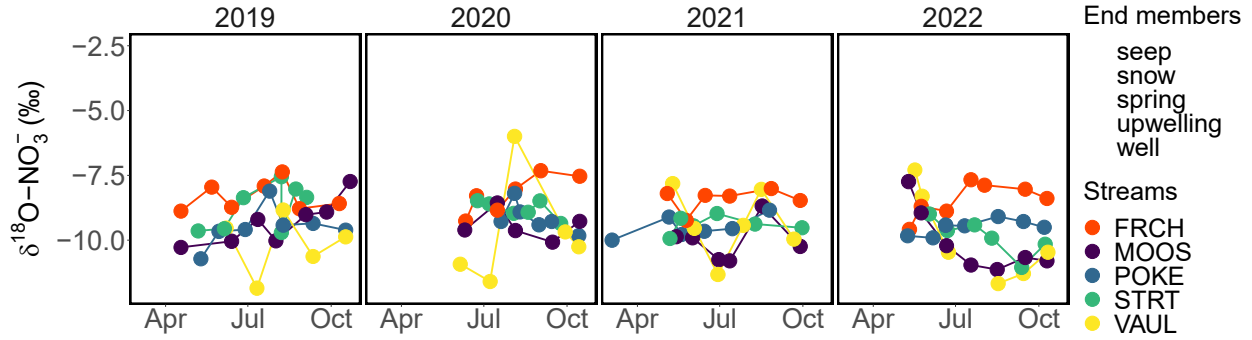


Figure 20. δ^{18}O-NO_3^- in stream water and potential source waters.

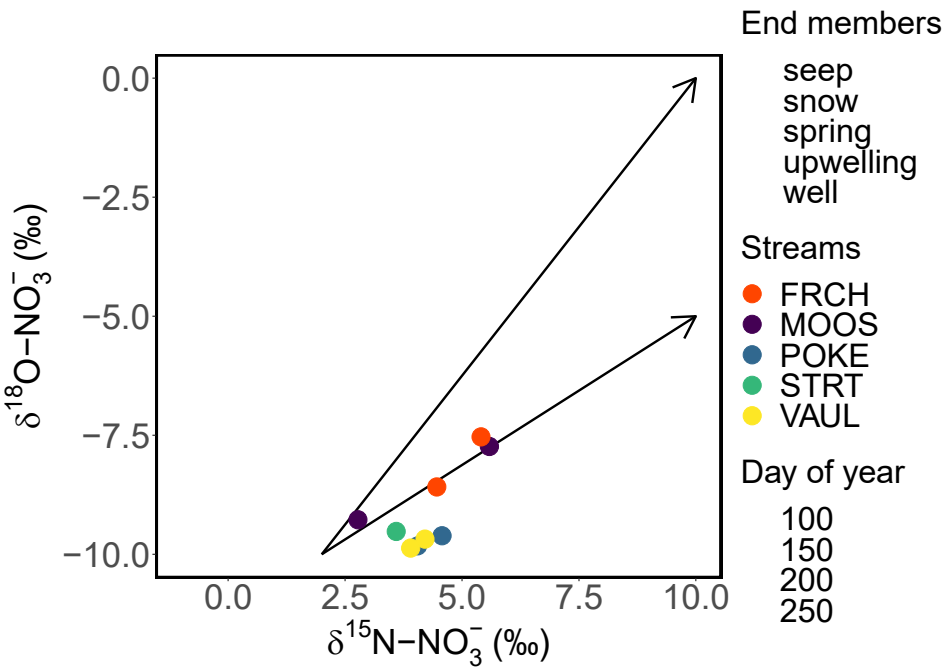


Figure 22. Dual isotope plot of NO_3^- in stream water and potential source waters. Vectors depict expected ratios of the remaining NO_3^- pool when denitrification removes NO_3^- following theoretical 1:1 and 2:1 fractionation ratios.

A biplot of $^{15}\delta$N and $^{18}\delta$O indicated that denitrification had a strong influence on the NO_3^- pool in streams (Fig. 22). Theory predicts a 1:1 or 2:1 ratio of enrichment factors of ^{15}N relative to ^{18}O resulting from denitrification (Kendall 1998). Alignment of observations from many of the streams with these expectations suggests that denitrification has a strong influence on the NO_3^- pool in these catchments. Notably, Vault Creek typically departs from this expectation and Poker Creek departs later in the thaw season. In addition to denitrification, mixing of sources with contrasting isotopic ratios could explain departure of isotopic composition of NO_3^- from the pattern expected from denitrification. Flowpaths with contrasting residence times subject NO_3^- to different microbial processes or deliver NO_3^- derived from different sources (e.g., organic matter vs. rock). Finally, isotopic content of NO_3^- in streams was similar to isotope ratios of snow in samples collected during or soon after snowmelt (Fig. 22).

8.2.4 Implications

- Isotopes of NO_3^- indicated variation in the sources of NO_3^- delivered to streams corresponding to dominant hydrologic flowpaths draining catchments. Flowpath contributions therefore serve as a coarse proxy for variation in the pools of NO_3^- exported to streams.
- Denitrification, an understudied process in high-latitude ecosystems, left an isotopic imprint on NO_3^- delivered to streams, suggesting that predicting NO_3^- dynamics in boreal catchments requires greater consideration of this process.

Task 9: Time series models to estimate effects of disturbance on C and N fluxes

9.1 Overview

We analyzed storm-scale, daily, and multi-scale temporal variation in time series of stream chemistry to evaluate contrasts in temporal patterns among catchments varying in spatial extent of permafrost and fire history. This task is essential to identifying which temporal signals respond to disturbance and may provide the basis for metrics of regime change. Temporal patterns in stream chemistry and discharge reflect the hydrological and ecological state of whole catchments. However, stream chemistry integrates signals generated at multiple time scales and across both the stream and terrestrial components of the catchment.

We applied multiple analytical techniques aimed at deconvoluting multi-scale hydrologic and biogeochemical signals described by temporal patterns stream chemistry. These included wavelet decomposition, multivariate autoregressive state-space models (MARSS), and analysis of concentration-discharge relationships, all applied to high-frequency (15-min) records of stream discharge and chemistry. Storms enhance hydrologic connectivity between the catchment and stream, and thus could be times when biogeochemical signals from catchments are most strongly expressed in streams. To evaluate patterns at the storm scale, we delineated individual storm events and analyzed concentration-discharge relationships. At a daily timescale, we applied MARSS models to estimate seasonal trends, effects of potential covariates of biogeochemical signals, and stability of solute concentrations. Finally, we applied wavelet transforms and wavelet coherence analysis to evaluate temporal variation at sub-daily to approximately monthly frequencies. We first demonstrate application of each of these techniques to a small dataset of high-frequency observations from four headwater catchments in Interior Alaska with contrasting permafrost extent and fire history (Webster et al., 2022). We then present results of each technique applied to 4-6 years of observations from the five focal catchments of this project.

9.2 Demonstration of time series statistical approaches to a single season

9.2.1 Study sites. We monitored four headwater streams in the Caribou-Poker Creeks Research Watershed (CPCRW) in Interior Alaska (Fig. 23; Webster et al., 2022). During the study period (May–Sept 2017), mean monthly temperatures were similar to climate normals, with the exception of mean temperature in July ~2°C warmer than average. Compared to long-term means, monthly precipitation during the study period was higher in May (39.4 compared with 24.5 mm), lower in June (34.8 compared with 57.9 mm), and similar in July (104 compared with 96.9 mm) and August (83.1 compared with 82.0 mm).

Soils of the study area are generally thin (approximately 1 m) and underlain by a fractured bedrock aquifer of weathered schist, dispersed carbonate-bearing lithologies, bands of gravel and loess, and spatially discontinuous permafrost (Haugen et al., 1982; Yoshikawa et al., 2003). Permafrost occurs in valley bottoms and on north-facing slopes. North-facing slopes are dominated by black spruce (*Picea mariana*) with mosses in the understory (e.g., *Sphagnum spp.*, *Hylocomium spp.*). South-facing slopes and ridges are dominated by mixed hardwoods (*Betula neoalaskana* and *Populus tremuloides*) and develop little understory groundcover.

The catchments studied in this initial demonstration effort vary in fire history and aspect, which is correlated with spatial extent of permafrost (Fig. 23). A south-facing catchment (C2, hereafter “low permafrost”) is underlain by permafrost in approximately 4.5% of its total area and 10% of its drainage network area, defined as the stream network and likely areas of zero-

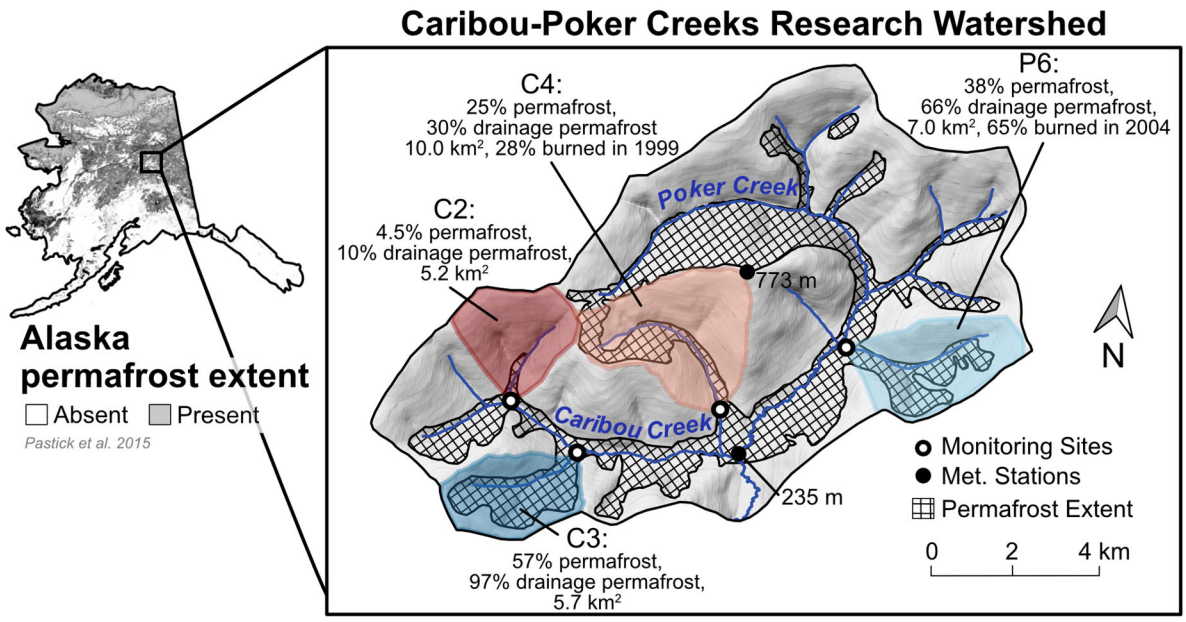


Figure 23. Headwater catchments monitored in 2017. Resulting data were used to demonstrate and select approaches for data analysis applied in this project.

order channels and shallow subsurface flow. A southeast-facing catchment (C4; hereafter "low-mid permafrost") is underlain by permafrost in 25% of its total area and 30% of its drainage network area. In contrast, a northwest-facing catchment (P6; hereafter "mid permafrost") is underlain by permafrost in 38% of its total area and 66% of its drainage network area, and a north-facing catchment (C3; hereafter "high permafrost") is underlain by permafrost in 57% of its total area and 97% of its drainage network area. The catchments also vary in fire history. An experimental fire burned 28% of the C4 catchment in 1999 (Hinzman et al., 2003) and a wildfire burned 65% of the P6 catchment in 2004 (Betts & Jones, 2009). Streams draining catchments are narrow (<1 m width) and are shaded by vegetation (Betts & Jones, 2009; Mutschlecner et al., 2018).

9.2.2 Data collection

Streams were monitored from May 23–Aug 31 2017 for discharge, temperature, SPC, dissolved oxygen, NO_3^-, turbidity, and fDOM with sensors as described in Task 5. Hourly precipitation and air temperature data supporting modeling were collected at the site by the Bonanza Creek Long-Term Ecological Research Program. We calculated daily growing degree units (GDU), which quantify heat accumulation above a threshold temperature (5°C for boreal regions; Ruosteenoja et al., 2016) as $[(Temp._{MAX} + Temp._{MIN}) * 2^{-1}] - 5°C)$. Growing degree units approximated growing conditions for terrestrial vegetation (Bugmann et al., 2001; Rollinson et al., 2017; Ueyama et al., 2013).

9.2.3 Data analysis

Stream metabolism— To examine possible attenuation of catchment signals by instream processes, we modeled rates of instream GPP and ER from dissolved oxygen concentration, light, and temperature. We used the BAyesian Single-station Estimation of Metabolism (BASEmetab) package (Giling & Bond, 2020; Grace et al., 2015) because it provides instantaneous rates that we applied to test hypotheses about diel variation in stream chemistry.

However, the model shares the same conceptual basis and DO mass balance with the approach to modeling instream metabolism described previously (Task 7).

Daily-scale variation in solute concentrations— We applied MARSS models to evaluate effects of instream and terrestrial primary productivity and precipitation on stream chemistry. The MARSS framework partitions variation among observation error, autoregressive processes, and covariate effects (Holmes et al., 2021). The observed time series of solute concentration, y_t, is described by the underlying true state process x_t:

Eq. 10: $x_t = B_t x_{t-1} + u_t + C_t c_t + w_t$ with $w_t \sim MVN(0, Q_t)$
Eq. 11: $y_t = Z x_t + v_t$ with $v_t \sim MVN(0, R_t)$

where $\mathbf{x}_t$ is a $p \times 1$ vector of log-concentrations of a solute for p different states of nature. We considered two possible states: 1) all catchments reflected a single state process, and 2) separate states for each headwater catchment. When the observations are assumed to represent unique states across catchments, p equals the total number of catchments with available time series data ($p = 2$ for NO_3^- and $p = 4$ for fDOM). $\boldsymbol{B}$ estimates the degree of mean-reversion in x. The $p \times 1$ vector $\mathbf{u}$ in Eq. 10 represents a bias term for each of the unique states, where bias captures a monotonic offset from the mean concentration. The $\boldsymbol{C}$ matrix estimates the effects of covariates, and $\boldsymbol{c_t}$ represents observed values of the covariates. The process errors $\mathbf{w}_t$ are assumed to be drawn from a multivariate normal distribution with a mean vector of $\mathbf{0}$ and covariance matrix $\mathbf{Q}$. We assumed that each state had its own unique variance with no covariance among states, such that $\mathbf{Q}$ is a diagonal matrix with variance terms along the diagonal and 0's elsewhere.

An observation model (Eq. 11) mapped the time series from each catchment onto each state. Here $\mathbf{y}_t$ is an $n \times 1$ vector of the measured ln-transformed and mean-centered concentration of a solute at time t for each of the n catchments, and $\mathbf{Z}$ is an $n \times p$ matrix of 1's and 0's that matches each measurement (row) to its hypothesized state (column). In the multi-state model, $p = n$ and $\mathbf{Z}$ is an $n \times n$ identity matrix with 1's on the diagonal and 0's elsewhere. We allowed for non-zero differences between the observations ($\mathbf{y}$) and true states ($\mathbf{x}$) to reflect analytical error. An additional $n \times 1$ vector represented these observation errors ($\mathbf{v}_t$). We assumed that observation errors were independent and identically distributed, with a mean vector of $\mathbf{0}$ and diagonal covariance matrix, $\mathbf{R}$, estimated from the analytical error of the fDOM and NO_3^- sensors.

Daily mean fDOM or NO_3^- concentrations were $\log_{10}$-transformed, centered, and standardized (mean = 0, standard deviation = 1) prior to model fitting. Covariate values were centered and standardized to facilitate comparison across effects. Covariates included precipitation, GDU, and stream GPP or PAR. Precipitation was included as same-day total and previous day's precipitation because stream discharge can lag precipitation by 4–48 h (McGuire and McDonnell, 2006; Koch and others, 2013). Growing degree days, a correlate of terrestrial primary production, were lagged by one day. Effects of instream processes were assessed in alternate models that included GPP or PAR as covariates. Rates of GPP were only available for two streams and instream production correlates with PAR. We also included a dummy covariate to account for a sudden "step change" in discharge and chemistry that occurred in some catchments. Covariates were uncorrelated with one another (Pearson's $r < |0.4|$) and with the exception of PAR, were uncorrelated with day of year.

To evaluate contrasts among catchments, we compared the magnitude and direction of covariate effects, where significant differences were determined by non-overlapping 95% confidence intervals. We also compared single and multi-state models to determine whether environmental processes driving variation in solute concentration varied in concert across

catchments or differed among individual catchments. We compared AIC values of single and multi-state models to determine data support for these alternative state processes.

Storm-scale dynamics— To evaluate pool sizes of solutes available for transport to streams and hydrologic mechanisms connecting catchments to streams, we analyzed storm-scale concentration-discharge relationships. We delineated individual storms, identifying the rising and falling limbs of the stream hydrograph. Storms were defined as events when discharge exceeded 41.9 L s^{-1} and 64.3 L s^{-1} in the high- and mid-permafrost catchments, respectively. These thresholds correspond to twice the mean baseflow for each catchment, which we calculated using a recursive digital filter approach from the *EcoHydRology* package for R (Fuka et al., 2018). The remaining two catchments had weaker discharge responses to precipitation, and we identified storms within the time windows of events identified in the nearest "responsive" catchment. In all catchments, we delineated the beginning of each storm as the inflection point when discharge began to rise and the end point when discharge returned to the pre-event level or when another storm began.

To compare storm dynamics across catchments and events, we calculated a hysteresis index (HI) and flushing index (FI) for NO_3^-, fDOM, turbidity, and SPC during each storm (Lloyd et al., 2016; Vaughan et al., 2017). The HI indicates the magnitude and direction of hysteretic responses of solute concentration relative to rising and falling discharge and was calculated at every 2% interval of normalized discharge of each event. The HI at each Q interval *i* was calculated as $HI_i = C_{RL} - C_{FL}$, where C_{RL} and C_{FL} are normalized concentrations on the rising and falling limb, respectively. The median of all HI_i summarizes the central tendency for each event and bootstrapped 95% CIs around the median HI describe uncertainty. HI ranges between −1 and 1, with negative and positive values indicating anti-clockwise and clockwise hysteresis, respectively. The FI quantifies dilution or flushing during each storm as the difference between mean solute concentration at the initiation of a storm compared to peak discharge. Mean solute concentration or turbidity at each time point were calculated as the mean of the burst of measurements (n=9–15 within 30 s) collected by the instream sensor. Bootstrapped 95% CI of the difference in these means provided an estimate of uncertainty for each FI.

Multi-scale temporal variation— We used wavelet transforms and wavelet coherence analysis to characterize variation in NO_3^- and fDOM concentrations across time scales. The wavelet transform decomposed 15-min observations into power spectra across a range of frequencies (0.25–32 d), with power defined as the squared amplitude of oscillations localized in time. We used a 'morlet' mother wavelet and determined the significance of wavelet power by comparison to an autoregressive ("red") background noise spectrum with 100 simulations in the *WaveletComp* package for R (Roesch & Schmidbauer, 2018). Wavelet analysis requires continuous time series and datasets with >12-h gaps were therefore analyzed separately.

We analyzed wavelet coherence to quantify correlations between NO_3^- or fDOM concentrations and discharge or primary production. Wavelet coherence is a measure of localized correlation and phase angles between time series across time-frequency space. Phase angles are in the interval $[-\pi, \pi]$ and describe whether two time series at a given frequency oscillate in synchrony (in-phase = absolute values less than $\pi/2$, e.g., NO_3^- is high when discharge is high), anti-synchronously (out-of-phase = absolute values greater than $\pi/2$, e.g., NO_3^- is high when discharge is low), whereas the sign of the phase angle describes which time series is leading in time (Roesch and Schmidbauer, 2018).

9.2.4 Results

Seasonal variation— A season-long, positive trend in NO_3^- concentration occurred in the high-permafrost catchment, consistent with the prediction that a seasonal increase in NO_3^- concentration would occur where permafrost is present (Fig. 24). The positive trend was significant both before (0.007 mg N L^{-1} wk^{-1}, 95% CI: 0.001–0.01) and including a rapid increase in NO_3^- concentration that occurred late in the monitoring period (0.02 mg N L^{-1} wk^{-1}, 95% CI: 0.002–0.03), and also when the snowmelt period prior to June 15 was excluded (0.02 mg N L^{-1} wk^{-1}, 95% CI: 0.0002–0.04). A significant increase in NO_3^- concentration in the high-permafrost catchment suggested seasonal changes in flowpath depth, whereas no trend in a low-permafrost catchment reflected the dominance of deep groundwater supporting streamflow there (Bolton & Hinzman, 2004).

Several mechanisms might have contributed to the observed increase in NO_3^- concentration at a seasonal timescale, including lower biological N demand or greater rate of nitrification at depth (Harms & Jones, 2012; Melvin et al., 2015), increased rates of N mineralization and nitrification as soils warm (Klingensmith & Van Cleve, 1993), or increasing contribution of NO_3^--rich groundwater later in the thaw season (Task 8). This temporal trend is complementary to a positive correlation of active layer depth with NO_3^- concentration previously documented in streams across Interior Alaska (Harms et al., 2016). The seasonal rate of NO_3^- increase estimated here provides a baseline against which to assess effects of continued warming, fire, or changes in precipitation regime on deepening of the active layer.

A rapid, sustained "step-change" increase in discharge and solute concentrations occurred in the high- and mid-permafrost catchment in response to intense precipitation occurring in August (Fig. 24). The "step-change" included increases in NO_3^-, fDOM, and discharge accompanied by a decline in SPC in the high- and mid-permafrost catchments (Fig. 24). No such changes occurred in catchments draining south-facing slopes that lack permafrost. Smaller step changes in NO_3^- concentration followed late summer and early autumn rain events in an adjacent, larger river (Douglas and others, 2013), suggesting that solute dynamics of headwater streams might propagate to larger rivers. The mechanism yielding these patterns remains unclear, but we hypothesize that precipitation might induce deepening of flowpaths or activation of new flowpaths that increase hydrologic connectivity within catchments. Supporting this hypothesis, previous observations in the region have measured rapid transport of water and solutes along the permafrost boundary (James et al., 2019; Koch et al., 2013) and increased active layer depth (thawed soils above permafrost) in years with more rain (Douglas et al., 2020). In contrast, absence of a step-change in the low- and low-mid-permafrost catchments underscored the role of infiltration and deep drainage in generating streamflow in boreal catchments where permafrost is absent.

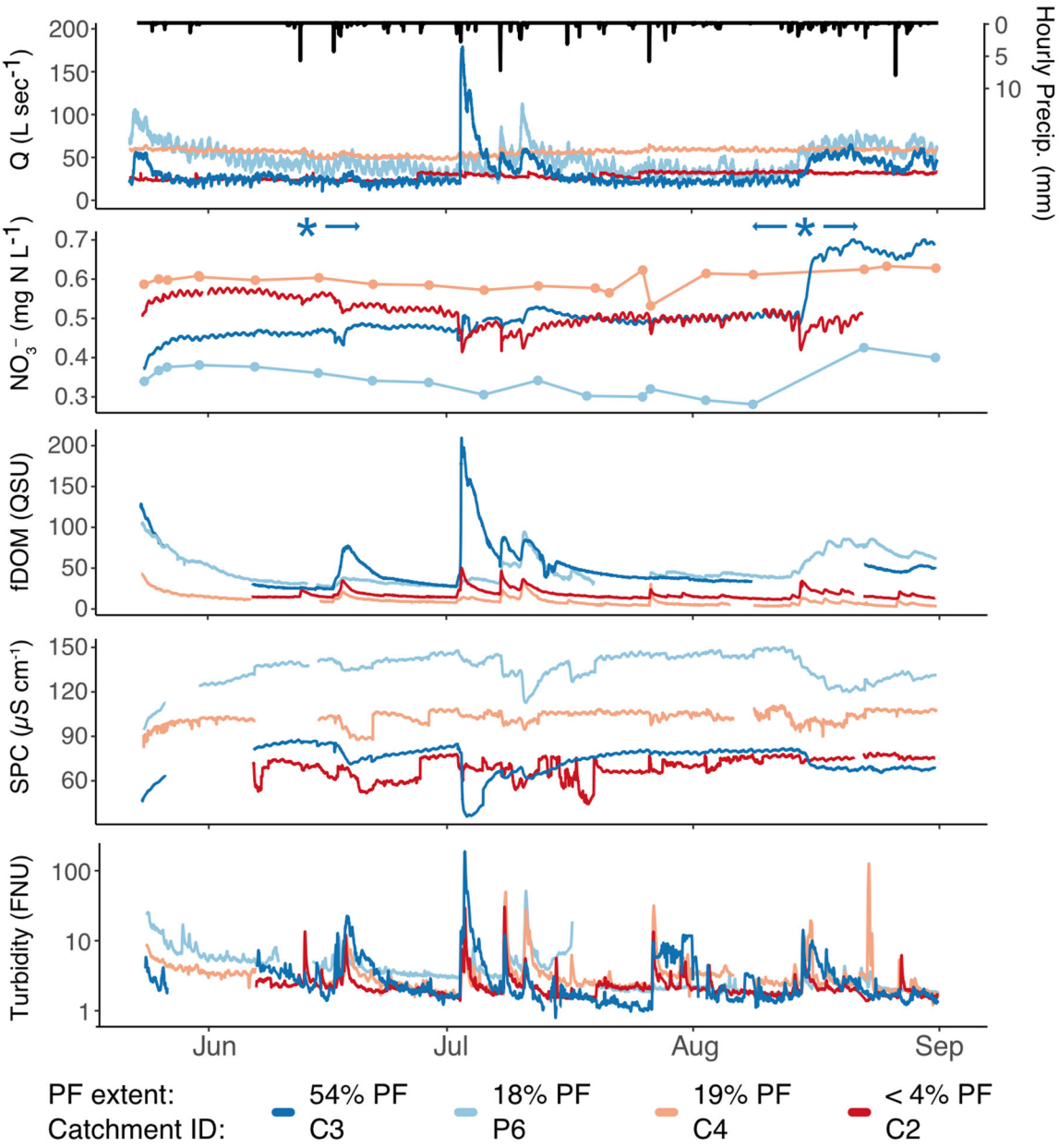


Figure 24. High-frequency (15-min) data collected by sensors installed in headwater streams that drain catchments of varying spatial extent of permafrost and burn history. The C4 catchment was partially burned (28%) in an experimental burn in 1999 and the P6 catchment was burned (65%) in a wildfire in 2004. Stars on the nitrate panel indicate that C3, the high permafrost catchment, showed a significant increase in nitrate concentration through the thaw season.

Daily-scale variation— Daily variation in stream chemistry within the period of measurement was strongly correlated with precipitation, as indicated by significant covariate effects in MARSS models. Nitrate and fDOM concentrations were significantly correlated with precipitation on the same or previous day in all catchments (Fig. 25). Previous-day precipitation had a strong positive effect on NO_3^- concentration in the high-permafrost catchment (Fig. 25a). However, both same- and previous-day precipitation had strong negative effects on NO_3^- concentration in the low-permafrost catchment (Fig. 25b), a pattern counter to that predicted to result from larger stores of mobilizable NO_3^- where permafrost is absent. Precipitation was positively correlated with fDOM in all catchments (Fig. 25c–f), which is inconsistent with the hypothesis that differential stores of soil OM in soils of varying permafrost extent and fire history would result in contrasting temporal dynamics among catchments. However, finer scale analysis revealed contrasts in the timing of storm flushing responses among catchments varying in permafrost extent (See *Section 9.2.4 Storm-scale analysis*).

Solute concentrations were correlated with indicators of within-stream and terrestrial productivity on a daily timescale. Nitrate concentration was negatively correlated with GDU on the previous day (an indicator of terrestrial productivity) in both the high- and low-permafrost catchments (Fig. 25a,b). Declining NO_3^- concentration during conditions favorable to terrestrial primary production suggests a potential effect of vegetation on N export, a pattern also observed in other forested catchments (Lucas et al., 2016). Growing degree units were not correlated with fDOM concentration (Fig. 25c-f). Nitrate concentration was also negatively correlated with in-stream GPP in the high-permafrost catchment, consistent with the predicted result of biotic retention of NO_3^- within streams but was not correlated with PAR (Fig. 25a, b), providing limited support for the hypothesis that instream biotic activity influences NO_3^- concentration in the study streams. Concentration of dissolved organic matter (fDOM) was positively correlated with PAR in the low-permafrost catchment and low-mid-permafrost catchments (Fig. 25d–f), a pattern that could suggest release of fDOM by primary producers in streams. Finally, data best supported MARSS models with a unique state process for each catchment, rather than a single state process for all catchments ($AIC_{single\text{-}state} >> AIC_{multi\text{-}state}$). Thus, temporal patterns were statistically distinguishable among the headwater catchments.

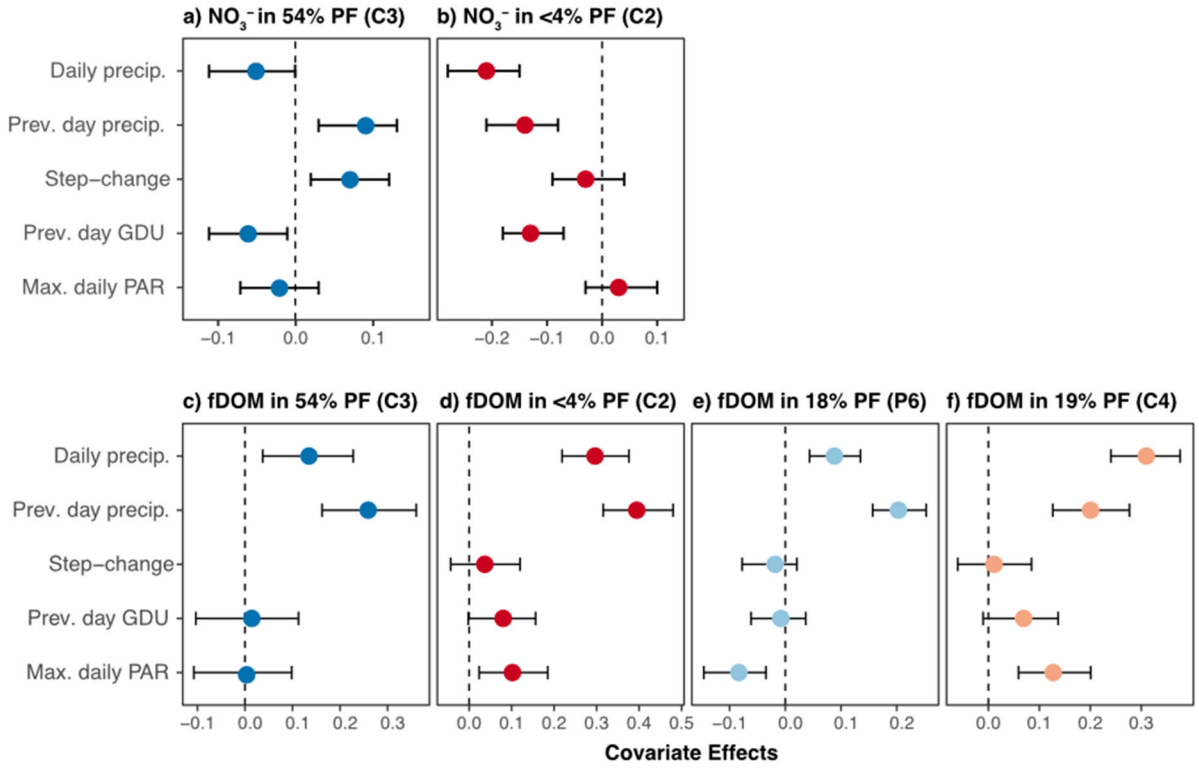


Figure 25. Covariate effects on daily NO_3^- (a–b) and fDOM (c-f) concentrations in headwater catchments estimated by MARSS models. Effects of mean daily precipitation, previous-day precipitation, previous-day growing degree units (GDU), and maximum daily photosynthetic active radiation (Max daily PAR) in streams draining catchments with varying permafrost extent (PF). Step-change is the effect of a dummy variable used to represent a sudden change in discharge and stream chemistry that occurred Aug 14–15 in some catchments. Predictor variables were centered and standardized prior to analysis and solute concentrations were log-transformed. Points are maximum likelihood estimates for effects of covariates on each response variable. Horizontal bars are bootstrapped 95% confidence intervals; bars crossing the vertical dashed line (zero) indicate non-significant effects.

Storm-scale dynamics— Concentration-discharge dynamics during storms varied with spatial extent of permafrost in the catchment. In the high-permafrost catchment, four of five storms resulted in increased NO_3^- concentration (+FI) and counterclockwise hysteresis (-HI; Fig. 26b). In the low-permafrost catchment, all storms resulted in dilution of NO_3^- (-FI), and all but one storm produced clockwise hysteresis (+HI; Fig. 26b). Flushing of NO_3^- on the falling limb of storms in the high-permafrost catchment suggests that NO_3^- was delivered to the stream from distal locations in the catchment. A positive correlation of daily mean NO_3^- concentration with the previous-day's precipitation in the high-permafrost catchment (Fig. 25) captured by daily-scale time series models corroborated this interpretation, because leaching of NO_3^- from distal stores would increase the transit time to streams (see also *Section 9.2.4 Daily-scale variation*). Together, these patterns underscore the role of permafrost in maintaining shallow flowpaths that connect soils to streams. In the low-permafrost catchment, dilution and clockwise hysteresis of NO_3^- during most storms was counter to our prediction that larger stores of NO_3^- in thawed, mineral soils exposed to flowpaths would generate flushing during storms. Instead, storms likely activated shallow flowpaths that diluted the NO_3^--rich groundwater supporting baseflow.

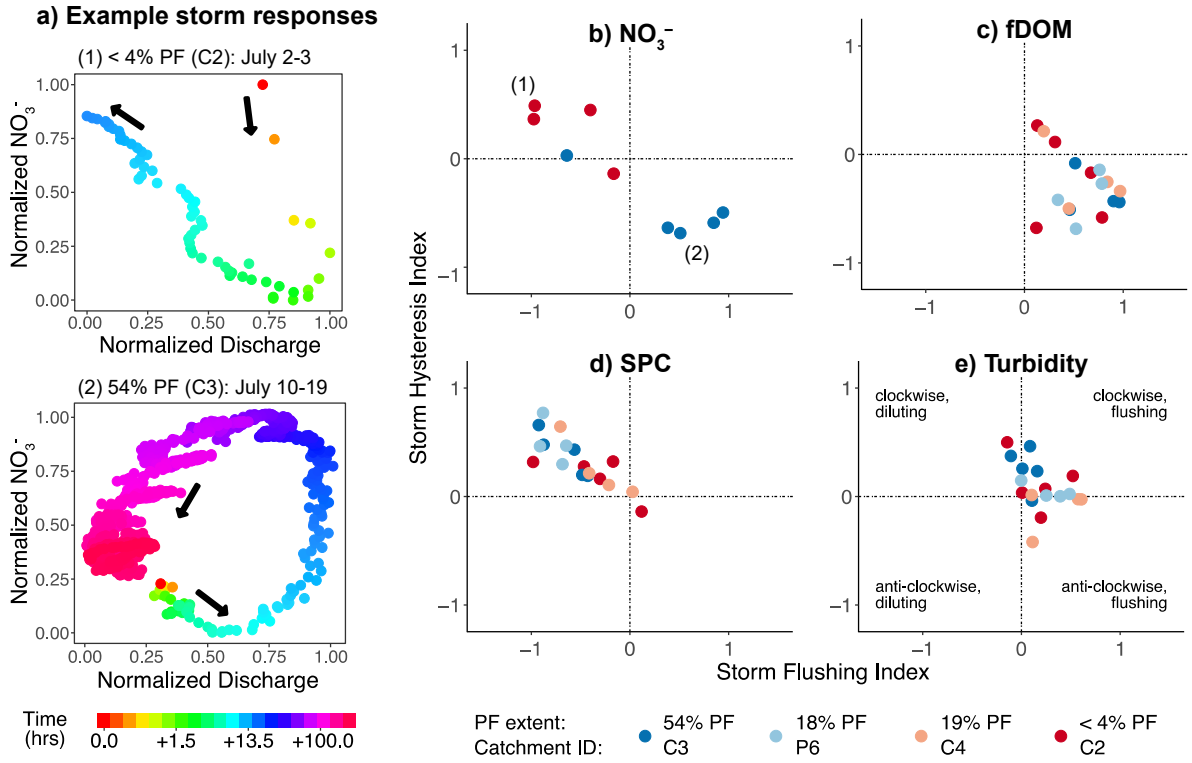


Figure 26. Concentration-discharge relationships during storms in headwater catchments. a) Concentration-discharge relationships for nitrate (NO_3^-) during two example storms (1, 2). Hysteresis index versus flushing index during all storms during monitoring in 2017 for: (b) NO_3^-, (c) fDOM, (d) specific conductivity (SPC), and (e) turbidity. The example storm responses for NO_3^- in (a) are identified in (b). Error bars for storm hysteresis indices are bootstrapped 95% confidence intervals around the median of hysteresis indices calculated at each 2% discharge interval for each event. Error bars for the flushing index are bootstrapped 95% confidence intervals for the difference between the mean of solute concentration at the onset of the event and at peak discharge.

Though all catchments and storms resulted in flushing of fDOM, only the low- and low-mid-permafrost catchment produced clockwise hysteresis (+HI) for fDOM. Simultaneous flushing of fDOM in the low-permafrost catchment (Fig. 26) is consistent with activation of shallow flowpaths during storms. Smaller flushes of fDOM in the low- and mid-low-permafrost catchments (Fig. 26) supported our expectation of smaller OM stores there, and instances of clockwise hysteresis of fDOM in these catchments (Fig. 26c) indicated that supply of leachable DOM was sometimes exhausted during storms. Overall, patterns on the timescale of storms emphasized that the distribution of solute supplies relative to locations of dominant flowpaths, rather than differences in total C and N stocks in catchments, influences the biogeochemical signals of permafrost observable in streams.

Multi-scale temporal variation

Wavelet analysis corroborated the significant influence of storms on NO_3^- and fDOM concentrations previously described at daily and storm timescales. Wavelet transforms detected oscillations of NO_3^- and fDOM that were significantly greater than expected of an autoregressive (red noise) spectrum in all catchments at frequencies of 2−8 d and instances of these significant oscillations corresponded in time with storms (Webster et al., 2022). In the high-permafrost catchment, oscillations in NO_3^- concentration were coherent with stream discharge at temporal frequencies and times associated with storms, typically varying in-phase with NO_3^- following discharge (Fig. 27a & b). This pattern coincided with flushing of NO_3^- during storms. Oscillations in NO_3^- were also coherent and in-phase with discharge at 4−16 d frequencies during the time period of the step-change in the high-permafrost catchment (Fig. 27), suggesting a hydrologic explanation of the step-change.

At a diel frequency, NO_3^- oscillated coherently with discharge in both the high- and low-permafrost catchments. Out-of-phase coherence with NO_3^- leading discharge tended to occur at a diel frequency in the high-permafrost catchment during the early thaw season, whereas NO_3^- varied in-phase, following discharge during the later season in the high-permafrost catchment and throughout the record in the low-permafrost catchment (Fig. 27a & b). Coherence of NO_3^- and discharge at a diel time scale might occur due to the effects of terrestrial evapotranspiration on water table elevation (Flewelling et al., 2013). A higher water table enhances capacity for denitrification in the riparian zone (Harms & Jones, 2012), whereas oxygenated soils above the water table might support nitrification (Duncan et al., 2015). However, this mechanism is plausible only in the high-permafrost catchment early in the thaw season, when daily peaks in NO_3^- concentration occurred when discharge was low (Fig. 24). Later in the thaw season, and throughout the record in the low-permafrost catchment, NO_3^- and discharge oscillated synchronously on a diel timescale, or peak daily NO_3^- concentration followed peak daily discharge, which is consistent with N uptake by either in-stream or terrestrial biota.

During inter-storm periods, NO_3^- was coherent and consistently out-of-phase with instream GPP, with peak NO_3^- following peak GPP in both the high- and low-permafrost catchments (Fig. 27c & d). This is evidence that NO_3^- uptake by instream biota influences diurnal variation in concentration. In contrast, wavelet power spectra indicated no diel pattern of variation in fDOM concentrations (Webster et al., 2022). Lack of diel variation in fDOM and inconsistent or non-significant correlations of either solute with daily max PAR suggest that in-stream photodegradation did not play a major role in DOM processing and was not coupled to diel NO_3^- variation, as expected in these narrow well-shaded streams.

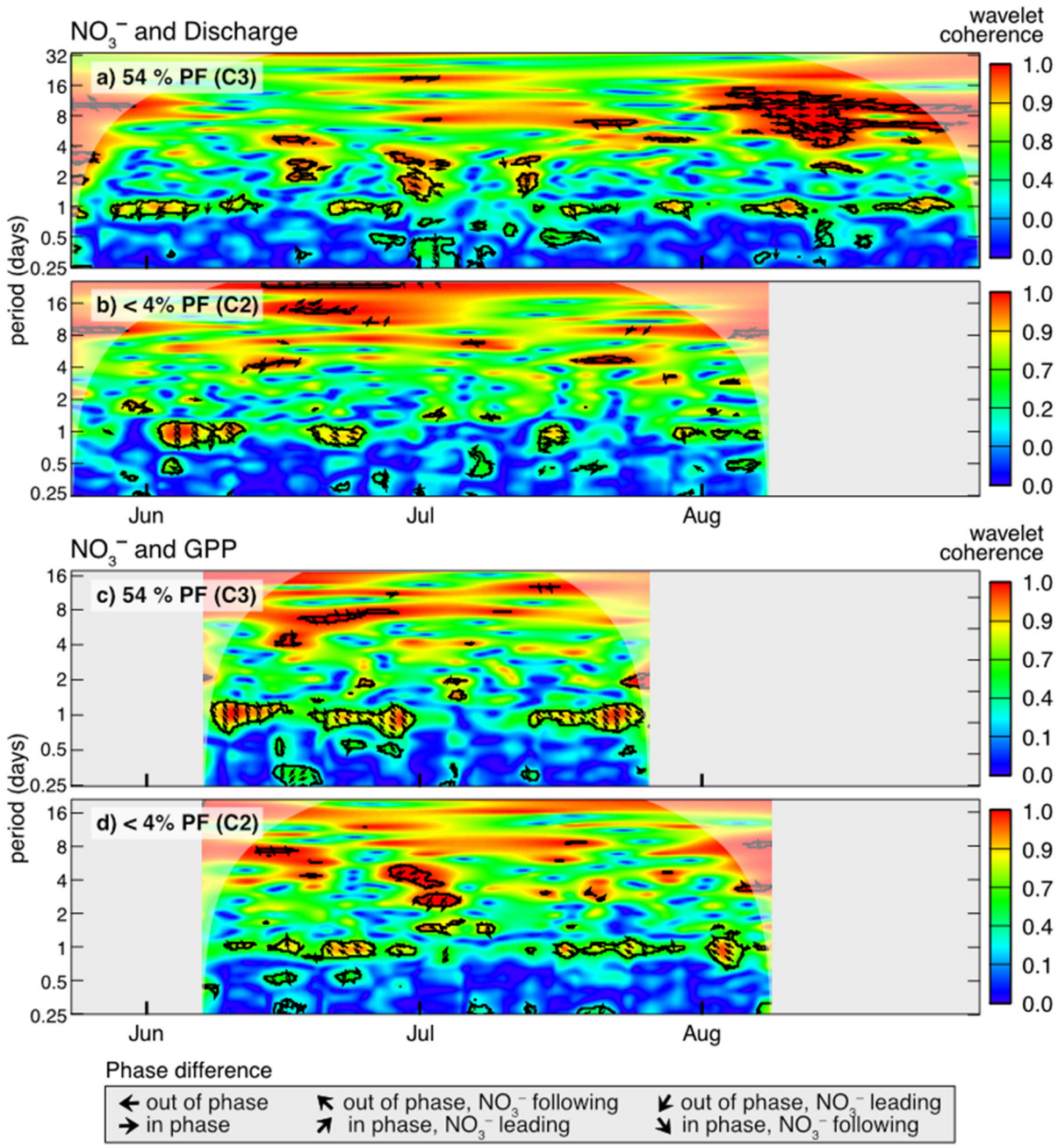


Figure 27. Wavelet coherence of nitrate (NO_3^-) concentration with discharge (a–b) and gross primary productivity (GPP) (c–d) in streams draining catchments with 54% permafrost (PF) (a, c) and <4% permafrost (b, d). Data are depicted in the time domain in Fig. 24. Black lines indicate significant coherence (p < 0.017) and shading denotes areas outside the cone of influence. Colors for coherence levels are set by quantiles to provide an even color distribution. Arrows indicate the phase difference between the time series: → = in phase; ← = out of phase; ↖ = out of phase, NO_3^- following; ↙ = out of phase, NO_3^- leading; ↗ = in phase, NO_3^- leading; ↘ = in phase, NO_3^- following. Coherence of nitrate with discharge on a diurnal timescale could indicate the effect of terrestrial evapotranspiration and water table elevation on delivery of NO_3^- to streams, whereas coherence over multi-day timescales indicates a strong effect of storms on NO_3^- dynamics. Coherence of NO_3^- oscillations with instream GPP at diurnal scales suggests an effect of stream biota on NO_3^- retention.

9.2.5. Implications

- Headwater catchments with higher spatial extent of permafrost were characterized by increasing NO_3^- concentration through the thaw season, an abrupt increase in NO_3^- and fluorescent dissolved organic matter (fDOM) and declining conductivity in late summer, and/or flushing of NO_3^- and fDOM during storms.
- In contrast, these patterns were absent, of lower magnitude, or reversed in catchments with lower permafrost extent.
- Shallow, seasonally dynamic flowpaths delivered solutes from high-permafrost catchments to streams.
- Lower spatial extent of permafrost resulted in static delivery of NO_3^- and limited transport of fDOM to streams, evidence of persistent discharge of groundwater to streams.
- Distinct temporal patterns in stream chemistry across catchments varying in spatial extent of permafrost suggest that stream biogeochemistry could be used to monitor ecosystem change caused by thawing permafrost.

9.3 Concentration-discharge relationships during storms, 2018-2022

9.3.1 Solute stores and hydrologic connectivity of boreal catchments disturbed by fire and permafrost thaw

We analyzed concentration-discharge relationships during all storms occurring within the study period of this SERDP project (2019-2022) for the set of five focal catchments, as well as an adjacent catchment monitored by the National Ecological Observatory Network (Table 3). In addition, data were available from three of the catchments in 2018. Catchments and streams are linked via hydrologic flowpaths and temporal patterns in stream chemistry might therefore reflect the total storage and distribution of materials including C and N within catchments (Musolff et al., 2015). In these permafrost-influenced catchments, accumulation of organic matter on the forest floor plays a central role in hydrologic, biogeochemical, and permafrost dynamics (detailed in *Background*). Wildfire also imparts biogeochemical signals by combusting OM and vegetation and thawing permafrost (detailed in *Background*).

Hydrologic and biogeochemical signals of catchment disturbances might be most apparent in streams during storms due to enhanced hydrologic connectivity. Storm C-Q dynamics, including hysteresis, flushing, and dilution patterns convey insights into the distribution of material pools within catchments and of hydrologic flowpaths connecting catchments to streams (Rose & Karwan, 2021; Vaughan et al., 2017). Hysteresis in the C-Q relationship indicates contrasts in concentration relative to discharge between the rising and falling limb of the storm hydrograph. Clockwise hysteresis defines greater constituent concentration on the rising limb versus the falling limb, suggesting that sources of the constituent are delivered from stores proximal to the stream and/or exhaustion of the solute pool during the storm event (i.e., source limitation). Conversely, counterclockwise hysteresis defines greater constituent concentration on the falling limb versus the rising limb, implying that materials originated from locations distal to the stream and/or that hydrologic transport limits export of material to the stream (i.e., transport limitation). Flushing occurs when material concentration rises with the initial increase in discharge whereas dilution occurs when concentration decreases as discharge increases. Analysis of a short-term dataset indicated characteristic storm C-Q dynamics in catchments varying in permafrost extent (*Section 9.2*; Webster et al., 2022).

Concentration-discharge relationships can vary due to hydrologic conditions including storm size and antecedent moisture. Larger or more intense storms can mobilize more materials because larger events hydrologically connect a greater fraction of the contributing area to the stream, resulting in chemostatic or flushing C-Q dynamics (Bracken et al., 2013; Koch et al., 2021; Petrone et al., 2007; Winter et al., 2022). Antecedent moisture conditions potentially influence both the size of material stores subject to export and the spatial extent of hydrologic connectivity during storms. Wetter conditions can foster sustained leaching of solutes and removal of N by denitrification, reducing material stores subject to export during storms (McMillan et al., 2018). In contrast, wetter conditions preceding storms can accelerate lateral extension of flowpaths, connecting distal stores of materials to the stream channel (Knapp et al., 2022). Finally, constituent pool sizes and availability for hydrologic export could vary seasonally due to changes in terrestrial productivity, soil moisture conditions, and flowpath depth as soils thaw (Ågren et al., 2007; Shogren et al., 2021). Temporal variation imparted by weather conditions could therefore obscure the imprint of catchment attributes, including disturbance history, on storm-scale signals.

We examined the effects of antecedent moisture conditions and disturbance (permafrost thaw and fire) on material stores and hydrologic flowpaths connecting catchments to streams to assess

the ecological state of boreal catchments in Interior Alaska. We hypothesized that wet antecedent conditions promote solute leaching, thereby reducing solute storage within catchments and potential for subsequent export. Alternatively, wet antecedent conditions could establish hydrologic connectivity between catchments and streams that facilitate rapid transport of solutes from distal sources to streams during storms. In catchments underlain with permafrost, we hypothesized that permafrost confines flowpaths to organic soils, resulting in increased potential for DOM export and reduced export of NO_3^-. We hypothesized that wildfires reduce catchment stores of OM due to combustion and increase pools of NO_3^- by reducing vegetative uptake of N. These conditions would result in flushing of NO_3^- and dilution of DOM during storms.

9.3.2 Data analysis

To provide context for storm-scale variation, we first compared concentration of each measured constituent (fDOM, NO_3^-, SPC, turbidity) across the study catchments within year of monitoring. Mean daily concentration of each measured constituent was compared across catchments for a common period of observations within each year using generalized least square models (GLS) that accounted for temporal autocorrelation of daily observations. First, we identified the day of peak snowmelt runoff on the Chena River, a large river in the same region as the study sites, for each study year. We then restricted analysis to a common window of time since peak snowmelt runoff in each year. This window was constrained by data availability due to later instrument deployment in 2020 and early freeze-up in 2021. Thus, the common window of analysis applied here and in subsequent analyses was approximately mid-June to late Sept. We fit GLS models that included terms describing autocorrelation of residuals with varying orders of autoregressive and moving average terms using the *nlme* package for R (Pinheiro et al., 2017). We then assessed remaining autocorrelation in residuals using plots of the autocorrelation and partial autocorrelation functions. We compared Akaike's information criterion (AIC) for models with no or minimal remaining autocorrelation to select the final model. When the omnibus test of significance indicated differences in material concentration among catchments, we subsequently assessed all pairwise comparisons of means while controlling the family-wise Type I error rate using the *multcomp* package for R (Hothorn et al., 2016).

We analyzed concentration-discharge relationships during storms occurring 2018-2022 in six catchments (Table 3, Fig. 2) using similar methods to those described in *Section 9.2.3*. We modified the criteria for delineating storms because the longer datasets included high flows caused by snowmelt runoff at the beginning of monitoring in some years that could not be accommodated by the recursive digital filter approach for separating storms from baseflow. Storms were therefore defined when precipitation was greater than 5 mm in a 24-hour period and accompanied by both an increase in discharge and a change in stream chemistry. Across all years (n=5) and sites (n=6), this procedure identified 310 individual storm events.

For each storm and constituent, we quantified HI as described in *Section 9.2.3* and used a modified index to describe flushing/dilution phenomena. Here we described flushing as the slope of the C-Q relationship on the rising limb of each event, with uncertainty estimated by the confidence intervals of this slope. The slope of the C-Q relationship is designated β, where positive values indicate flushing of the constituent as discharge rises, negative values quantify dilution of the constituent by high flows, and slopes with associated confidence intervals that overlap zero indicate chemostatic behavior (Godsey et al., 2009).

We regressed storm C-Q metrics against catchment attributes to assess whether catchments varying in landform or disturbance history yield characteristic patterns at the storm scale. We evaluated mean HI and β as well as the standard deviation of each metric across all storms

occurring in each catchment. Potential predictors included mean catchment slope, burn extent, and deciduous cover, which serves as a proxy for permafrost extent (Table 3). Predictor variables were centered and standardized prior to analysis. Regressions were analyzed as single-predictor models with R^2 used as a metric to select the model capturing the strongest correlation.

Concentration-discharge dynamics during storms reflect enhanced hydrologic connectivity and thus might reflect not only catchment signals, but also the hydrologic or other weather conditions during and preceding each storm. To evaluate the potential for climate to obscure biogeochemical signals during storms, we estimated effects of storm attributes, antecedent moisture conditions, and seasonality on storm C-Q dynamics (i.e., HI, β) using multiple linear regression analysis for individual catchments. Potential predictors included antecedent precipitation at varying temporal scales before a storm (one week, one month, three months), and storm attributes (total precipitation and intensity). We also included mean air temperature during a storm and mean air temperature in the week prior to each storm. Finally, we assessed the role of seasonality by including the time since peak flow during snowmelt in the Chena River. We eliminated predictor variables that were correlated (variance inflation factors >2), resulting in four uncorrelated predictors (storm precipitation, precipitation [week], precipitation [month], and seasonality). Predictor variables were centered and standardized such that reported regression coefficients represent the change in storm C-Q response resulting from a 1 SD change in the predictor variable. Regression coefficients are reported as standardized coefficients and bootstrapped 95% confidence intervals (*boot* package for R, Canty & Ripley, 2017).

9.3.3 Results

Variation in solute and turbidity concentrations across catchments

Mean daily solute and turbidity concentrations were largely similar across catchments, though the north-facing catchment draining yedoma soils (Vault Creek) differed for many constituents (Figs. 28-31). For example, mean daily NO_3^- concentration in Vault Creek was significantly less (~1.4 times) than in other catchments in most years (Fig. 28). Concentration of fDOM varied significantly across catchments and was ~3 times greater in Vault Creek and ~2 times greater in Moose Creek compared to all other catchments (Fig. 29). Specific conductivity was significantly greater in Vault Creek than in all other catchments in all study years (~3.5-fold greater; Fig. 30). Finally, turbidity was ~2 times greater in Vault Creek than in all other catchments (Fig. 31).

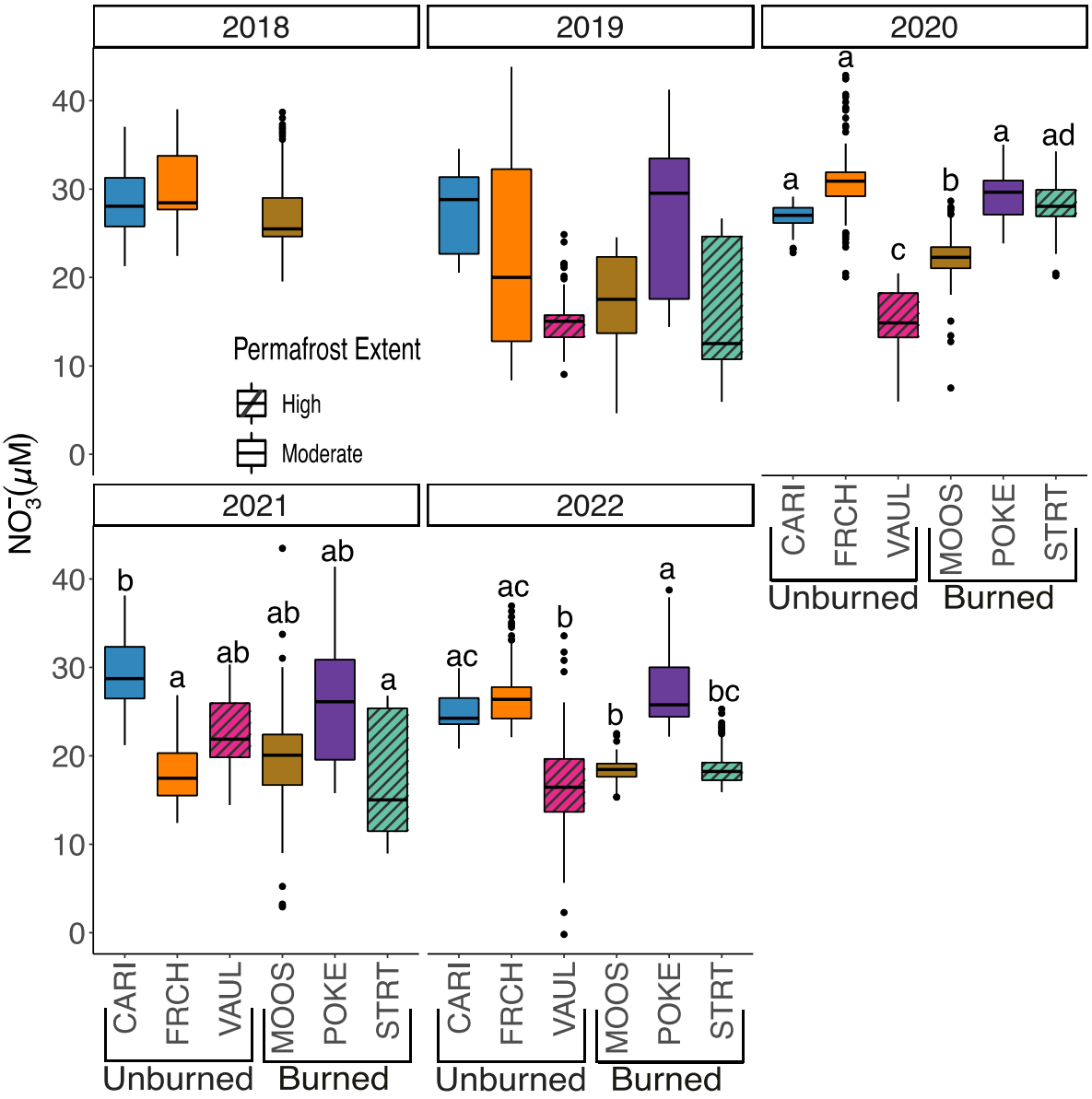


Figure 28. Daily mean NO_3^- concentration for each catchment and year of the study (35-142 days after peak snowmelt runoff in the Chena River). Center line indicates median concentration, boxes encompass 25th and 75th percentiles, whiskers are 1.5x the interquartile ranges, and points reflect values beyond this range. Letters represent significant differences (p-value<0.05) among catchments within a year determined by pairwise comparisons following generalized least squares models that included autocorrelated error terms.

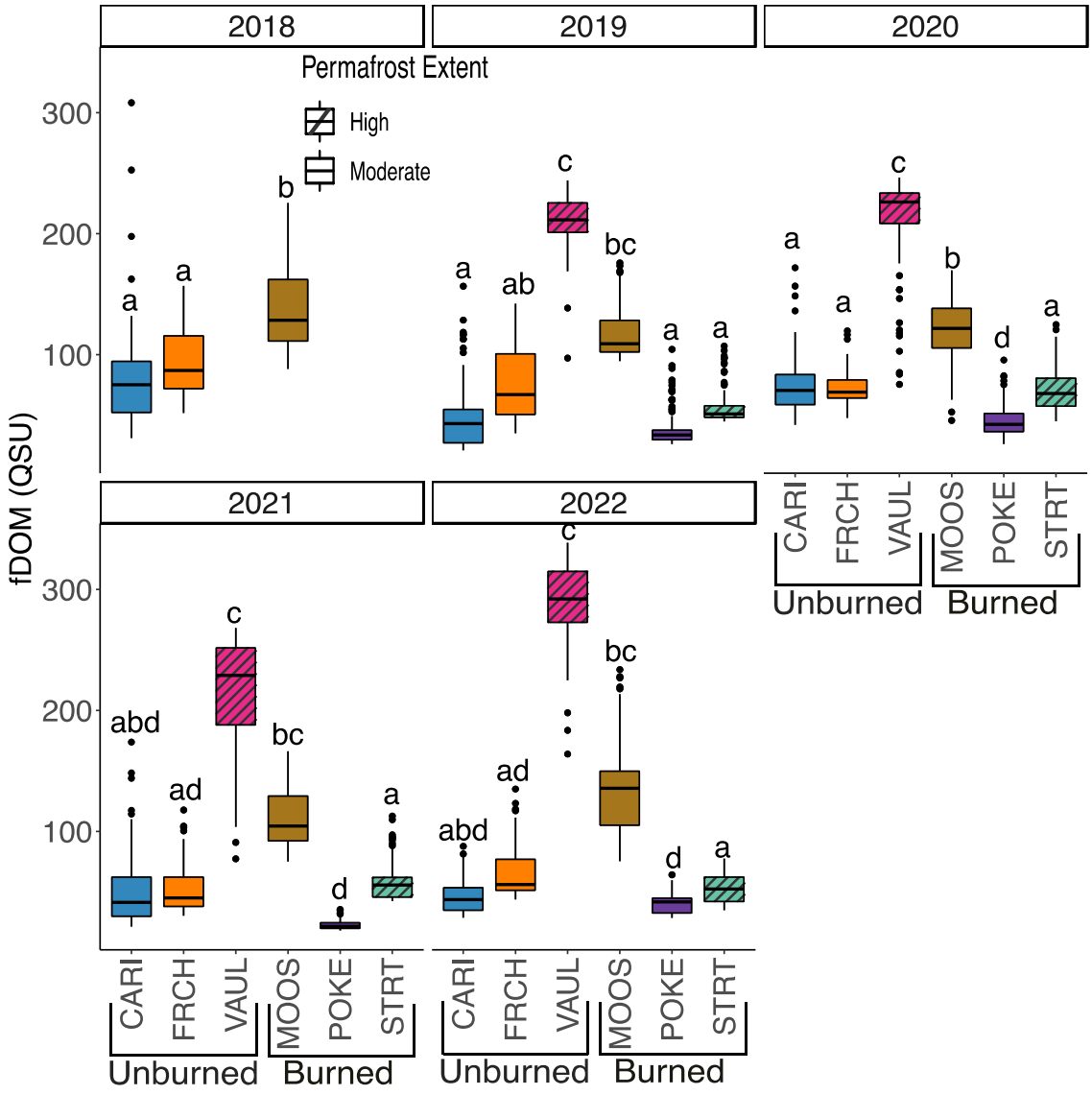


Figure 29. Daily mean fDOM concentration for each catchment and year of the study. Symbology as defined in Fig. 28.

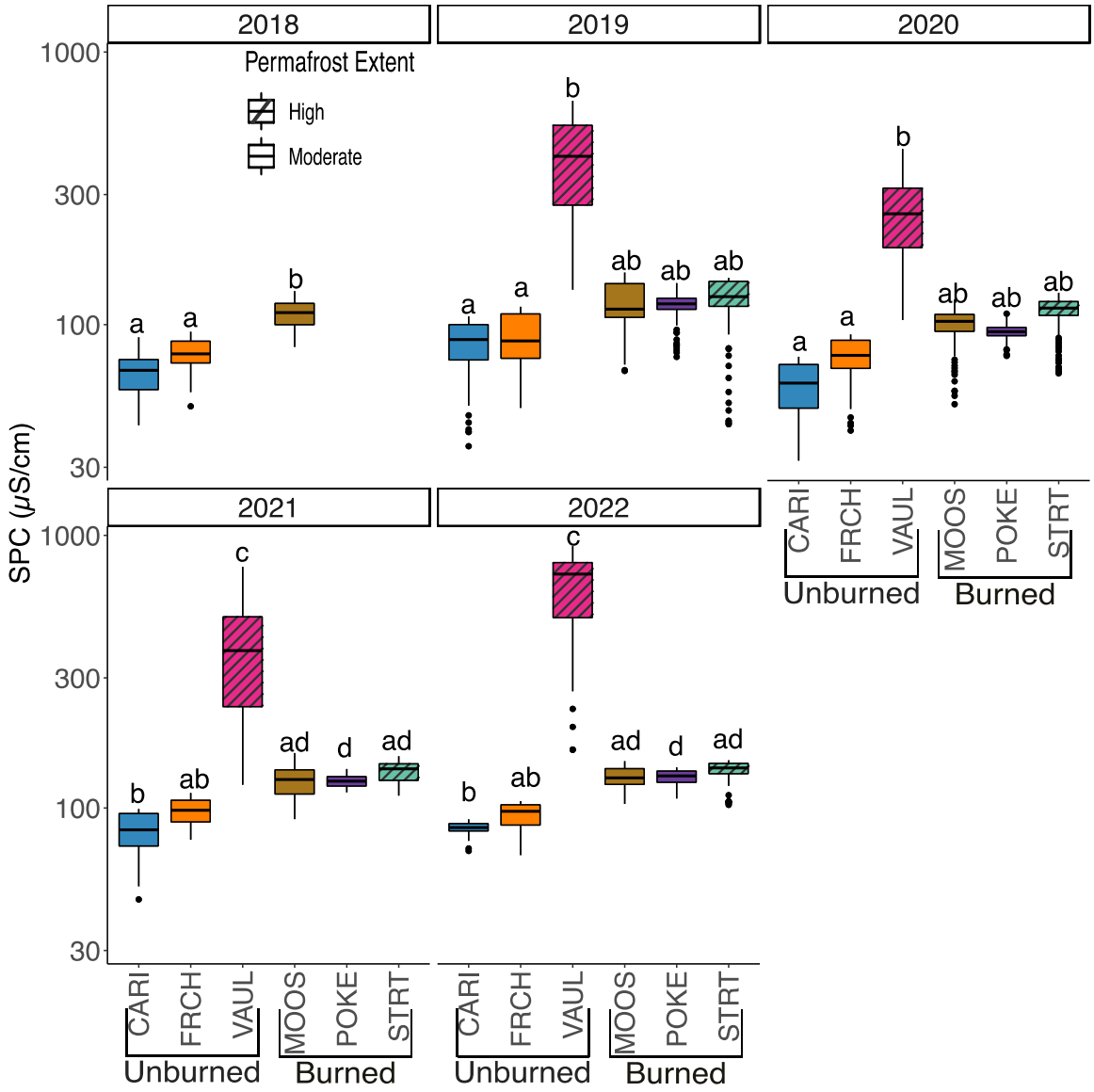


Figure 30. Daily mean SPC for each catchment and year of the study. Symbology as defined in Fig. 28.

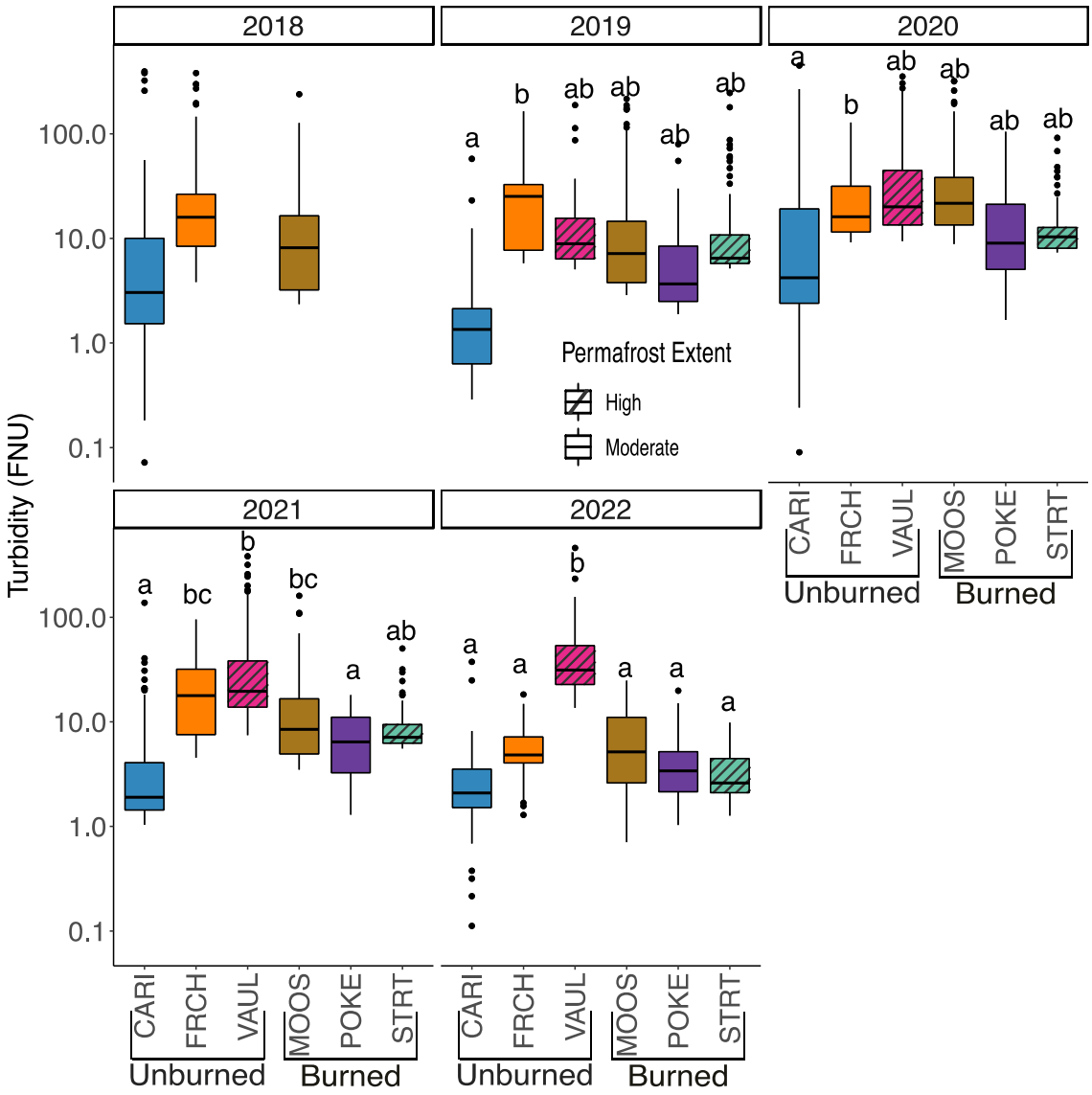


Figure 31. Daily turbidity concentration within each year of the study. Symbology as defined in Fig. 28.

Material storage and hydrologic transport mechanisms reflected by storm C-Q dynamics

Storm-scale dynamics of fDOM differed across the monitored catchments (Fig. 32). In the catchments with the highest mean daily fDOM concentration (Moose and Vault Creeks, Fig. 29), clockwise hysteresis (+HI) indicated rapid mobilization of nearstream stores of DOM to streams whereas counterclockwise hysteresis (–HI) in the remaining sites indicated delayed mobilization of DOM from sources distal to the stream (Fig. 33a; one-way ANOVA: F-value = 6.86; df = 5, 21; p-value = 0.006). However, fDOM concentration was rapidly diluted by rising discharge at the beginning of storms in the catchments with high background fDOM, whereas all other catchments generally showed flushing of fDOM during storms (Fig. 34a; one-way ANOVA: F-value = 2.4; df = 5, 21; p-value = 0.07). Thus, the lower-relief catchments likely contain substantial stores of OM that are diluted during storms by newer event water that is transported via flowpaths of low residence time. Conversely, steeper catchments were characterized by counterclockwise hysteresis (i.e., transport limitation, -HI; Fig. 33a) and flushing (+β; Fig. 34a) suggesting that OM delivery to the stream is delayed in these catchments until hydrologic connectivity is established during storms.

Dynamics of fDOM were more variable among storms at the sites draining silty uplands (Moose, Stuart, and French Creek) compared to sites draining rocky uplands (Caribou and Poker Creeks; Fig. 35a). This pattern was reflected in significant contrasts in the SD of HI-fDOM across catchments (one-way ANOVA: F-value = 5.6; df = 5, 21; p-value = 0.002). However, we found no significant differences in temporal variation of flushing/dilution dynamics of fDOM across catchments (i.e., SD of β-fDOM; Fig. 36a).

Storm-scale dynamics of inorganic solutes such as NO_3^- and mineral ions contributing to SPC were more similar across catchments than C-Q dynamics of fDOM. Most storms (68%) diluted NO_3^- compared to baseflow and resulted in significant clockwise hysteresis (+HI; 61% of events, indicating greater concentration on the rising limb than the falling limb (Fig. 32). Neither mean HI nor mean β differed significantly across catchments for NO_3^- (Figs. 33 & 34). We found no significant differences in temporal variation of hysteresis or flushing/dilution dynamics across catchments (Figs. 35 & 36).

Dynamics of SPC were similar to NO_3^-, with most storms (79%) exhibiting greater SPC on the rising compared to the falling limb (+HI; Fig. 32). The majority of storms (77%) also resulted in significant dilution of SPC on the rising limb (–β; Fig. 32). Neither mean nor inter-storm variation in C-Q relationships for SPC contrasted significantly across catchments (Figs. 33 & 34). Similar dynamics of NO_3^- and SPC (i.e., clockwise hysteresis and dilution) during storms indicated that inorganic solutes were primarily source-limited, with either insufficient supply to sustain flux throughout the storm event or limited hydrologic connection of supplies to streams. This could result if shallow event water dilutes the more mineral-rich groundwater supplying baseflow.

Unlike the other constituents, turbidity typically showed no hysteresis with discharge and most storms (82%) increased sediment delivery to the stream on the rising limb of the hydrograph (+β; Fig. 32). Neither HI nor β of turbidity in these metrics differed significantly across catchments (Figs. 33 & 34) and temporal variation was similar across catchments as well (Figs. 35 & 36). Thus, storm-scale variation in turbidity was contributed by strong coupling between runoff and sediment transport that operated similarly across catchments occupying regional gradients in disturbance history and landforms.

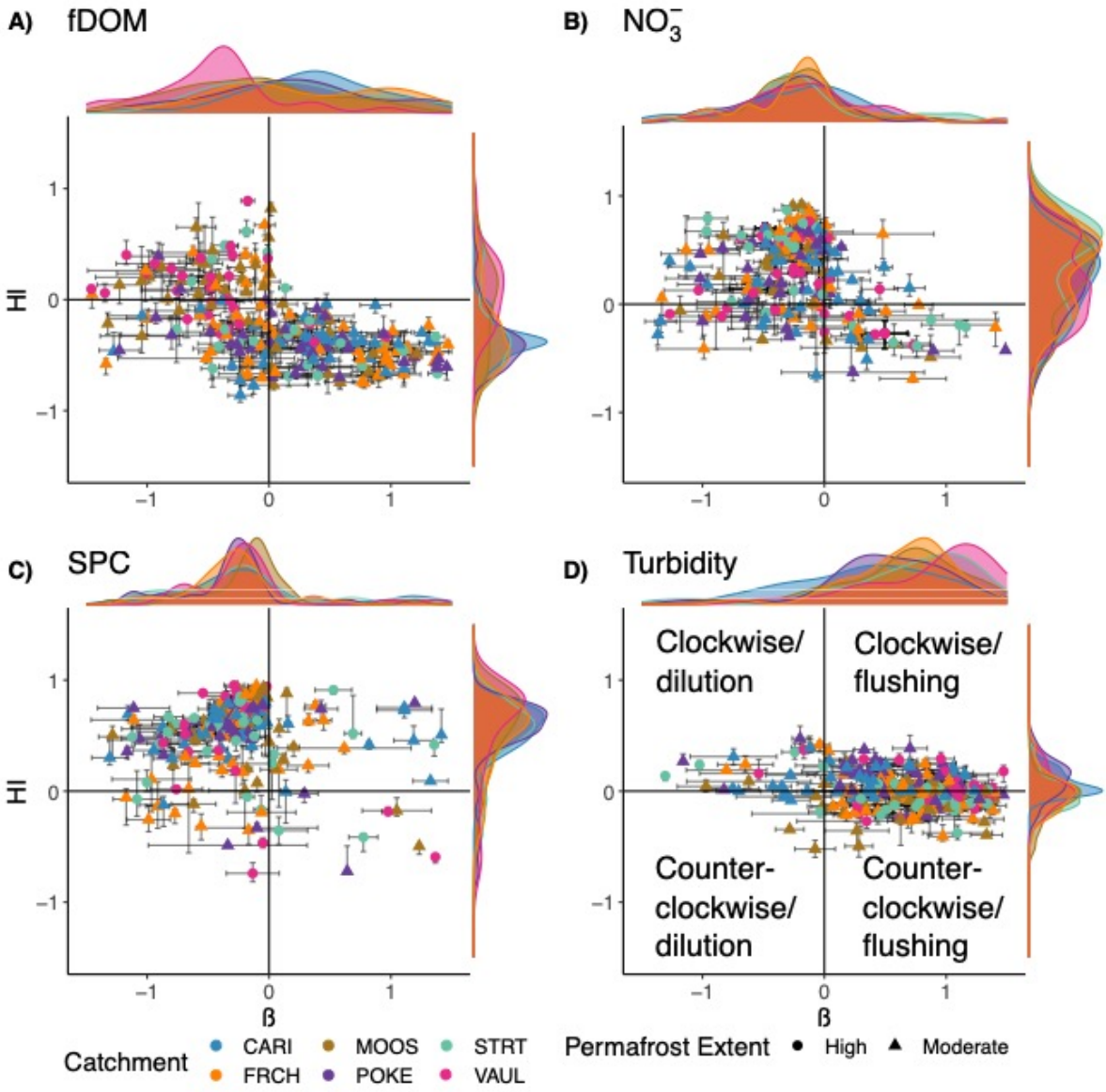


Figure 32. Hysteresis index versus β during all delineated storms for fDOM (A), NO_3^- (B), SPC (C), and turbidity (D). Triangles indicate high spatial extent of permafrost whereas circles indicate medium extent. Error bars indicate 95% confidence intervals.

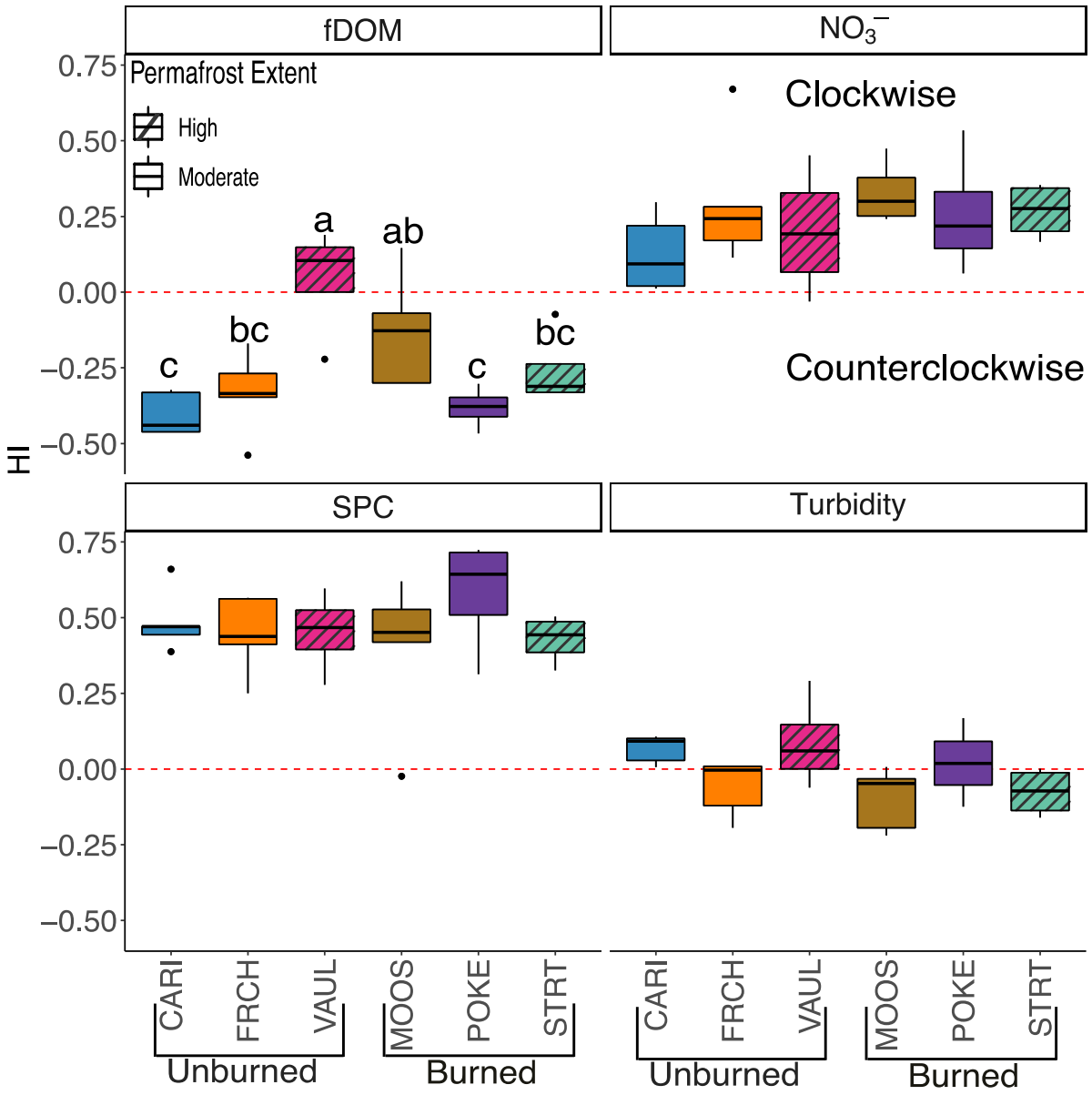


Figure 33. Hysteresis index across all storms for fDOM (A), NO_3^- (B), SPC (C), and turbidity (D). Center line indicates median concentration, boxes encompass 25th and 75th percentiles, whiskers are 1.5x the interquartile ranges, and points reflect values beyond this range. Letters represent significant differences (p-value<0.05) among catchments within a year determined by pairwise comparisons.

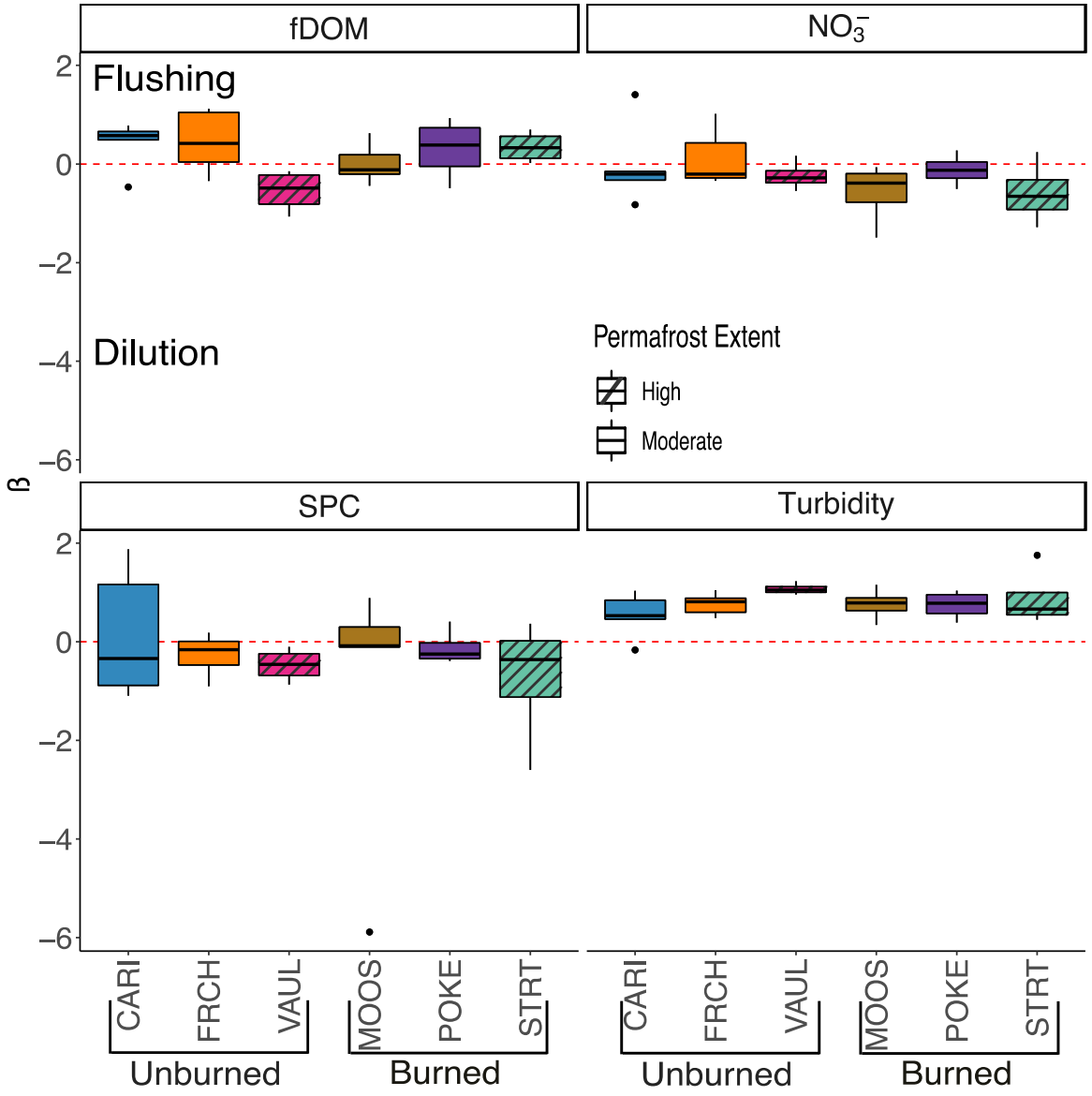


Figure 34. Slope of the concentration-discharge relationship on the rising limb of each storm (β), across all storms for fDOM (A), NO_3^- (B), SPC (C), and turbidity (D). Symbology as defined in Fig. 33.

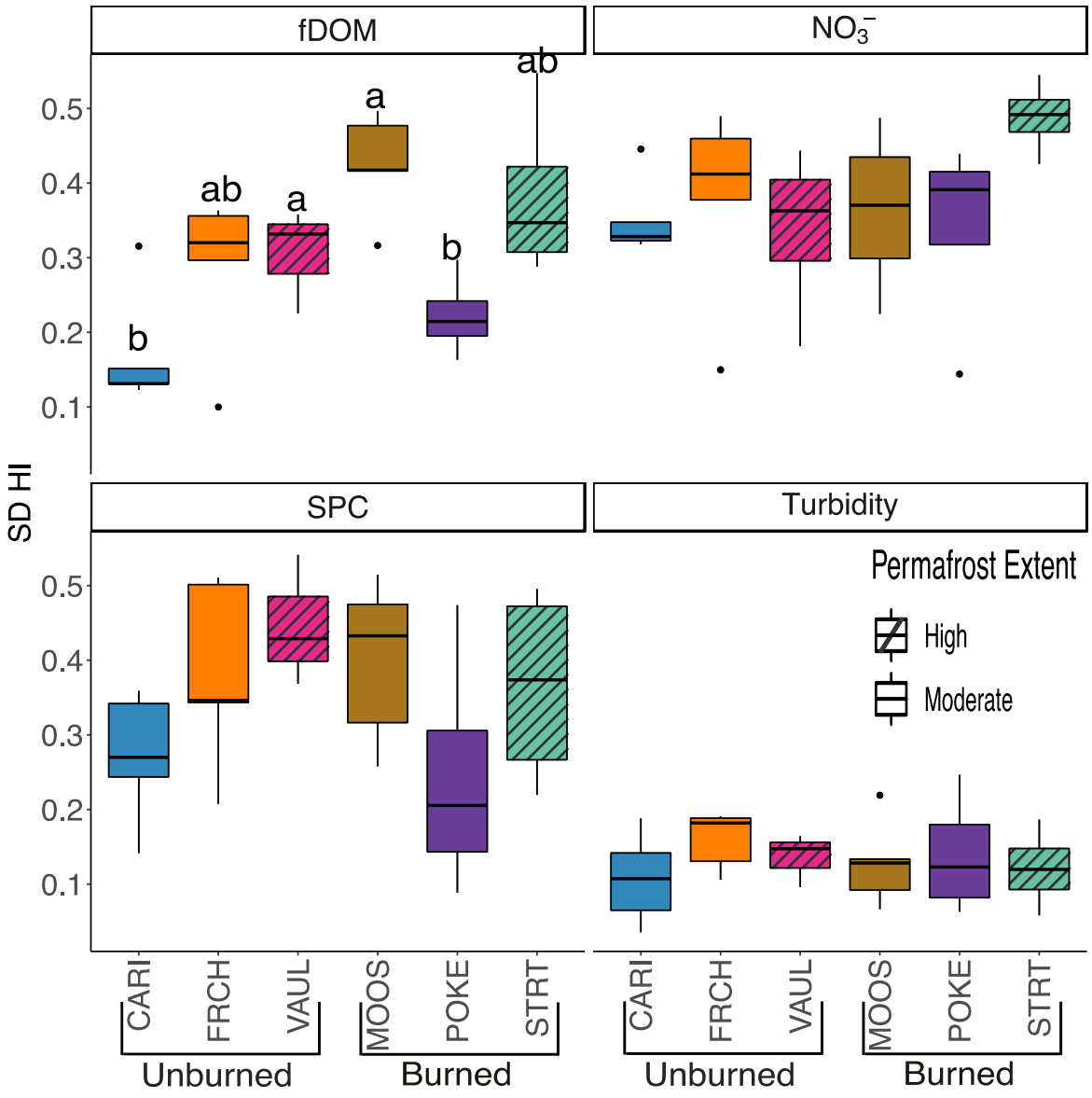


Figure 35. Standard deviation of HI across all storms for fDOM (A), NO_3^- (B), SPC (C), and turbidity (D). Symbology as defined in Fig. 33.

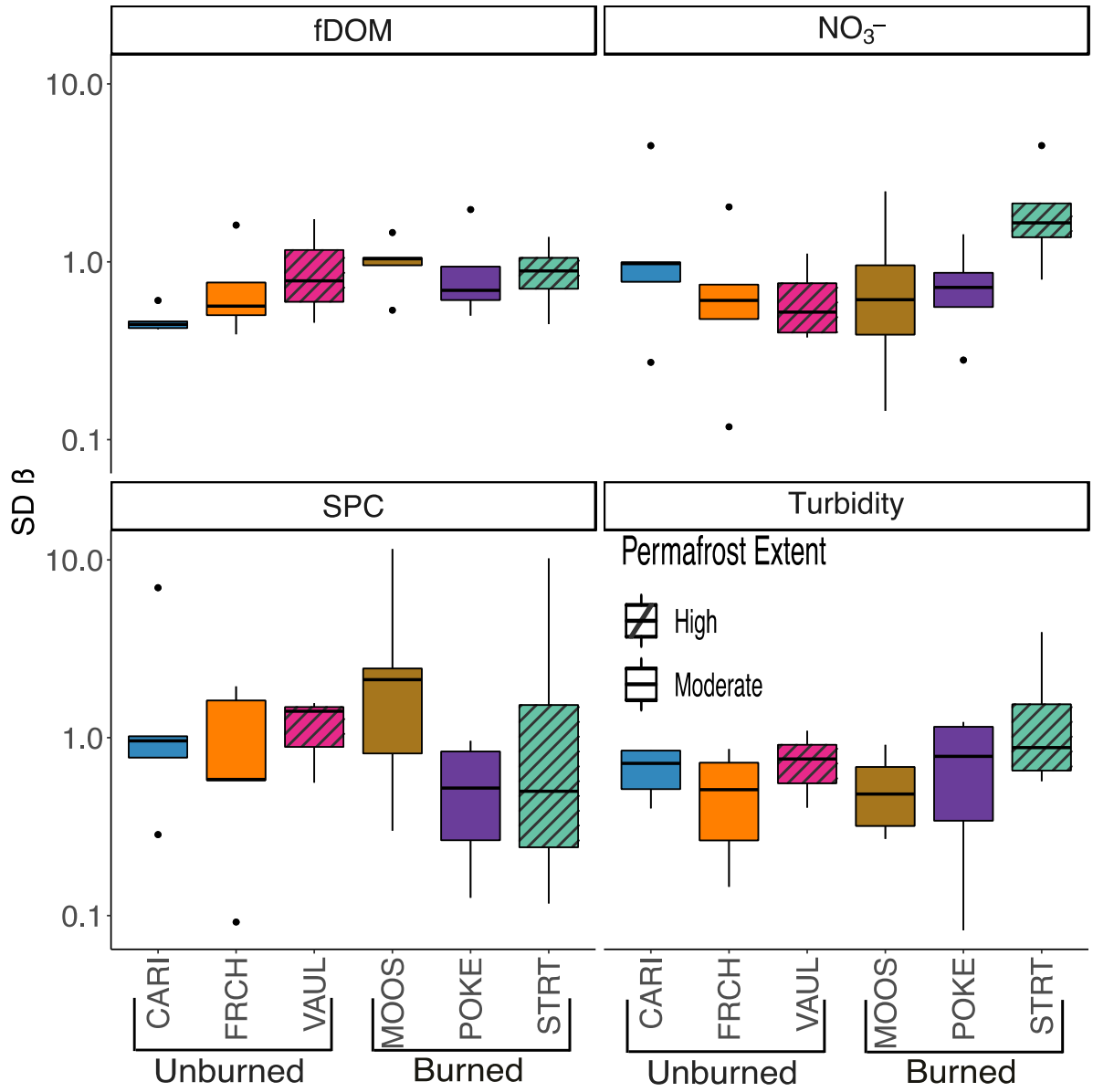


Figure 36. Standard deviation of β across all storms for fDOM (A), NO_3^- (B), SPC (C), and turbidity (D). Symbology as defined in Fig. 33.

Contrasts in storm C-Q dynamics across gradients in topography and disturbance history

Concentration-discharge dynamics during storms varied with catchment slope, the fraction of the catchment that burned, and % deciduous cover (a proxy for permafrost extent). Variation across catchments in HI and β values for fDOM correlated with the slope of the catchment (Fig. 36a & c). A shift from positive to negative hysteresis with increasing catchment slope indicates a change from source-limitation in low-relief to transport-limitation in steeper catchments. The observed positive correlation of catchment slope with β-fDOM indicates greater flushing in steeper catchments (Fig. 36c). Stores of OM are likely heterogeneously distributed in steep catchments, such that exports of DOM depend on spatial patterns in hydrologic connectivity.

Catchment-level variation in storm C-Q dynamics of NO_3^- were explained by burn extent and deciduous vegetation cover (Fig. 38). Greater HI-NO_3^- in more extensively burned catchments indicated that fire causes greater source limitation of NO_3^- delivery to streams. This is counter to the hypothesis that decreased vegetation cover would result in increased N available for hydrologic export. Instead, source limitation of NO_3^- during storms in burned catchments might result if flowpaths traverse shallow soils due to hydrophobicity, reduced evapotranspiration, or decreased hydrologic storage (Murphy et al., 2018; Pimentel & Arheimer, 2021). Deciduous cover was positively correlated with β-NO_3^-, and catchments encompassed a shift from strong dilution to chemostatic behavior during storms with increasing deciduous cover (Fig. 38c). This pattern is consistent with increased stores of NO_3^- that are susceptible to hydrologic export in warmer, organic-poor soils. Further, temporal variation in β-NO_3^- was negatively correlated with deciduous cover (Fig. 38d). Strong contrasts in storm C-Q dynamics of NO_3^- across gradients of permafrost extent and vegetation cover indicate that storm dynamics could be used to characterize ecosystem state at catchment scales. Shifts in storm C-Q dynamics detected by long-term monitoring could indicate permafrost degradation and colonization by deciduous forests.

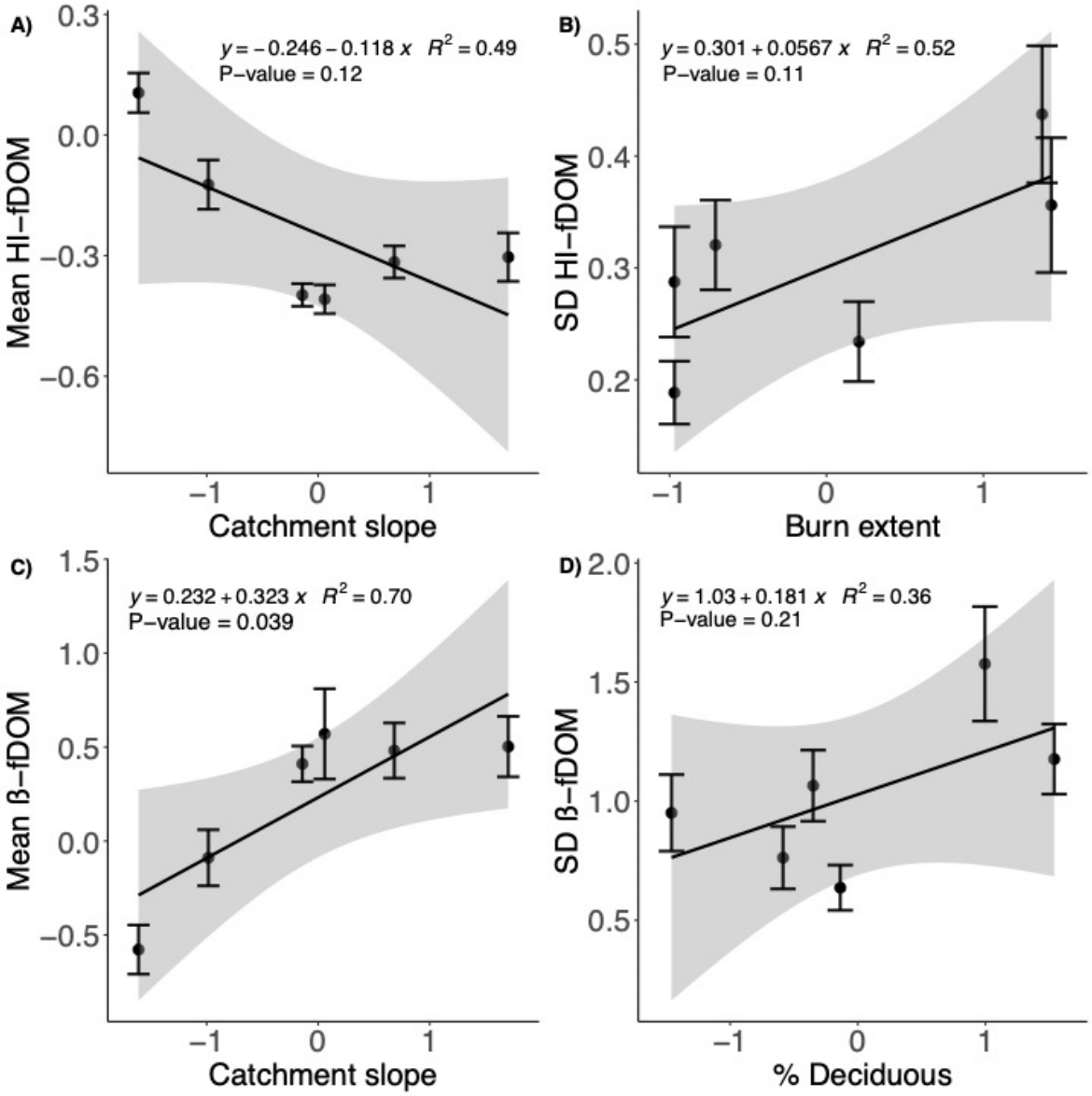


Figure 37. Catchment attributes explaining variation in concentration-discharge dynamics of fDOM summarized across all storms observed within each catchment across all study years. (A) mean HI-fDOM, (B) SD HI-fDOM, (C) mean β-fDOM, and (D) SD β-fDOM. Predictor variables reflect standardized values. Error bars represent standard error across all storms observed in each catchment. Shading represents 95% confidence band of the regression relationship.

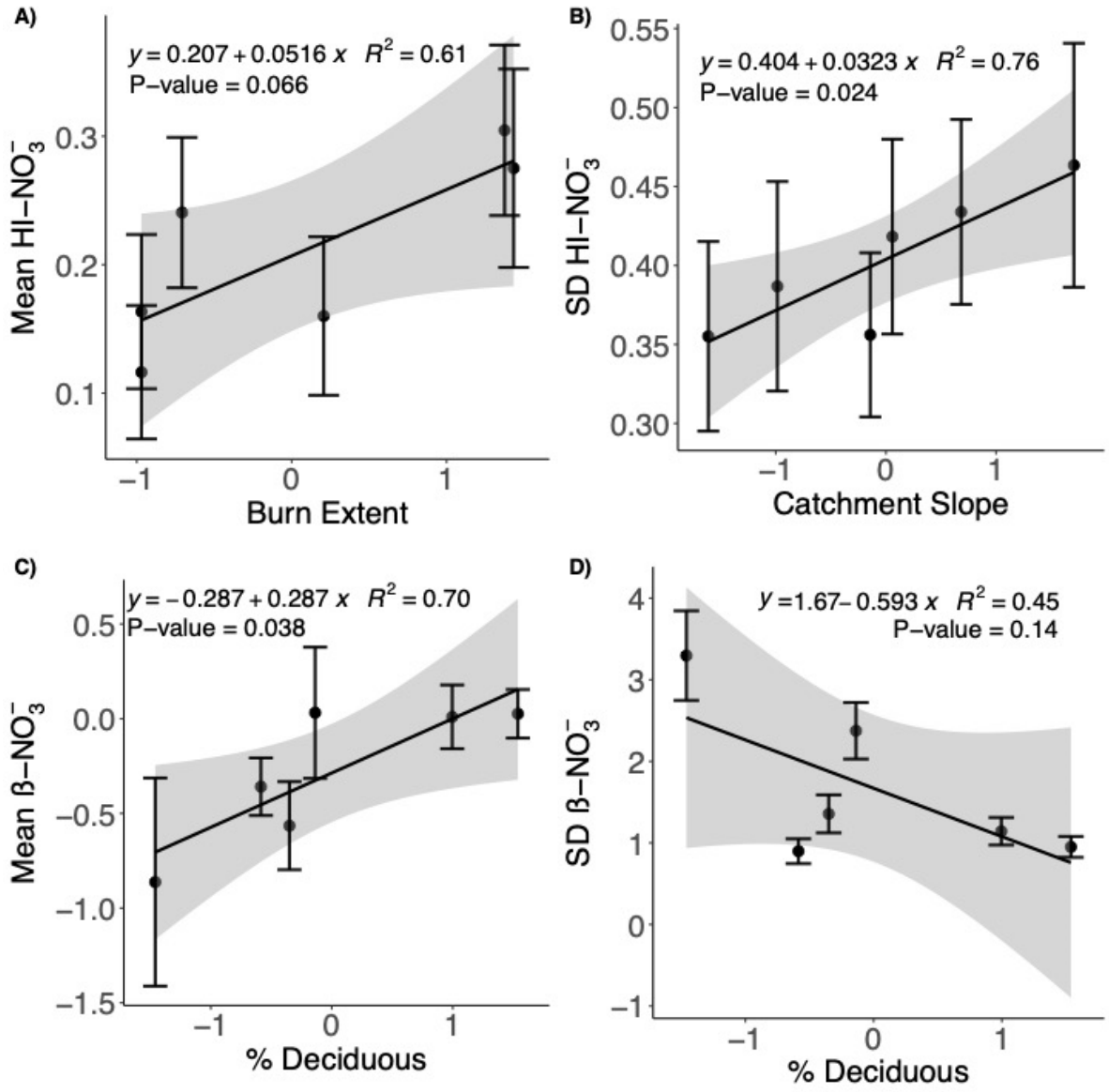


Figure 38. Catchment attributes explaining variation in concentration-discharge dynamics of NO_3^- summarized across all storms observed within each catchment across all study years. (A) mean HI-NO_3^-, (B) SD HI-NO_3^-, (C) mean β-NO_3^-, and (D) SD β-NO_3^-. Predictor variables reflect standardized values. Error bars represent standard error across all storms observed in each catchment. Shading represents 95% confidence band of the regression relationship.

Effects of weather conditions on storm C-Q dynamics

Effects of seasonality, storm precipitation, and antecedent precipitation on storm C-Q relationships were modest, with no linear models explaining greater than 35% of observed variation among storms within each catchment, and many explaining < 10% (Figs. 39 & 40). Few significant relationships between flushing dynamics and event size suggested significant contributions of groundwater to streamflow that are not influenced by short-term precipitation (Knapp et al., 2022).

Strongest effects of antecedent moisture occurred at the unburned, high-permafrost catchment (Vault), where precipitation had a significant positive effect on HI for fDOM and turbidity, and negative effects on HI for NO_3^- and SPC. Similar effects of precipitation on inorganic solutes also occurred at various timescales in other catchments (Figs. 39 & 40). These patterns likely occurred because increased water in the catchment activates more spatially distributed hydrologic flowpaths, yielding increasingly chemostatic dynamics for inorganic solutes as the source area expands. The opposite dynamic for fDOM and turbidity likely reflects larger stocks of these materials stored near the stream channel, or erosion of channel sediments. Additional negative effects of antecedent precipitation on β of NO_3^- and SPC at Vault Creek provide evidence of depletion of source pools by cumulative leaching, at least from the shallow soils intercepting stormflow in this high-permafrost catchment. The moderate-permafrost catchments also generated increased HI for SPC and/or NO_3^- later in the year, indicating increased source-limitation of material exports. This could also result from cumulative leaching losses during repeated storms.

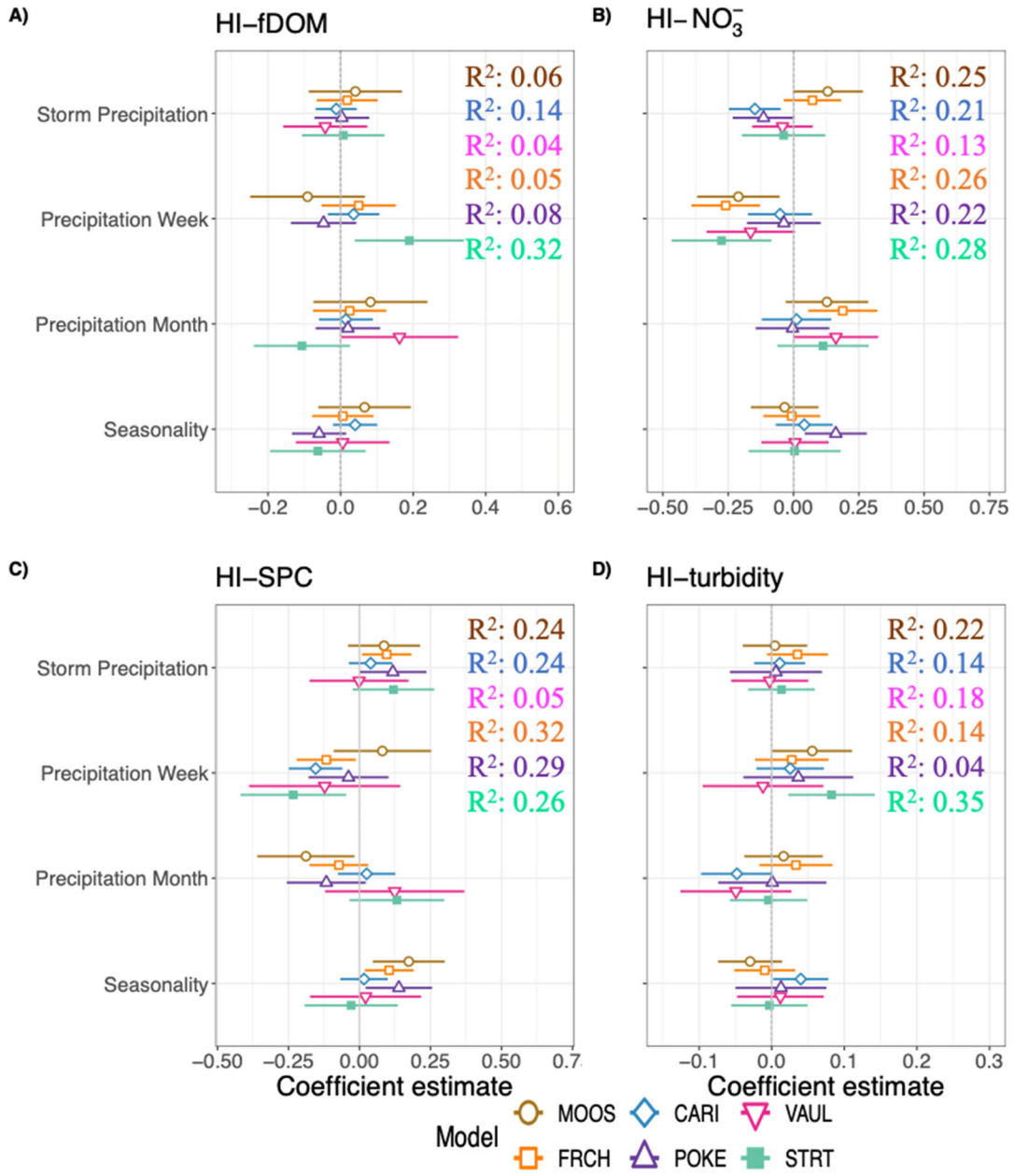


Figure 39. Standardized effects of storm size, antecedent precipitation, and seasonality on HI estimated by linear regression on all storms observed within each catchment across all study years. (A) fDOM, (B) NO_3^-, (C) SPC, and (D) turbidity. Error bars are bootstrapped 95% confidence intervals.

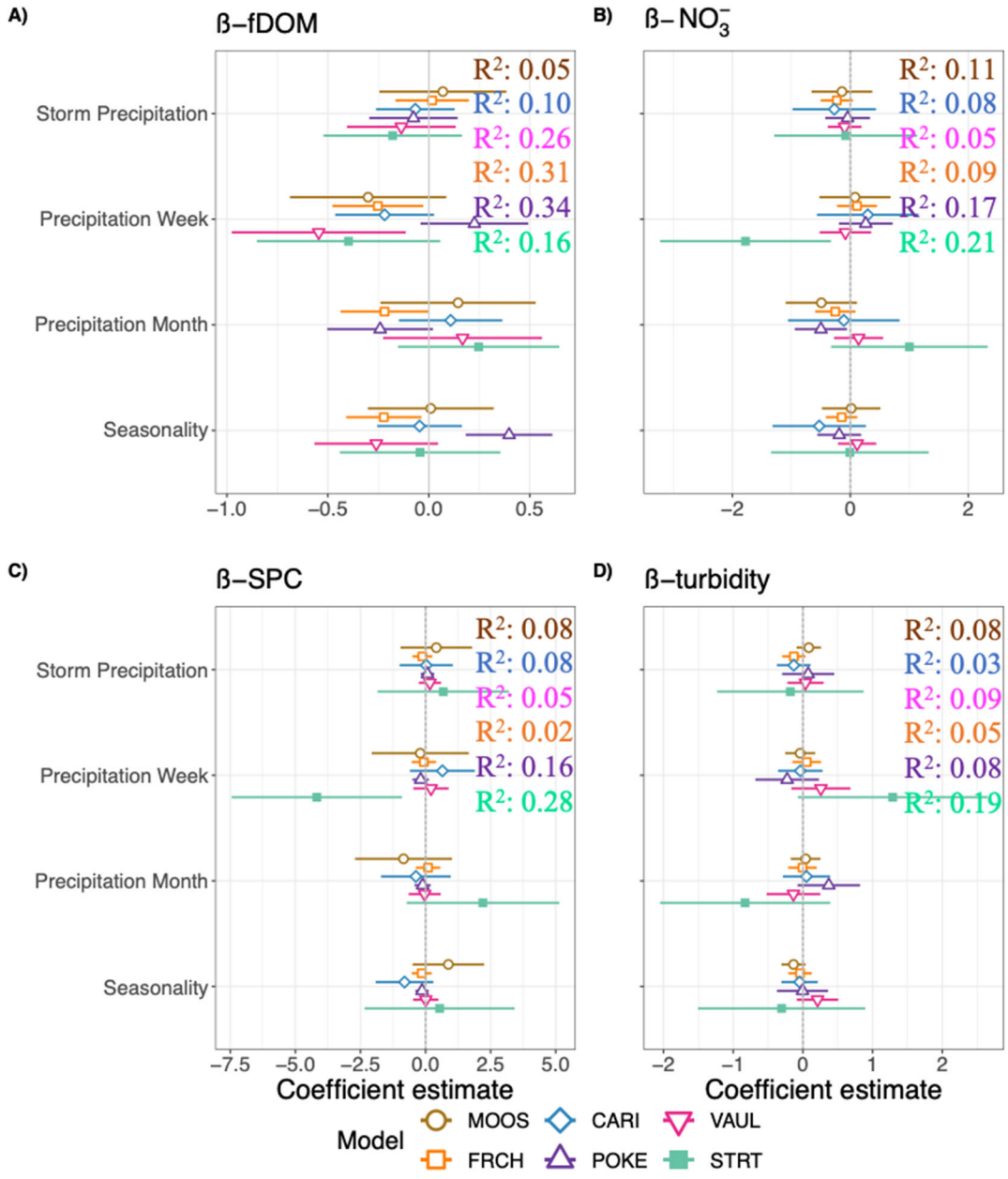


Figure 40. Standardized effects of storm size, antecedent precipitation, and seasonality on β estimated by linear regression on all storms observed within each catchment across all study years. (A) fDOM, (B) NO_3^-, (C) SPC, and (D) turbidity. Error bars are bootstrapped 95% confidence intervals.

9.3.4 Implications

- Concentration-discharge relationships during storms were dynamic, with characteristic patterns attributed to constituent and catchment attributes.
- Delivery of NO_3^- and SPC was typically source-limited in all catchments, but the source-limitation became stronger in more extensively burned catchments.
- Catchments with less extensive permafrost (using deciduous forest cover as a proxy) yielded more chemostatic dynamics of NO_3^-, consistent with the hypothesis of more rapid N cycling and leaching in permafrost-free soils.
- Dynamics of fDOM were related to catchment topography, and therefore assessments of ecosystem state from dynamics of organic matter must carefully control for topography.
- Antecedent hydrologic conditions and seasonality had little influence on storm-normalized C-Q dynamics.
- A strong imprint of catchment attributes on hydrology and biogeochemistry during storms and limited effects of storm to seasonal-scale variation in moisture conditions suggests that measuring C-Q dynamics during storms could contribute to characterizing ecosystem state of whole catchments. Long-term monitoring of storm C-Q dynamics could signal ecological state changes caused by fire and/or permafrost thaw.

9.4 Daily-scale variation in stream chemistry

9.4.1 Data analysis

We applied MARSS models to assess daily-scale variation in concentrations of fDOM and NO_3^-. The modeling approach was similar to that described in *Section 9.2.3*, with the following exceptions. Models represented a single state and each site*year was modeled separately. Response variables (fDOM and NO_3^- concentrations) were ln-transformed and mean centered. Predictor variables included stream GPP, water temperature, and precipitation in the preceding week (informed by findings described in *Sections 9.2.4* and *9.3.3*). Observation error was estimated by the model. To facilitate comparisons of model output across years, models included observations from a common time demarcated by time since peak flow on the Chena River, which was approximately mid-June to late Sept.

9.4.2 Results

Environmental covariates of mean daily fDOM and NO_3^- concentrations

MARSS models explained a large fraction of the variance in mean-centered, ln-transformed mean daily concentrations of fDOM and NO_3^-. Average pseudo-R^2 was 0.84 for fDOM (range: 0.42-0.99) and was typically lowest for Vault Creek. Pseudo-R^2 values were greater, on average for NO_3^-, with a mean of 0.91 (range: 0.75-0.99).

Covariate effects in MARSS models confirmed the strong role of precipitation in generating temporal patterns in stream chemistry. Cumulative weekly precipitation had a significant, positive effect on fDOM in most catchments and most years (Fig. 41). Precipitation had weakest effects on fDOM concentration in Vault Creek (unburned, high permafrost). Gross primary production had significant negative effects on fDOM concentration in some catchments and study years, though these effects were generally less common and weaker than effects of precipitation (Fig. 41). Primary production in streams is a potential source of DOM in streams, but a negative relationship between fDOM and GPP suggested a correlational, rather than causal relationship. Effects of water temperature on fDOM were not significant in most catchments and study years, further suggesting that biotic processes in streams (e.g., heterotrophic uptake of C) had little influence on daily-scale variation in fDOM concentration (Fig. 41). Thus, fDOM

dynamics observed in the stream are largely the result of hydrologic transport of DOM from the catchment to the stream.

Nitrate concentration was less strongly or consistently influenced by precipitation than fDOM. Cumulative weekly precipitation had small positive effects on NO_3^- concentration in the moderate-permafrost catchments, though these effects were sporadic across the study years (Fig. 42). In contrast, precipitation had negative effects on NO_3^- concentration in the unburned, high permafrost catchment (Vault) in some years (Fig. 42). Weaker effects of precipitation on NO_3^- than fDOM likely occur because groundwater provides a continuous supply of NO_3^- to streams. In the moderate-permafrost catchments, infiltration of stormwater into thawed soils could flush soil-derived NO_3^- to streams, whereas flowpaths activated by storms likely remain near the surface in the unburned, high-permafrost catchment, diluting the groundwater-supplied NO_3^- during storms.

Water temperature had a negative effect on NO_3^- concentration in the burned catchments during most study years (Fig. 42). Significant effects of temperature did not occur in streams draining the unburned catchments (Fig. 42). Water temperature varies in concert with air temperature. Warmer temperatures could promote biotic activity, including uptake by plants or denitrification in the catchment or stream. Instream uptake of N is unlikely a major influence on NO_3^- concentration because aquatic GPP was uncorrelated with NO_3^- concentration (Fig. 42).

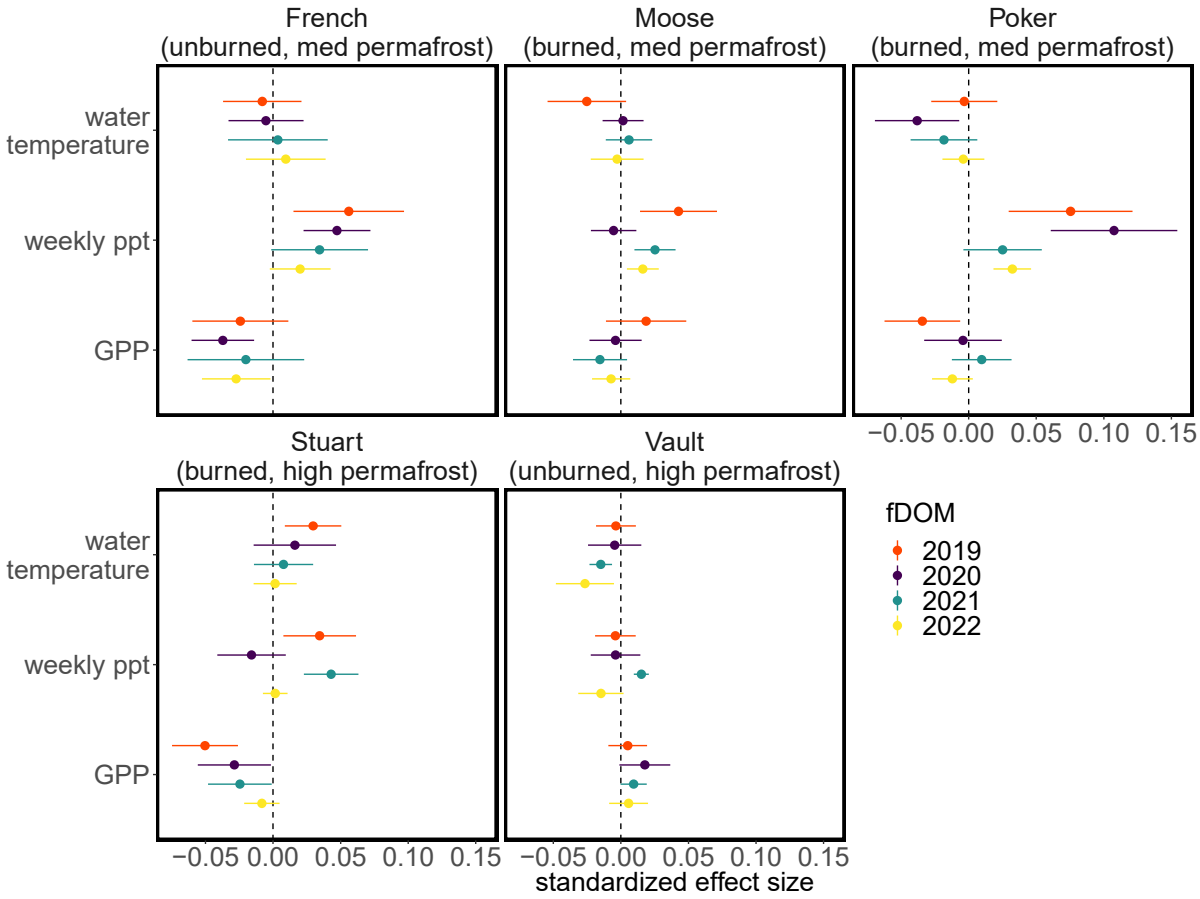


Figure 41. Standardized effects of covariates on mean daily fDOM concentration (ln-transformed) estimated by MARSS models. Points reflect standardized estimates and error bars are 95% confidence intervals.

Denitrification rates were unlikely different within burned and unburned stream-riparian corridors because the riparian zones did not burn. Instead, contrasts in N uptake by terrestrial vegetation in burned compared to unburned catchments might have contributed to the differential effects of temperature on NO_3^- dynamics in burned and unburned streams. Warmer conditions promote plant growth and rapidly regrowing deciduous trees and shrubs in burned catchments likely respond more strongly to temperature than the black spruce forests dominant in unburned catchments.

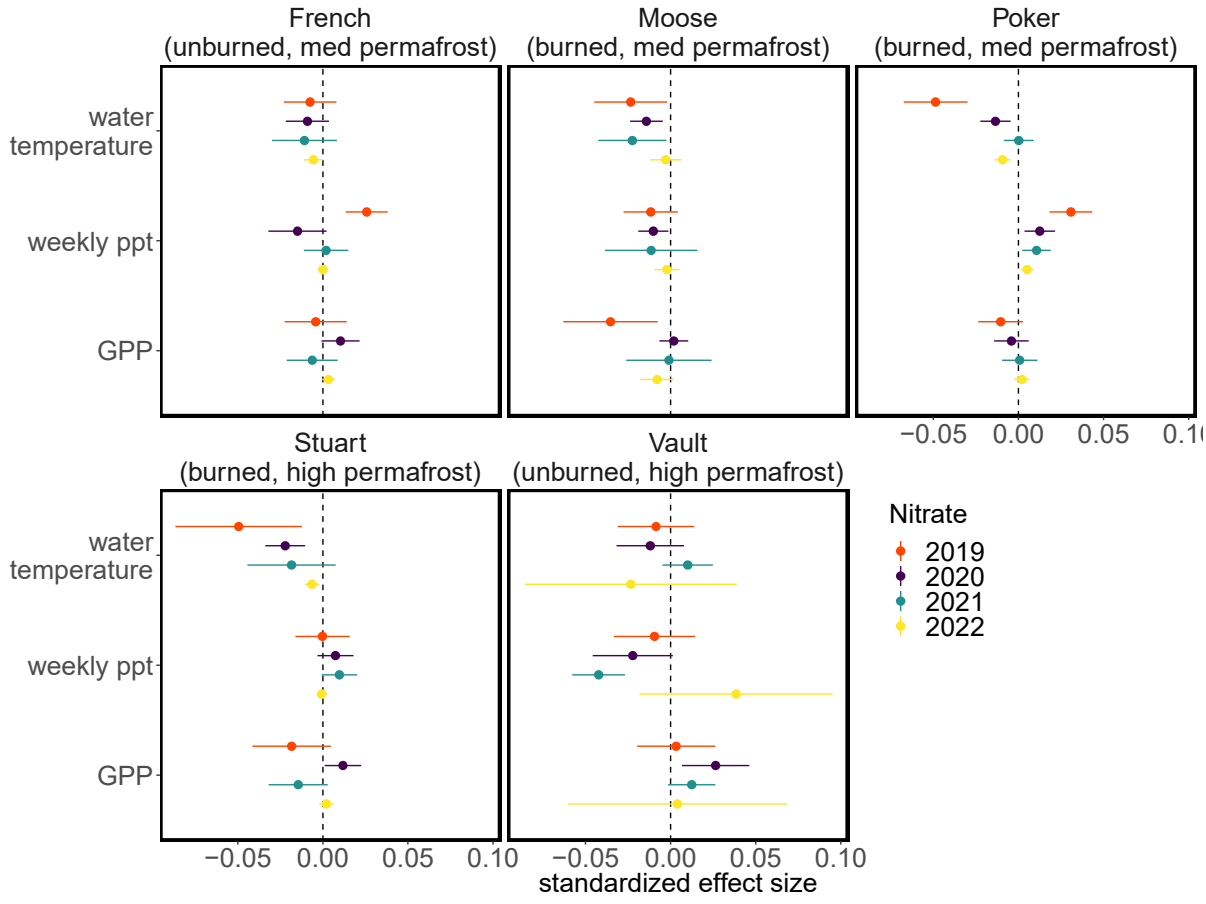


Figure 42. Standardized effects of covariates on mean daily NO_3^- concentration (ln-transformed) estimated by MARSS models. Points reflect standardized estimates and error bars are 95% confidence intervals.

Seasonal trends

We hypothesized that deepening of hydrologic flowpaths through catchments due to downward migration of the thaw front on a seasonal timescale would result in increased concentration of NO_3^- and decreased concentration of fDOM in streams. Dissolved organic matter originates from soil OM, which is abundant on the forest floor and in upper, organic soil horizons but sparse in mineral soils. Increased relative stores of NO_3^- are expected in mineral, compared to organic soils, where lower C:N promotes nitrification and inorganic N escapes uptake by shallow-rooted plants and microbial denitrifiers (Harms & Jones 2012). Contrary to the season-long increase in NO_3^- concentration previously observed in one north-facing, headwater catchment (*Section 9.2.4*), we found no evidence of increasing NO_3^- concentration at a seasonal timescale in the focal catchments (i.e., non-significant bias terms in MARSS models; Fig. 43). There were two instances, both in 2022, of significant though modest seasonal declines in NO_3^- concentration (Fig. 43). We detected no significant seasonal-scale changes in fDOM concentration (Fig. 43).

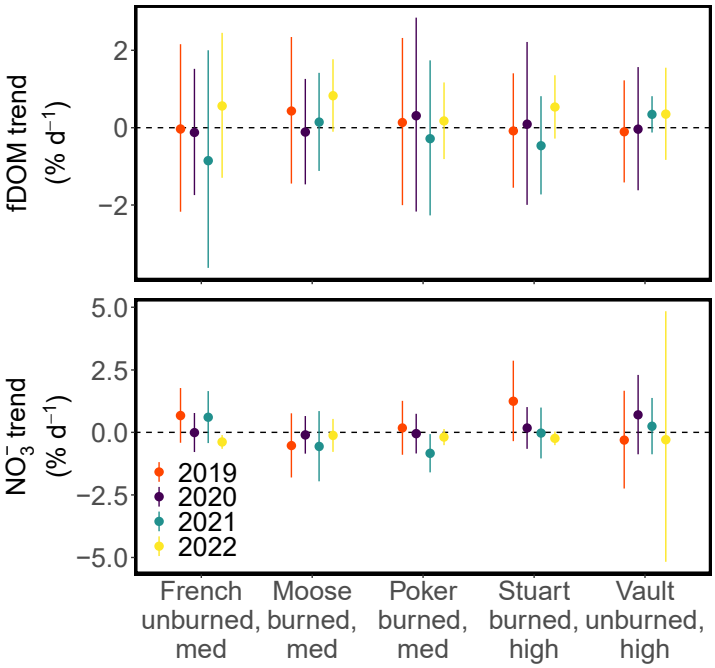


Figure 43. Seasonal trends in fDOM (top) and NO_3^- concentrations for each catchment and year of the study. Points indicate standardized estimates and error bars are 95% confidence intervals.

Solute chemistry is likely strongly influenced by the sources of water supplying streamflow and these sources are temporally variable (*Section 8.1*, Fig. 17). Whereas increased thaw depth promotes deeper drainage, the downward seasonal shift in flowpath depth is punctuated by storms that rapidly route water via shallow flowpaths. Further, deep groundwater likely supplies a significant fraction of baseflow (Fig. 18) and NO_3^- (Figs. 20 & 21) in these catchments characterized by spatially discontinuous permafrost. Therefore, mixing of water sources draining catchments likely limits the appearance of seasonal trends in solute concentration. Specifically, a constant supply of NO_3^- in groundwater at baseflow and punctuated inputs of stormwater that is rich in DOM and of variable NO_3^- concentration reduce the likelihood of directional seasonal trends in solute concentrations.

Stability of solute concentrations

We measured the tendency for daily mean fDOM and NO_3^- concentrations to return to the mean value using the MARSS approach (B in Eq. 10). This metric quantifies deviation from a random walk pattern and therefore captures one dimension of stability, characterized by the solute concentration. On average, fDOM tended to revert to the mean more strongly than NO_3^- (Fig. 44). However, there were no significant differences in mean reversion across catchments or years for fDOM (Fig. 44). These patterns are perhaps a reflection of the large supplies of OM in the catchments. Reversion to mean NO_3^- concentration was significantly stronger in Moose Creek than in many other catchments in some years (Fig. 44). There were also significant

differences in stability of NO_3^- concentration across years within some catchments (Fig. 44). However, patterns in stability of NO_3^- concentration were heterogeneous among catchments and the drivers of the patterns remain unclear. Further monitoring could reveal whether stability varies due to the precipitation regime or due to catchment processes such as vegetation dynamics and rate of soil thaw.

9.4.3 Implications

- Daily time series yielded fewer contrasts between catchments varying in disturbance history than analyses on the storm scale.
- Analysis at the daily time scale confirmed the key role of precipitation in contributing to temporal variation in solute chemistry, particularly for fDOM.
- Daily-scale variation in solute chemistry was not strongly related to instream processes, and temporal patterns in solute concentrations can therefore be interpreted as signals emerging from catchments.
- N uptake by rapidly regrowing vegetation in burned catchments potentially explains negative effects of temperature on NO_3^- concentration in burned catchments.
- Seasonal trends are not a reliable indicator of catchment responses to disturbance due to heterogeneity introduced by storms.
- Explanations of stability in solute concentrations remain unclear. Additional monitoring could contribute to discerning how processes including precipitation regime, vegetation dynamics, and rate of soil thaw might influence stability of catchment biogeochemistry.

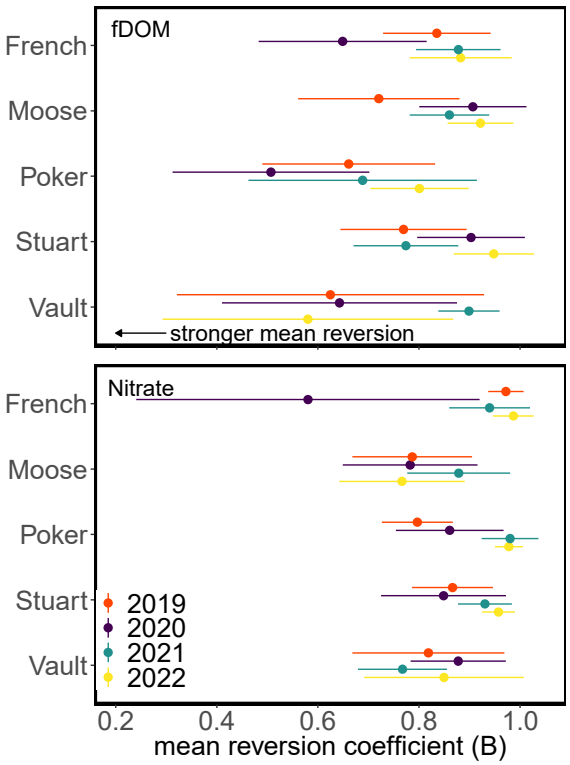


Figure 44. Rate of reversion of mean daily fDOM (top) and NO_3^- (bottom) concentration to the mean of the time series for each catchment and year. Points indicate estimates of the B coefficient from MARSS models and error bars are 95% confidence intervals. Smaller values indicate stronger mean reversion, whereas larger values indicate tendency toward a random walk pattern.

9.5 Multi-scale temporal variation in stream chemistry

9.5.1 Rationale

Temporal patterns can be characterized by oscillations over a range of frequencies that occur at particular instances in time or at recurring intervals. We proposed that disturbance of catchments by fire or permafrost thaw would yield associated signals in time series of stream chemistry. Here we analyze time series in the frequency domain to detect temporal patterns at multiple time scales. We then assess similarity of patterns across catchments with similar fire history and spatial extent of permafrost to locate particular frequencies that might contain signals of disturbance.

9.5.2 Data analysis

We conducted analyses in the frequency domain to characterize temporal variation in stream

chemistry from sub-daily to approximately monthly timescales. We applied wavelet analyses following the approaches detailed in *Section 9.2.3*. Briefly, we used the wavelet transform to decompose 15-min resolution time series of water chemistry (i.e., SPC, turbidity, fDOM and NO_3^- concentrations, and abs254) and water temperature into power spectra across a range of frequencies (0.25–32 d). We determined significance of wavelet power by comparing to an autoregressive ("red noise") spectrum. We then analyzed wavelet coherence to quantify correlations between water chemistry and stream discharge across a range of frequencies. Relationships between chemistry and discharge quantify the role of catchment hydrology in transporting biogeochemical signals to streams. Wavelet analysis requires continuous data and we therefore imputed missing values within time series using a Kalman filter or linear interpolation function in the *imputeTS* package for R (Moritz & Bartz-Beielstein, 2017).

9.5.3 Results

Wavelet decomposition— Wavelet decomposition of stream chemistry identified storms as the dominant source of temporal variation across all sites and in all years of the study. Storms that were large enough to increase stream discharge initiated oscillations in most chemical constituents at frequencies of several days to approximately two weeks that were significantly greater than expected for autoregressive time series. Whereas all measured chemical attributes responded to storms in most years of the study, water temperature was unresponsive to storms. Select figures are included within the description of results below to highlight salient patterns. The full set of figures resulting from wavelet transforms and coherence analysis are included in Appendix 2.

Concentration of DOM (indexed by fDOM and abs254) and turbidity responded most strongly to storms compared to other measured constituents. Significant oscillations in DOM occurred more often (i.e., in response to more storms), oscillations persisted longer, and significant oscillations occurred over a wider range of frequencies compared to other measured constituents. Organic matter dynamics were least responsive to storms in 2021 and 2022 (Figs. 44-45, Appendix 2), which encompassed a later onset of summer rains with fewer storms and low cumulative precipitation, respectively (Figs. 9 & 10). Under these relatively drier conditions, oscillations were less frequent and maximum wavelet power (squared amplitude of oscillations) was approximately 2-3 times less, on average, compared to 2019 and 2020. Temporal patterns in dissolved organic matter were most consistently responsive to storms across years at Vault Creek, the unburned, high-permafrost catchment.

Nitrate and SPC also oscillated significantly in response to storms. With the exception of Vault Creek, significant oscillations in NO_3^- concentration were more frequent and tended to occur at longer frequencies in the wetter years than in the drier years (Figs. 46 & 47). At Vault Creek (high permafrost, unburned), temporal dynamics of NO_3^- concentration were more consistently responsive to storms, which typically generated oscillations at frequencies of days to weeks. Specific conductivity oscillated significantly only following storms and was least temporally dynamic in 2022.

Storms influence stream chemistry by increasing hydrologic connectivity with the catchment and changing the depths of dominant flowpaths contributing water, solutes, and particles to streams. Significant oscillations in water chemistry associated with storms confirmed the importance of storms as time periods when terrestrial signals are apparent in streams. However, wavelet analysis revealed contrasts among catchments in responsiveness to storms. The unburned, high-permafrost catchment was most reliably responsive to storms, generating significant oscillations at a storm scale even in the drier years when other catchments were less

responsive to storms. Rapid responses to storms regardless of antecedent hydrologic conditions likely results from high spatial extent of permafrost, which contributes to shallow flowpaths and rapid runoff through organic-rich soils. High variance in solute concentrations at a storm scale might therefore provide a signal of ecosystems characterized by high spatial extent of permafrost and thick organic soils.

Additional oscillations in fDOM and NO_3^- occurred independently of storms at a diurnal frequency. Diurnal oscillations in fDOM were most consistent in the burned catchments (Figs. 45 & 46, Appendix 2). Significant diurnal oscillations in NO_3^- concentration occurred during at least one of the study years in all streams except Vault Creek (unburned, high permafrost), though diurnal oscillations in NO_3^- were more sporadic than diurnal variation in fDOM (Figs. 47 & 48, Appendix 2). Diurnal variation in solute concentrations can occur due to uptake of solutes by primary producers in the stream or catchment or to vertical fluctuation in the water table caused by evapotranspiration. Lack of diurnal oscillations in SPC or turbidity suggests that evapotranspiration is less likely the cause, though fDOM concentrations might be particularly sensitive to small changes in the vertical position of the water table in burned catchments where organic soils are thin and heterogeneously distributed.

Finally, significant oscillations also occurred at a frequency of weeks to one month though these appeared sporadically among constituents, sites, and years. Longer-frequency oscillations in DOM occurred at all sites, were typically associated with storms or snowmelt, and were more common in the wetter years (Figs. 45 & 46, Appendix 2). Oscillations in NO_3^- concentration occurring at frequencies greater than two weeks occurred sporadically among all sites and years, but were most commonly associated with the snowmelt period (Figs. 47 & 48, Appendix 2). Oscillations at these longer frequencies are associated with seasonal patterns, including contrasts in dynamics between earlier (snowmelt-influenced) and later (storm-influenced) phases of the open-water period and non-linear “step changes” associated with precipitation in August that elevated NO_3^- concentration through autumn.

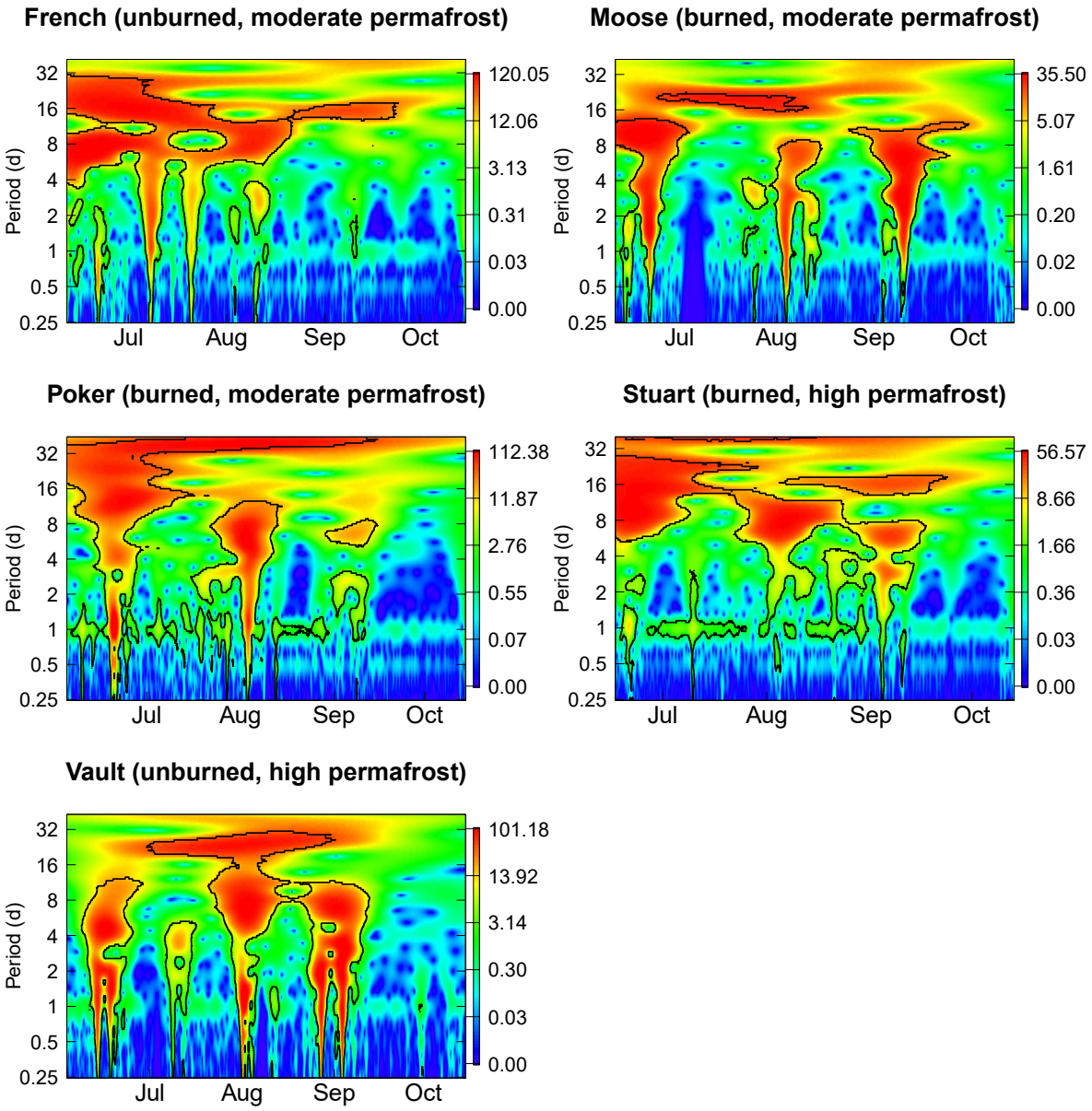


Figure 45. Wavelet decomposition of fDOM concentration in 2020. The vertical axis displays frequencies and the scale bar indicates wavelet power (square of amplitude), with warmer colors associated with greater variation. Black outlines designate variation that is significantly greater ($\alpha = 0.05$) than expected from an autoregressive time series. The shaded cone indicates values with little data support. Note that the temporal extent varies slightly across the streams. 2020 was the wettest year of the study with 333 mm precipitation during Jun-Aug.

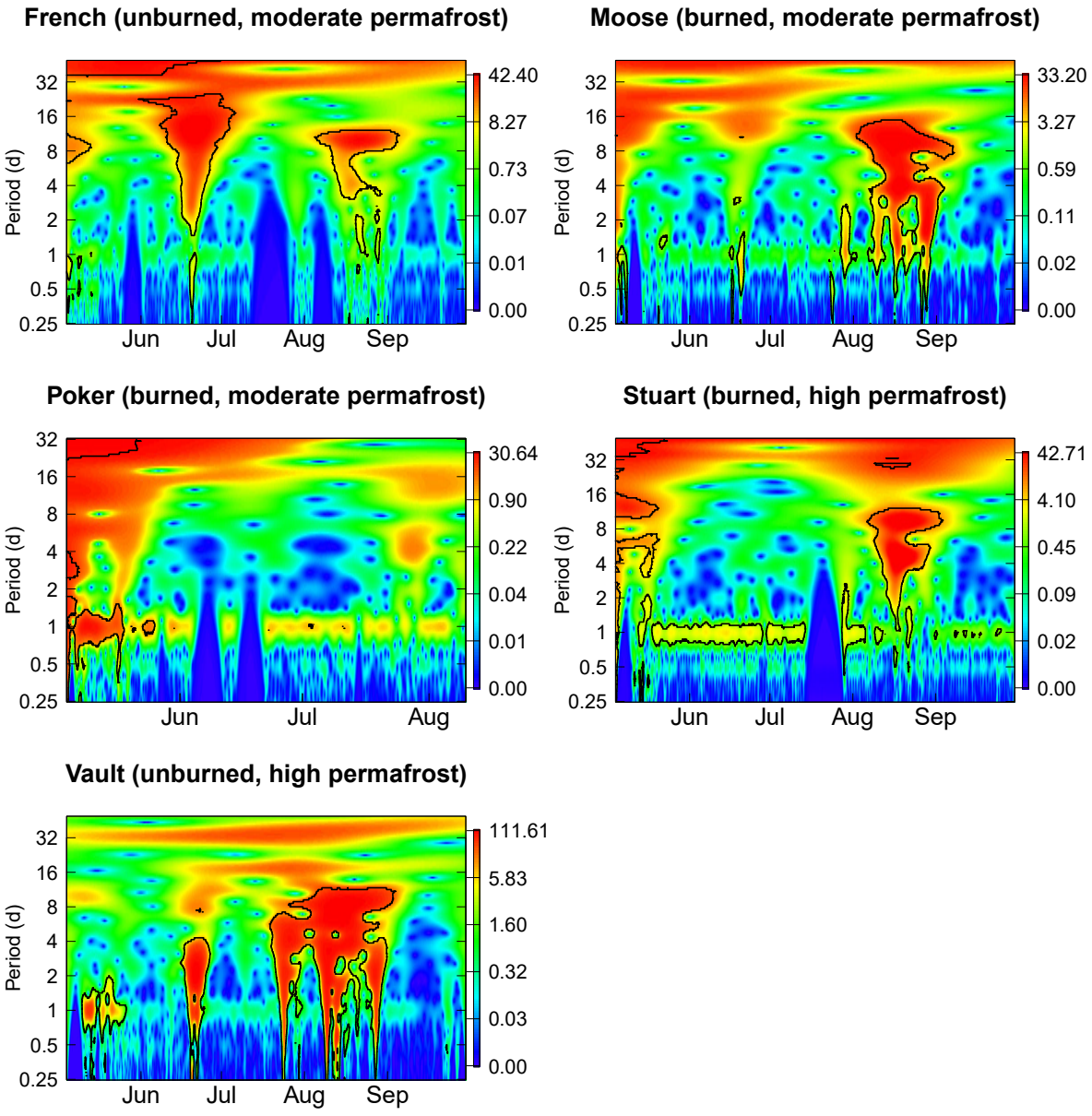


Figure 46. Wavelet decomposition of fDOM concentration in 2022. Symbology is the same as described for Fig. 45. Total precipitation for Jun-Aug was 125 mm in 2022, less than the long-term mean. Note fewer instances of significant variation at the weekly timescale and lower power (smaller amplitude of oscillations) compared to 2020 (Fig. 45) for all sites other than Vault.

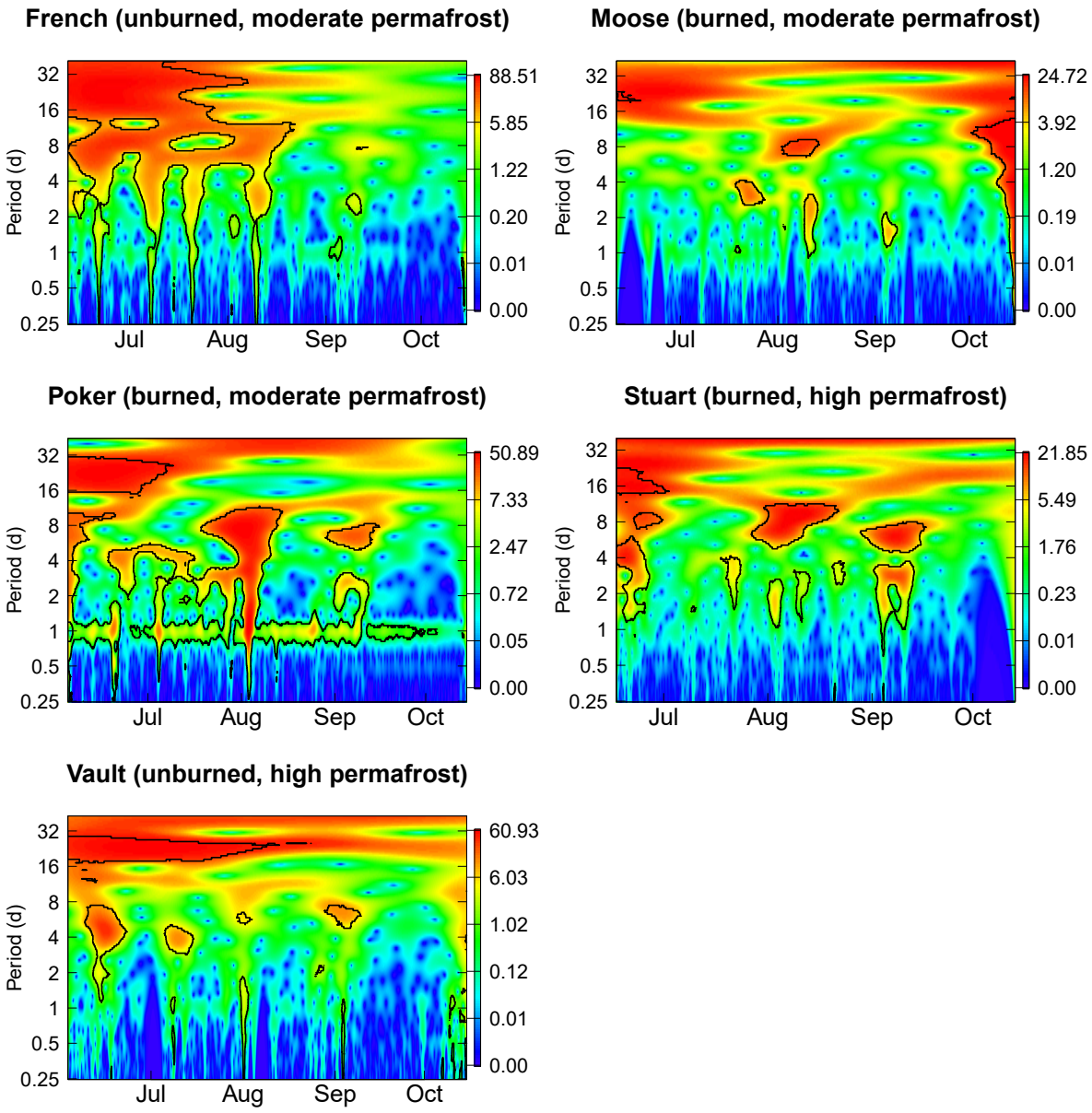


Figure 47. Wavelet decomposition of NO_3^- concentration in 2020, the wettest monitoring period during the study. Symbology as described for Fig. 45.

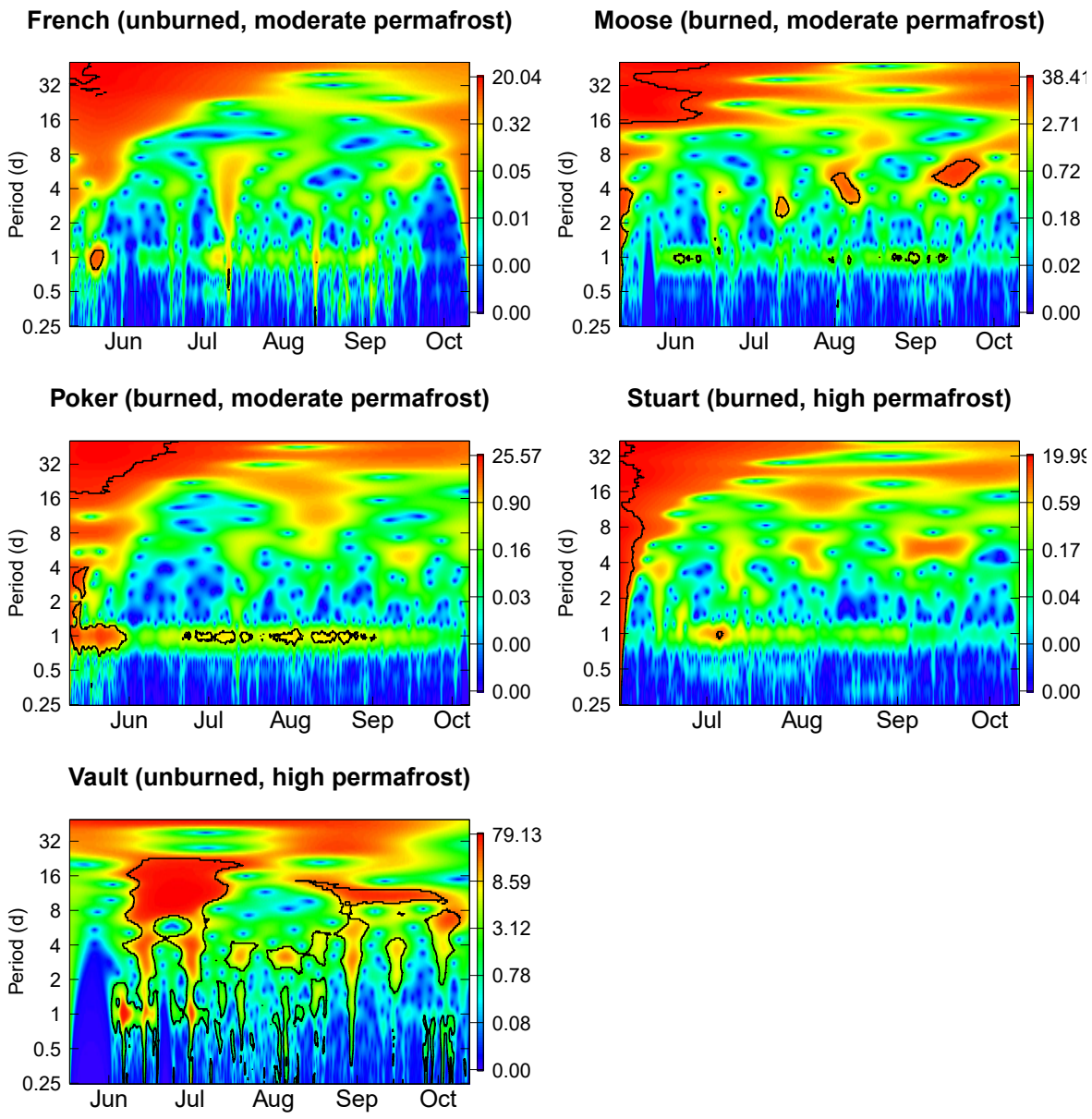


Figure 48. Wavelet decomposition of NO_3^- concentration in 2022, the driest monitoring period during the study. Symbology is the same as described for Fig. 45. Compared to wetter years, (e.g., 2020; Fig. 47) there were fewer instances of significant oscillations initiated by storms in drier years.

Wavelet coherence— Dissolved organic matter was strongly coherent with discharge at frequencies from sub-daily to weeks or longer and coherence was typically initiated by storms (Fig. 49, Appendix 2). The relative timing of peaks in discharge and fDOM contrasted between catchments (Fig. 49, Appendix 2). In the catchments with highest fDOM concentration at baseflow (Vault and Moose), discharge and fDOM were coherent but out-of-phase at frequencies of days to weeks, whereas discharge led fDOM in all other catchments. The out-of-phase dynamics of discharge and fDOM at Vault and Moose reflect the initial dilution of fDOM by storm flowpaths of low residence time in the catchment, followed by flushing of fDOM by stormwaters of sufficient residence time to leach OM.

Storms similarly initiated coherence between discharge and the aromatic components of DOM measured by abs254 (Appendix 2). The aromatic components of DOM measured by abs254 were typically in phase with discharge, oscillating either simultaneously with discharge or following discharge, and less often leading discharge (Appendix 2). These dynamics indicate rapid delivery of DOM to streams via shallow flowpaths. Oscillations of DOM that led discharge were most common in the driest year (2022) and indicate flushing of disproportionately DOM-rich water from soils to streams on the rising limb of storms. This likely reflects accumulation of DOM in catchments during dry periods. Unlike fDOM, the dynamics of abs254 did not differ among catchments. Coherence with discharge at a diurnal frequency also occurred for both abs254 and fDOM (Fig. 49, Appendix 2), but these dynamics were more sporadic than at the longer frequencies and are unlikely to provide reliable indicators of catchment dynamics.

Coherence of NO_3^- and discharge was initiated by storms and typically occurred at frequencies of days to weeks, as well as at frequencies of weeks to a month (Fig. 50). However, coherence of NO_3^- and discharge was more sporadic than for DOM and was heterogeneous among catchments and across years. Coherence at frequencies of days to a week associated with storms was typically out-of-phase, indicating initial dilution of NO_3^- concentration by stormflows, though in-phase coherence occurred for a smaller number of storms in some catchments (Fig. 50). These patterns are consistent with activation of shallow flowpaths during storms that traverse NO_3^--poor, shallow soils and dilute the groundwater-derived NO_3^- that supplies baseflow.

Coherence between discharge and NO_3^- also occurred at frequencies of weeks to a month (Fig. 50), longer than the direct influence of storms. Coherence at these longer frequencies coincided with a rapid, non-linear increase ("step-change") in NO_3^- concentration (Figs. 7 & 50). This step-change was strongest and most consistent among years at Poker (burned, moderate-permafrost draining rocky uplands), but also occurred in some years at French, Moose, and Stuart, but never at Vault (unburned, high-permafrost). We hypothesized that intense precipitation occurring in August or later contributes to rapid thaw of permafrost and abrupt rerouting of hydrologic flowpaths that deliver more NO_3^- to streams (Douglas et al., 2020; Webster et al., 2022). In-phase coherence of NO_3^- and discharge at a timing and frequency consistent with the step-change in NO_3^- concentration confirms a hydrologic component of the mechanism driving the late-season increase in NO_3^- concentration. Co-monitoring of stream chemistry, soil moisture/groundwater table, and thaw dynamics (e.g., using methods from geophysics) could be applied to test the hypothesized mechanism underlying non-linear changes in biogeochemistry of boreal ecosystems likely undergoing permafrost thaw.

SPC and turbidity were consistently coherent with discharge during storms (Appendix 3). SPC and discharge were always out-of-phase, indicating dilution of SPC by increased flows. In contrast, turbidity varied in-phase with discharge, resulting from delivery of sediment, or

resuspension of channel substrate, by storm flows. Patterns of coherence between discharge and SPC or turbidity were consistent across catchments and thus are not effective for discerning how disturbance influences catchment biogeochemistry.

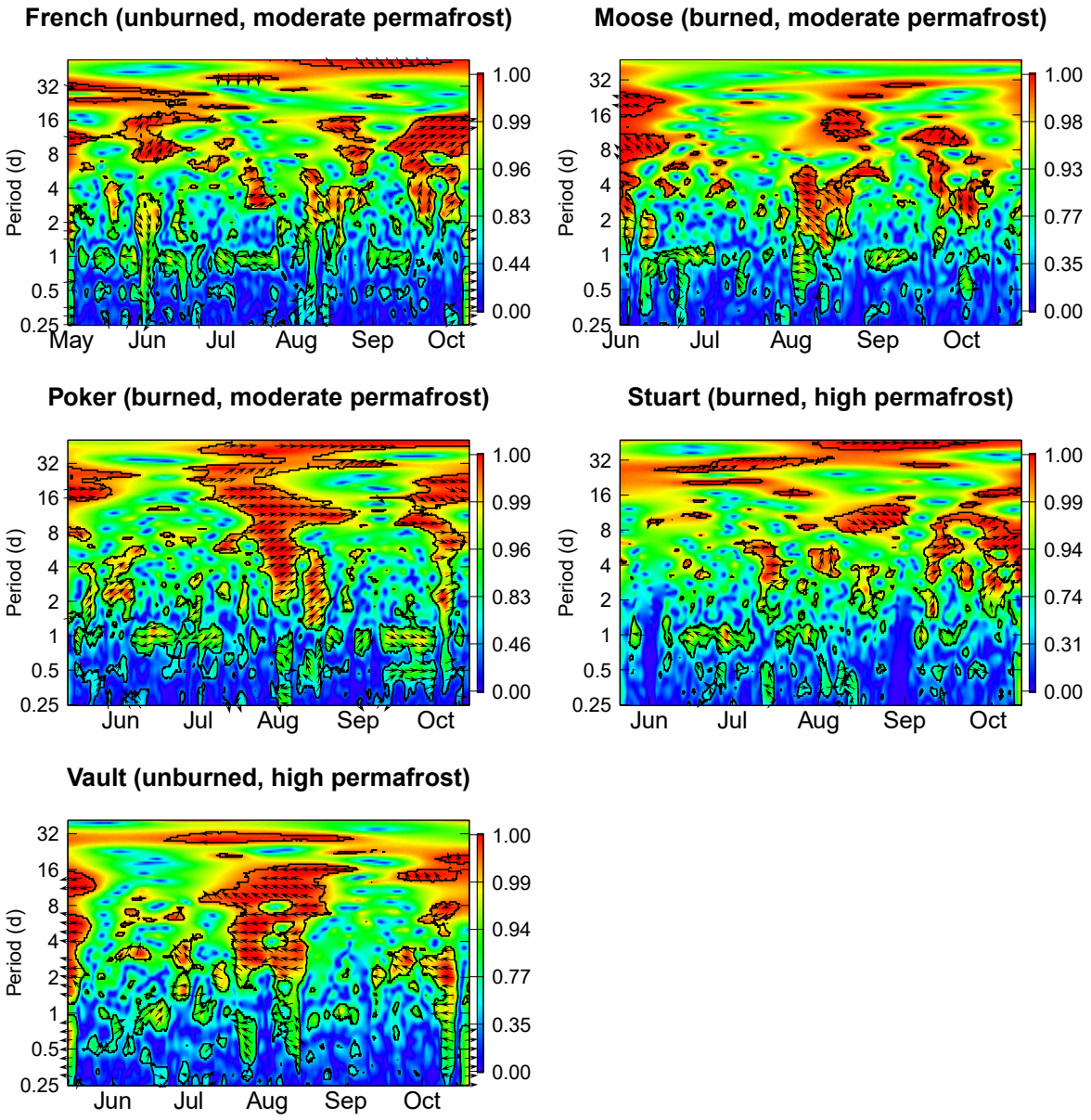


Figure 49. Wavelet coherence of fDOM concentration and discharge in 2019. Scale bar indicates coherence, with greater coherence depicted by warmer colors. Black outlines indicate times and frequencies when coherence is significantly greater than expected from an autoregressive time series. Arrows indicate the phase match when coherence is significant: → = in phase; ← = out of phase; ↖ = out of phase, fDOM following discharge; ↙ = out of phase, fDOM leading; ↗ = in phase, fDOM leading; ↘ = in phase, fDOM following. Note that the temporal extent (x axis) varies slightly across the streams. Out-of-phase coherence of fDOM with discharge at daily to weekly frequencies in Vault and Moose compared to in-phase coherence in the other catchments.

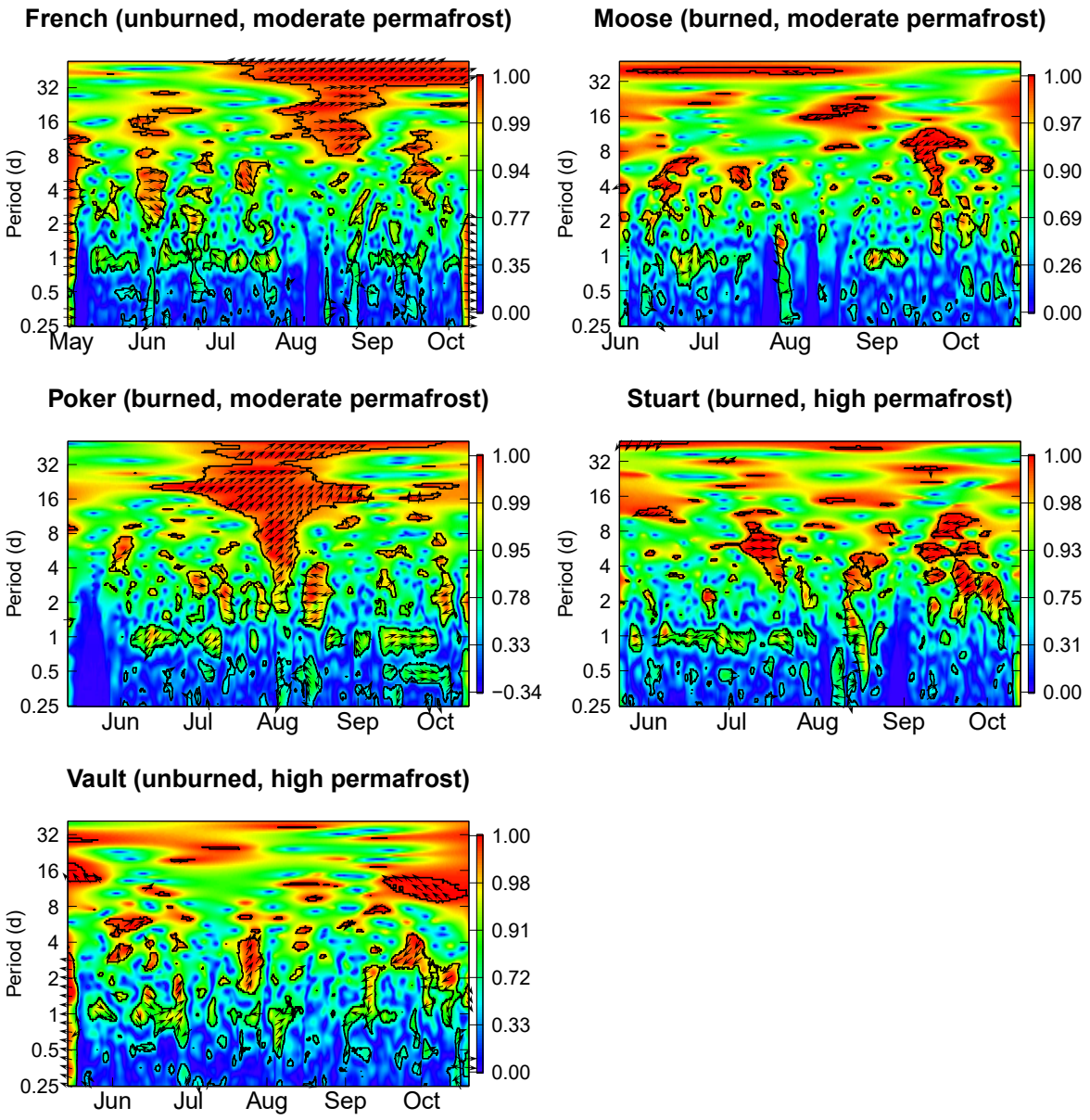


Figure 50. Wavelet coherence of NO_3^- concentration and discharge in 2019. Scale bar indicates coherence, with greater coherence depicted by warmer colors. Black outlines indicate times and frequencies when coherence is significantly greater than expected from an autoregressive time series. Arrows indicate the phase match when coherence is significant: → = in phase; ← = out of phase; ↖ = out of phase, NO_3^- following discharge; ↙ = out of phase, NO_3^- leading; ↗ = in phase, NO_3^- leading; ↘ = in phase, NO_3^- following. Note that the temporal extent (x axis) varies slightly across the streams. Significant, in-phase coherence at multi-week to month frequencies was associated with an abrupt, non-linear increase in NO_3^- concentration in French and Poker Creeks.

9.5.4 Implications

- Wavelet transforms and wavelet coherence analysis confirmed delivery of catchment biogeochemical signals to streams primarily during storms.
- An abrupt, non-linear increase in NO_3^- concentration generated oscillations that occurred in-phase with discharge, underscoring the role of catchment hydrology in generating or transporting this signal.
- Stream chemistry was most consistently responsive to storms in the unburned, high-permafrost catchment. High relative temporal variance in solute concentrations therefore provides a signal of intact permafrost and thick organic soils.
- Diel oscillations in fDOM concentration were most consistent in the burned catchments. Rapid oscillations of fDOM likely result from thin organic soils that are heterogeneously distributed and these oscillations are therefore expected to dampen as OM reaccumulates in the forest floor. Long-term monitoring of diel oscillations could therefore track whether an organic layer re-establishes following fire.

9.6 Decadal-scale effects of fire history on stream solute chemistry

9.6.1 Rationale

We hypothesized that fire imparts biogeochemical signals that are hydrologically transported from catchments to streams and that these signals persist beyond the duration of the disturbance, tracking recovery or loss of resilience. Reduced uptake of nutrients by vegetation, increased rates of mineralization in warmer soils, and changes in C:nutrient ratios of soils and vegetation following fire cause increased availability of inorganic N and phosphorus (P) in soils of many forested ecosystems (DeLuca & Sala, 2006; Dove et al., 2020; Treseder et al., 2004). Streams in turn contain elevated concentrations of nutrients following fire, including N (typically as NO_3^-) and P, though the duration of these signals varies (Bayley et al., 1992; Burd et al., 2018; Rhoades et al., 2019; Rust et al., 2019). In contrast, combustion of OM and slow regrowth of vegetation limits supply of DOM to streams. Decreased DOC concentration often occurs in the years following fire in lakes and streams of relatively C-rich ecosystems (Betts & Jones, 2009; Evans et al., 2016; Lydersen et al., 2014; Zolkos et al., 2022).

In regions with permafrost, fire could additionally influence catchment biogeochemistry by thawing permafrost (Brown et al., 2015; Gibson et al., 2018), deepening flowpaths to bypass organic soils. Because frozen ground impedes infiltration, loss of permafrost or deepening active layer promote drainage through deeper soils (Walvoord & Striegl, 2007). Mineral soils contain greater relative stores of inorganic ions from weathering products but smaller stocks of organic matter than surface soils (Barker et al., 2014; Kokelj & Burn, 2005). Low spatial extent of permafrost or deepening active layer in the catchment therefore correlates with diminished concentration of DOC in streams and increased concentrations of inorganic solutes (Harms et al. 2016, Webster et al., 2022).

We used a space-for-time approach to test hypothesized mechanisms linking fire to biogeochemical signals in streams. Using a synoptic survey, we observed stream chemistry across gradients of fire history and fire extent in catchments representative of Interior Alaska. We applied regression models to estimate effects of hypothesized processes influencing stream chemistry.

9.6.2 Methods

Sample collection and analysis— We measured solute concentrations in streams using a synoptic sampling campaign that included 76 catchments of varying burn extent and history, distributed

across Interior Alaska (Fig. 51). Spatial surveys included largely road-accessible streams that drained catchments lacking significant human land use. Streams drained forests developed on spatially discontinuous permafrost. The catchments spanned a gradient in fire history from unburned in the past 80 y to fires that occurred 1–79 y before sampling.

Stream water was collected during summer baseflow in July of 2018 and 2019. Each stream was represented by a single date in analyses. Duplicate water samples were collected from the thalweg of each stream, filtered (0.45 or 0.7 μm) at the time of collection, and stored in HDPE bottles. Samples were stored on ice and preserved by freezing (major anions and cations, total dissolved P) or acidification and refrigeration (total dissolved N [TDN], DOC) upon return to the laboratory, within 10 h of collection.

Stream water was analyzed for concentrations of major anions and cations, TDP, NH_4^+, DOC, and total dissolved N. Samples were analyzed in duplicate, except for NH_4^+. Nitrate (limit of quantitation [LOQ]: 0.02 μM, chloride (LOQ: 0.29 μM), and sulfate (LOQ: 0.02 μM) were measured by ion chromatography (ICS-2100 with AS-11 columns, Thermo Scientific). Calcium (LOQ: 1.29 μM), potassium (LOQ: 0.06 μM) and ammonium (LOQ: 0.22 μM) were analyzed on the same instrument with CS-16 columns. Total dissolved P (LOQ: 0.05 μM) was measured colorimetrically on a Smartchem autoanalyzer using the molybdate method following acid-persulfate digestion. Dissolved organic C (LOQ = 0.10 mg/L) and TDN (LOQ = 0.02 mg/L) were measured by combustion followed by non-dispersive infrared gas analysis and chemiluminescence, respectively, on a Shimadzu TOC-L. For all analytes, values less than the lowest concentration calibrant were set to the mid-point of zero and the LOQ.

Data analysis— We characterized physical and ecological attributes of each catchment, including topography, vegetation, fire history, and permafrost extent. Topographic data were extracted from a 2-arc second (approximately 60 m) digital elevation model (US Geological Survey National Elevation Dataset; https://www.usgs.gov/publications/national-elevation-dataset) and used to delineate contributing areas upstream of each stream sampling point in ArcMap 10. Total area (km^2) and mean slope (degrees) were estimated for each catchment.

Fire perimeters for years 1940–2019 were obtained from the Alaska Wildland Fire Information Map Series (Alaska Interagency Coordination Center, https://fire.ak.blm.gov). Data from 2018 and 2019 were adjusted to include only fires that occurred prior to stream sampling. Fires that burned before 1987 include only those >1000 acres whereas fires included in the dataset after 1987 burned >100 acres. Fire history for each catchment was characterized as the percent catchment area burned and time since fire for the largest and most recent burns since 1940, as well as cumulative burn area.

We also estimated catchment-scale vegetation cover and permafrost extent based on remote sensing and imagery analysis at a 30-m resolution. We characterized vegetation cover within each catchment using the normalized-differenced vegetation index (NDVI) extracted from Landsat imagery. Spatial extent of near-surface permafrost (within 1 m of the ground surface) was modeled from climate, imagery, and topography (Pastick et al., 2015).

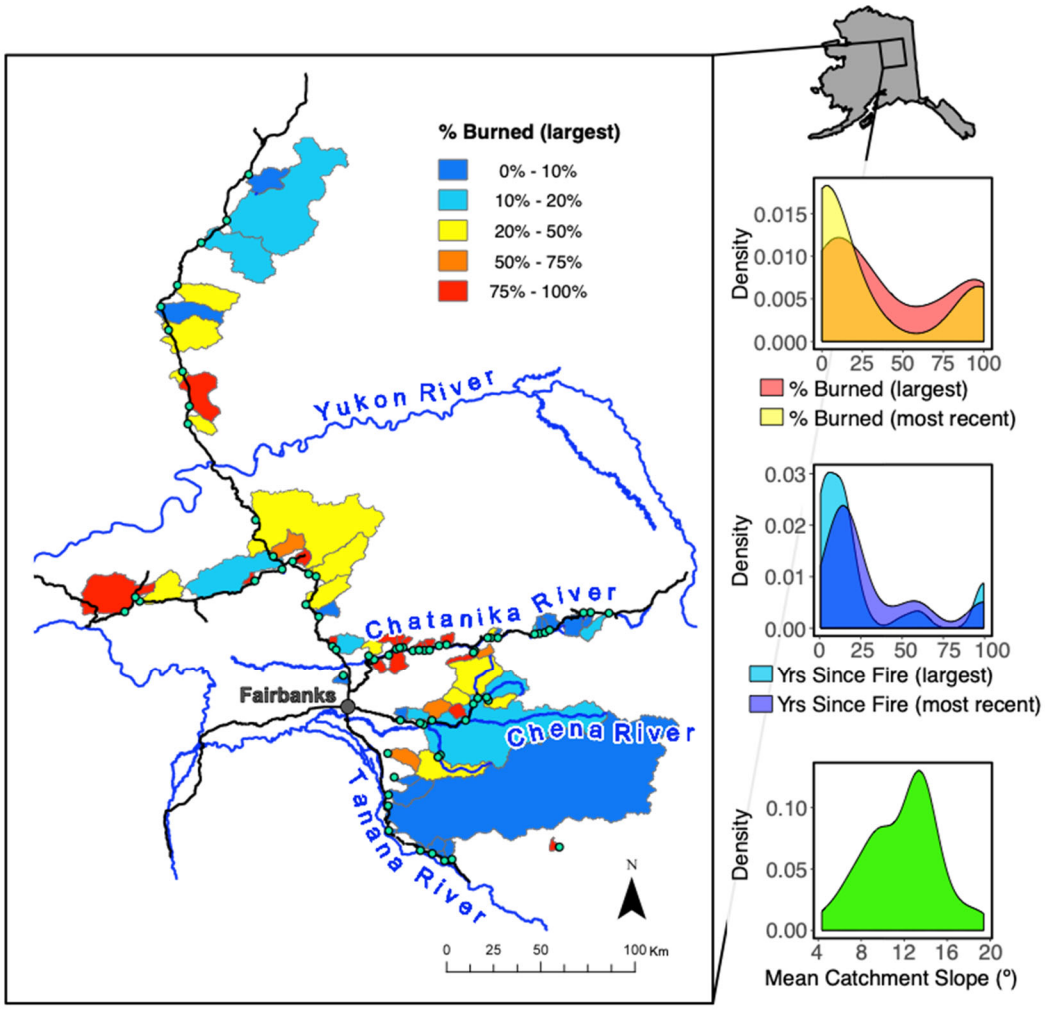


Figure 51. A synoptic survey of streams in Interior Alaska included variation in catchment slope, permafrost, and burn history. Catchments on the map are shaded according to the percent of the catchment burned in the largest fire within the catchment boundary occurring since ~1940. Histograms depict areal extent and time since largest and most recent fires within each catchment, and the mean catchment slope.

We applied multiple regression to assess predictors of solute concentrations in streams. Candidate predictor variables included mean catchment slope, years since fire, NDVI, spatial extent of near-surface permafrost, and percent catchment area burned. Predictor variables other than years since fire were centered and standardized, such that coefficients can be interpreted as the change in ln-solute concentration per 1 SD change in the predictor. Descriptors of time since burn and area burned were considered for the most recent fire, the largest fire, and cumulative area burned in each watershed in separate models. For catchments that had not burned in the period of record, years since fire was set to 100 years. We compared AIC values for each of the three models to select the most parsimonious model with greatest data support. We considered models within 2 AIC units equivalent, and for most constituents, the model including extent and time since the largest fire was better supported by the data or was equivalent to one of the other models. The model including cumulative burn area was best supported for TDP, but the model including descriptors of the largest fire differed by only 2.55 AIC units, so to facilitate

comparison of effects with other constituents, we report on models including descriptors of the largest fire for all constituents.

Using the fitted regression models, we estimated fluvial fluxes of C and nutrients across a gradient in burn extent. First, we used the fitted regression models to predict solute concentrations at quartiles of burn extent in each catchment. We then applied the discharge-catchment area relationship for n=11 gauged streams (gauging records from this SERDP study and from the USGS discharge monitoring program [www.waterdata.usgs.gov]) to estimate baseflow for all streams during the study period in July. Specific yield of each solute at baseflow was then calculated as the product of discharge and predicted concentration, normalized for catchment area. Parametric confidence intervals on estimates of yield were propagated from uncertainty in the discharge-area and multiple regression models.

9.6.3 Results

Catchment-level predictors of stream solute chemistry— Multiple regression models including time since the largest fire, percent of the catchment burned in the largest fire, median NDVI, modeled extent of shallow permafrost, and mean catchment slope explained broad-scale variation in C, N, and P concentrations across boreal catchments of Interior Alaska (Fig. 52). Catchment slope was strongly negatively correlated with concentrations of DOC, TDP, and NH_4^+ and positively correlated with NO_3^- (Fig. 53). This confirms previous findings in the region and elsewhere, and likely results from greater accumulation and leaching of DOM and retention of NO_3^- in catchments of low relief (e.g., Creed et al., 2008; Harms et al., 2016). Thus, controlling for catchment slope is a key consideration when comparing potential effects of disturbance across catchments.

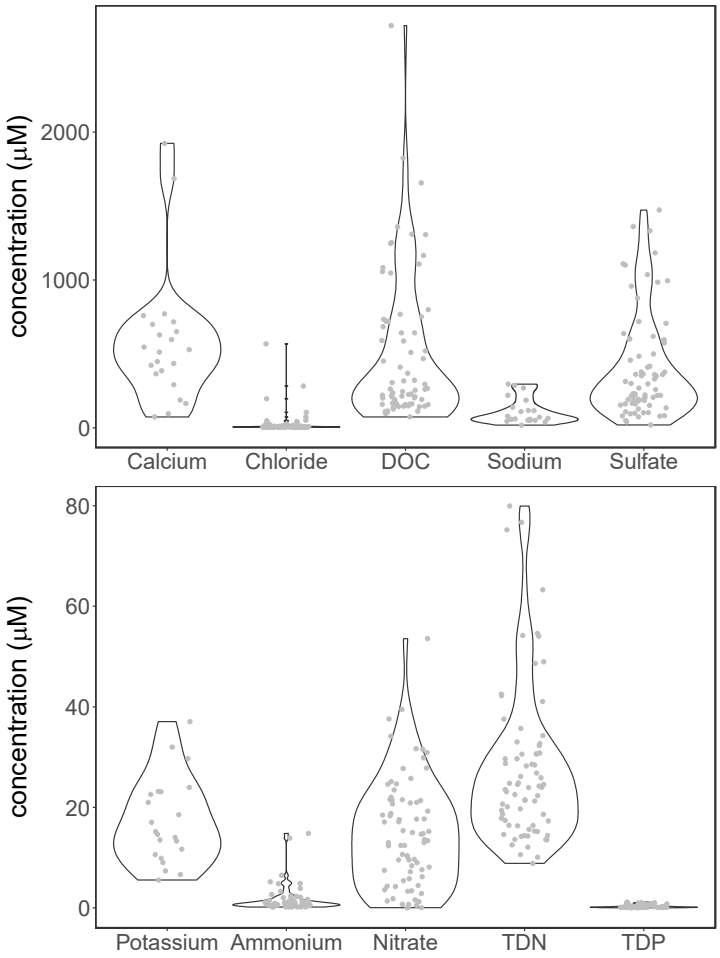


Figure 52. Observed solute concentrations in streams of Interior Alaska during baseflow. Top: DOC and conservative ions. Bottom: Nutrient concentrations. Black outlines depict density distributions and gray points show observations.

Modeled extent of shallow permafrost had a significant negative effect on concentrations of inorganic N in streams (Fig. 53). Organic forms of N are expected to dominate the TDN pool in streams draining catchments where permafrost restricts hydrologic flowpaths to shallow, organic soil horizons. Organic soils are sources of organic N and foster removal of NO_3^- by denitrification (Harms &

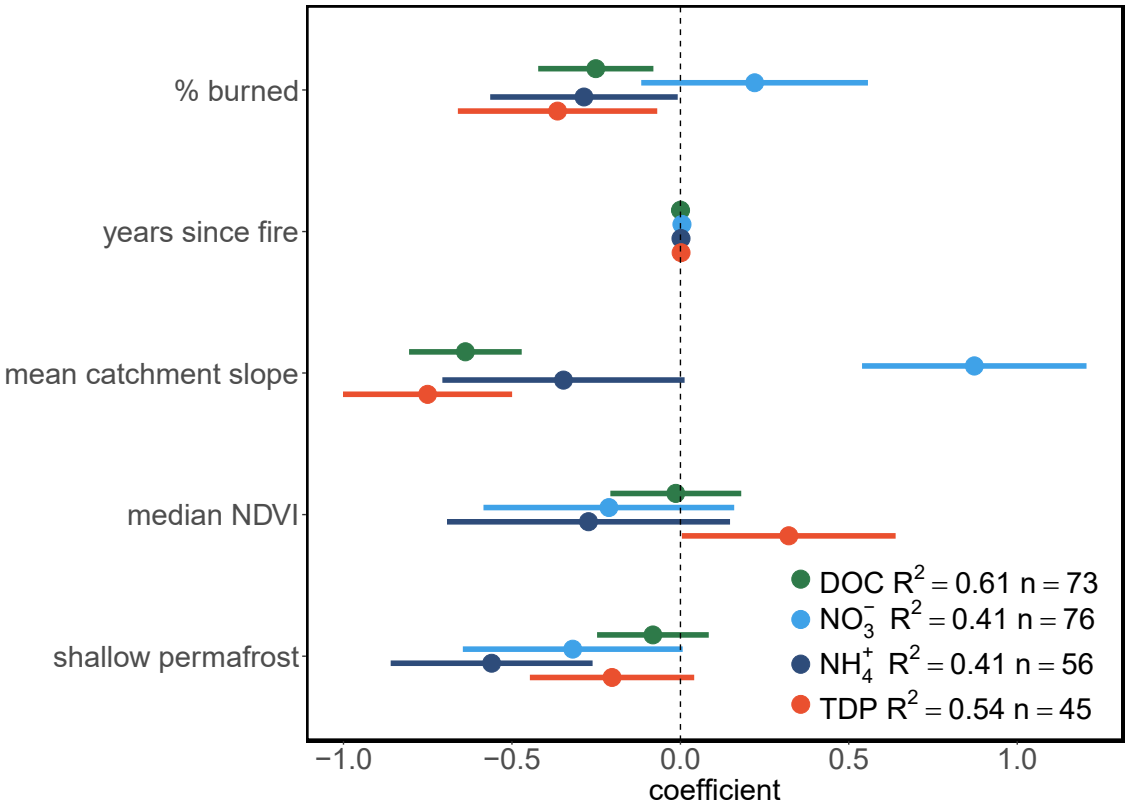


Figure 53. Coefficients from multiple regression models estimating effects of catchment attributes on ln-transformed solute concentrations in streams. Except for years since fire, predictor variables were centered and standardized. Error bars represent bootstrapped 95% confidence intervals.

Jones 2012). A deeper active layer or permafrost-free soils allow infiltration and drainage through mineral soils and increased contributions of groundwater to streamflow (Fig. 18). Permafrost-free soils also foster more rapid rates of N mineralization and nitrification (Melvin et al. 2015).

Catchments with more productive vegetation (indexed by NDVI) had higher concentration of TDP in stream water (Fig. 53). Though N often limits primary production in boreal forests, P can also limit, co-limit, or secondarily limit production (Ellison et al., 2019; Yarie & Van Cleve, 2006). Thus, a positive correlation between NDVI and TDP in streams could occur if greater P availability also results in greater forest productivity.

Finally, the proportion of the catchment that burned had a significant negative effect on DOC, TDP, and NH_4^+ and a positive, though non-significant effect on NO_3^- concentration (Fig. 53). These effects illustrate the expected patterns if removal of organic matter by combustion and slow regrowth of vegetation constrains organic matter available for hydrologic uptake and limits biological retention of inorganic N. However, time since fire had no effect on any measured constituent, indicating that the observed effects of burn extent on stream chemistry can persist for a decade or more. Catchment attributes explained little of the observed variation in concentrations of the rock-derived solutes (e.g., chloride, calcium; $R^2 < 0.11$, data not shown). Concentrations of these solutes is expected to increase if thawing permafrost results in deepening of hydrologic flowpaths to encompass mineral soils. Therefore, we conclude that the effects of

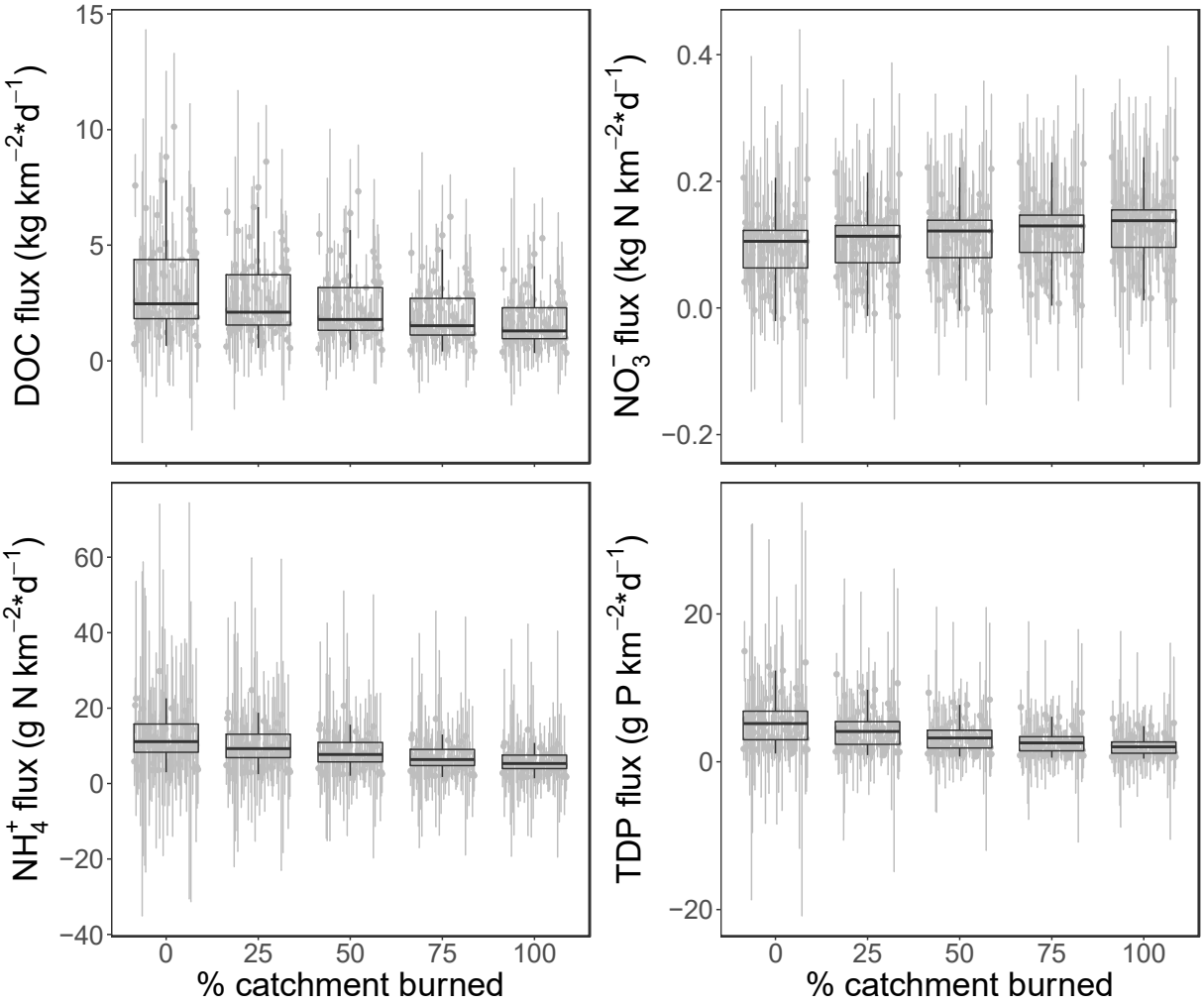


Figure 54. Model-predicted yields of solutes from boreal catchments at baseflow across a gradient of burn extent. Gray points and error bars reflect the predicted yield (+/- 95% CI) for each catchment in the dataset. Boxes summarize predictions across all catchments with center line depicting median yield, box extents drawn at the 25th and 75th quartiles, and error bars extending to 1.5x this range.

fire on C, N, and P concentrations estimated from this broad-scale survey result from changes in OM pools and vegetation dynamics, rather than from effects of fire on permafrost.

Fire influence on yields of C, N, and P— We applied the fitted regression models to predict specific yields of C, N, and P during summer baseflow across a range in fraction of the catchment that burned. Model-predicted specific yields of DOC declined by 52%, on average, between unburned and completely burned catchments, yield of TDP decreased 39%, and NH_4^+ yield decreased 48%, whereas NO_3^- yield increased 20% (Fig. 54). Though small relative to terrestrial fluxes, changes in fluvial fluxes have consequences for river and coastal ecosystems.

Broad-scale patterns in stream chemistry across Interior Alaska provide context for interpreting the high-frequency data collected from a smaller set of catchments. First, the synoptic survey confirms that concentrations of NO_3^- and DOC observed in the five focal catchments are typical of moderately sloped catchments in Interior Alaska. The catchments that were the focus of intensive monitoring are reflective of a broad spatial area, though will not

provide reliable indication of responses of steeply sloped or high-elevation catchments in the region. More importantly, the synoptic survey validated expected correlations between fire and stream biogeochemistry. Specifically, the synoptic survey confirmed that fire has long-term consequences for delivery of DOM and NO_3^- to streams, as time since fire was not a significant predictor in regression models. Thus, stream chemistry provides a reliable indicator of the catchment-scale effects of fire on biogeochemical processes in the boreal forest.

9.6.4 Implications

- Significant declines in DOC, NH_4^+, and TDP concentrations in streams draining more extensively burned catchments indicated reduced stores of OM in soils and the forest floor.
- Fire likely influenced solute concentrations in streams by changing biotic mechanisms of material processing and storage, rather than physical processes, as concentrations of biologically non-limiting elements derived from weathering were uninfluenced by fire.
- Solute concentrations were uninfluenced by time since fire, which could result from slow reaccumulation of soil OM.

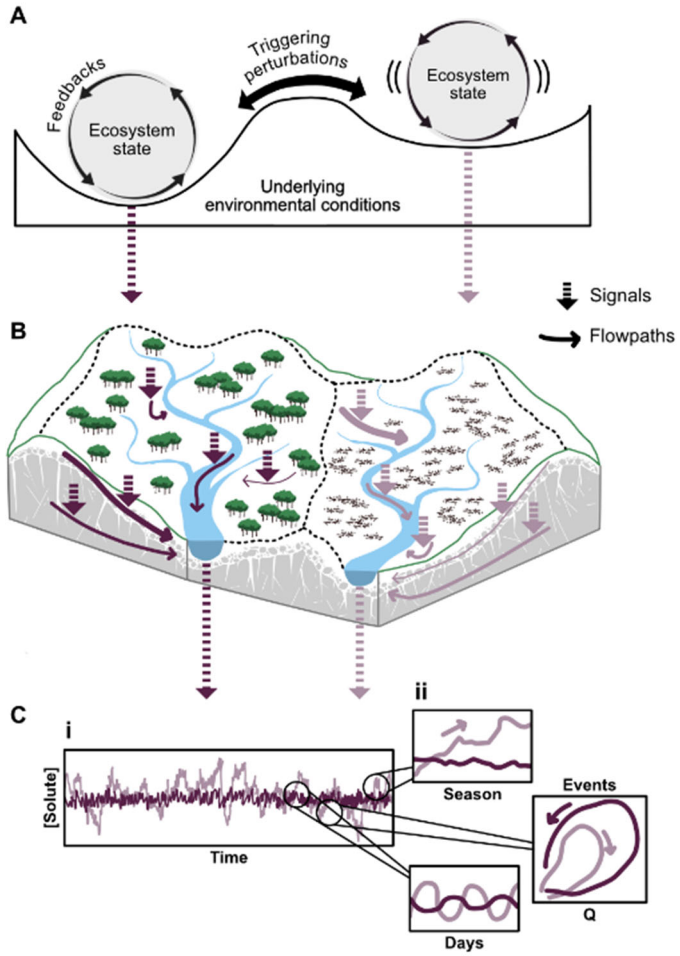


Figure 55. Conceptual model integrating resilience theory with catchment biogeochemistry. Hydrologic flowpaths propagate ecological signals through catchments, and signals manifest at multiple time scales in time series of stream chemistry.

Task 10: Quantify leading indicators of regime change

10.1 Overview

The central objectives of this SERDP project was to determine whether stream chemistry can indicate the ecological state of catchments, describe ecosystem resilience, and predict state changes between alternative stable states (Fig. 55). Previous sections have outlined biogeochemical signals of fire history and permafrost extent observable in streams that indicate ecosystem state. These signals characterize the existing state of ecosystems but do not characterize whether disturbance has eroded ecosystem resilience to perturbations. In this section we demonstrate application of a suite of "leading indicators" of regime change to determine whether time series of solute chemistry can detect state changes precipitated by disturbance of terrestrial ecosystems.

Time series of observations serve as the input for a diverse set of metrics used to provide advanced warning of ecological regime change. These "leading indicators" of regime change are not unique to ecosystems, but are

rooted in the mathematical theory of systems, and have been applied in economics and engineering as well as to ecological observations (Scheffer et al. 2015). Critical slowing down describes diminished capacity of systems to return to a stable equilibrium following perturbation as resilience is lost near the transition to an alternative stable state. Thus, increased variance in ecological attributes occurs in ecosystems that are nearing a regime shift (Carpenter & Brock, 2006). Critical slowing down also manifests as increased recovery time, which strengthens the autoregressive coefficient (Biggs et al. 2009). A second phenomenon describes rapid bi-directional shifts between two basins of attraction (stable states) when a system has lost resilience, termed flickering (Scheffer et al., 2009). Indicators of flickering include bimodality, which reflects observation of ecosystem characteristics of both states and increased skew and kurtosis in the distribution of observed attributes (Wang et al., 2012).

Ecological applications of leading indicators of regime change have primarily been demonstrated in mesocosms and lakes, but there is little empirical evidence of their utility in other ecosystems. Further, previous applications are based on attributes of ecosystems directly affected by the disturbance and originating within the boundaries of the ecosystem of interest. Here we apply leading indicators of regime change to multi-decadal time series of stream chemistry and discharge encompassing experimental disturbance.

10.2 Effectiveness of leading indicators in detecting state changes from stream chemistry and discharge

10.2.1 Methods

*Long-term observations of stream chemistry and discharge—*As test cases, we chose two long-term, paired catchment studies that included experimental disturbance. Data are from temperate deciduous forests at Hubbard Brook Experimental Forest (New Hampshire, USA; Campbell et al., 2021) and Coweeta Hydrologic Laboratory (North Carolina, USA; Webster et al., 2016). Both sites include multi-decadal records of stream chemistry and discharge in a reference headwater catchment and a paired site that was experimentally disturbed by clearcutting. At Hubbard Brook, we analyzed WS6 (reference) and WS2 (clearcut 1965). At Coweeta, we analyzed WS2 (reference) and WS7 (clearcut 1977). Datasets were chosen because of the paired design, which allowed for evaluation of the effectiveness of leading indicators in identifying regime shifts relative to background variation. The duration of both datasets (~50 years) encompassed the successional trajectory following forest harvest, which is necessary for discerning between transient variation and state changes. Though our observations from boreal forests of Alaska do not encompass harvest, removal of vegetation by harvest produces similar patterns to removal of vegetation by fire. Thus, this demonstration analysis provides a reasonable analog to analyzing state changes resulting from fire in the boreal forest.

Leading indicators— We applied leading indicators of regime change to long-term records of volume-weighted NO_3^- concentration in the stream draining each headwater catchment. Missing values were interpolated by applying a Kalman filter to forecasts from an ARIMA model. Prior to application of leading indicators, data were detrended using the seasonal decomposition of timeseries by loess (STL) decomposition method. Stationarity of the resulting residual timeseries was confirmed using the Kwiatkowski-Phillips-Schmidt-Shin (KPSS) test.

We calculated standard deviation (SD) and autoregression coefficient at lag-1 (AR1) over rolling windows for each time series. These metrics capture changes in temporal variation that theory predicts to increase prior to changes in state. Increased SD indicates that temporal variance is increasing. An increase in the AR1 coefficient indicates that the time series more closely resembles a random walk pattern, wherein observations are more similar to the previous

observation, rather than maintaining constant variation around the mean. These metrics capture "critical slowing down". In paired-catchment studies, evidence of state change occurs when the SD and AR1 metrics in the clearcut catchment exceed values in the reference catchment.

The rolling window size applied to evaluate change in leading indicators influences interpretation of the indicators (Batt et al., 2019; Wen et al., 2018; Wilkinson et al., 2018). Larger window size captures longer-term changes but can reduce precision in identifying exactly when a state change occurred. Smaller window sizes offer greater precision and are also applicable to shorter time series. We tested multiple window sizes and report on results for a window of 5 years.

10.2.2 Results

Leading indicators of state change provided evidence that clearcutting stimulated a regime shift in the clearcut catchment at Coweeta, but not at Hubbard Brook. At both sites, NO_3^- concentration was elevated in the clearcut catchment by several-fold following forest harvest (Fig. 56). Elevated concentration of NO_3^- in the clearcut relative to reference catchment persisted for less than a decade at Hubbard Brook, whereas NO_3^- remained elevated for the multi-decadal period of record at Coweeta. The moving-window SD and AR1 metrics also indicated increased temporal variation in NO_3^- concentration in the clearcut relative to the reference catchment at both sites. At Hubbard Brook, clearcutting resulted in a temporary increase in SD and AR1, suggesting that the disturbance perturbed ecosystem dynamics but did not erode the catchment's resilience and it returned to the initial, pre-disturbance state within 10 years (Fig. 56). Sensitivity of the leading indicators to detect regime shifts was possibly limited by the short duration of observations collected prior to the experimental clearcut at Hubbard Brook. The moving window approach limited comparison of the reference and clearcut catchments prior to the disturbance, which is needed to establish similar temporal dynamics prior to disturbance in the paired catchments.

In contrast to Hubbard Brook, elevated temporal variation in NO_3^- concentration has persisted for several decades at Coweeta (Fig. 56). Elevated SD of NO_3^- concentration in the stream draining the clearcut catchment at Coweeta indicates that small perturbations (e.g., variation in weather, invasive species) now result in much larger changes to ecosystem dynamics than before the clearcut. The elevated AR1 coefficient in the clearcut compared to reference catchment indicates greater return time to baseline conditions following perturbations. In summary, though clearcutting had a significant influence on ecosystem dynamics at both sites, feedbacks contributing to resilience in the clearcut catchment at Hubbard Brook maintained the ecosystem in its initial state. At Coweeta, persistence of increased variance in ecosystem dynamics suggests that clearcutting severed some critical feedbacks contributing to ecosystem resilience.

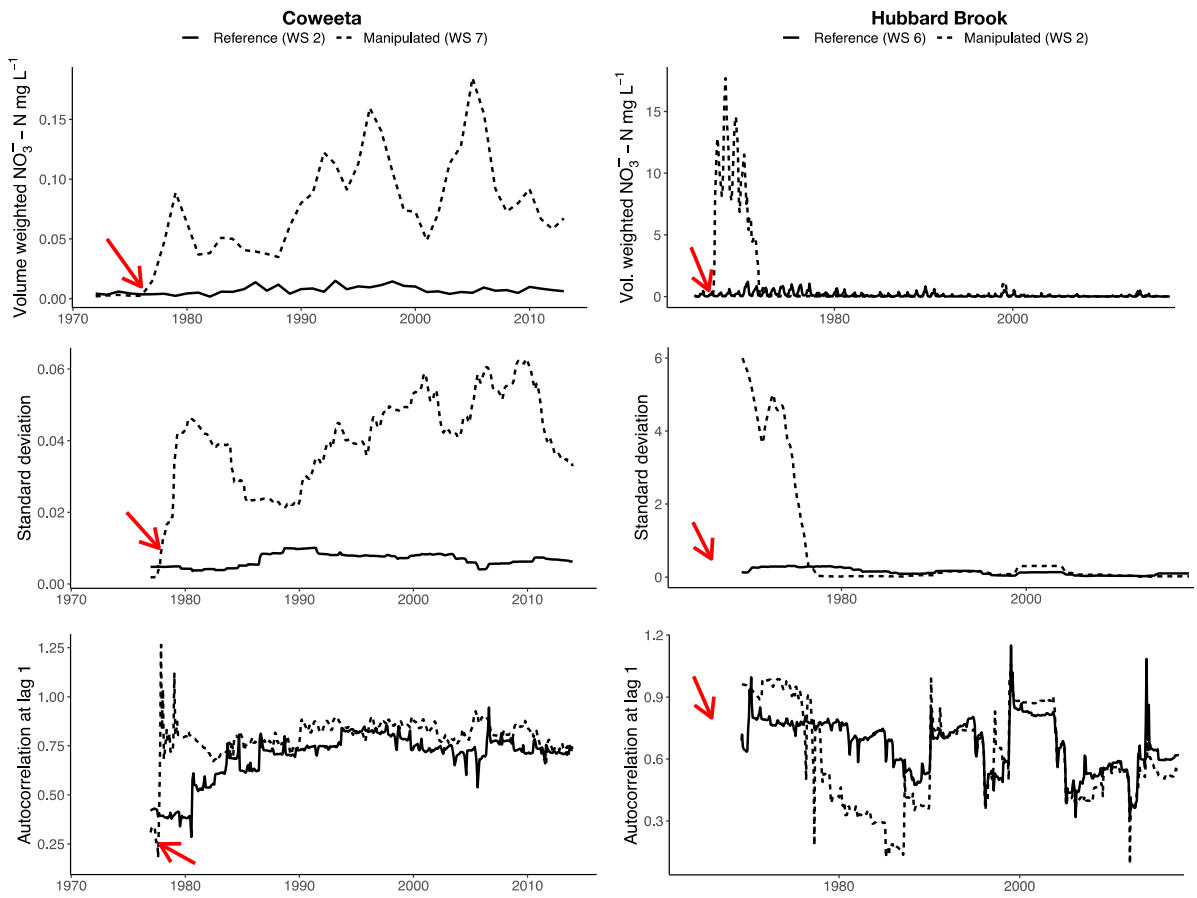


Figure 56. Leading indicators of regime change were applied to long-term observations of monthly stream nitrate concentration from reference and clearcut catchments in the experimental forests of Coweeta, NC (left column) and Hubbard Brook, NH (right column). Red arrows designate the clear-cutting treatment of the manipulated watershed. Top panels: observed flow-weighted monthly average concentration of nitrate. Middle panels: standard deviation of observed concentration over a 5-year moving window. At Hubbard Brook, clear-cutting resulted in a temporary increase in standard deviation, suggesting that the clear-cut catchment quickly returned to the initial, reference state. In contrast, standard deviation of nitrate concentration in the stream draining the clear-cut catchment at Coweeta remains elevated several decades after the treatment, suggestive of a regime shift stimulated by the clear-cut disturbance. The auto-regressive coefficient at lag 1 (AR1; bottom panels) provided subtle evidence of a regime shift at Coweeta, with AR1 typically elevated in the clear-cut compared to reference catchment. This indicates greater return time to baseline conditions following perturbations. Though the AR1 coefficient was elevated relative to the reference state in the first few years following the clear-cut at Hubbard Brook, this effect was not sustained, indicating resilience of this catchment to the clear-cut disturbance.

10.3 Baseline values of leading indicators for boreal catchments varying in disturbance history

10.3.1 Rationale

Leading indicators of regime shift identify attributes of time series that theory predicts will precede regime shifts. These patterns have been confirmed in studies of lakes and mesocosms, where leading indicators have been applied to time series of attributes directly participating in the regime shift or in feedbacks that maintain resilience. Here we estimated leading indicators from stream chemistry, which is affected by, but does not directly participate in the feedbacks known and ecological time series.

Monitoring of boreal catchments in Alaska that were the focus of this SERDP project entailed high-frequency observations of stream chemistry maintained for the open-water period of four years. The resulting dataset provides insights into temporal patterns characterizing the ecological state of catchments due to contrasts in disturbance history across catchments. The temporal extent of this dataset is insufficient for diagnosing ecological resilience because the length of the records is short relative to the duration of ecosystem recovery from these disturbances. However, we apply several leading indicators of regime change for comparison across catchments of contrasting disturbance history and to provide a baseline for comparison against longer-term data as they become available.

10.3.2 Methods

We applied several leading indicators of regime change to high-frequency observations of chemistry in boreal streams, including metrics capturing "flickering" (i.e., skewness, kurtosis) and "critical slowing down" (i.e., SD). Pearson's measure of skewness and Fisher's measure of kurtosis were applied to quantify presence of tailed distributions, indicating increasing frequency of extreme values that deviate from the mean. Both metrics equal zero for a normal distribution. Positive skewness indicates a long tail of values greater than a mean, and a negative value of the skewness metric indicates presence of extreme values less than the mean. Positive values of kurtosis indicate heavy tails of the distribution. Metrics were calculated for each year of observations within a common time window (~mid-Jun to late Sept) to standardize against the timing of snowmelt in each year. Previous sections summarize additional leading indicators, including SD of storm-scale C-Q relationships (Figs. 35 & 36) and the autoregression coefficient applied to daily time series (Fig. 44).

10.3.3 Results

All attributes of stream chemistry deviated from a normal distribution, due to presence of extreme values (Figs. 57-61). These non-normal distributions were due at least in part to variation in concentrations during storms. Nitrate was least skewed of all constituents, possibly reflective of a constant source of NO_3^- in groundwater. However, the high-permafrost catchment showed a high density of concentrations less than the mean (Fig. 57). Specific conductivity also showed a high density of values less than the mean in most catchments, reflective of dilution during storms (Fig. 60). With the exception of negative skew in fDOM at Vault, all other constituents showed modest positive skew, with longest tails in abs254 at Poker and for turbidity at Poker and Stuart, as well as Vault (Figs. 58 & 59). These long tails of values greater than the mean likely reflect flushing dynamics during storms.

All measured constituents were leptokurtic, indicating presence of extreme values that deviated from the mean. Turbidity reflected greatest kurtosis (Fig. 61), and movement of sediments during storms was the predominant influence on turbidity (Appendix 2). Largest values of kurtosis occurred in the Poker (burned) catchment for many attributes, including

turbidity, abs254, and specific conductivity (Figs. 58, 60, & 61). Kurtosis was similarly elevated for many constituents at Stuart, another burned catchment, though Vault (high permafrost) also generated high relative values of kurtosis for some constituents (Figs. 57-61).

Previous sections of this report contain metrics of temporal stability at the storm-scale (*Section 9.3.3*) and on a daily timescale (Section 9.4.2). The SD of HI and β, reflecting variation in C-Q dynamics across individual storms, showed few significant differences across catchments (Figs. 35 & 36). However, rocky upland catchments (e.g., Poker) tended to be less variable in fDOM and SPC dynamics among storms than some of the catchments characterized by silty substrate (Fig. 34). This contrasts with the skew and kurtosis metrics, which were often greatest for Poker, indicating appearance of extreme values (Figs. 57-61). This latter analysis was conducted on the full time series, suggesting that events in addition to storms (e.g., late season "step-change") contribute to variation there. Stuart, another burned catchment, produced the greatest variation in NO_3^- dynamics among storms (Figs. 35 & 36) and also showed greater skew and kurtosis throughout the time series than several other catchments (Figs. 57-61).

In Section 9.4.2, we reported strong autoregressive coefficients at a lag of 1 day for daily mean concentrations of fDOM and NO_3^-, indicating that variation in the time series that was not strongly centered on mean values. Chemistry of the streams is thus responsive to perturbations and could thus provide an indicator of resilience to particular perturbations. However, the autoregression coefficients did not vary significantly among catchments (Fig. 44) and the AR1 metric does not indicate variation in resilience to perturbations across the focal catchments.

Overall, patterns emerged in the relative temporal variation in stream chemistry among catchments varying in disturbance history that might provide indicators of regime change over longer timescales. For example, two burned catchments showed greatest evidence of extreme values and storm-scale variation for some constituents. These patterns, however, cannot be ascribed to resilience of ecological processes in the catchments because the four-year time series do not encompass timescales consistent with successional processes or of gradual permafrost thaw. The contrasts among catchments provide evidence that stream chemistry contains signals of processes within catchments that are influenced by disturbance regimes.

10.4 Implications

- Application of leading indicators of regime change to long-term records of stream chemistry from experimental forests detected regime shifts in the upslope ecosystem.
- Leading indicators will be most sensitive to predicting a change in temporal variation and autocorrelation when data are available preceding disturbances.
- Long-term monitoring is key to generating advanced warning of potential regime shifts in catchments.

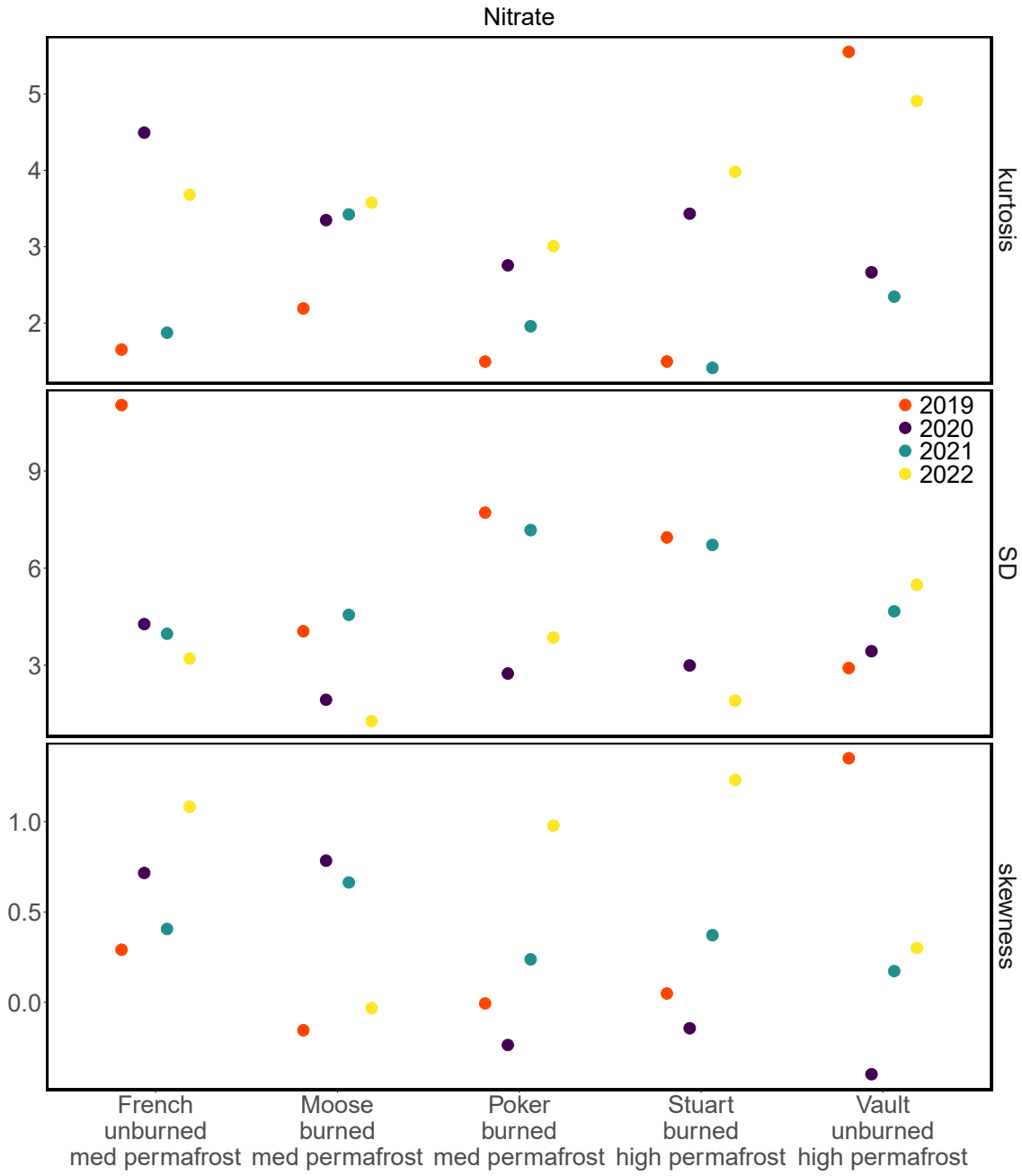


Figure 57. Leading indicators of regime change estimated from seasonal time series of nitrate concentration measured at 15-min resolution.

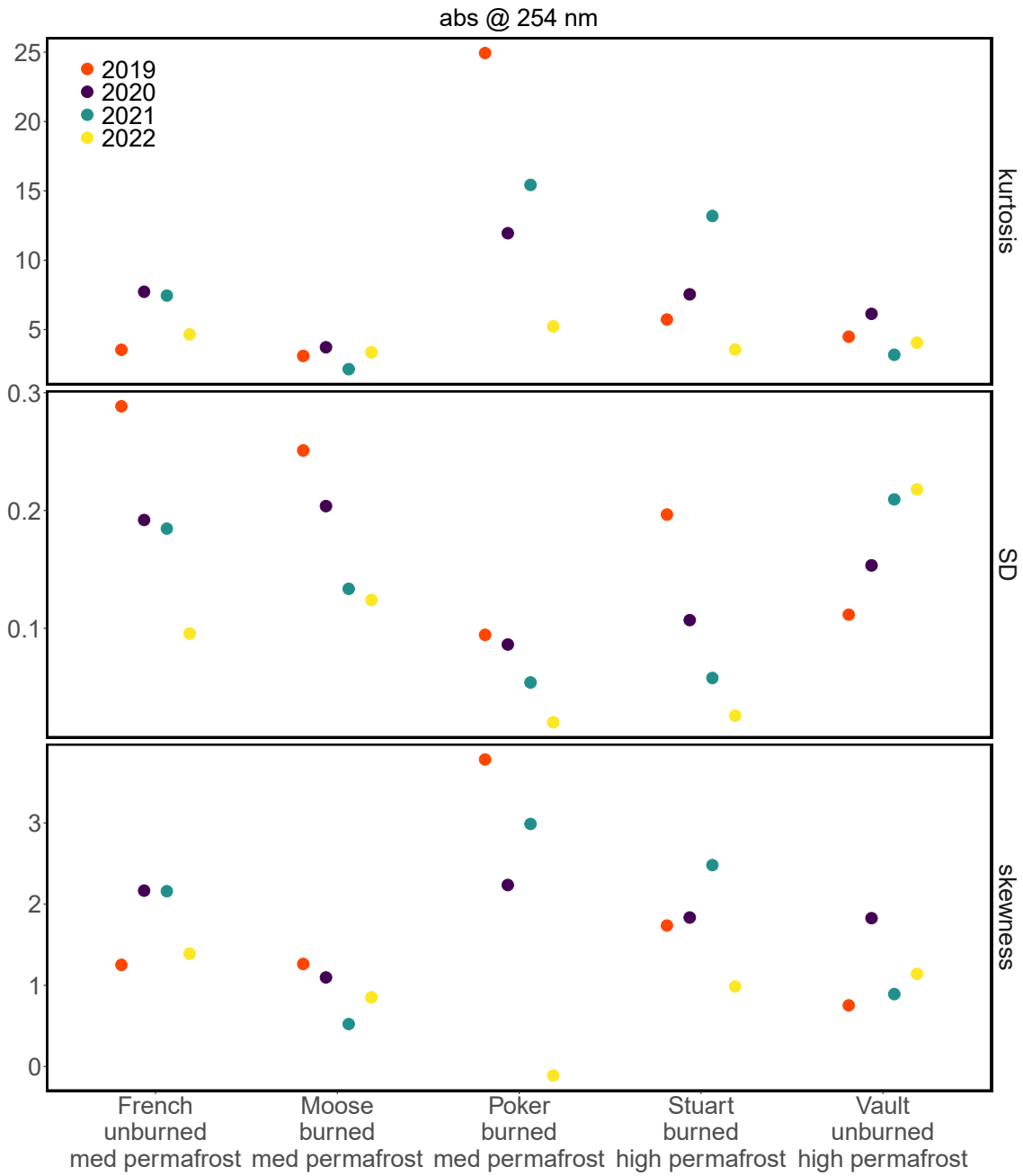


Figure 58. Leading indicators of regime change estimated from seasonal time series of absorbance at 254 nm (a proxy for DOM concentration) measured at 15-min resolution.

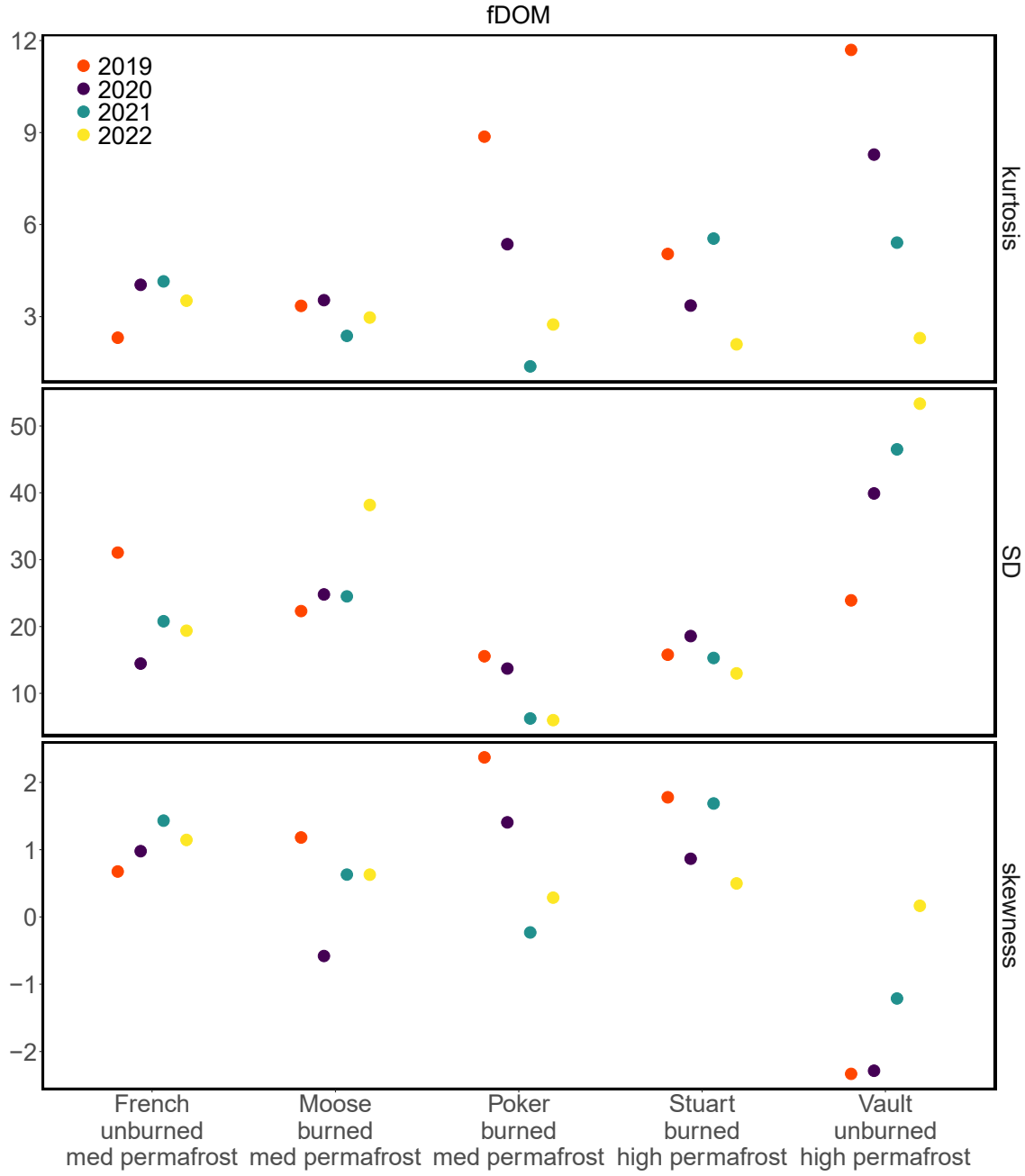


Figure 59. Leading indicators of regime change estimated from seasonal time series of fDOM concentration measured at 15-min resolution.

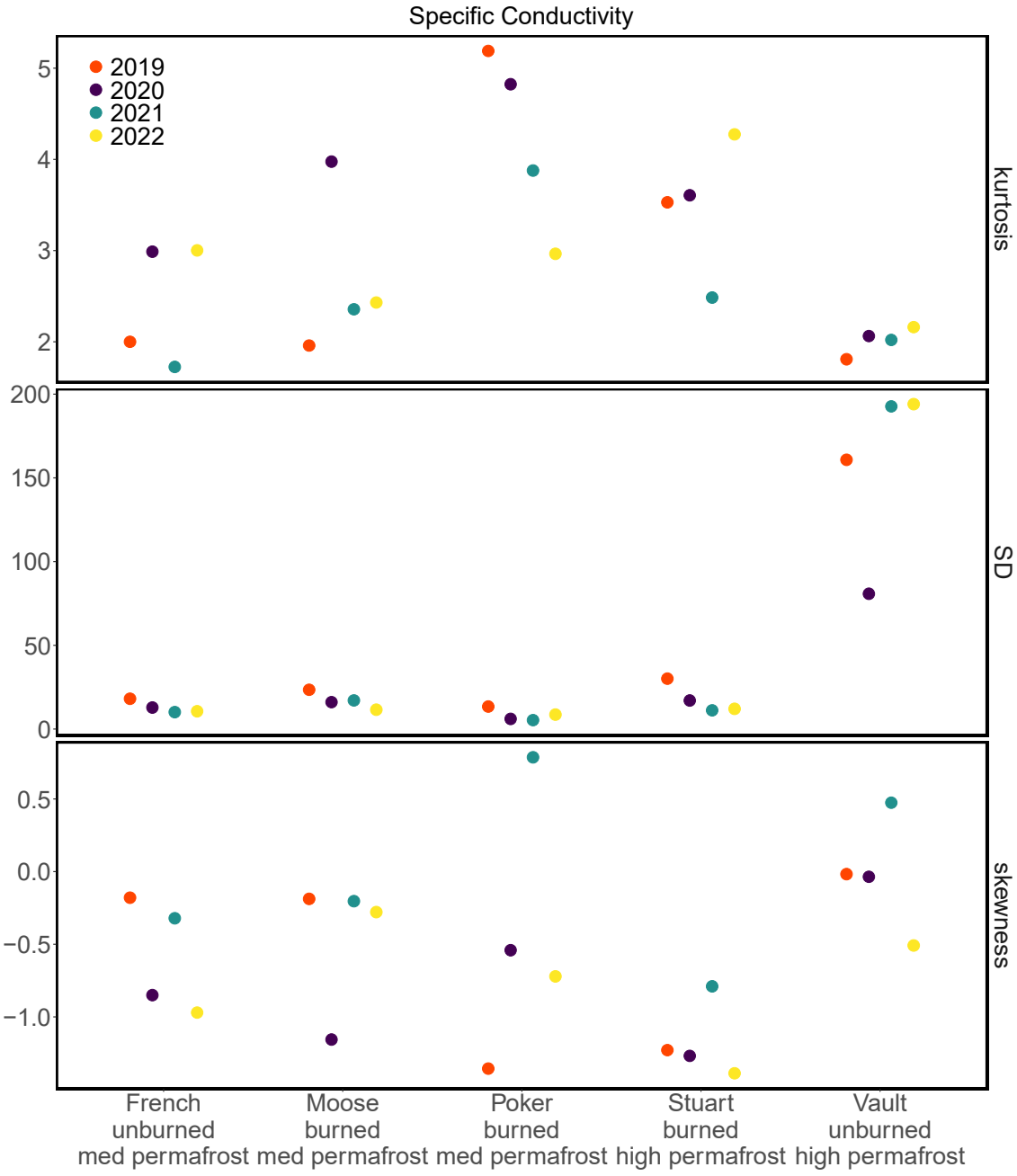


Figure 60. Leading indicators of regime change estimated from seasonal time series of specific conductivity measured at 15-min resolution.

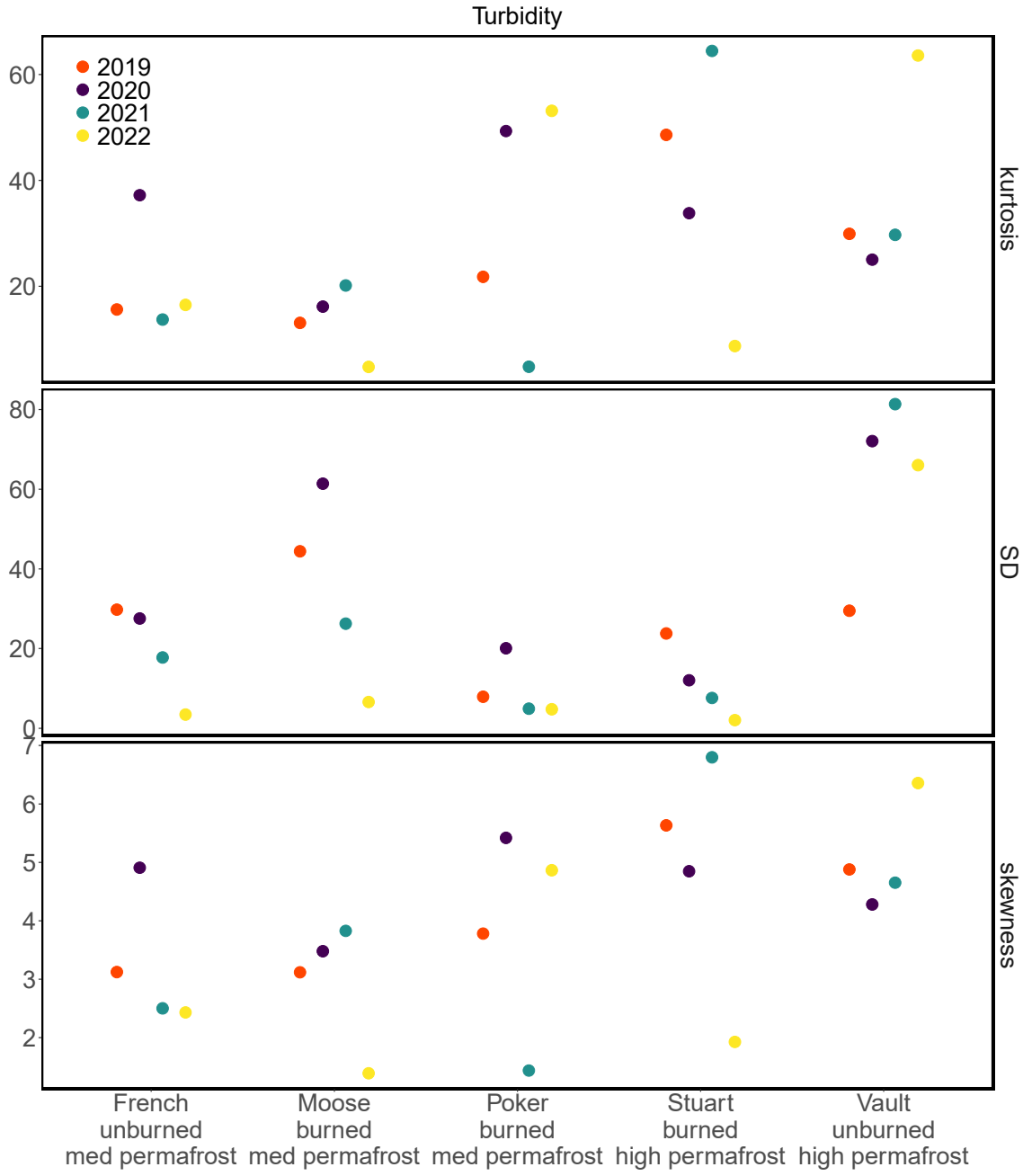


Figure 61. Leading indicators of regime change estimated from seasonal time series of turbidity measured at 15-min resolution.

CONCLUSIONS AND IMPLICATIONS FOR FUTURE RESEARCH/IMPLEMENTATION

We investigated whether temporal patterns in stream biogeochemistry can summarize the ecological state of adjacent terrestrial ecosystems and provide evidence of ecosystem resilience to disturbance in the boreal forest. The research program focused on: i) collecting high-frequency (15-min) records of stream biogeochemistry using instream sensors, ii) developing automated routines for handling high-frequency data, and iii) applying statistical analyses of time series at multiple temporal scales to identify signals of ecosystem response to disturbance. Stream chemistry could be used as integrative signals to monitor DoD lands in the boreal forest and manage training and construction activities to reduce loss of functional training grounds and ecosystem services.

1) Signals of catchment state in the boreal forest derived from stream chemistry included:
   i) Variation in storm-scale concentration-discharge dynamics across gradients of fire and permafrost extents in the catchment (Figs. 37 & 38)
   ii) Abrupt, non-linear increases in solute concentration, particularly of NO_3^-, associated with precipitation in August or thereafter that could indicate flowpath rerouting related to permafrost thaw (Fig. 7 & 24)
   iii) Significant diurnal oscillations in fDOM concentration in burned catchments that could derive from patchy distribution of soil organic matter following fire (Fig. 45 & 46)
   iv) Greatest temporal variation in chemistry, discharge, and water sources at storm and seasonal time scales in an unburned, high-permafrost catchment (Figs. 17, 20-21, 45-46) identified flashiness in discharge and stream chemistry as potential indicators of extensive permafrost
   v) Mean daily NO_3^- concentration is negatively related to temperature in burned catchments, potentially reflecting dynamics of regrowing variation (Fig. 42)
   vi) Reduced fluvial export of DOM from burned catchments persists on a decadal timescale (Fig. 53 & 54)
2) Dynamics during storms were more sensitive at discerning differences among catchments than variation at daily or longer time scales. High-frequency monitoring over short (single season) time scales could diagnose the current state of catchments. Understanding the distribution of military lands with extensive compared to sparse permafrost and identifying areas recovering slowly from fire could augment efforts to inventory ecosystem services including carbon storage and wildlife habitat.
3) Longer-term (~decadal scale) monitoring of storm dynamics could indicate loss of catchment resilience if characteristic concentration-discharge patterns shift over time. Training activities might then be relocated to avoid further disturbance to catchments exhibiting loss of resilience.
4) Instream processes (e.g., gross primary production) had weak influences on stream chemistry and catchment signals were therefore preserved in stream chemistry (Figs. 25, 27, 41-42).
5) Co-monitoring of precipitation, ground temperature, and stream chemistry could identify mechanisms linking permafrost thaw with deepening hydrologic flowpaths (Fig. 18) and solute export to reduce uncertainty in projected changes to runoff and water quality.
6) Low-frequency, long-term monitoring of DOM concentrations could indicate which catchments are recovering from fire and which remain in a state that accumulates little belowground OM and therefore lack ecosystem protection of permafrost (Fig. 54). Intensive

training activities or construction projects might be avoided or modified to mitigate further disturbance in catchments recovering slowly from fire.

7) Multi-decadal time series of stream chemistry indicated loss of resilience in experimentally harvested forests (Fig. 56). This demonstration indicated the importance of pre-disturbance observations. Long-term monitoring of stream chemistry in the boreal forest might similarly provide early warnings of state changes caused by disturbances to vegetation in the catchment.
8) Precipitation imparted patterns in catchment hydrology and biogeochemistry on storm and inter-annual timescales. A strong influence of precipitation portends significant changes to water and solute exports as precipitation becomes more variable in high-latitude regions (e.g., Bintanja et al. 2020). Continued research, capturing wider variation in precipitation, is needed to reduce uncertainty in predicting ecosystem responses to the changing precipitation regime.

LITERATURE CITED

Ågren, A., Buffam, I., Jansson, M., & Laudon, H. (2007). Importance of seasonality and small streams for the landscape regulation of dissolved organic carbon export. *Journal of Geophysical Research: Biogeosciences*, *112*(G3). https://doi.org/10.1029/2006JG000381

Alexander, H. D., & Mack, M. C. (2016). A canopy shift in interior Alaskan boreal forests: consequences for above-and belowground carbon and nitrogen pools during post-fire succession. *Ecosystems*, *19*, 98–114.

Appling, A. P., Hall Jr., R. O., Yackulic, C. B., & Arroita, M. (2018). Overcoming Equifinality: Leveraging Long Time Series for Stream Metabolism Estimation. *Journal of Geophysical Research: Biogeosciences*, *123*(2), 624–645. https://doi.org/10.1002/2017JG004140

Balcarczyk, K. L., Jones, J. B., Jaffé, R., & Maie, N. (2009). Stream dissolved organic matter bioavailability and composition in watersheds underlain with discontinuous permafrost. *Biogeochemistry*, *94*(3), 255–270. https://doi.org/10.1007/s10533-009-9324-x

Barker, A. J., Douglas, T. A., Jacobson, A. D., McClelland, J. W., Ilgen, A. G., Khosh, M. S., et al. (2014). Late season mobilization of trace metals in two small Alaskan arctic watersheds as a proxy for landscape scale permafrost active layer dynamics. *Chemical Geology*, *381*(C), 180–193.

Batt, R. D., Eason, T., & Garmestani, A. (2019). Time scale of resilience loss: Implications for managing critical transitions in water quality. *PLoS ONE*, *14*(10), e0223366.

Bayley, S. E., Schindler, D. W., Parker, B. R., Stainton, M. P., & Beaty, K. G. (1992). Effects of forest fire and drought on acidity of a base-poor boreal forest stream: similarities between climatic warming and acidic precipitation. *Ecosystems*, *17*(3), 191–204.

Beel, C. R., Lamoureux, S. F., Orwin, J. F., Pope, M. A., Lafrenière, M. J., & Scott, N. A. (2020). Differential impact of thermal and physical permafrost disturbances on High Arctic dissolved and particulate fluvial fluxes. *Scientific Reports*, *10*(1), 1–13.

Bernhardt, E. S., Savoy, P., Vlah, M. J., Appling, A. P., Koenig, L. E., Hall, R. O., et al. (2022). Light and flow regimes regulate the metabolism of rivers. *Proceedings of the National Academy of Sciences*, *119*(8), e2121976119. https://doi.org/10.1073/pnas.2121976119

Betts, E. F., & Jones, J. B. (2009). Impact of Wildfire on Stream Nutrient Chemistry and Ecosystem Metabolism in Boreal Forest Catchments of Interior Alaska. *Arctic, Antarctic, and Alpine Research*, *41*(4), 407–417. https://doi.org/10.1657/1938-4246-41.4.407

Bintanja, R., van der Wiel, K., van der Linden, E. C., Reusen, J., Bogerd, L., Krikken, F., & Selten, F. M. (2020). Strong future increases in Arctic precipitation variability linked to poleward moisture transport. *Science Advances*, *6*(7), eaax6869.

Bolton, W. R., & Hinzman, L. (2004). Water balance dynamics of three small catchments in. *Northern Research Basins Water Balance*, *290*(290), 213.

Bond-Lamberty, B., Peckham, S. D., Gower, S. T., & Ewers, B. E. (2009). Effects of fire on regional evapotranspiration in the central Canadian boreal forest. *Global Change Biology*, *15*(5), 1242–1254. https://doi.org/10.1111/j.1365-2486.2008.01776.x

Boshers, D. S., & Granger, J. (2019). Constraining the oxygen isotopic composition of nitrate produced by nitrification. *Environmental Science & Technology*.

Bracken, L. J., Wainwright, J., Ali, G. A., Tetzlaff, D., Smith, M. W., Reaney, S. M., & Roy, A. G. (2013). Concepts of hydrological connectivity: Research approaches, pathways and future agendas. *Earth-Science Reviews*, *119*, 17–34. https://doi.org/10.1016/j.earscirev.2013.02.001

Brown, D. R. N., Jorgenson, M. T., Douglas, T. A., Romanovsky, V. E., Kielland, K., Hiemstra, C., et al. (2015). Interactive effects of wildfire and climate on permafrost degradation in Alaskan lowland forests. *Journal of Geophysical Research: Biogeosciences*, *120*(8), 1619–1637. https://doi.org/10.1002/2015JG003033

Bugmann, H. K. M., Wullschleger, S. D., Price, D. T., Ogle, K., Clark, D. F., & Solomon, A. M. (2001). Comparing the performance of forest gap models in North America. *Climatic Change*, *51*(3/4), 349–388. https://doi.org/10.1023/A:1012537914881

Burd, K., Tank, S. E., Dion, N., & Quinton, W. (2018). Seasonal shifts in export of DOC and nutrients from burned and unburned peatland-rich catchments, Northwest Territories, Canada. *Hydrol Earth Syst Sci*, *22*, 4455–4472.

Burns, D. A., Pellerin, B. A., Miller, M. P., Capel, P. D., Tesoriero, A. J., & Duncan, J. M. (2019). Monitoring the riverine pulse: Applying high-frequency nitrate data to advance integrative understanding of biogeochemical and hydrological processes. *WIREs Water*, *6*(4). https://doi.org/10.1002/wat2.1348

Campbell, J. L., Rustad, L. E., Bailey, S. W., Bernhardt, E. S., Driscoll, C. T., Green, M. B., et al. (2021). Watershed studies at the Hubbard Brook Experimental Forest: Building on a long legacy of research with new approaches and sources of data. *Hydrological Processes*, *35*(1). https://doi.org/10.1002/hyp.14016

Canty, A., & Ripley, B. (2017). Package 'boot.' *Bootstrap Functions. CRAN R Proj*.

Carey, S. K., & Woo, M. (2001). Spatial variability of hillslope water balance, wolf creek basin, subarctic yukon. *Hydrological Processes*, *15*(16), 3113–3132. https://doi.org/10.1002/hyp.319

Carey, S. K., & Woo, M.-K. (1999). Hydrology of two slopes in subarctic Yukon, Canada. *Hydrological Processes*, *13*(16), 2549–2562.

Carey, S. K., Tetzlaff, D., Buttle, J., Laudon, H., McDonnell, J., McGuire, K., et al. (2013). Use of color maps and wavelet coherence to discern seasonal and interannual climate influences on streamflow variability in northern catchments. *Water Resources Research*, *49*(10), 6194–6207.

Carpenter, S. R., & Brock, W. A. (2006). Rising variance: a leading indicator of ecological transition. *Ecology Letters*, *9*(3), 311–318.

Chapin, F. S., Mcguire, A. D., Ruess, R. W., Hollingsworth, T. N., Mack, M. C., Johnstone, J. F., et al. (2010). Resilience of Alaska's boreal forest to climatic change. *Canadian Journal of Forest Research*, *40*(7), 1360–1370.

Connon, R. F., Quinton, W. L., Craig, J. R., & Hayashi, M. (2014). Changing hydrologic connectivity due to permafrost thaw in the lower Liard River valley, NWT, Canada. *Hydrological Processes*, *28*(14), 4163–4178.

Creed, I. F., Beall, F. D., Clair, T. A., Dillon, P. J., & Hesslein, R. H. (2008). Predicting export of dissolved organic carbon from forested catchments in glaciated landscapes with shallow soils. *Global Biogeochemical Cycles*, *22*(4). https://doi.org/10.1029/2008GB003294

Degnan, J. R., Böhlke, J. K., Pelham, K., Langlais, D. M., & Walsh, G. J. (2016). Identification of Groundwater Nitrate Contamination from Explosives Used in Road Construction: Isotopic, Chemical, and Hydrologic Evidence. *Environmental Science and Technology*, *50*(2), 593–603.

DeLuca, T. H., & Sala, A. (2006). Frequent fire alters nitrogen transformations in ponderose pine stands of the inland northwest. *Ecology*, *87*(10), 2511–2522.

Douglas, T. A., Turetsky, M. R., & Koven, C. D. (2020). Increased rainfall stimulates permafrost thaw across a variety of Interior Alaskan boreal ecosystems. *Npj Climate and Atmospheric Science*, *3*(1), 1–7.

Dove, N. C., Safford, H. D., Bohlman, G. N., Estes, B. L., & Hart, S. C. (2020). High-severity wildfire leads to multi-decadal impacts on soil biogeochemistry in mixed-conifer forests. *Ecological Applications*, eap.2072.

Downing, B. D., Pellerin, B. A., Bergamaschi, B. A., Saraceno, J. F., & Kraus, T. E. (2012). Seeing the light: The effects of particles, dissolved materials, and temperature on in situ measurements of DOM fluorescence in rivers and streams. *Limnol. Oceanogr. Methods*, *10*, 767–775.

Duncan, J. M., Band, L. E., Groffman, P. M., & Bernhardt, E. S. (2015). Mechanisms driving the seasonality of catchment-scale nitrate export: Evidence for riparian ecohydrologic controls. *Water Resources Research*. https://doi.org/10.1002/2015WR016937

Ebel, B. A., & Moody, J. A. (2013). Rethinking infiltration in wildfire-affected soils. *Hydrological Processes*, *27*(10), 1510–1514. https://doi.org/10.1002/hyp.9696

Ellison, S. B., Sullivan, P. F., Cahoon, S. M., & Hewitt, R. E. (2019). Poor nutrition as a potential cause of divergent tree growth near the Arctic treeline in northern Alaska. *Ecology*, *100*(12), e02878.

Evans, C. D., Malcolm, I. A., Shilland, E. M., Rose, N. L., Turner, S. D., Crilly, A., et al. (2016). Sustained Biogeochemical Impacts of Wildfire in a Mountain Lake Catchment. *Ecosystems*, *20*(4), 813–829.

Farquharson, L. M., Romanovsky, V. E., Kholodov, A., & Nicolsky, D. (2022). Sub-aerial talik formation observed across the discontinuous permafrost zone of Alaska. *Nature Geoscience*, *15*, 475–481. https://doi.org/10.1038/s41561-022-00952-z

Flannigan, M., Stocks, B., Turetsky, M., & Wotton, M. (2009). Impacts of climate change on fire activity and fire management in the circumboreal forest. *Global Change Biology*, *15*(3), 549–560.

Flewelling, S. A., Hornberger, G. M., Herman, J. S., Mills, A. L., & Robertson, W. M. (2013). Diel patterns in coastal-stream nitrate concentrations linked to evapotranspiration in the riparian zone of a low-relief, agricultural catchment. *Hydrological Processes*, *28*(4), 2150–2158.

Fork, M. L., Sponseller, R. A., & Laudon, H. (2020). Changing source-transport dynamics drive differential browning trends in a boreal stream network. *Water Resources Research*, *56*(2). https://doi.org/10.1029/2019WR026336

Fuka, D. R., Walter, M. T., Archibald, J. A., Steenhuis, T. S., & Easton, Z. M. (2018). A Community Modeling Foundation for Eco-Hydrology (Version 0.4.12.1).

Gibson, C. M., Chasmer, L. E., Thompson, D. K., & Quinton, W. L. (2018). *Wildfire as a major driver of recent permafrost thaw in boreal peatlands. Nat Commun 9: 3041*.

Giling, D., & Bond, N. (2020). BASEmetab: Estimate Single-station Whole-stream Metabolic Rates from Diel Dissolved Oxygen Curves (Version 3).

Godsey, S. E., Kirchner, J. W., & Clow, D. W. (2009). Concentration-discharge relationships reflect chemostatic characteristics of US catchments. *Hydrological Processes*, *23*(13), 1844–1864.

Grace, M. R., Giling, D. P., Hladyz, S., Caron, V., Thompson, R. M., & Mac Nally, R. (2015). Fast processing of diel oxygen curves: Estimating stream metabolism with BASE

(BAyesian Single-station Estimation): Fast processing of diel oxygen curves. *Limnology and Oceanography: Methods*, *13*(3), e10011. https://doi.org/10.1002/lom3.10011
de Groot, W. J., Flannigan, M. D., & Cantin, A. S. (2013). Climate change impacts on future boreal fire regimes. *Forest Ecology and Management*, *294*, 35–44.
Hall, R. O., Tank, J. L., Baker, M. A., Rosi-Marshall, E. J., & Hotchkiss, E. R. (2016). Metabolism, Gas Exchange, and Carbon Spiraling in Rivers. *Ecosystems*, *19*(1), 73–86. https://doi.org/10.1007/s10021-015-9918-1
Harms, T., & Jones, J. (2012). Thaw depth determines reaction and transport of inorganic nitrogen in valley bottom permafrost soils. *Global Change Biology*, *18*, 2958–2968.
Harms, T. K., Edmonds, J. W., Genet, H., Creed, I. F., Aldred, D., Balser, A., & Jones, J. B. (2016). Catchment influence on nitrate and dissolved organic matter in Alaskan streams across a latitudinal gradient. *Journal of Geophysical Research: Biogeosciences*, *121*(2), 350–369. https://doi.org/10.1002/2015JG003201
Haugen, R. K., Slaughter, C. W., Howe, K. E., & Dingman, S. L. (1982). *Hydrology and climatology of the Caribou-Poker creeks research watershed, Alaska*. Cold Regions Research and Engineering Lab, Hanover, NH.
Hendry, M. J., Wassenaar, L. I., Barbour, S. L., Schabert, M. S., Birkham, T. K., Fedec, T., & Schmeling, E. E. (2018). Assessing the fate of explosives derived nitrate in mine waste rock dumps using the stable isotopes of oxygen and nitrogen. *Science of The Total Environment*, *640–641*, 127–137. https://doi.org/10.1016/j.scitotenv.2018.05.275
Hinzman, L. D., Fukuda, M., Sandberg, D. V., Chapin III, F. S., & Dash, D. (2003). FROSTFIRE: An experimental approach to predicting the climate feedbacks from the changing boreal fire regime. *Journal of Geophysical Research: Atmospheres*, *108*(D1), FFR-9.
Hinzman, L. D., Bettez, N. D., Bolton, W. R., Chapin, F. S., Dyurgerov, M. B., Fastie, C. L., et al. (2005). Evidence and Implications of Recent Climate Change in Northern Alaska and Other Arctic Regions. *Climatic Change*, *72*(3), 251–298. https://doi.org/10.1007/s10584-005-5352-2
Holling, C. S. (1973). Resilience and stability of ecological systems. *Annual Review of Ecology and Systematics*, *4*, 1–23.
Holloway, J. M., & Dahlgren, R. A. (2002). Nitrogen in rock: occurrences and biogeochemical implications. *Global Biogeochemical Cycles*, *16*(4).
Holmes, E. E., Ward, E. J., Scheuerell, M. D., & Wills, K. (2021). MARSS: Multivariate Autoregressive State-Space Modeling (Version 3.11.4). Retrieved from DOI: 10.5281/zenodo.5781847
Hothorn, T., Bretz, F., Westfall, P., Heiberger, R. M., Schuetzenmeister, A., Scheibe, S., & Hothorn, M. T. (2016). Package 'multcomp.' *Simultaneous Inference in General Parametric Models. Project for Statistical Computing, Vienna, Austria*.
James, S. R., Knox, H. A., Abbott, R. E., Panning, M. P., & Screaton, E. J. (2019). Insights Into Permafrost and Seasonal Active-Layer Dynamics From Ambient Seismic Noise Monitoring. *Journal of Geophysical Research: Earth Surface*, *124*(7), 1798–1816.
Johnstone, J. F., Chapin, F. S., Hollingsworth, T. N., Mack, M. C., Romanovsky, V., & Turetsky, M. (2010). Fire, climate change, and forest resilience in interior Alaska. *Canadian Journal of Forest Research*, *40*(7), 1302–1312.

Jones, C. S., Wang, B., Schilling, K. E., & Chan, K. (2017). Nitrate transport and supply limitations quantified using high-frequency stream monitoring and turning point analysis. *Journal of Hydrology*, *549*, 581–591. https://doi.org/10.1016/j.jhydrol.2017.04.041

Jones, J., & Rinehart, A. (2010). The long-term response of stream flow to climatic warming in headwater streams of interior Alaska. *Canadian Journal of Forest Research*, *40*(7), 1210–1218.

Jorgenson, M. T., & Osterkamp, T. E. (2005). Response of boreal ecosystems to varying modes of permafrost degradation. *Canadian Journal of Forest Research*, *35*(9), 2100–2111. https://doi.org/10.1139/x05-153

Jorgenson, M. Torre, Romanovsky, V., Harden, J., Shur, Y., O'Donnell, J., Schuur, E. A. G., et al. (2010). Resilience and vulnerability of permafrost to climate change. *Canadian Journal of Forest Research*, *40*(7), 1219–1236.

Kasischke, E. S., & Turetsky, M. R. (2006). Recent changes in the fire regime across the North American boreal region—Spatial and temporal patterns of burning across Canada and Alaska. *Geophysical Research Letters*, *33*(9), 1996.

Keller, K., Blum, J. D., & Kling, G. W. (2010). Stream geochemistry as an indicator of increasing permafrost thaw depth in an arctic watershed. *Chemical Geology*, *273*(1–2), 76–81. https://doi.org/10.1016/j.chemgeo.2010.02.013

Kendall, C. (1998). Tracing nitrogen sources and cycling in catchments. In *Isotope Tracers in Catchment Hydrology*. Elsevier. Retrieved from https://www.sciencedirect.com/science/article/pii/B9780444815460500239

Kirchner, J. W., Feng, X., Neal, C., & Robson, A. J. (2004). The fine structure of water-quality dynamics: the(high-frequency) wave of the future. *Hydrological Processes*, *18*(7), 1353–1359. https://doi.org/10.1002/hyp.5537

Klingensmith, K., & Cleve, K. van. (1993). Denitrification and nitrogen fixation in floodplain successional soils along the Tanana River, interior Alaska. *Canadian Journal of Forest Research*, *23*(5), 956–963.

Knapp, J. L., Li, L., & Musolff, A. (2022). Hydrologic connectivity and source heterogeneity control concentration–discharge relationships. *Hydrological Processes*, *36*(9), e14683.

Koch, J C, Ewing, S. A., Striegl, R., & McKnight, D. M. (2013). Rapid runoff via shallow throughflow and deeper preferential flow in a boreal catchment underlain by frozen silt (Alaska, USA). *Hydrogeology Journal*, *21*(1), 93–106.

Koch, Joshua C., Dornblaser, M. M., & Striegl, R. G. (2021). Storm-scale and seasonal dynamics of carbon export from a nested subarctic watershed underlain by permafrost. *Journal of Geophysical Research: Biogeosciences*, *126*(8). https://doi.org/10.1029/2021JG006268

Kokelj, S. V., & Burn, C. R. (2005). Geochemistry of the active layer and near-surface permafrost, Mackenzie delta region, Northwest Territories, Canada, *42*, 12.

Kokelj, S. V., Lacelle, D., & Lantz, T. C. (2013). Thawing of massive ground ice in mega slumps drives increases in stream sediment and solute flux across a range of watershed scales. *Journal of Geophysical Research: Earth Surface*, *118*(2), 681–692.

Lader, R., Walsh, J. E., Bhatt, U. S., & Bieniek, P. A. (2017). Projections of Twenty-First-Century Climate Extremes for Alaska via Dynamical Downscaling and Quantile Mapping. *Journal of Applied Meteorology and Climatology*, *56*(9), 2393–2409. https://doi.org/10.1175/JAMC-D-16-0415.1

Likens, G. E. (2004). Some perspectives on long-term biogeochemical research from the Hubbard Brook Ecosystem Study. *Ecology*, *85*(9), 2355–2362.

Lloyd, C. E. M., Freer, J. E., Johnes, P. J., & Collins, A. L. (2016). Using hysteresis analysis of high-resolution water quality monitoring data, including uncertainty, to infer controls on nutrient and sediment transfer in catchments. *The Science of the Total Environment*, *543*(Pt A), 388–404.

Lucas, R. W., Sponseller, R. A., Gundale, M. J., Stendahl, J., Fridman, J., Högberg, P., & Laudon, H. (2016). Long-term declines in stream and river inorganic nitrogen (N) export correspond to forest change. *Ecological Applications*, *26*(2), 545–556. https://doi.org/10.1890/14-2413

Lydersen, E., Høgberget, R., Moreno, C. E., Garmo, Ø. A., & Hagen, P. C. (2014). The effects of wildfire on the water chemistry of dilute, acidic lakes in southern Norway. *Ecosystems*, *119*(1), 109–124.

Mack, M. C., Walker, X. J., Johnstone, J. F., Alexander, H. D., Melvin, A. M., Jean, M., & Miller, S. N. (2021). Carbon loss from boreal forest wildfires offset by increased dominance of deciduous trees. *Science*, *372*(6539), 280–283.

McMillan, S. K., Wilson, H. F., Tague, C. L., Hanes, D. M., Inamdar, S., Karwan, D. L., et al. (2018). Before the storm: antecedent conditions as regulators of hydrologic and biogeochemical response to extreme climate events. *Ecosystems*, *141*(3), 487–501.

Mekonnen, Z. A., Riley, W. J., Randerson, J. T., Grant, R. F., & Rogers, B. M. (2019). Expansion of high-latitude deciduous forests driven by interactions between climate warming and fire. *Nature Plants*, 1–7.

Melvin, A. M., Mack, M. C., Johnstone, J. F., & Mcguire, A. D. (2015). Differences in ecosystem carbon distribution and nutrient cycling linked to forest tree species composition in a mid-successional boreal forest. *Ecosystems*, *18*, 1472–1488.

Moritz, S., & Bartz-Beielstein, T. (2017). imputeTS: time series missing value imputation in R. *R J.*, *9*(1), 207.

Murphy, S. F., McCleskey, R. B., Martin, D. A., Writer, J. H., & Ebel, B. A. (2018). Fire, flood, and drought: extreme climate events alter flow paths and stream chemistry. *Journal of Geophysical Research-Biogeosciences*, *123*, 2513–2526.

Musolff, A., Schmidt, C., Selle, B., & Fleckenstein, J. H. (2015). Catchment controls on solute export. *Advances in Water Resources*, *86*, 133–146. https://doi.org/10.1016/j.advwatres.2015.09.026

Mutschlecner, A. E., Guerard, J. J., Jones, J. B., & Harms, T. K. (2018). Phosphorus enhances uptake of dissolved organic matter in boreal streams. *Ecosystems*, *21*(4), 675–688. https://doi.org/10.1007/s10021-017-0177-1

Myrstener, M., Gómez-Gener, L., Rocher-Ros, G., Giesler, R., & Sponseller, R. A. (2021). Nutrients influence seasonal metabolic patterns and total productivity of Arctic streams. *Limnology and Oceanography*, *66*(S1), S182–S196. https://doi.org/10.1002/lno.11614

Odum, H. T. (1956). Primary Production in Flowing Waters1. *Limnology and Oceanography*, *1*(2), 102–117. https://doi.org/10.4319/lo.1956.1.2.0102

Osterkamp, T. E. (2007). Characteristics of the recent warming of permafrost in Alaska. *Journal of Geophysical Research*, *112*(F2), F02S02. https://doi.org/10.1029/2006JF000578

Park, T., Ganguly, S., Tømmervik, H., Euskirchen, E. S., Høgda, K.-A., Karlsen, S. R., et al. (2016). Changes in growing season duration and productivity of northern vegetation inferred from long-term remote sensing data. *Environmental Research Letters*, *11*(8), 084001. https://doi.org/10.1088/1748-9326/11/8/084001

Pastick, N. J., Jorgenson, M. T., Wylie, B. K., Nield, S. J., Johnson, K. D., & Finley, A. O. (2015). Distribution of near-surface permafrost in Alaska: Estimates of present and future conditions. *Remote Sensing of Environment*, *168*, 301–315. https://doi.org/10.1016/j.rse.2015.07.019

Peralta-Tapia, A., Sponseller, R. A., Ågren, A., Tetzlaff, D., Soulsby, C., & Laudon, H. (2015). Scale-dependent groundwater contributions influence patterns of winter baseflow stream chemistry in boreal catchments. *Journal of Geophysical Research: Biogeosciences*, *120*(5), 847–858. https://doi.org/10.1002/2014JG002878

Petrone, K., Hinzman, L., Shibata, H., Jones, J., & Boone, R. (2007). The influence of fire and permafrost on sub-arctic stream chemistry during storms. *Hydrological Processes*, *21*(4), 423–434.

Pimentel, R., & Arheimer, B. (2021). Hydrological impacts of a wildfire in a Boreal region: The Västmanland fire 2014 (Sweden). *Science of The Total Environment*, *756*, 143519. https://doi.org/10.1016/j.scitotenv.2020.143519

Pinheiro, J., Bates, D., DebRoy, S., Sarkar, D., Heisterkamp, S., Van Willigen, B., & Maintainer, R. (2017). Package 'nlme.' *Linear and Nonlinear Mixed Effects Models, Version*, *3*(1), 274.

Quinton, W., & Marsh, P. (1999). A conceptual framework for runoff generation in a permafrost environment. *Hydrological Processes*, *13*(16), 2563–2581.

Rhoades, C. C., Chow, A. T., Covino, T. P., Fegel, T. S., Pierson, D. N., & Rhea, A. E. (2019). The legacy of a severe wildfire on stream nitrogen and carbon in headwater catchments. *Ecosystems*, *22*(3), 643–657.

Rocher-Ros, G., Sponseller, R. A., Bergström, A., Myrstener, M., & Giesler, R. (2020). Stream metabolism controls diel patterns and evasion of CO_2 in Arctic streams. *Global Change Biology*, *26*(3), 1400–1413. https://doi.org/10.1111/gcb.14895

Rocher-Ros, G., Harms, T. K., Sponseller, R. A., Väisänen, M., Mörth, C., & Giesler, R. (2021). Metabolism overrides photo-oxidation in CO_2 dynamics of Arctic permafrost streams. *Limnology and Oceanography*, *66*(S1), S169–S181. https://doi.org/10.1002/lno.11564

Rodríguez-Cardona, B. M., Coble, A. A., Wymore, A. S., Kolosov, R., Podgorski, D. C., Zito, P., et al. (2020). Wildfires lead to decreased carbon and increased nitrogen concentrations in upland arctic streams. *Scientific Reports*, *10*(1), 8722. https://doi.org/10.1038/s41598-020-65520-0

Roesch, A., & Schmidbauer, H. (2018). WaveletComp (Version 1.1).

Rollinson, C. R., Liu, Y., Raiho, A., Moore, D. J. P., McLachlan, J., Bishop, D. A., et al. (2017). Emergent climate and CO $_2$ sensitivities of net primary productivity in ecosystem models do not agree with empirical data in temperate forests of eastern North America. *Global Change Biology*, *23*(7), 2755–2767. https://doi.org/10.1111/gcb.13626

Rose, L. A., & Karwan, D. L. (2021). Stormflow concentration–discharge dynamics of suspended sediment and dissolved phosphorus in an agricultural watershed. *Hydrological Processes*, *35*(12), e14455.

Ruosteenoja, K., Räisänen, J., Venäläinen, A., & Kämäräinen, M. (2016). Projections for the duration and degree days of the thermal growing season in Europe derived from CMIP5 model output. *International Journal of Climatology*, *36*(8), 3039–3055.

Rust, A. J., Saxe, S., McCray, J., Rhoades, C. C., Hogue, T. S., Rust, A. J., et al. (2019). Evaluating the factors responsible for post-fire water quality response in forests of the western USA. *International Journal of Wildland Fire*, *28*(10), 769–784.

Scheffer, M, Carpenter, S. R., Dakos, V., & van Nes, E. H. (2015). Generic indicators of ecological resilience: inferring the chance of a critical transition. *Annual Review of Ecology, Evolution, and Systematics*.

Scheffer, Marten, Bascompte, J., Brock, W. A., Brovkin, V., Carpenter, S. R., Dakos, V., et al. (2009). Early-warning signals for critical transitions. *Nature*, *461*(7260), 53–59.

Shogren, A. J., Zarnetske, J. P., Abbott, B. W., Iannucci, F., Medvedeff, A., Cairns, S., et al. (2021). Arctic concentration–discharge relationships for dissolved organic carbon and nitrate vary with landscape and season. *Limnology and Oceanography*, *66*(S1), S197–S215. https://doi.org/10.1002/lno.11682

Sigman, D. M., Casciotti, K. L., Andreani, M., Barford, C., Galanter, M., & Böhlke, J. K. (2001). A bacterial method for the nitrogen isotopic analysis of nitrate in seawater and freshwater. *Analytical Chemistry*, *73*(17), 4145–4153.

Smith, S. L., O'Neill, H. B., Isaksen, K., Noetzli, J., & Romanovsky, V. E. (2022). The changing thermal state of permafrost. *Nature Reviews Earth & Environment*, *3*(1), 10–23. https://doi.org/10.1038/s43017-021-00240-1

Snyder, L., Potter, J. D., & McDowell, W. H. (2018). An evaluation of nitrate, fDOM, and turbidity sensors in New Hampshire streams. *Water Resources Research*, *54*(3), 2466–2479.

Stock, B. C., Jackson, A. L., Ward, E. J., Parnell, A. C., Phillips, D. L., & Semmens, B. X. (2018). Analyzing mixing systems using a new generation of Bayesian tracer mixing models. *PeerJ*, *6*, e5096. https://doi.org/10.7717/peerj.5096

Tank, S. E., Striegl, R. G., McClelland, J. W., & Kokelj, S. V. (2016). Multi-decadal increases in dissolved organic carbon and alkalinity flux from the Mackenzie drainage basin to the Arctic Ocean. *Environmental Research Letters*, *11*(5), 054015. https://doi.org/10.1088/1748-9326/11/5/054015

Tetzlaff, D., Buttle, J., Carey, S. K., McGuire, K., Laudon, H., & Soulsby, C. (2015). Tracer-based assessment of flow paths, storage and runoff generation in northern catchments: a review. *Hydrological Processes*, *29*(16), 3475–3490. https://doi.org/10.1002/hyp.10412

Treseder, K. K., Mack, M. C., & Cross, A. (2004). Relationships among fires, fungi, and soil dynamics in Alaskan boreal forests. *Ecological Applications*, *14*(6), 1826–1838. https://doi.org/10.1890/03-5133

Ueyama, M., Iwata, H., Harazono, Y., Euskirchen, E. S., Oechel, W. C., & Zona, D. (2013). Growing season and spatial variations of carbon fluxes of Arctic and boreal ecosystems in Alaska (USA). *Ecological Applications*, *23*(8), 1798–1816. https://doi.org/10.1890/11-0875.1

Vaughan, M. C. H., Bowden, W. B., Shanley, J. B., Vermilyea, A., Sleeper, R., Gold, A. J., et al. (2017). High-frequency dissolved organic carbon and nitrate measurements reveal differences in storm hysteresis and loading in relation to land cover and seasonality. *Water Resources Research*, *53*(7), 5345–5363.

Walvoord, M A, & Kurylyk, B. L. (2016). Hydrologic impacts of thawing permafrost—A review. *Vadose Zone Journal*.

Walvoord, Michelle A., & Striegl, R. G. (2007). Increased groundwater to stream discharge from permafrost thawing in the Yukon River basin: Potential impacts on lateral export of carbon and nitrogen. *Geophysical Research Letters*, *34*(12), L12402. https://doi.org/10.1029/2007GL030216

Wang, R., Dearing, J. A., Langdon, P. G., Zhang, E., Yang, X., Dakos, V., & Scheffer, M. (2012). Flickering gives early warning signals of a critical transition to a eutrophic lake state. *Nature*, *492*, 419–422.

Watras, C. J., Hanson, P. C., Stacy, T. L., Morrison, K. M., Mather, J., Hu, Y.-H., & Milewski, P. (2011). A temperature compensation method for CDOM fluorescence sensors in freshwater: CDOM temperature compensation. *Limnology and Oceanography: Methods*, *9*(7), 296–301. https://doi.org/10.4319/lom.2011.9.296

Watras, C. J., Morrison, K. A., Mather, J., & Hanson, P. C. (n.d.). Correcting CDOM fluorescence measurements for temperature effects under field conditions in freshwaters. *Limnology and Oceanography*, *12*(1), 23–24.

Webster, A. J., Douglas, T. A., Regier, P., Scheuerell, M. D., & Harms, T. K. (2022). Multi-scale temporal patterns in stream biogeochemistry indicate linked permafrost and ecological dynamics of boreal catchments. *Ecosystems*, *25*, 1189–1206.

Webster, J. R., Knoepp, J. D., Swank, W., & Miniat, C. F. (2016). Evidence for a regime shift in nitrogen export from a forested watershed. *Ecosystems*, *19*, 881–895.

Wen, H., Ciamarra, M. P., & Cheong, S. A. (2018). How one might miss early warning signals of critical transitions in time series data: A systematic study of two major currency pairs. *PLOS ONE*, *13*(3), e0191439. https://doi.org/10.1371/journal.pone.0191439

Wickland, K. P., Neff, J. C., & Aiken, G. R. (2007). Dissolved organic carbon in Alaskan boreal forest: sources, chemical characteristics, and biodegradability. *Ecosystems*, *10*(8), 1323–1340. https://doi.org/10.1007/s10021-007-9101-4

Wilkinson, G. M., Carpenter, S. R., Cole, J. J., Pace, M. L., Batt, R. D., Buelo, C. D., & Kurtzweil, J. T. (2018). Early warnings precede cyanobacteria blooms in multiple whole-lake experiments. *Ecological Monographs*, *88*, 188–203.

Winter, C., Tarasova, L., Lutz, S. R., Musolff, A., Kumar, R., & Fleckenstein, J. H. (2022). Explaining the variability in high-frequency nitrate export patterns using long-term hydrological event classification. *Water Resources Research*, *58*(1). https://doi.org/10.1029/2021WR030938

Wolken, J. M., Hollingsworth, T. N., Rupp, T. S., Chapin, F. S., III, Trainor, S. F., Barrett, T. M., et al. (2011). Evidence and implications of recent and projected climate change in Alaska's forest ecosystems. *Ecosphere*, *2*(11), art124.

Wolock, D. M., Fan, J., & Lawrence, G. B. (1997). Effects of basin size on low-flow stream chemistry and subsurface contact time in the Neversink River watershed, New York. *Hydrological Processes*, *11*(9), 1273–1286.

Yarie, J., & Van Cleve, K. (2006). Controls over forest production in interior Alaska. *Alaska's Changing Boreal Forest*, *171*, 188.

Yoshikawa, K., White, D., Hinzman, L., Goering, D., Petrone, K., Bolton, W., et al. (2003). Water in permafrost; case study of aufeis and pingo hydrology in discontinuous permafrost (pp. 21–25). Presented at the Proceedings, Eighth International Conference on Permafrost, Zurich.

Yuan, W., Liu, S., Liu, H., Randerson, J. T., Yu, G., & Tieszen, L. L. (2010). Impacts of precipitation seasonality and ecosystem types on evapotranspiration in the Yukon River Basin, Alaska. *Water Resources Research*, *46*(2). https://doi.org/10.1029/2009WR008119

Zolkos, S., MacDonald, E., Hung, J. K. Y., Schade, J. D., Ludwig, S., Mann, P. J., et al. (2022). Physiographic Controls and Wildfire Effects on Aquatic Biogeochemistry in Tundra of

the Yukon-Kuskokwim Delta, Alaska. *Journal of Geophysical Research: Biogeosciences*. https://doi.org/10.1029/2022JG006891

APPENDIX A: Supporting Data

Temporal patterns in instream gross primary production

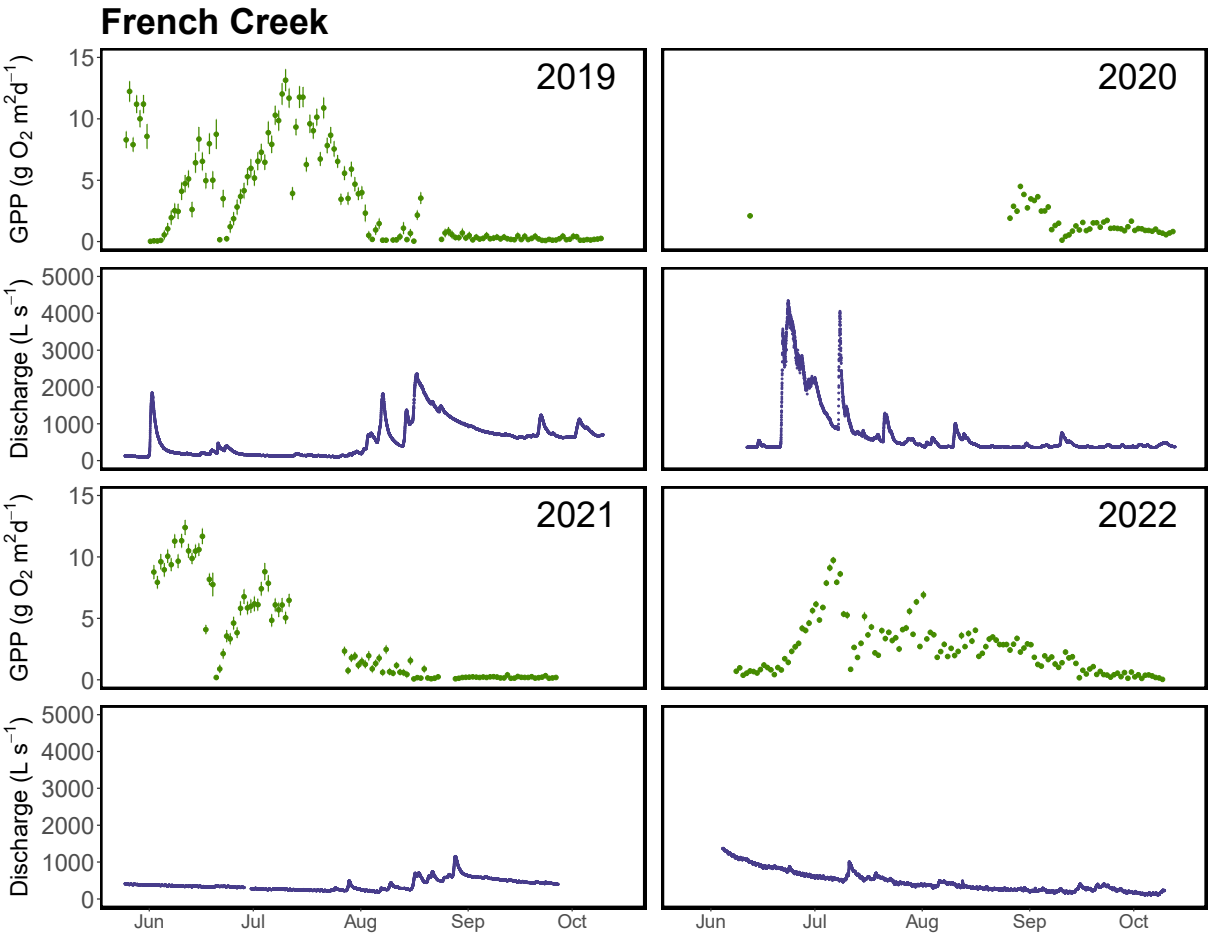


Figure A1.1. Modeled rates of gross primary production (GPP) and stream discharge in French Creek.

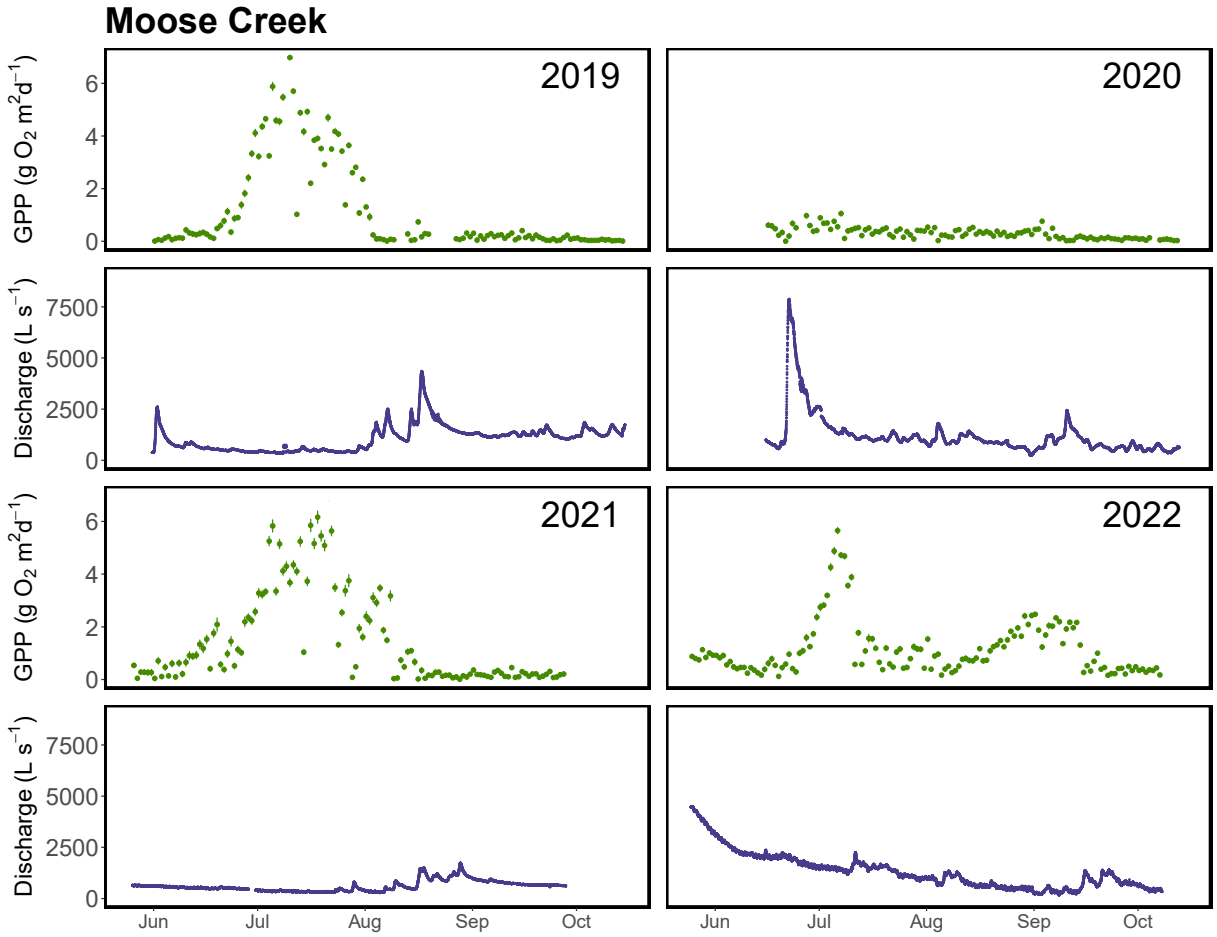


Figure A1.2. Modeled rates of gross primary production (GPP) and stream discharge in Moose Creek.

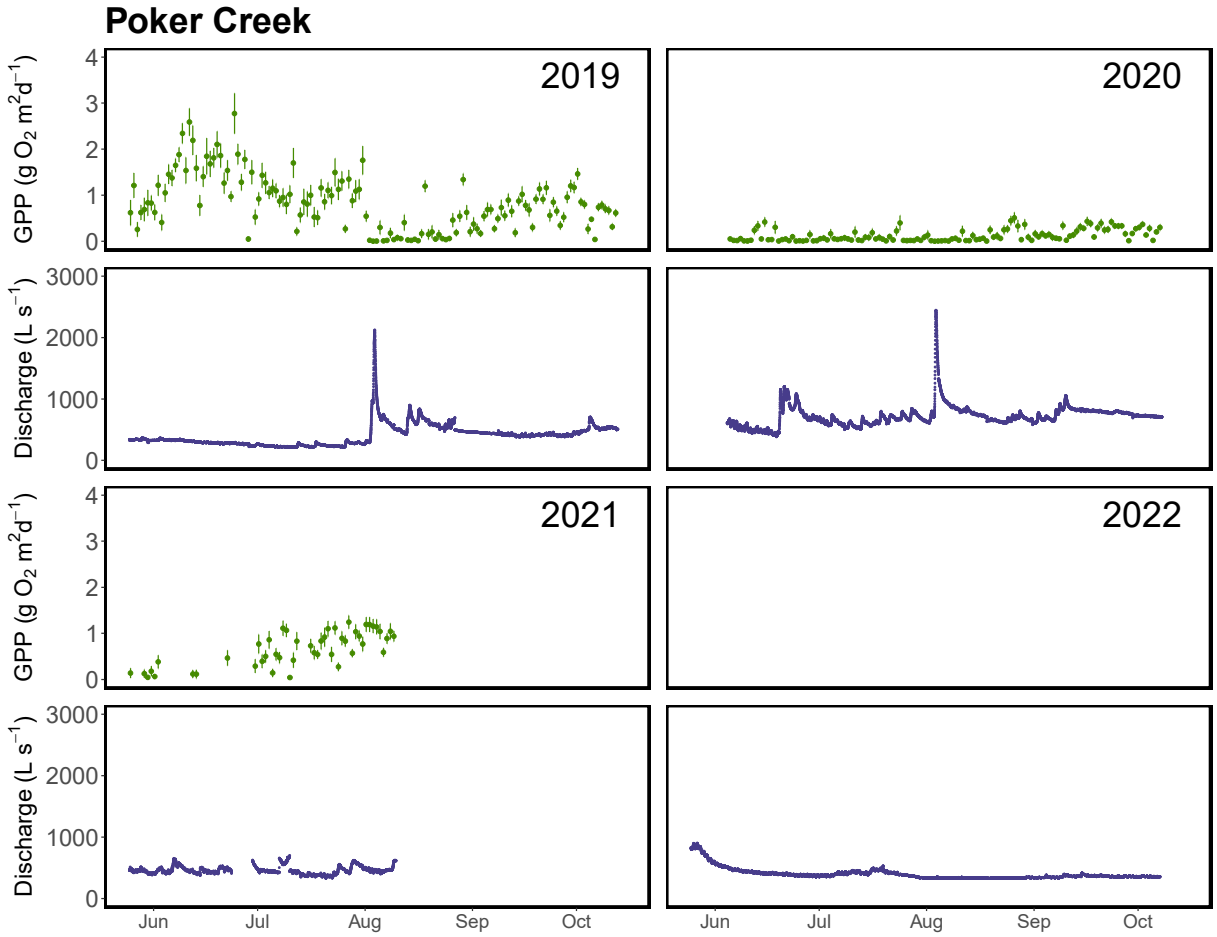


Figure A1.3. Modeled rates of gross primary production (GPP) and stream discharge in Poker Creek.

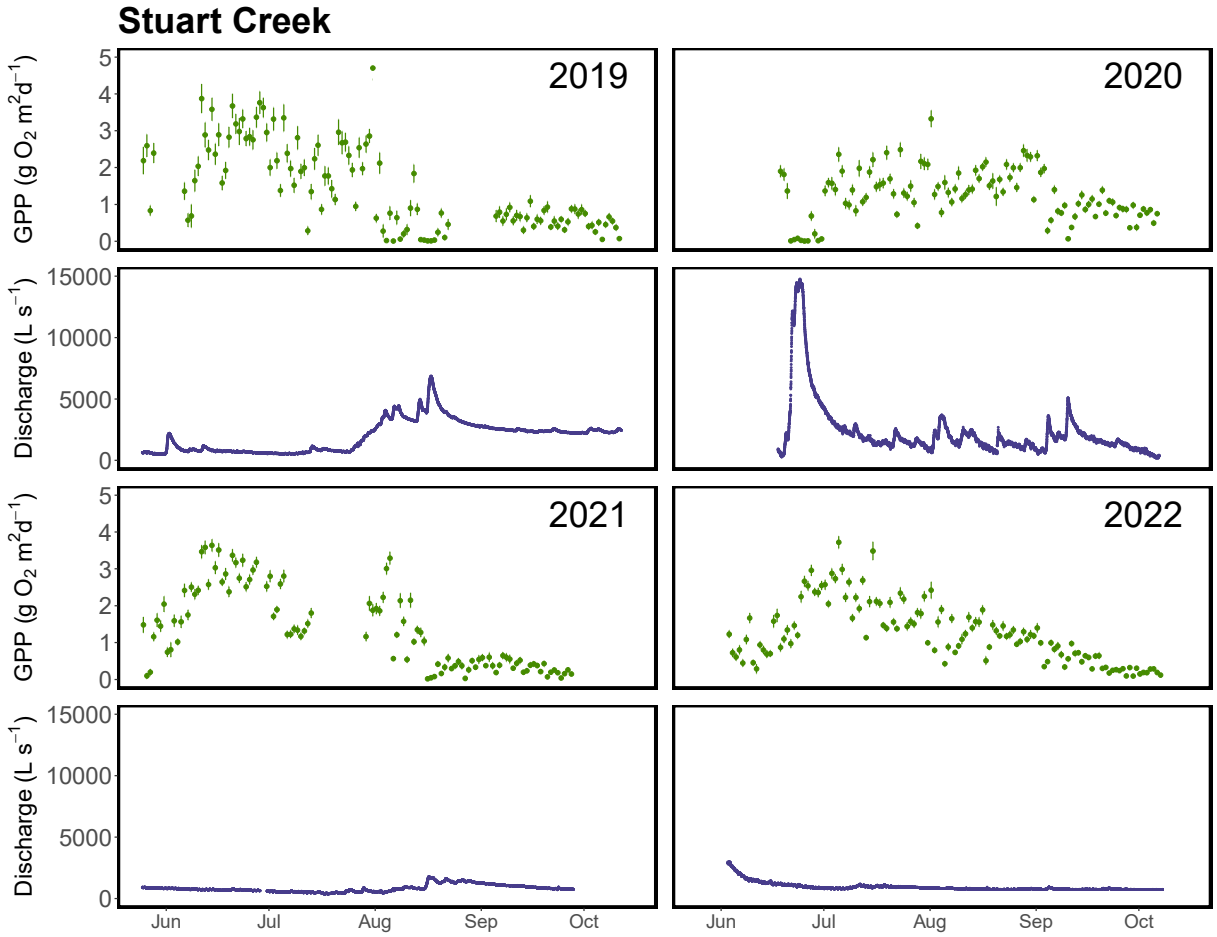


Figure A1.4. Modeled rates of gross primary production (GPP) and stream discharge in Stuart Creek.

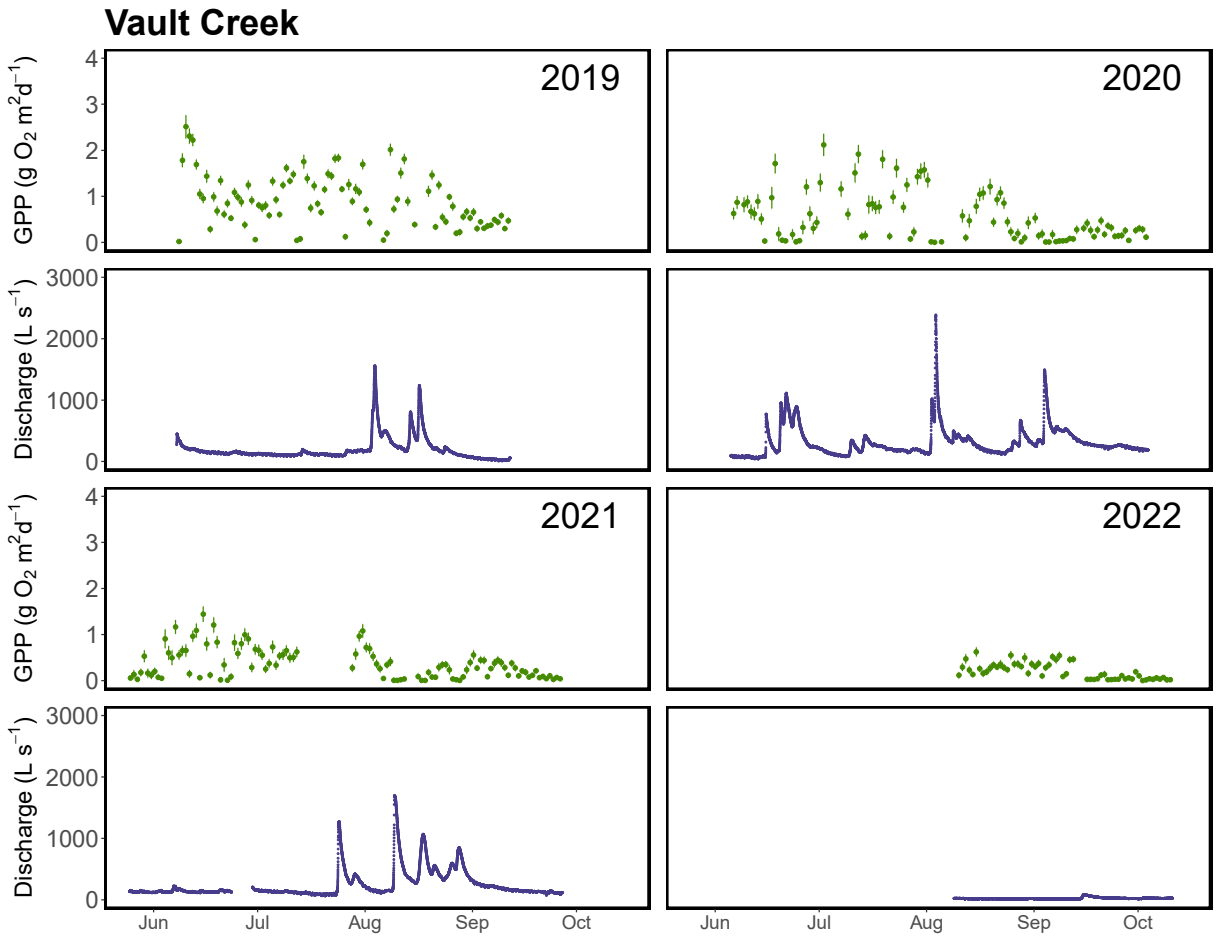


Figure A1.5. Modeled rates of gross primary production (GPP) and stream discharge in Vault Creek.

Wavelet transform and wavelet coherence plots

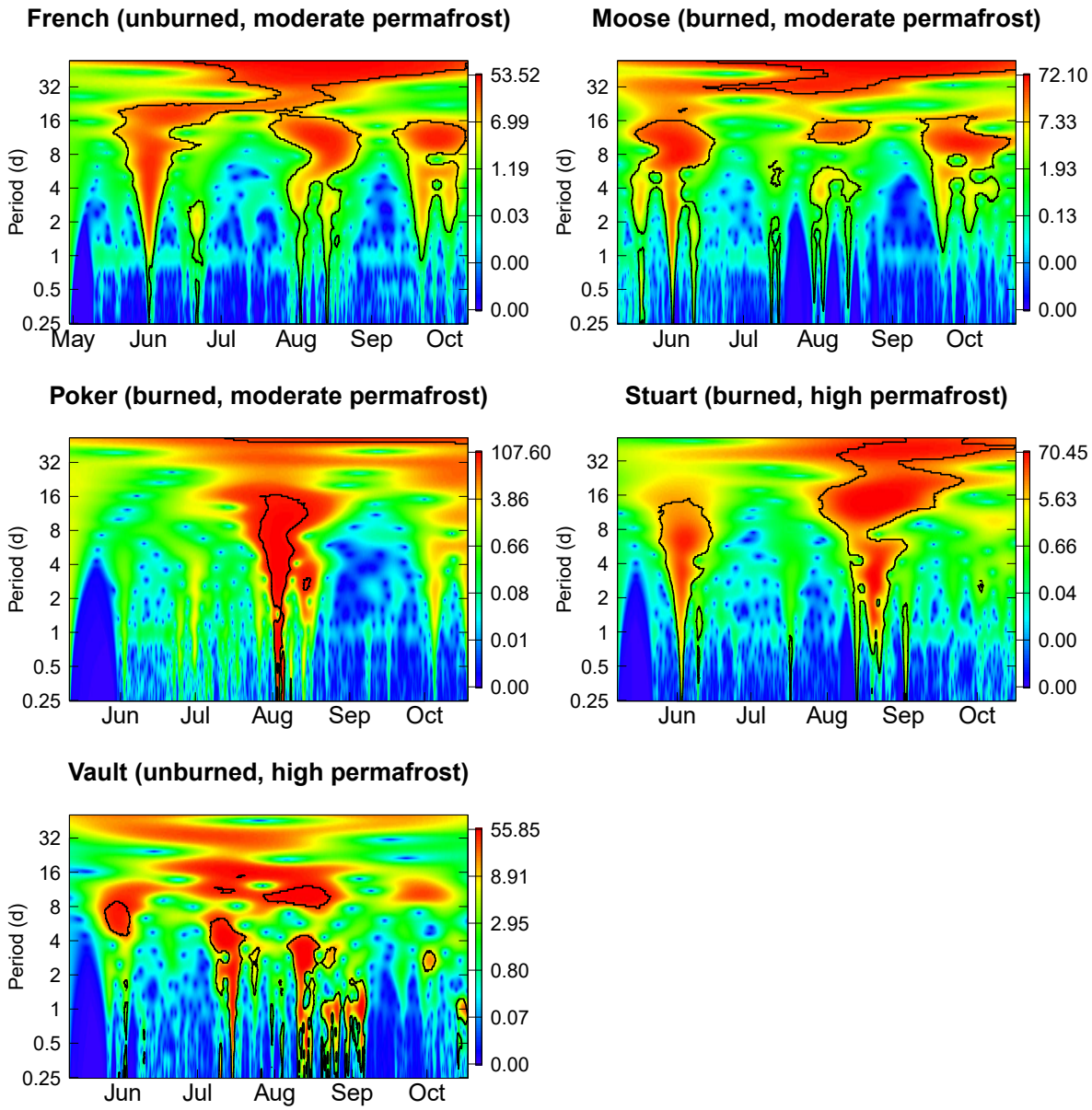


Figure A2.1. Wavelet transform of abs254 in 2019. The vertical axis displays frequencies and the scale bar indicates wavelet power (square of amplitude), with warmer colors associated with greater variation. Black outlines designate variation that is significantly greater ($\alpha = 0.05$) than expected from an autoregressive time series. The shaded cone indicates values with little data support. Note that the temporal extent (horizontal axis) varies across the streams.

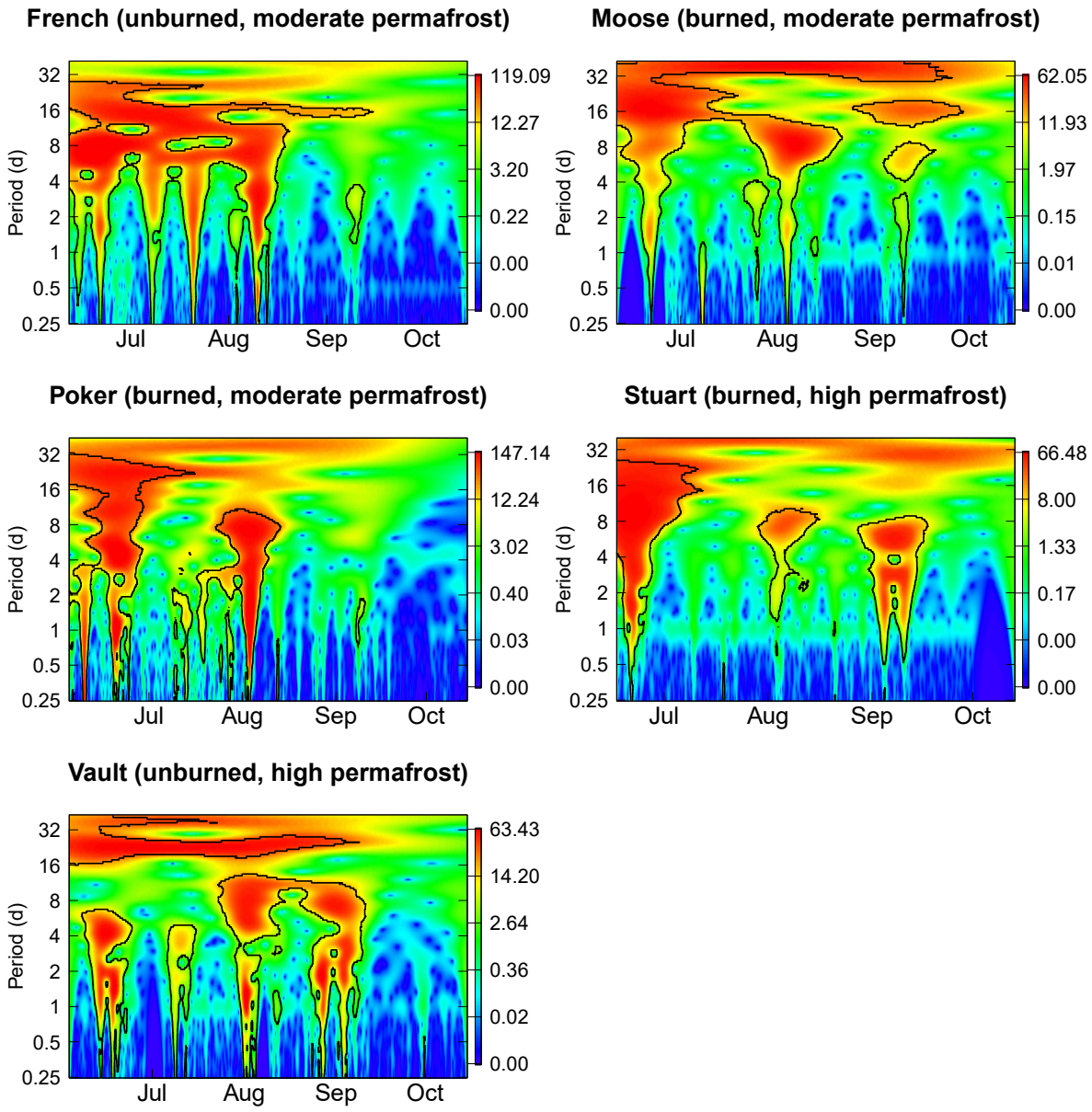


Figure A2.2. Wavelet transform of abs254 in 2020. The vertical axis displays frequencies and the scale bar indicates wavelet power (square of amplitude), with warmer colors associated with greater variation. Black outlines designate variation that is significantly greater (α = 0.05) than expected from an autoregressive time series. The shaded cone indicates values with little data support. Note that the temporal extent (horizontal axis) varies across the streams.

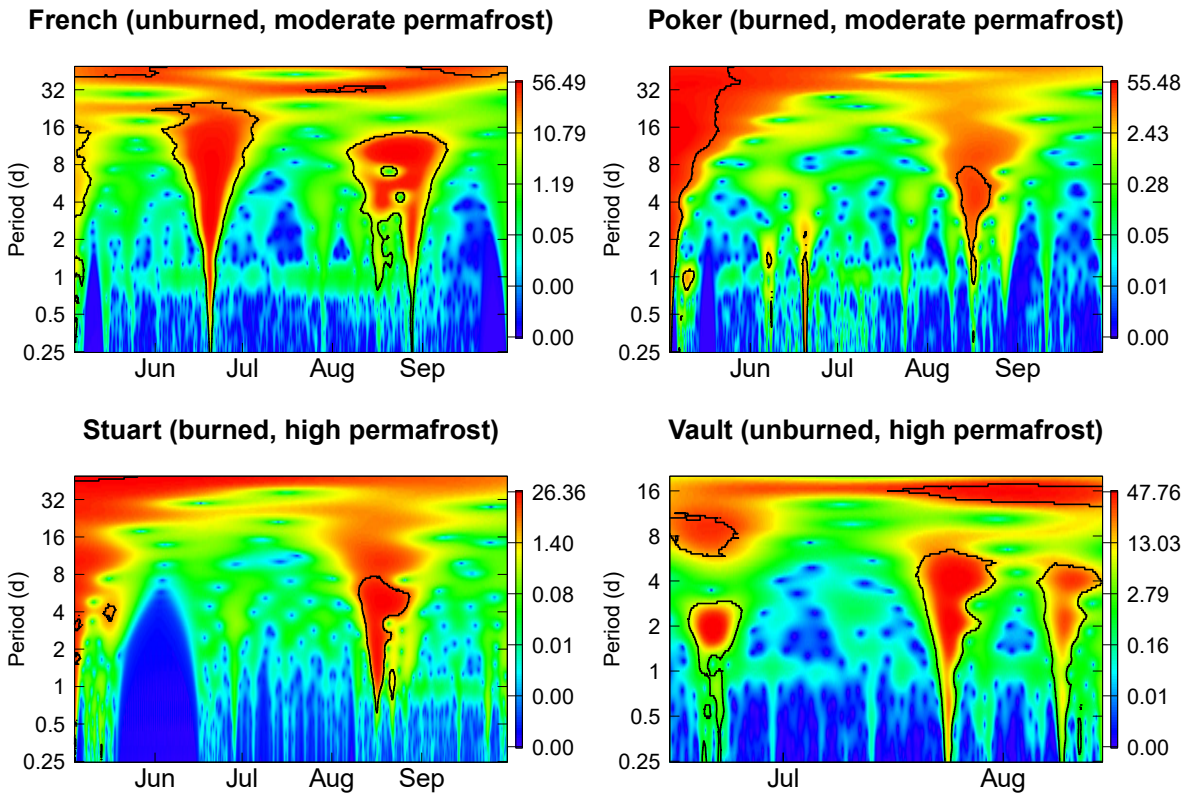


Figure A2.3. Wavelet transform of abs254 in 2021. The vertical axis displays frequencies and the scale bar indicates wavelet power (square of amplitude), with warmer colors associated with greater variation. Black outlines designate variation that is significantly greater ($\alpha = 0.05$) than expected from an autoregressive time series. The shaded cone indicates values with little data support. Note that the temporal extent (horizontal axis) varies across the streams. Insufficient data were available from Moose Creek in 2021 to support the analysis.

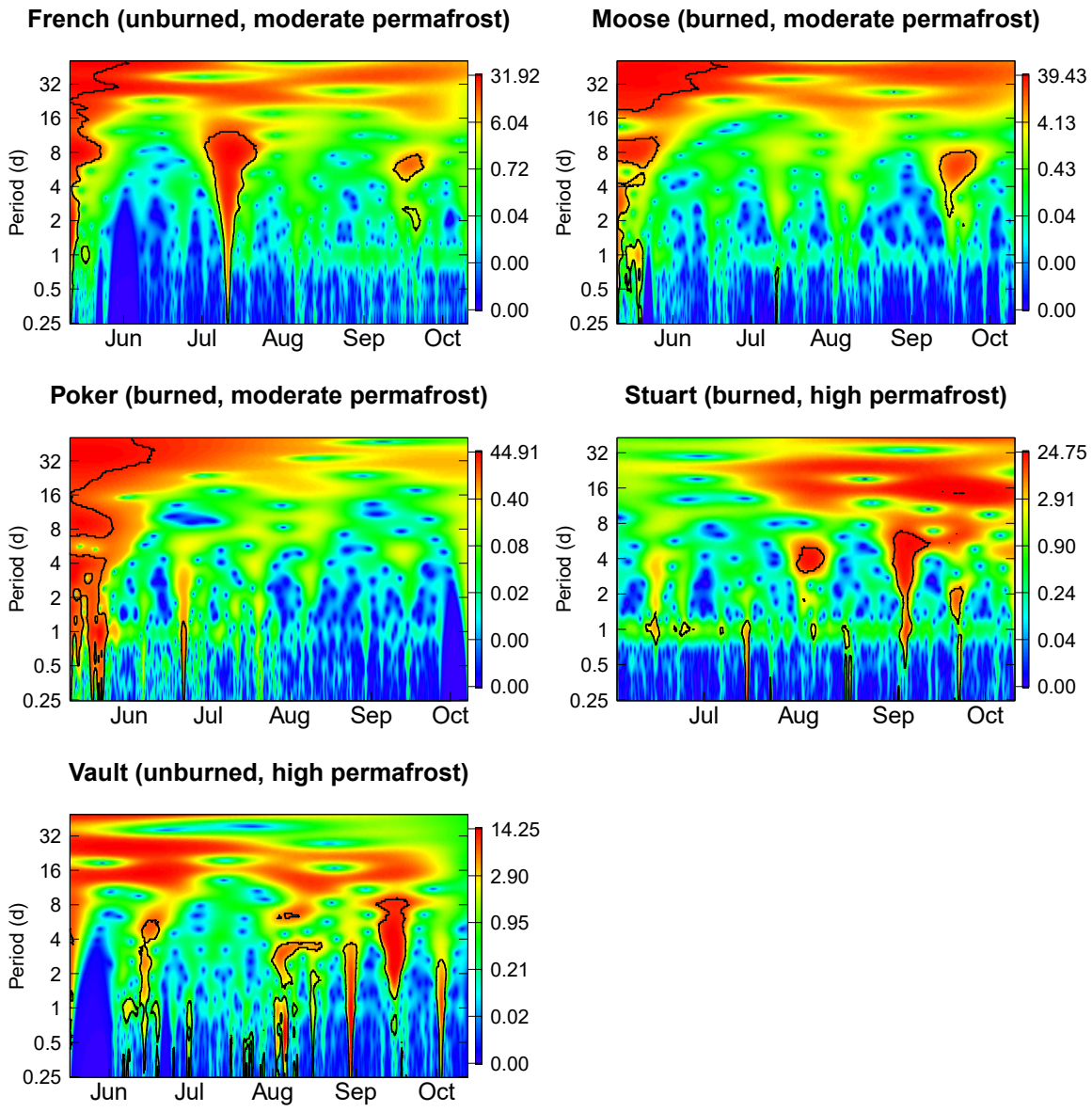


Figure A2.4. Wavelet transform of abs254 in 2022. The vertical axis displays frequencies and the scale bar indicates wavelet power (square of amplitude), with warmer colors associated with greater variation. Black outlines designate variation that is significantly greater ($\alpha = 0.05$) than expected from an autoregressive time series. The shaded cone indicates values with little data support. Note that the temporal extent (horizontal axis) varies across the streams.

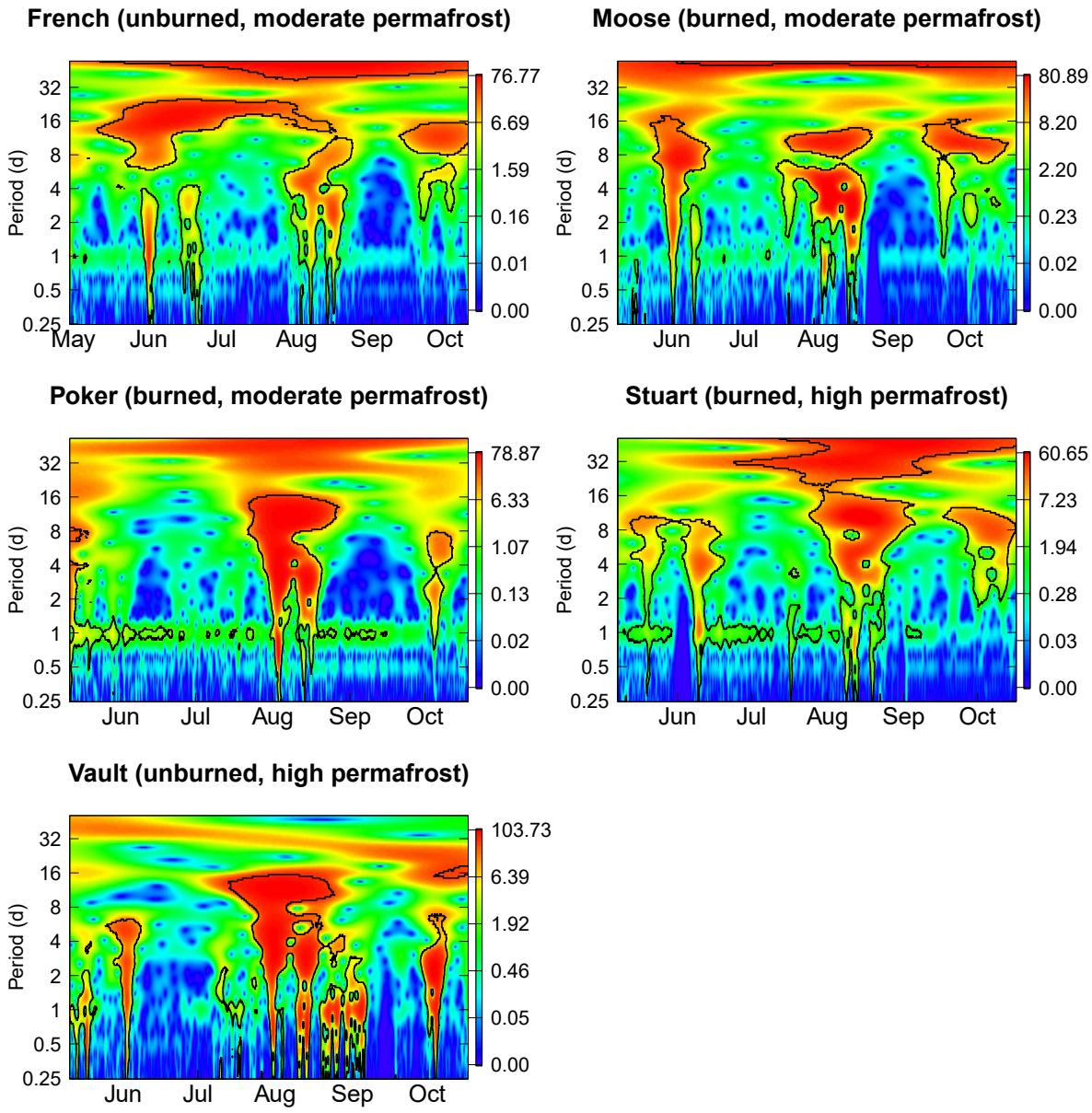


Figure A2.5. Wavelet transform of fDOM in 2019. The vertical axis displays frequencies and the scale bar indicates wavelet power (square of amplitude), with warmer colors associated with greater variation. Black outlines designate variation that is significantly greater (α = 0.05) than expected from an autoregressive time series. The shaded cone indicates values with little data support. Note that the temporal extent (horizontal axis) varies across the streams.

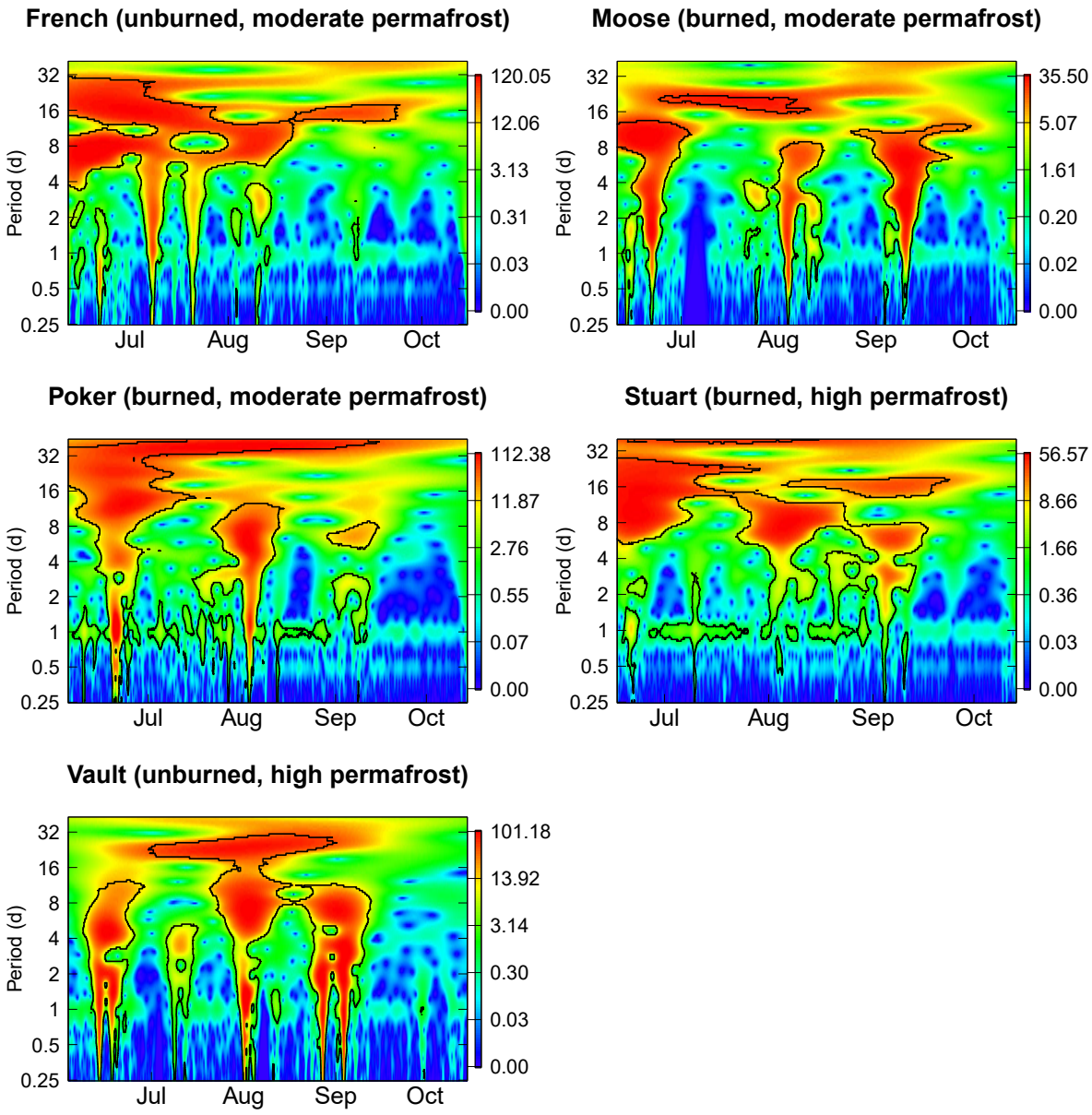


Figure A2.6. Wavelet transform of fDOM in 2020. The vertical axis displays frequencies and the scale bar indicates wavelet power (square of amplitude), with warmer colors associated with greater variation. Black outlines designate variation that is significantly greater (α = 0.05) than expected from an autoregressive time series. The shaded cone indicates values with little data support. Note that the temporal extent (horizontal axis) varies across the streams.

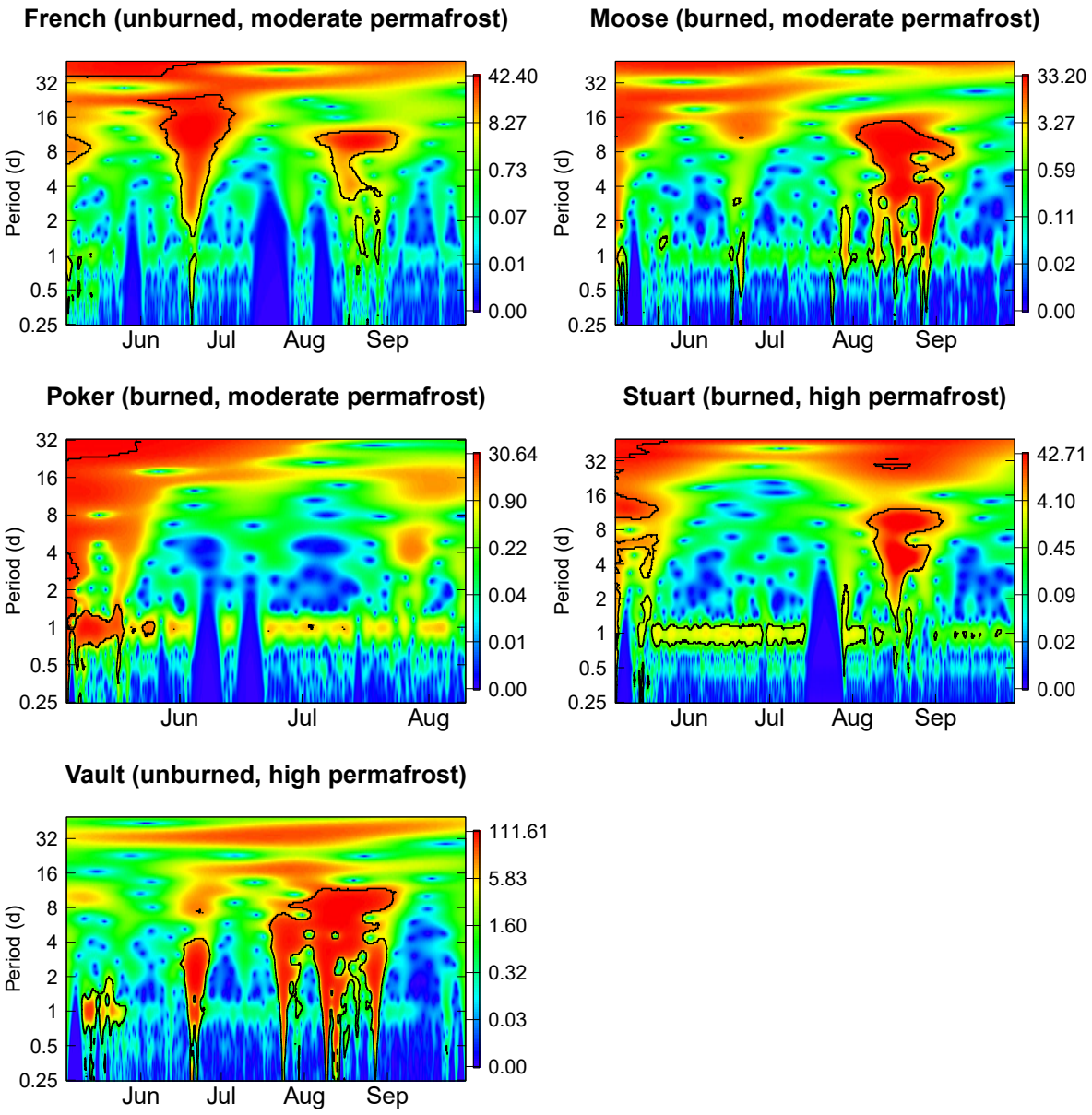


Figure A2.7. Wavelet transform of fDOM in 2021. The vertical axis displays frequencies and the scale bar indicates wavelet power (square of amplitude), with warmer colors associated with greater variation. Black outlines designate variation that is significantly greater (α = 0.05) than expected from an autoregressive time series. The shaded cone indicates values with little data support. Note that the temporal extent (horizontal axis) varies across the streams.

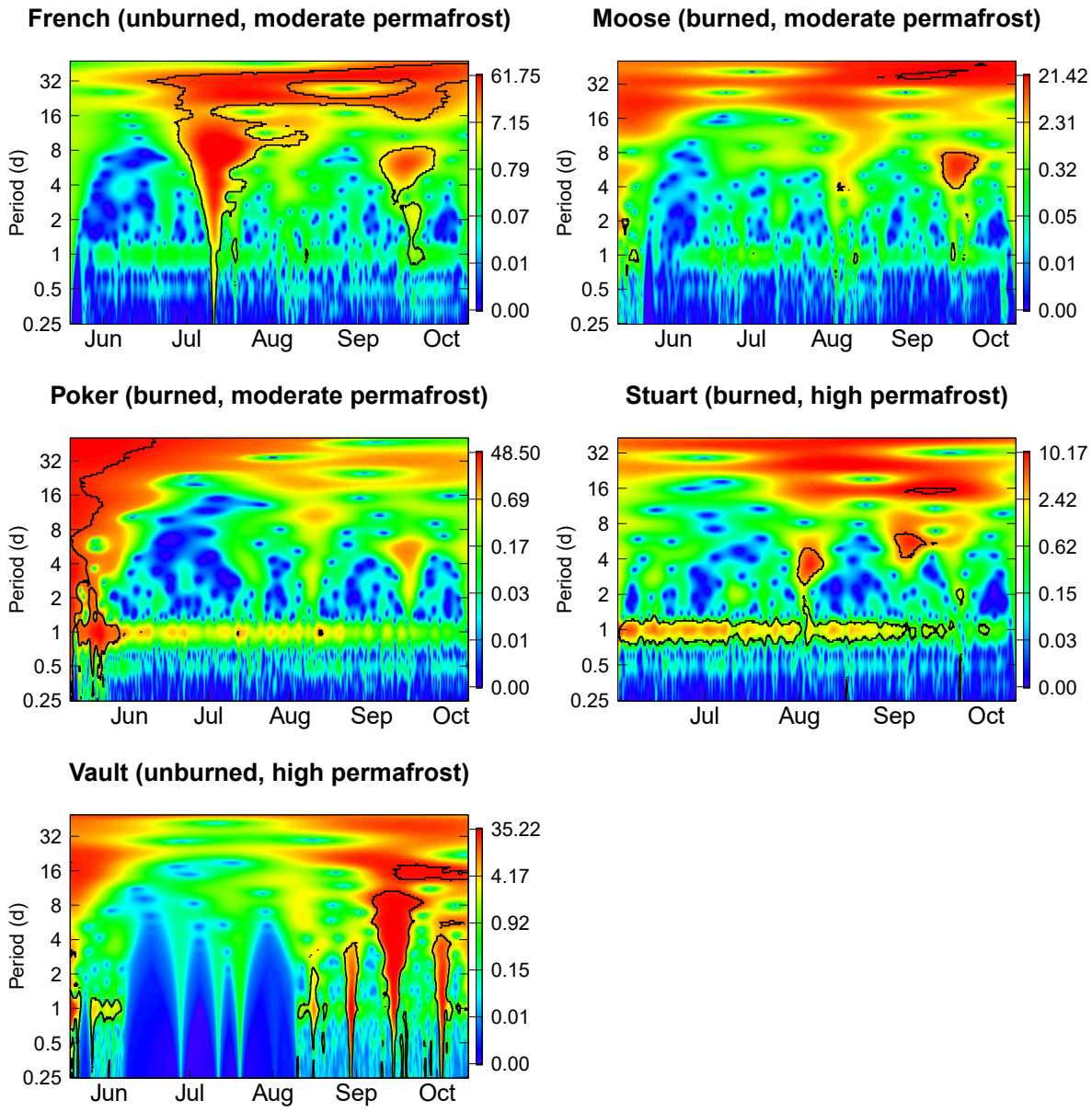


Figure A2.8. Wavelet transform of fDOM in 2022. The vertical axis displays frequencies and the scale bar indicates wavelet power (square of amplitude), with warmer colors associated with greater variation. Black outlines designate variation that is significantly greater (α = 0.05) than expected from an autoregressive time series. The shaded cone indicates values with little data support. Note that the temporal extent (horizontal axis) varies across the streams.

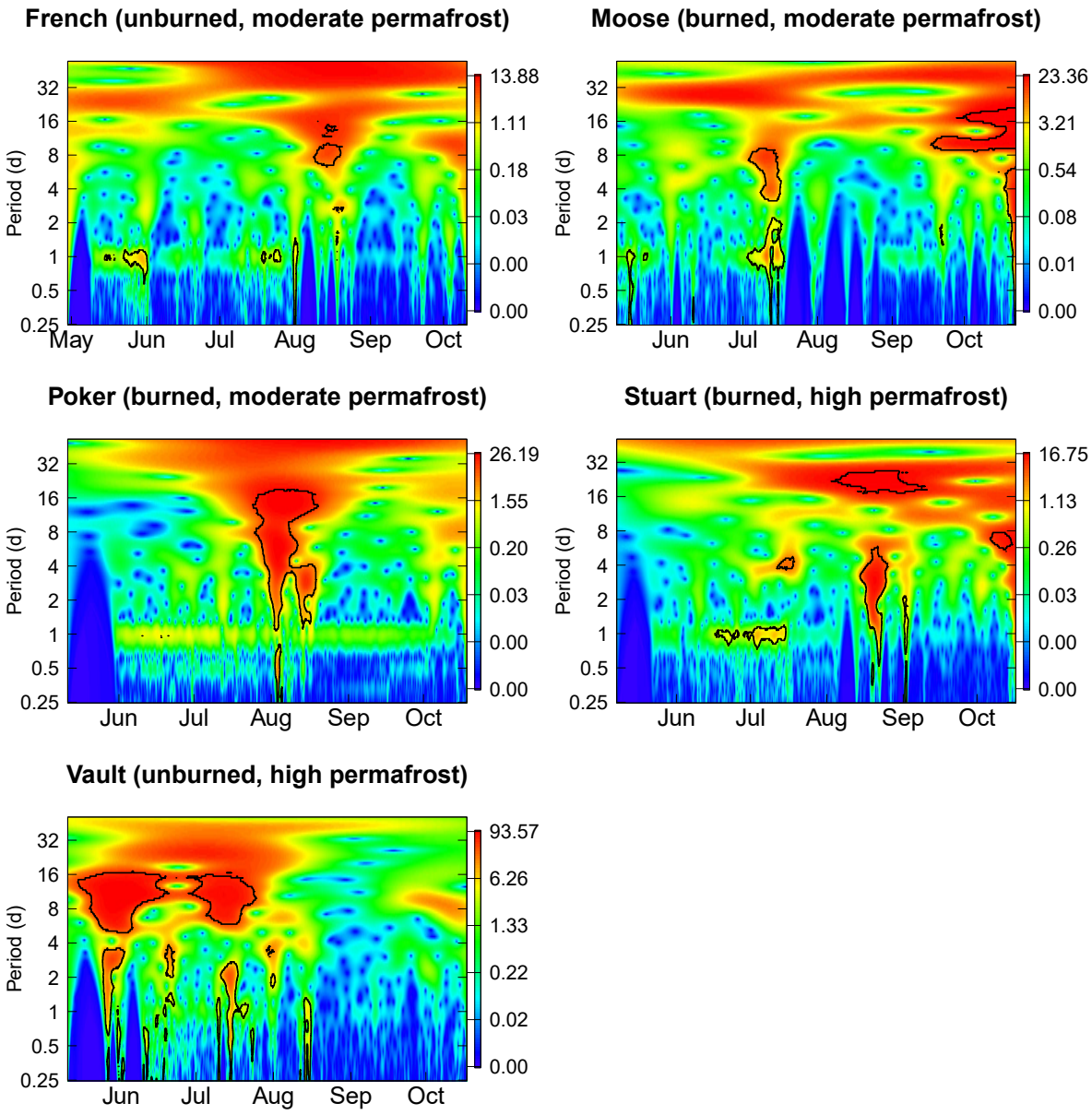


Figure A2.9. Wavelet transform of NO_3^- in 2019. The vertical axis displays frequencies and the scale bar indicates wavelet power (square of amplitude), with warmer colors associated with greater variation. Black outlines designate variation that is significantly greater ($\alpha = 0.05$) than expected from an autoregressive time series. The shaded cone indicates values with little data support. Note that the temporal extent (horizontal axis) varies across the streams.

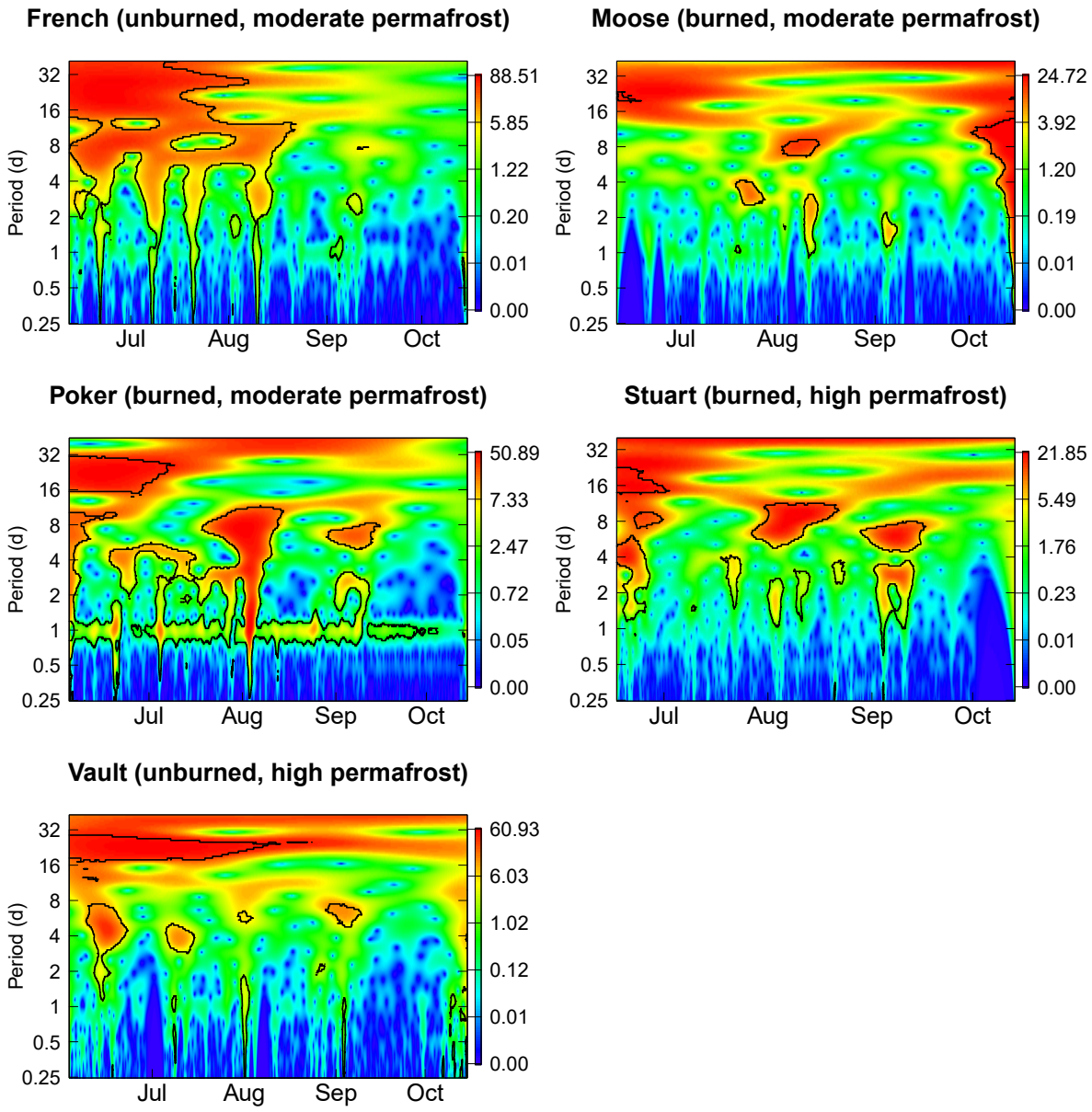


Figure A2.10. Wavelet transform of NO_3^- in 2020. The vertical axis displays frequencies and the scale bar indicates wavelet power (square of amplitude), with warmer colors associated with greater variation. Black outlines designate variation that is significantly greater ($\alpha = 0.05$) than expected from an autoregressive time series. The shaded cone indicates values with little data support. Note that the temporal extent (horizontal axis) varies across the streams.

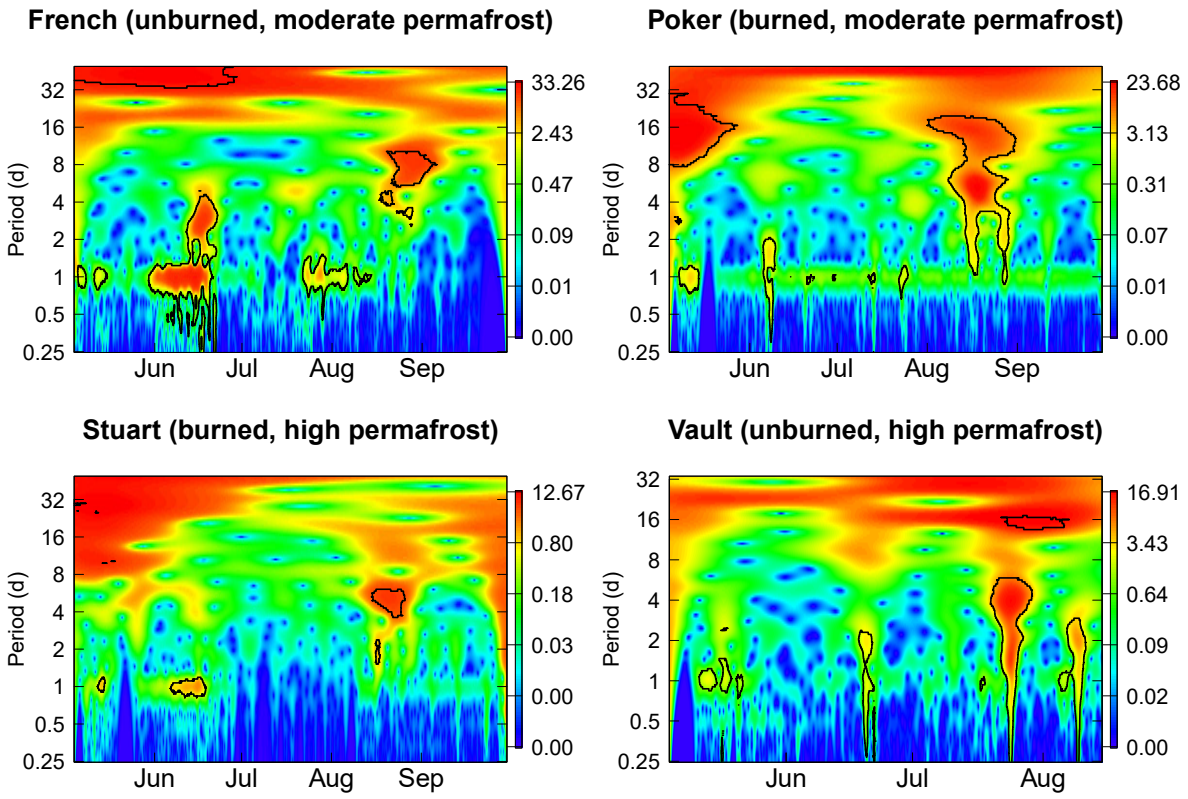


Figure A2.11. Wavelet transform of NO_3^- in 2021. The vertical axis displays frequencies and the scale bar indicates wavelet power (square of amplitude), with warmer colors associated with greater variation. Black outlines designate variation that is significantly greater ($\alpha = 0.05$) than expected from an autoregressive time series. The shaded cone indicates values with little data support. Note that the temporal extent (horizontal axis) varies across the streams. Insufficient data from Moose Creek were available to support the analysis.

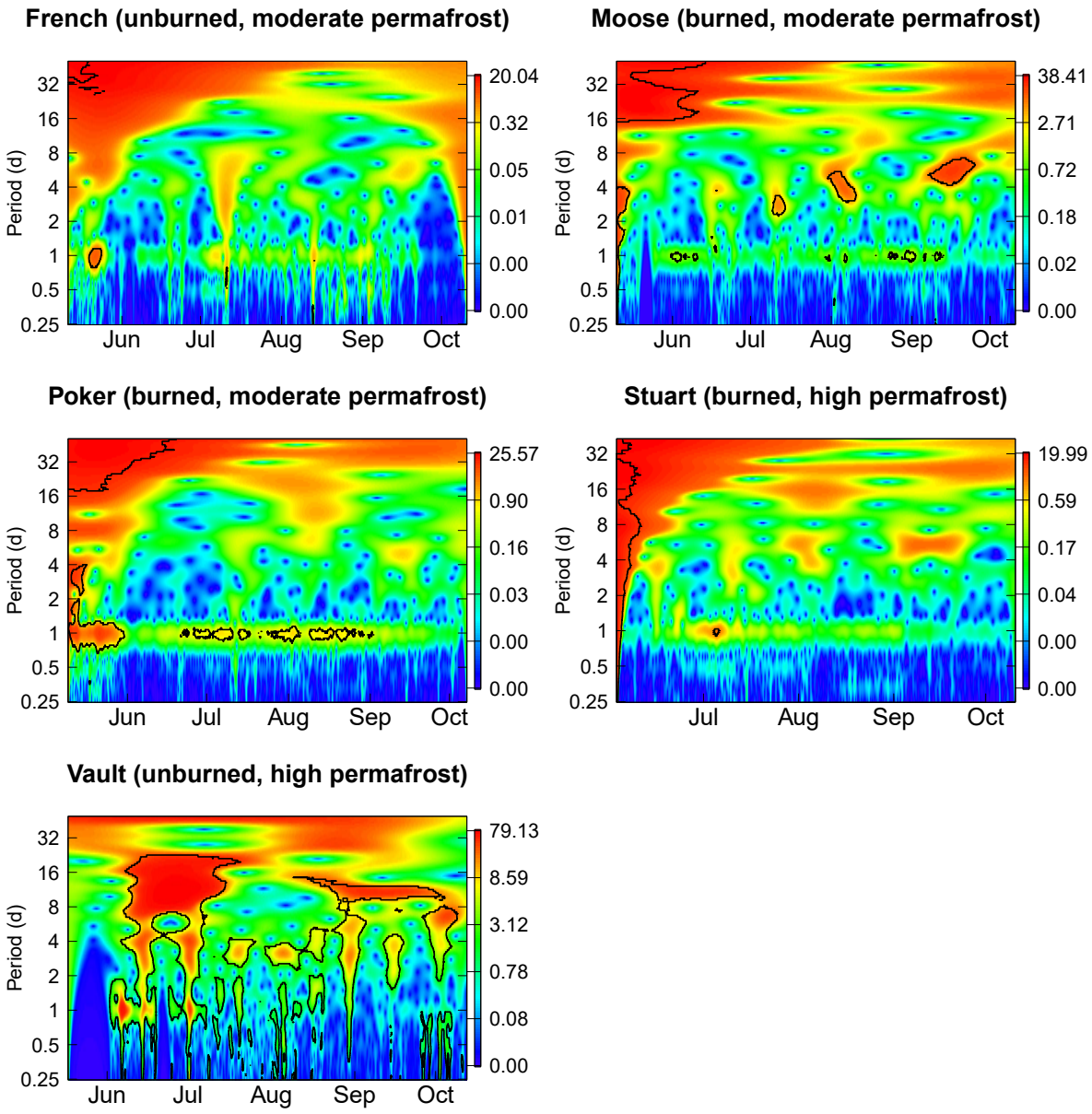


Figure A2.12. Wavelet transform of NO_3^- in 2022. The vertical axis displays frequencies and the scale bar indicates wavelet power (square of amplitude), with warmer colors associated with greater variation. Black outlines designate variation that is significantly greater ($\alpha = 0.05$) than expected from an autoregressive time series. The shaded cone indicates values with little data support. Note that the temporal extent (horizontal axis) varies across the streams.

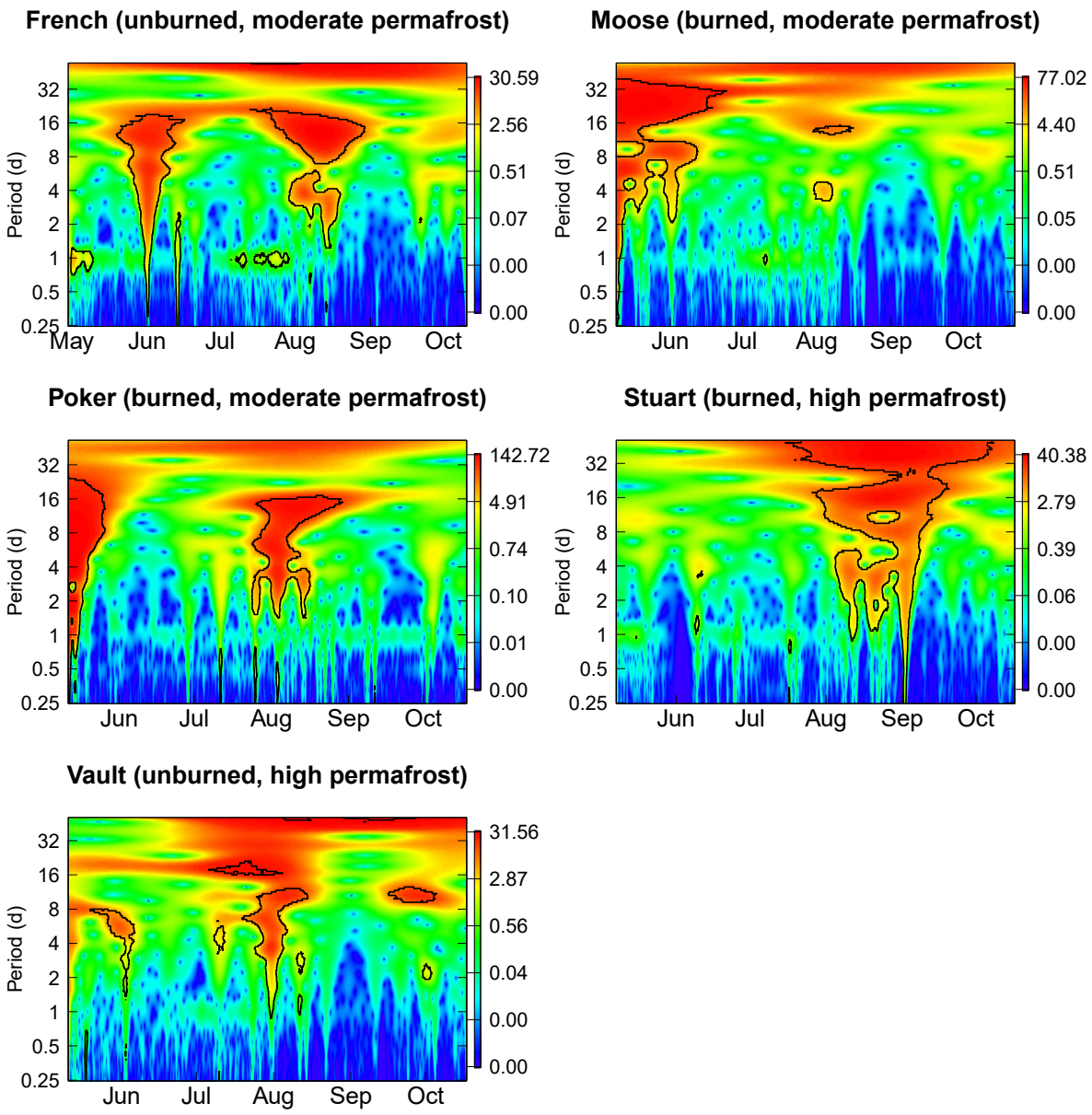


Figure A2.13. Wavelet transform of specific conductivity in 2019. The vertical axis displays frequencies and the scale bar indicates wavelet power (square of amplitude), with warmer colors associated with greater variation. Black outlines designate variation that is significantly greater ($\alpha = 0.05$) than expected from an autoregressive time series. The shaded cone indicates values with little data support. Note that the temporal extent (horizontal axis) varies across the streams.

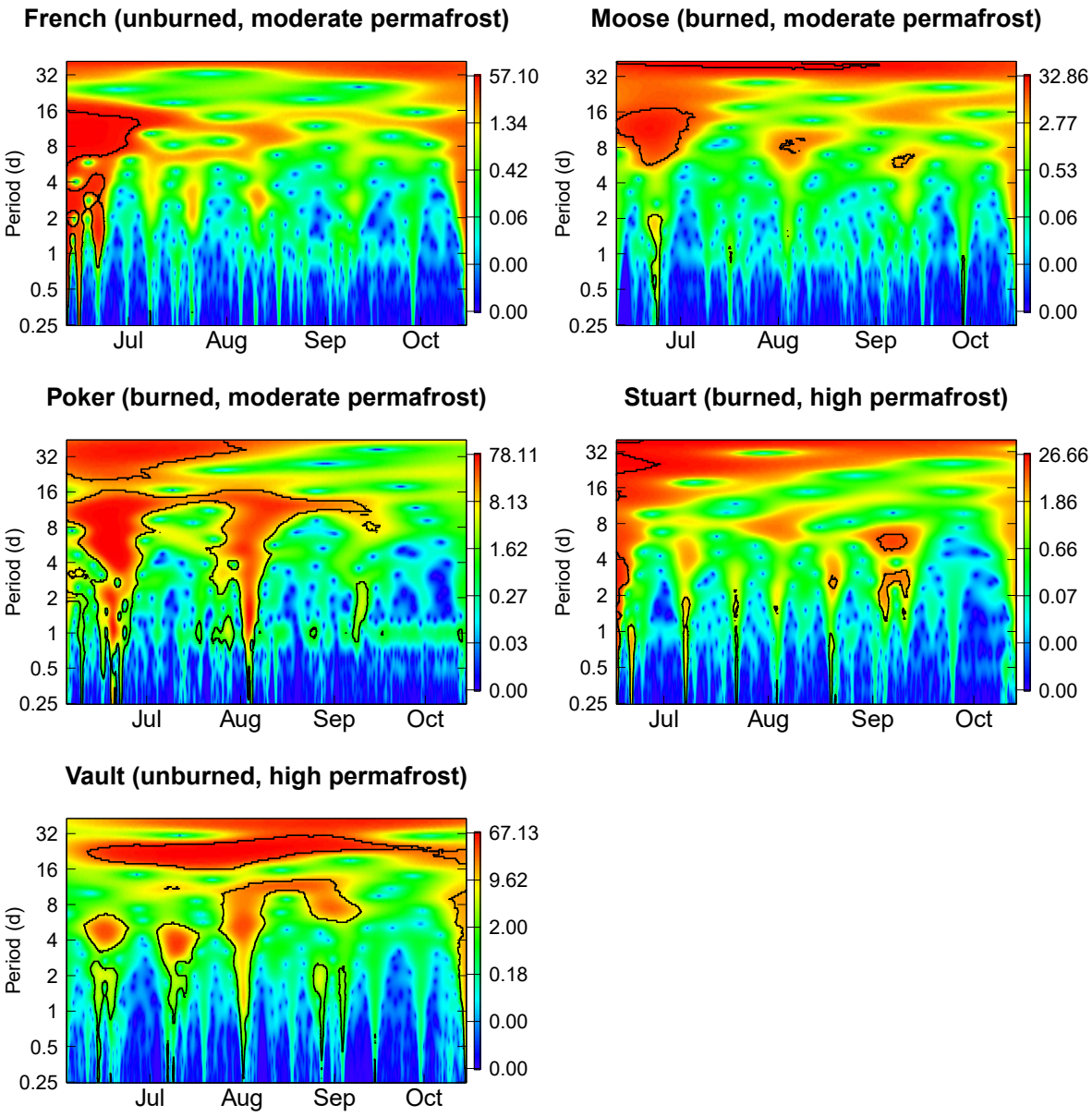


Figure A2.14. Wavelet transform of specific conductivity in 2020. The vertical axis displays frequencies and the scale bar indicates wavelet power (square of amplitude), with warmer colors associated with greater variation. Black outlines designate variation that is significantly greater ($\alpha = 0.05$) than expected from an autoregressive time series. The shaded cone indicates values with little data support. Note that the temporal extent (horizontal axis) varies across the streams.

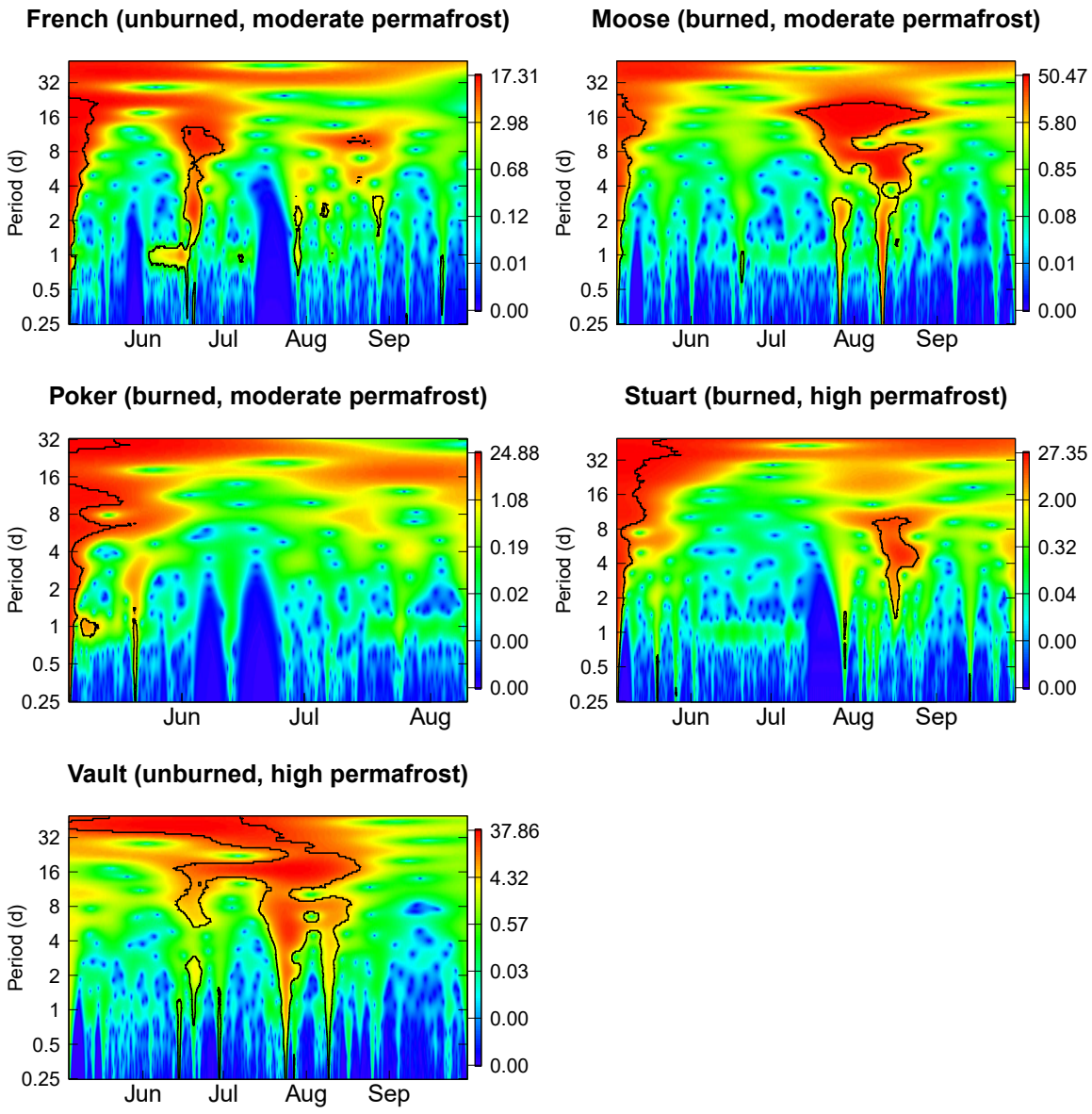


Figure A2.15. Wavelet transform of specific conductivity in 2021. The vertical axis displays frequencies and the scale bar indicates wavelet power (square of amplitude), with warmer colors associated with greater variation. Black outlines designate variation that is significantly greater ($\alpha = 0.05$) than expected from an autoregressive time series. The shaded cone indicates values with little data support. Note that the temporal extent (horizontal axis) varies across the streams.

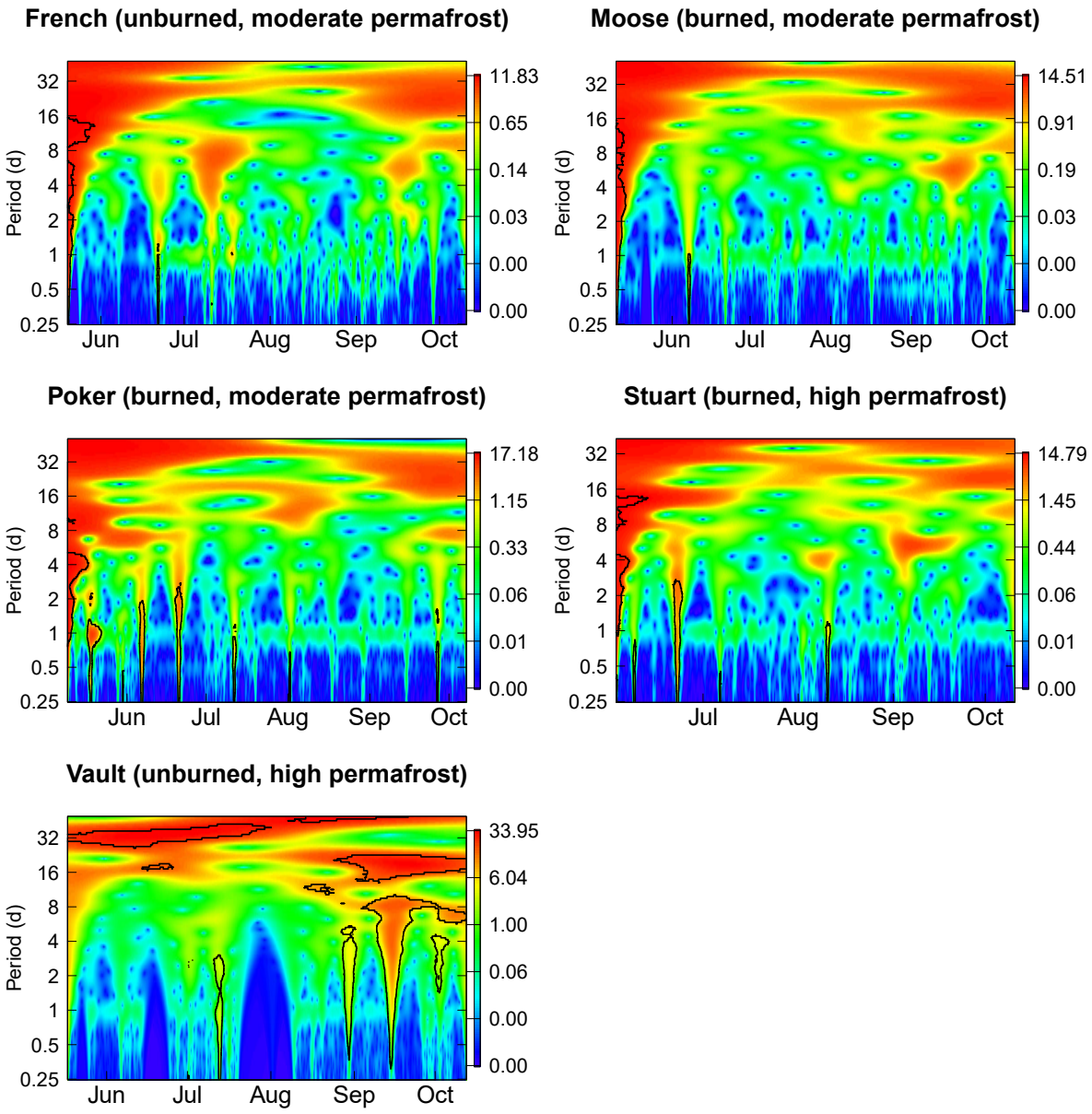


Figure A2.16. Wavelet transform of specific conductivity in 2022. The vertical axis displays frequencies and the scale bar indicates wavelet power (square of amplitude), with warmer colors associated with greater variation. Black outlines designate variation that is significantly greater ($\alpha = 0.05$) than expected from an autoregressive time series. The shaded cone indicates values with little data support. Note that the temporal extent (horizontal axis) varies across the streams.

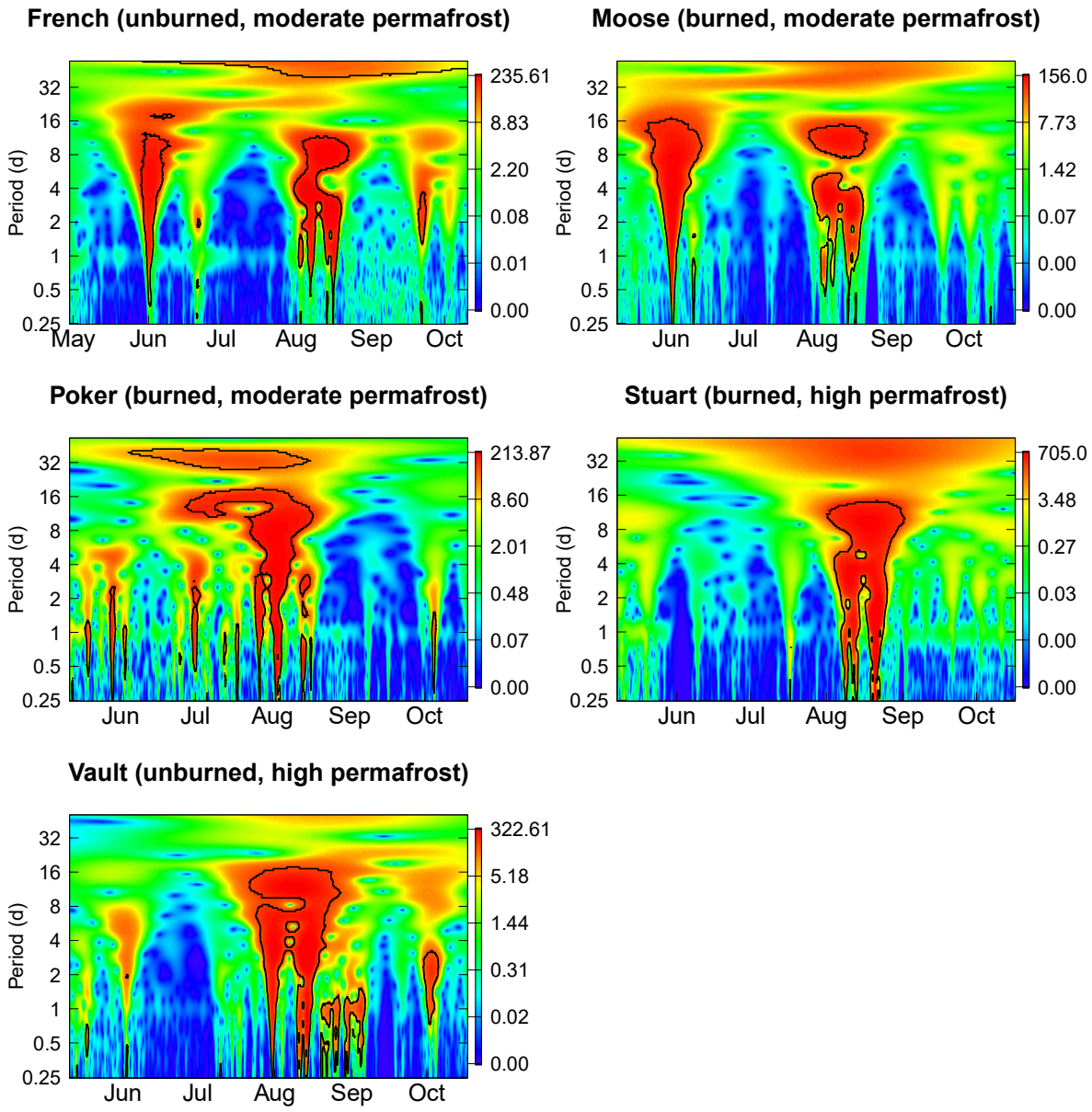


Figure A2.17. Wavelet transform of turbidity in 2019. The vertical axis displays frequencies and the scale bar indicates wavelet power (square of amplitude), with warmer colors associated with greater variation. Black outlines designate variation that is significantly greater (α = 0.05) than expected from an autoregressive time series. The shaded cone indicates values with little data support. Note that the temporal extent (horizontal axis) varies across the streams.

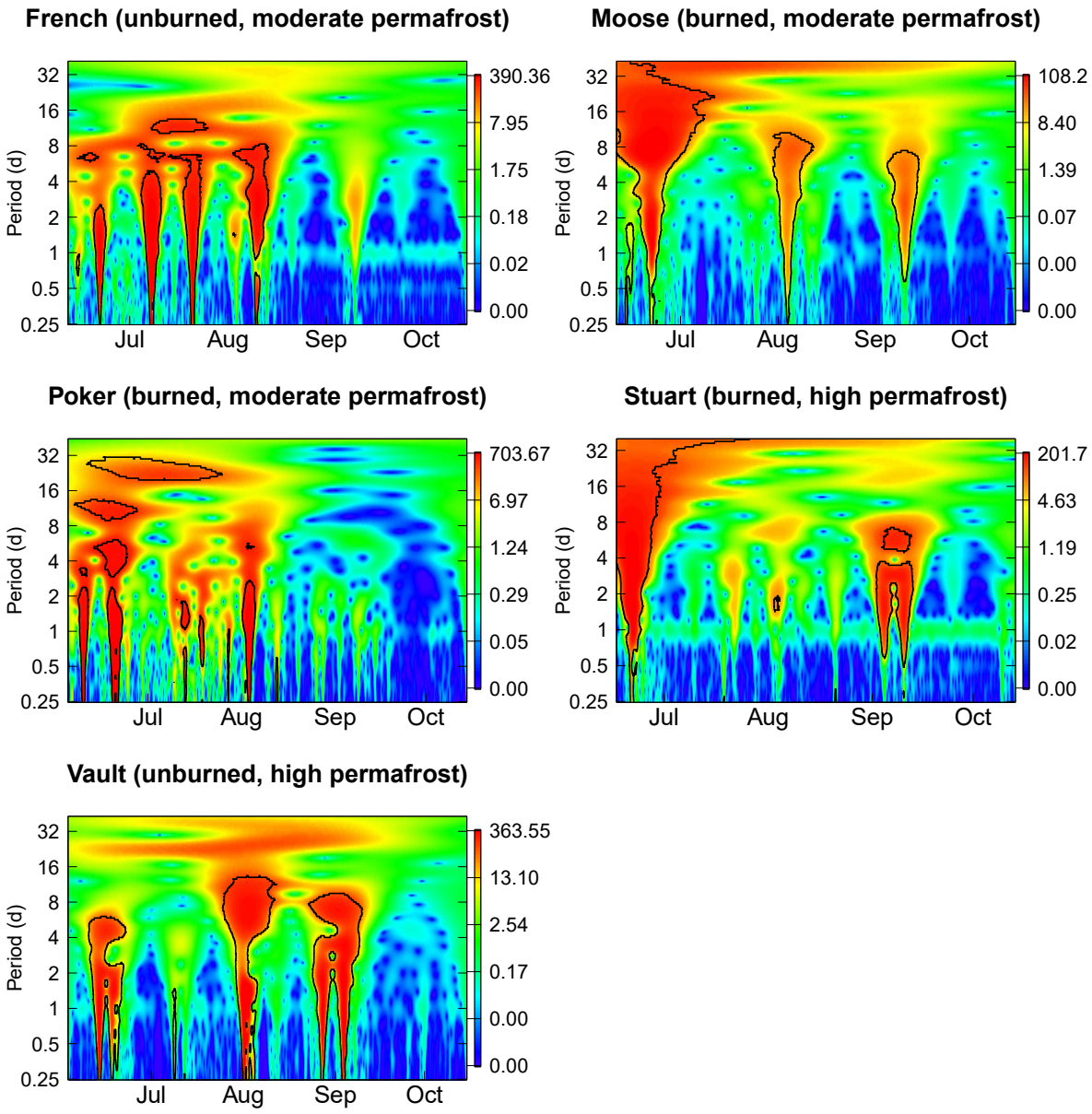


Figure A2.18. Wavelet transform of turbidity in 2020. The vertical axis displays frequencies and the scale bar indicates wavelet power (square of amplitude), with warmer colors associated with greater variation. Black outlines designate variation that is significantly greater (α = 0.05) than expected from an autoregressive time series. The shaded cone indicates values with little data support. Note that the temporal extent (horizontal axis) varies across the streams.

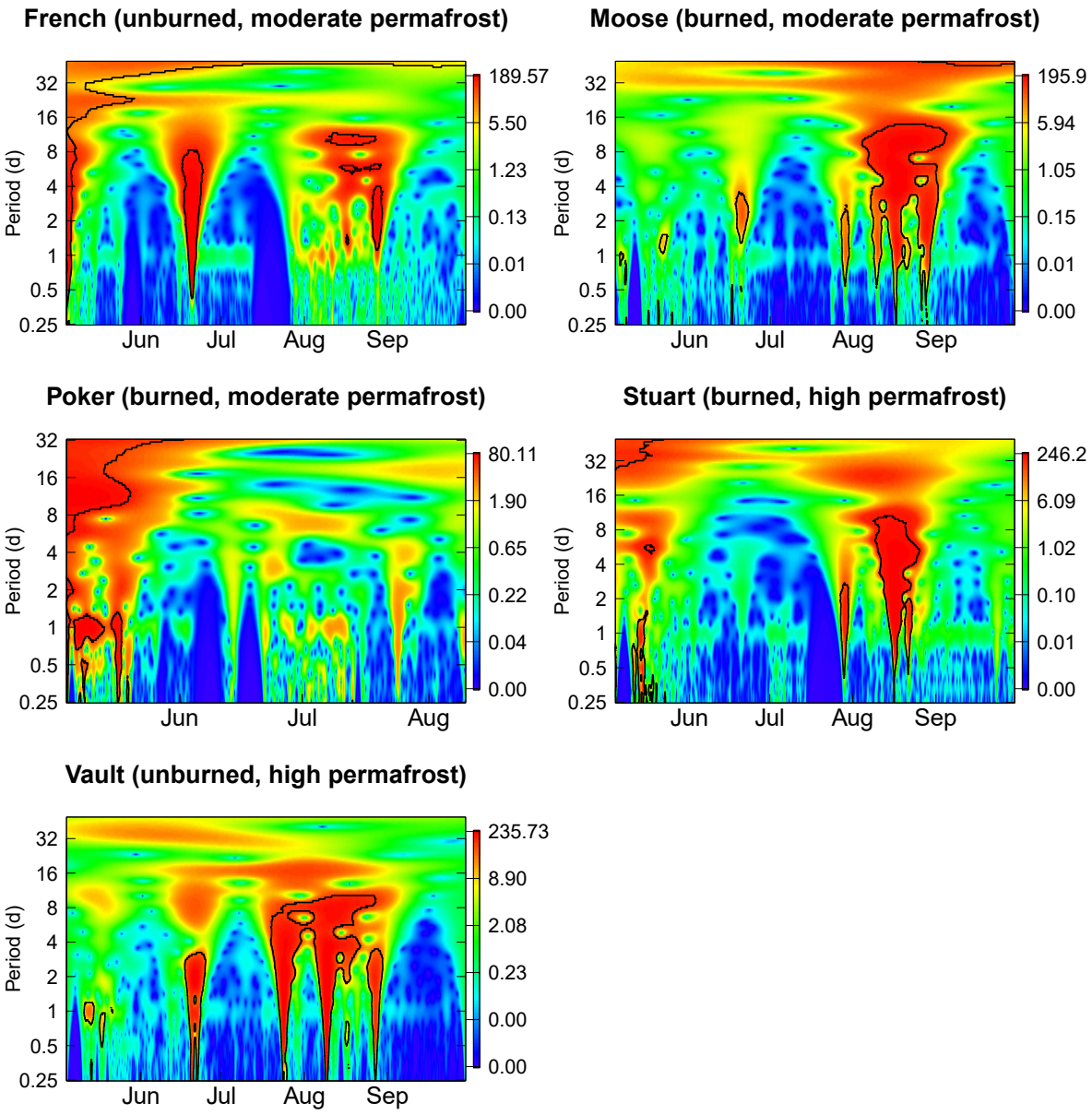


Figure A2.19. Wavelet transform of turbidity in 2021. The vertical axis displays frequencies and the scale bar indicates wavelet power (square of amplitude), with warmer colors associated with greater variation. Black outlines designate variation that is significantly greater (α = 0.05) than expected from an autoregressive time series. The shaded cone indicates values with little data support. Note that the temporal extent (horizontal axis) varies across the streams.

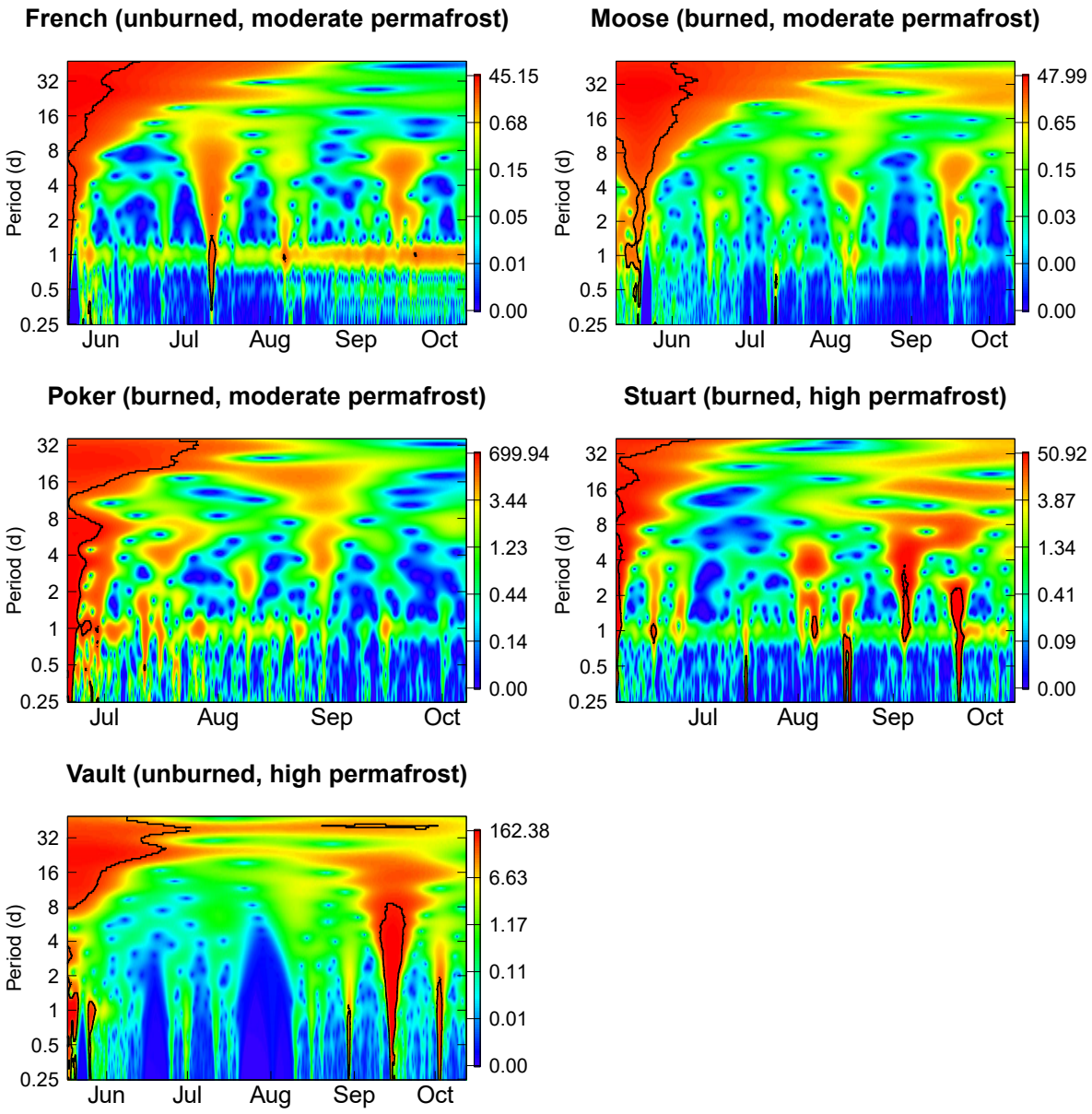


Figure A2.20. Wavelet transform of turbidity in 2022. The vertical axis displays frequencies and the scale bar indicates wavelet power (square of amplitude), with warmer colors associated with greater variation. Black outlines designate variation that is significantly greater (α = 0.05) than expected from an autoregressive time series. The shaded cone indicates values with little data support. Note that the temporal extent (horizontal axis) varies across the streams.

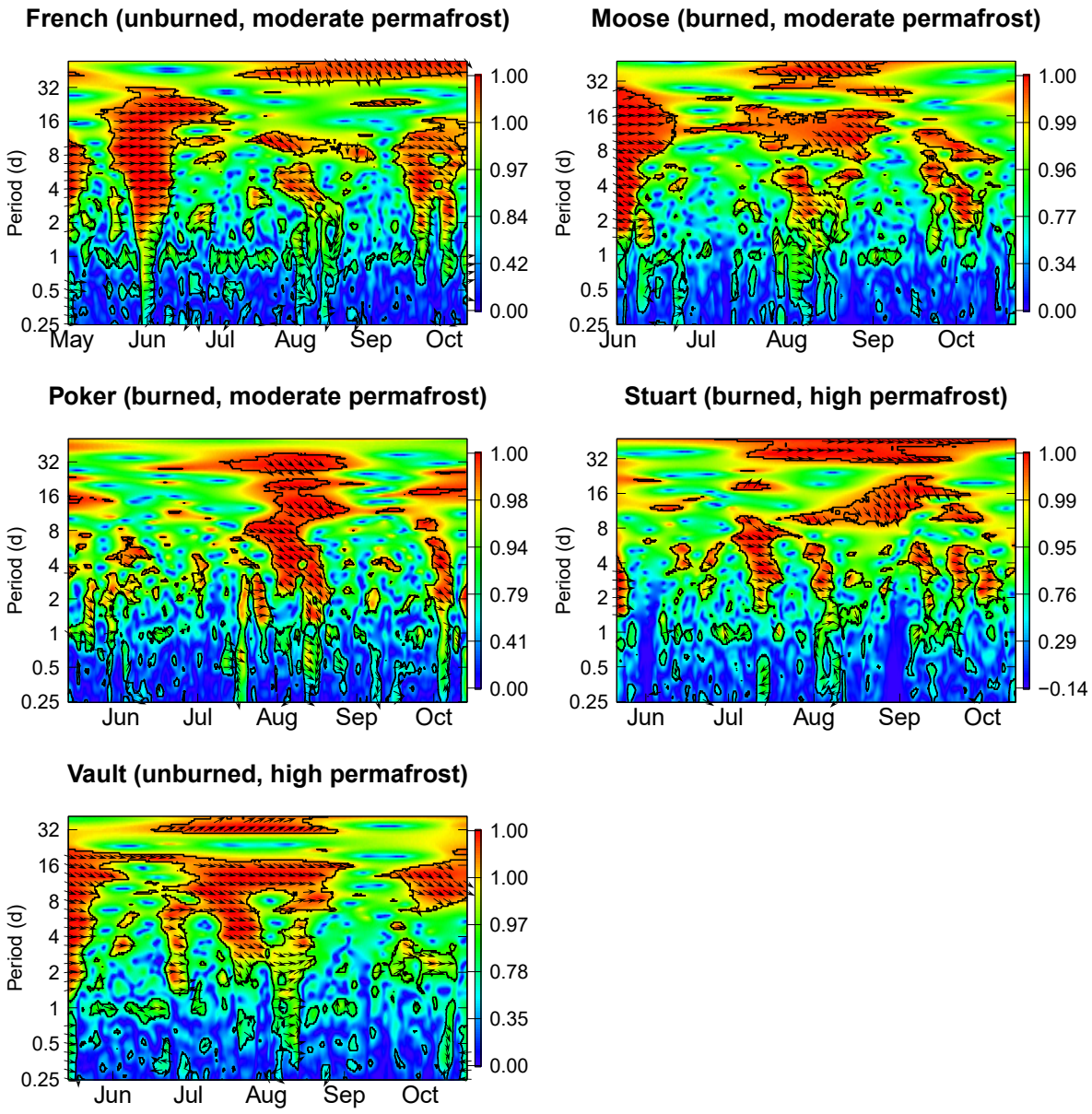


Figure A2.21. Wavelet coherence of abs254 concentration and discharge in 2019. Scale bar indicates coherence, with greater coherence depicted by warmer colors. Black outlines indicate times and frequencies when coherence is significantly greater than expected from an autoregressive time series. Arrows indicate the phase match when coherence is significant: → = in phase; ← = out of phase; ↖ = out of phase, abs254 following discharge; ↙ = out of phase, abs254 leading; ↗ = in phase, abs254 leading; ↘ = in phase, abs254 following. Note that the temporal extent (x axis) varies across the streams.

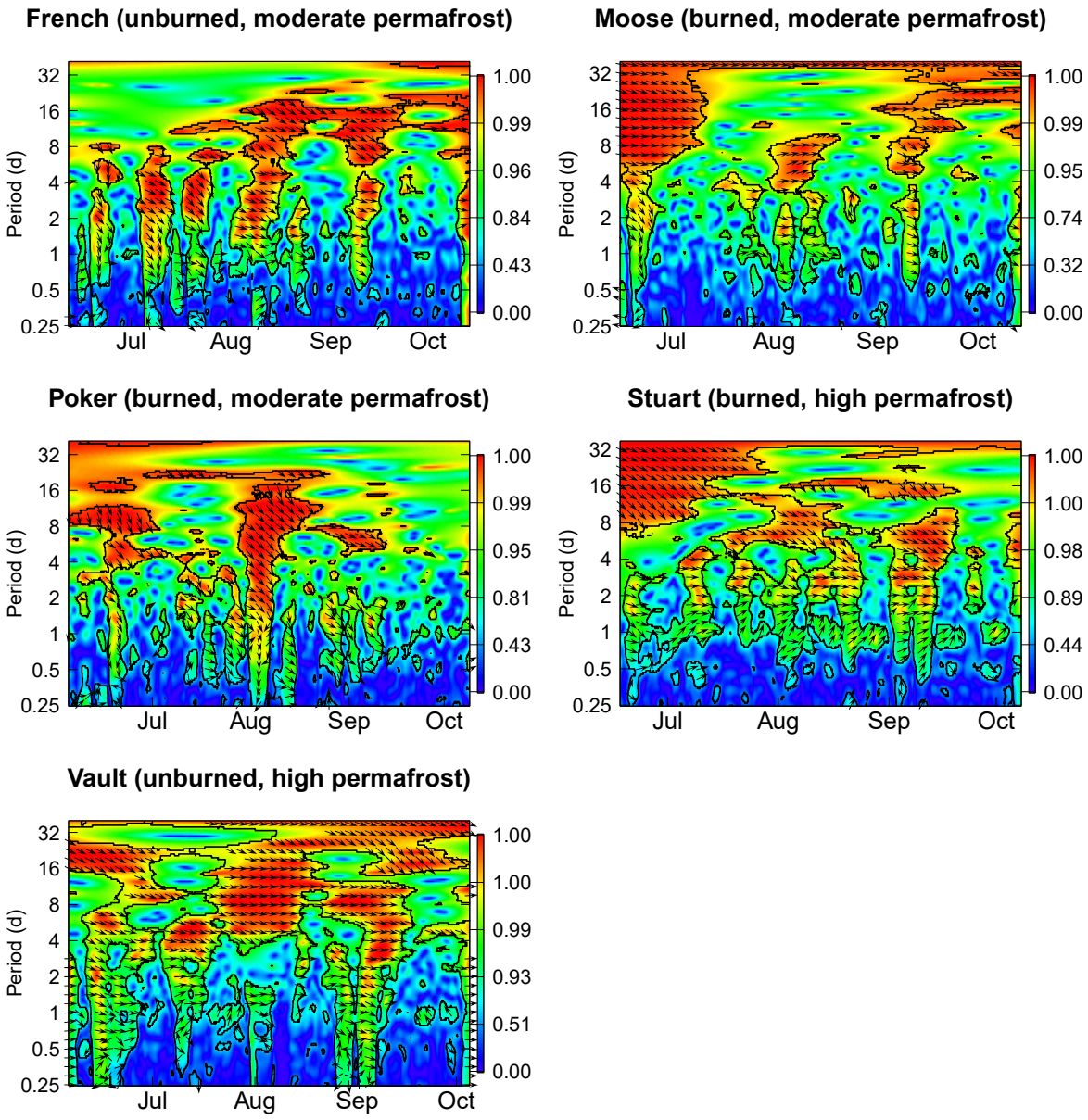


Figure A2.22. Wavelet coherence of abs254 concentration and discharge in 2020. Scale bar indicates coherence, with greater coherence depicted by warmer colors. Black outlines indicate times and frequencies when coherence is significantly greater than expected from an autoregressive time series. Arrows indicate the phase match when coherence is significant: → = in phase; ← = out of phase; ↖ = out of phase, abs254 following discharge; ↙ = out of phase, abs254 leading; ↗ = in phase, abs254 leading; ↘ = in phase, abs254 following. Note that the temporal extent (x axis) varies across the streams.

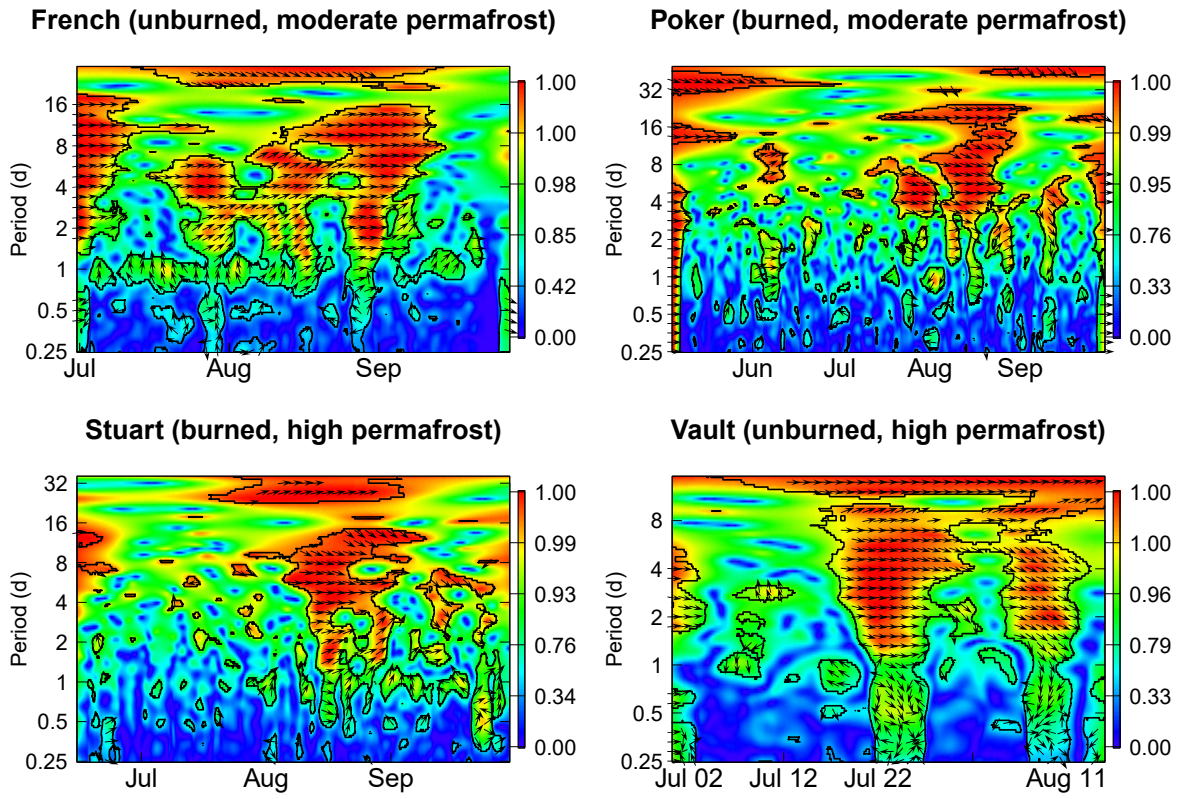


Figure A2.23. Wavelet coherence of abs254 concentration and discharge in 2021. Scale bar indicates coherence, with greater coherence depicted by warmer colors. Black outlines indicate times and frequencies when coherence is significantly greater than expected from an autoregressive time series. Arrows indicate the phase match when coherence is significant: → = in phase; ← = out of phase; ↖ = out of phase, abs254 following discharge; ↙ = out of phase, abs254 leading; ↗ = in phase, abs254 leading; ↘ = in phase, abs254 following. Note that the temporal extent (x axis) varies across the streams. Insufficient data were available for Moose Creek to support the analysis.

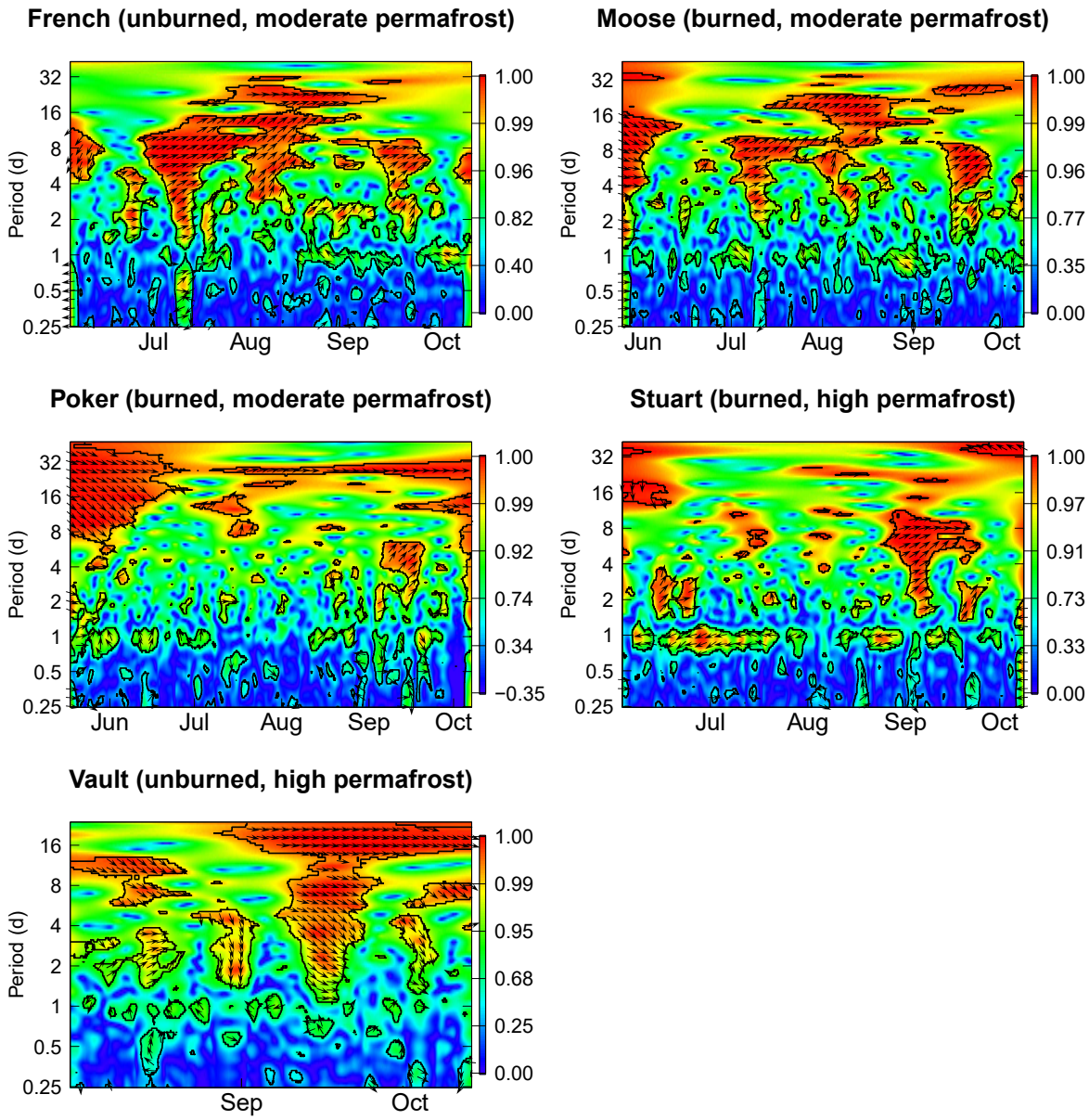


Figure A2.24. Wavelet coherence of abs254 concentration and discharge in 2022. Scale bar indicates coherence, with greater coherence depicted by warmer colors. Black outlines indicate times and frequencies when coherence is significantly greater than expected from an autoregressive time series. Arrows indicate the phase match when coherence is significant: → = in phase; ← = out of phase; ↖ = out of phase, abs254 following discharge; ↙ = out of phase, abs254 leading; ↗ = in phase, abs254 leading; ↘ = in phase, abs254 following. Note that the temporal extent (x axis) varies across the streams.

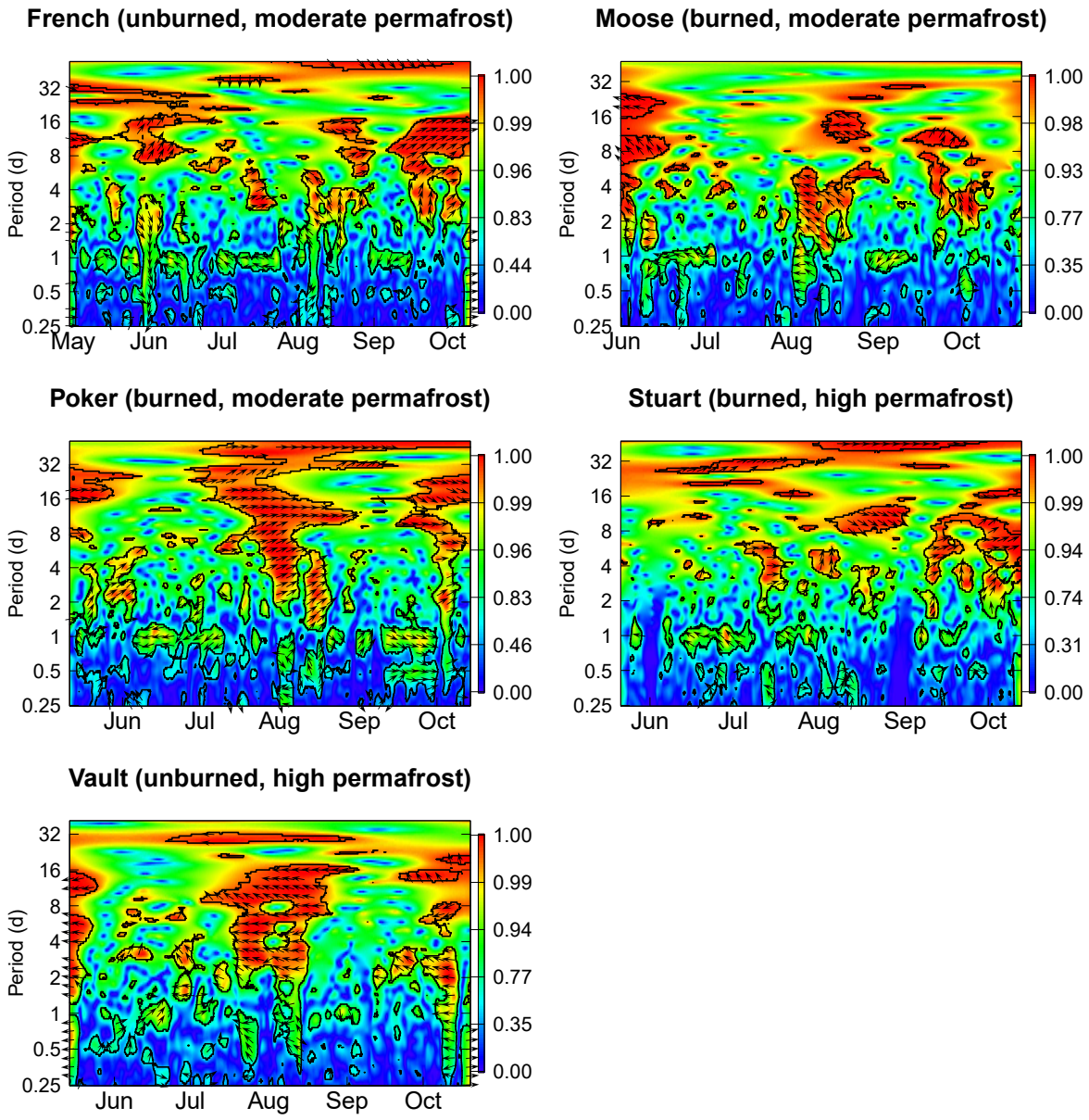


Figure A2.25. Wavelet coherence of fDOM concentration and discharge in 2019. Scale bar indicates coherence, with greater coherence depicted by warmer colors. Black outlines indicate times and frequencies when coherence is significantly greater than expected from an autoregressive time series. Arrows indicate the phase match when coherence is significant: → = in phase; ← = out of phase; ↖ = out of phase, fDOM following discharge; ↙ = out of phase, fDOM leading; ↗ = in phase, fDOM leading; ↘ = in phase, fDOM following. Note that the temporal extent (x axis) varies across the streams.

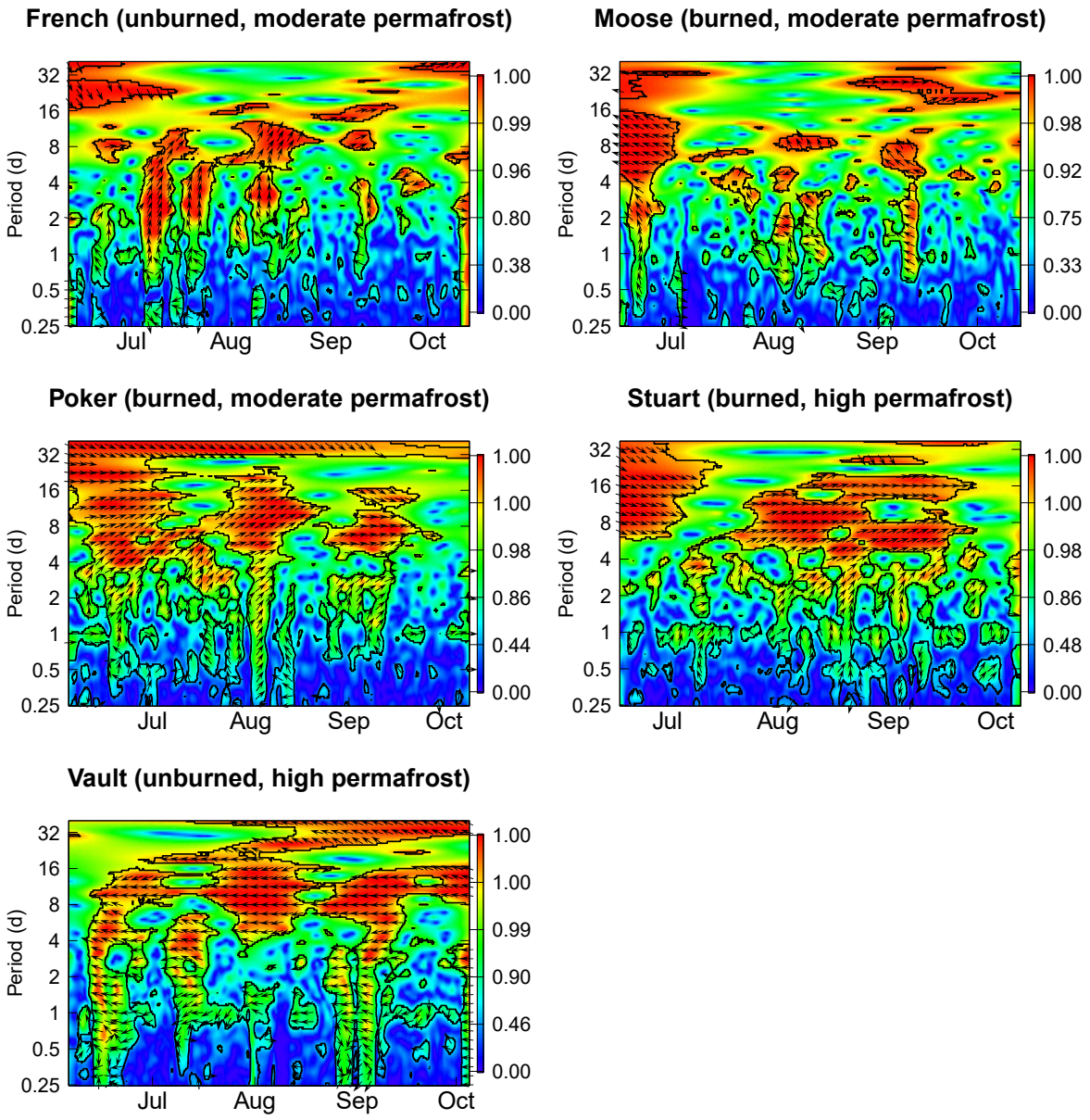


Figure A2.26. Wavelet coherence of fDOM concentration and discharge in 2020. Scale bar indicates coherence, with greater coherence depicted by warmer colors. Black outlines indicate times and frequencies when coherence is significantly greater than expected from an autoregressive time series. Arrows indicate the phase match when coherence is significant: → = in phase; ← = out of phase; ↖ = out of phase, fDOM following discharge; ↙ = out of phase, fDOM leading; ↗ = in phase, fDOM leading; ↘ = in phase, fDOM following. Note that the temporal extent (x axis) varies across the streams.

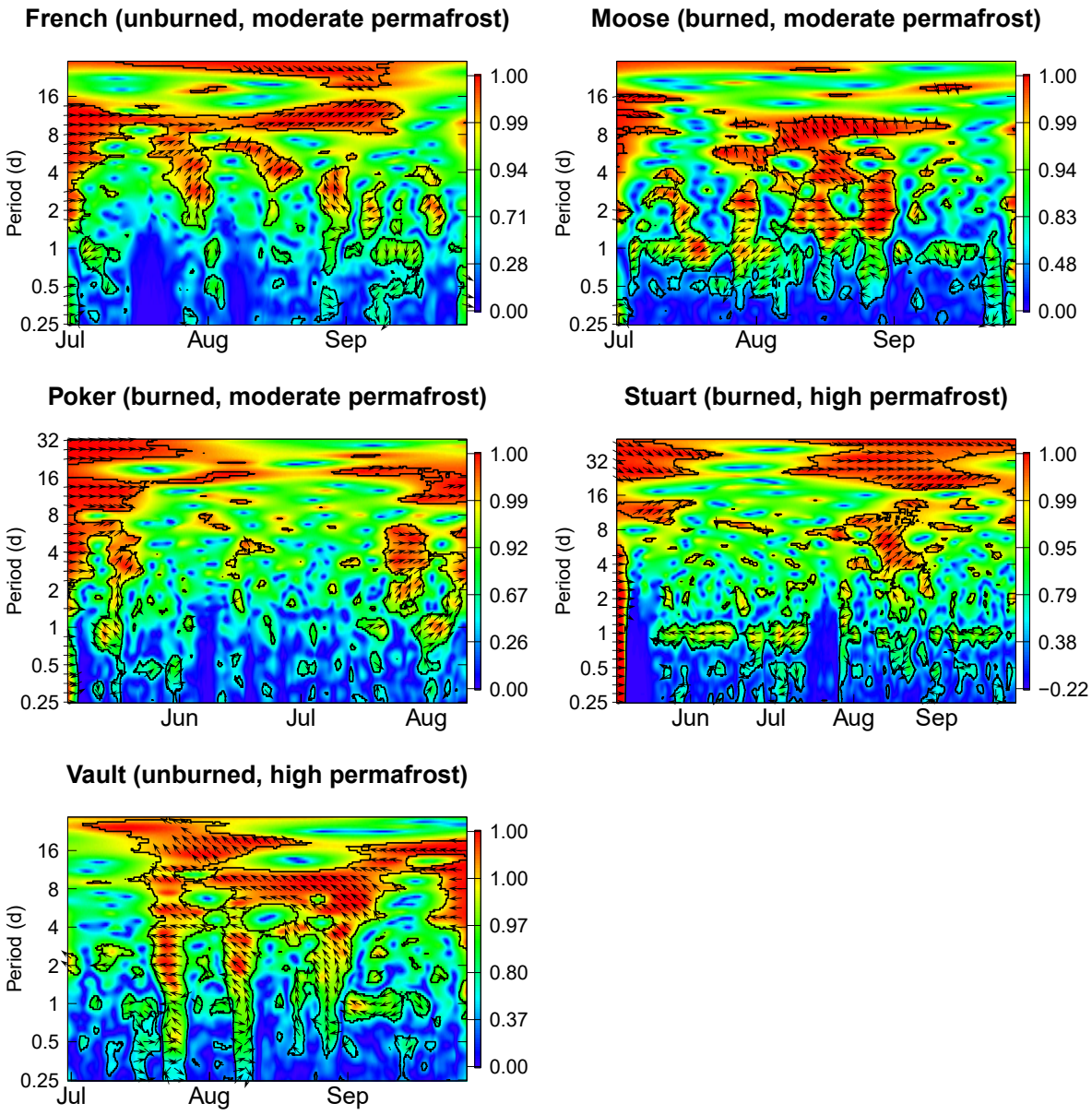


Figure A2.27. Wavelet coherence of fDOM concentration and discharge in 2021. Scale bar indicates coherence, with greater coherence depicted by warmer colors. Black outlines indicate times and frequencies when coherence is significantly greater than expected from an autoregressive time series. Arrows indicate the phase match when coherence is significant: → = in phase; ← = out of phase; ↖ = out of phase, fDOM following discharge; ↙ = out of phase, fDOM leading; ↗ = in phase, fDOM leading; ↘ = in phase, fDOM following. Note that the temporal extent (x axis) varies across the streams.

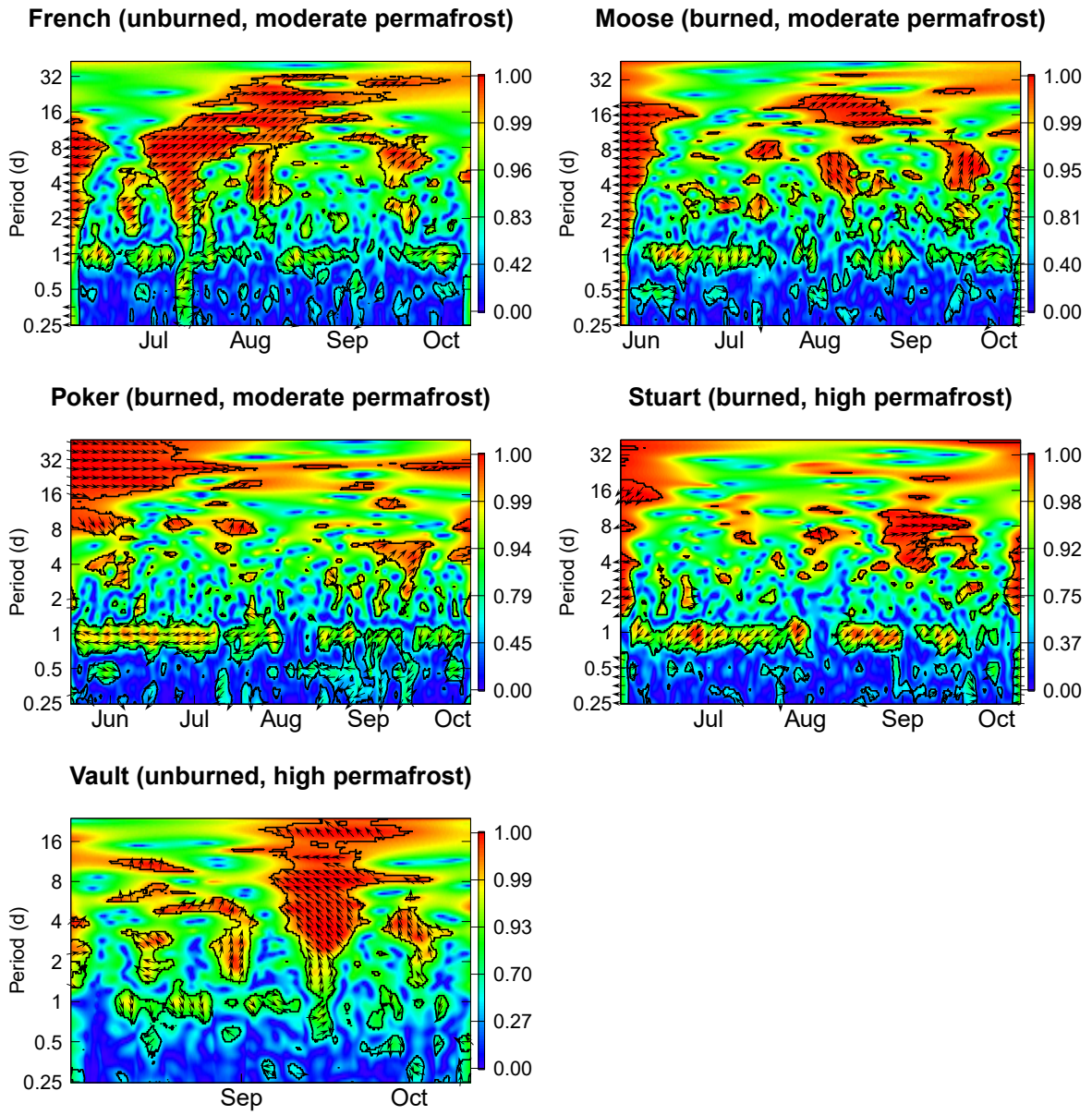


Figure A2.28. Wavelet coherence of fDOM concentration and discharge in 2022. Scale bar indicates coherence, with greater coherence depicted by warmer colors. Black outlines indicate times and frequencies when coherence is significantly greater than expected from an autoregressive time series. Arrows indicate the phase match when coherence is significant: → = in phase; ← = out of phase; ↖ = out of phase, fDOM following discharge; ↙ = out of phase, fDOM leading; ↗ = in phase, fDOM leading; ↘ = in phase, fDOM following. Note that the temporal extent (x axis) varies across the streams.

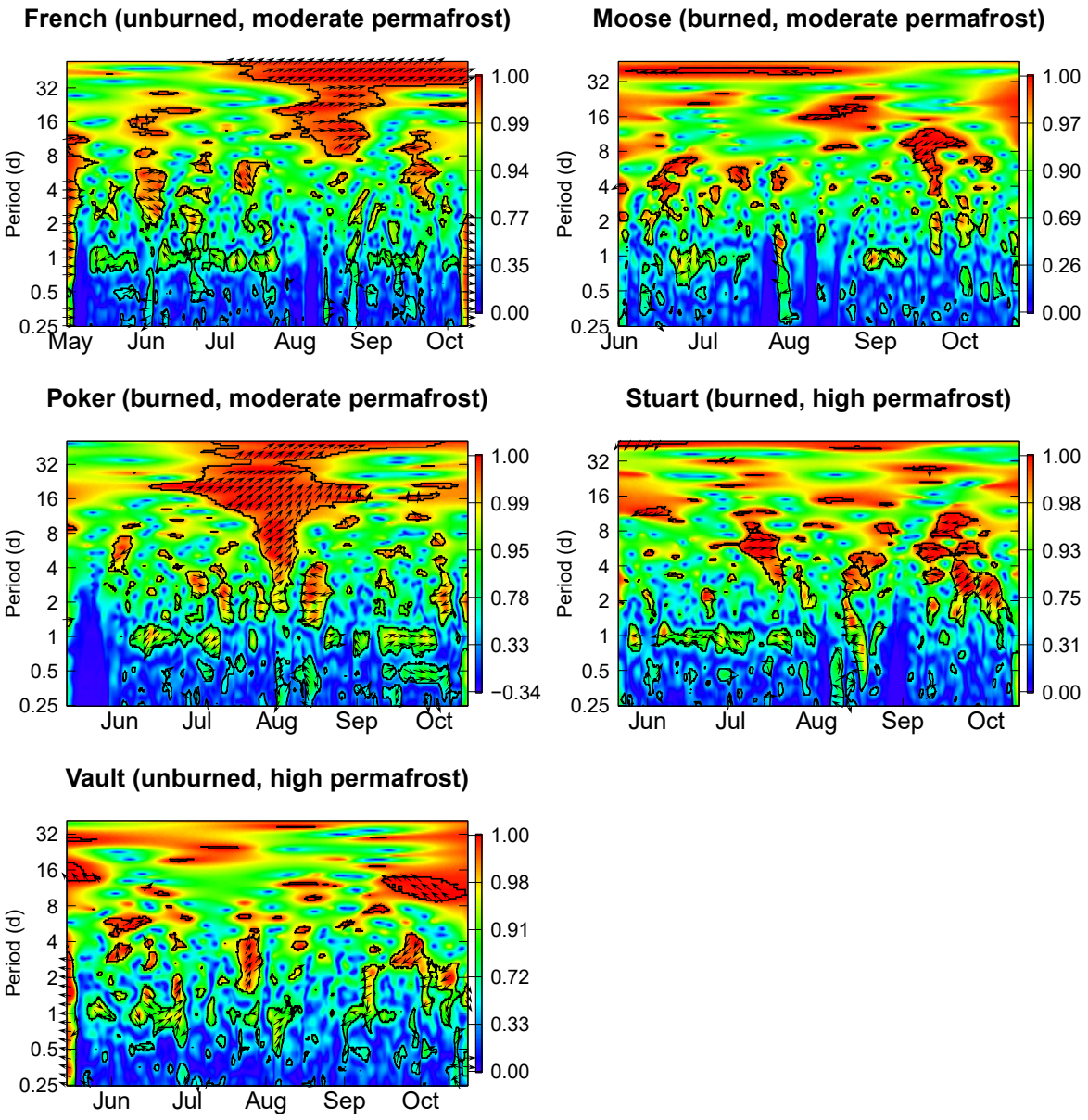


Figure A2.29. Wavelet coherence of NO_3^- concentration and discharge in 2019. Scale bar indicates coherence, with greater coherence depicted by warmer colors. Black outlines indicate times and frequencies when coherence is significantly greater than expected from an autoregressive time series. Arrows indicate the phase match when coherence is significant: → = in phase; ← = out of phase; ↖ = out of phase, NO_3^- following discharge; ↙ = out of phase, NO_3^- leading; ↗ = in phase, NO_3^- leading; ↘ = in phase, NO_3^- following. Note that the temporal extent (x axis) varies across the streams.

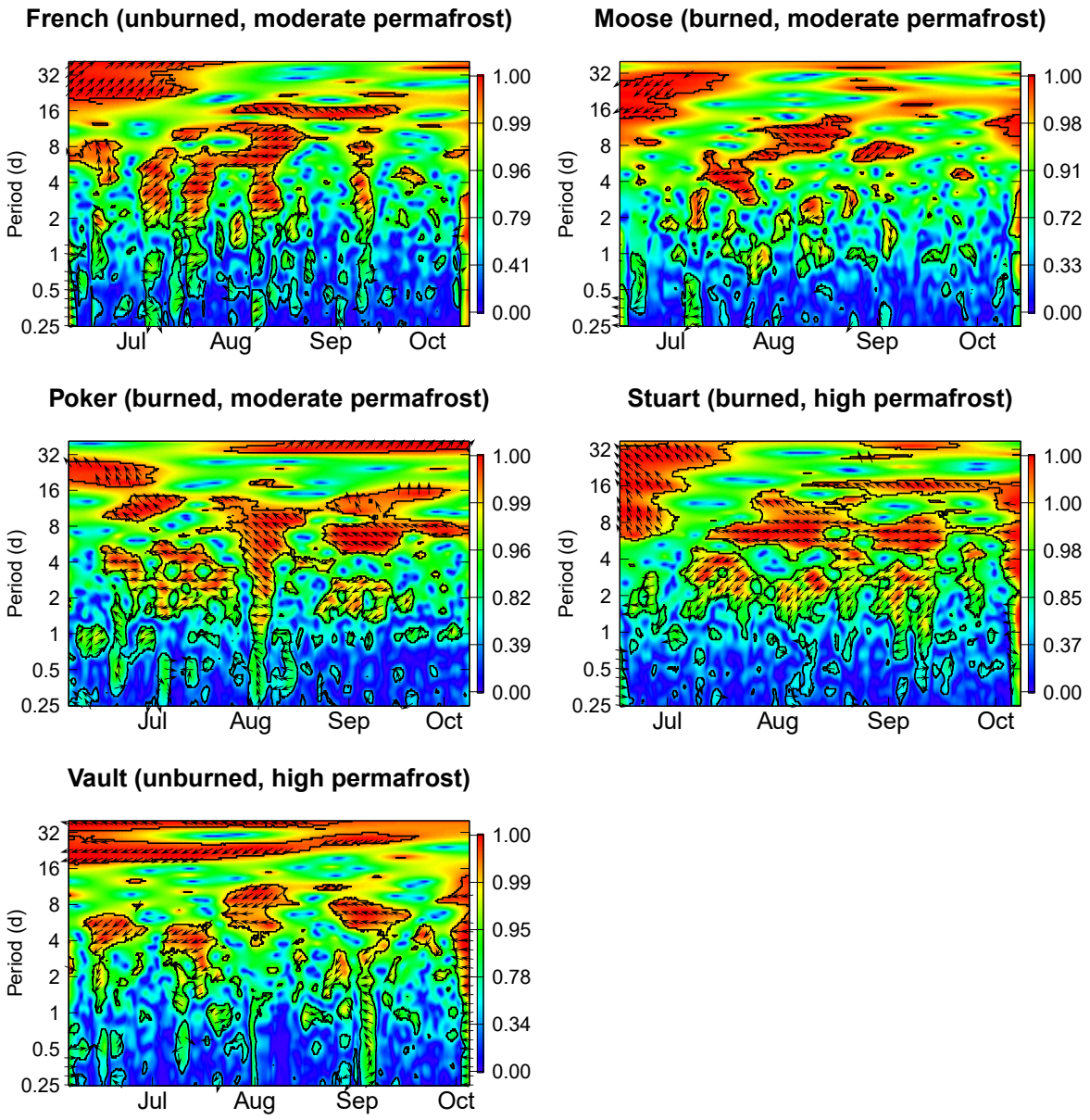


Figure A2.30. Wavelet coherence of NO_3^- concentration and discharge in 2020. Scale bar indicates coherence, with greater coherence depicted by warmer colors. Black outlines indicate times and frequencies when coherence is significantly greater than expected from an autoregressive time series. Arrows indicate the phase match when coherence is significant: → = in phase; ← = out of phase; ↖ = out of phase, NO_3^- following discharge; ↙ = out of phase, NO_3^- leading; ↗ = in phase, NO_3^- leading; ↘ = in phase, NO_3^- following. Note that the temporal extent (x axis) varies across the streams.

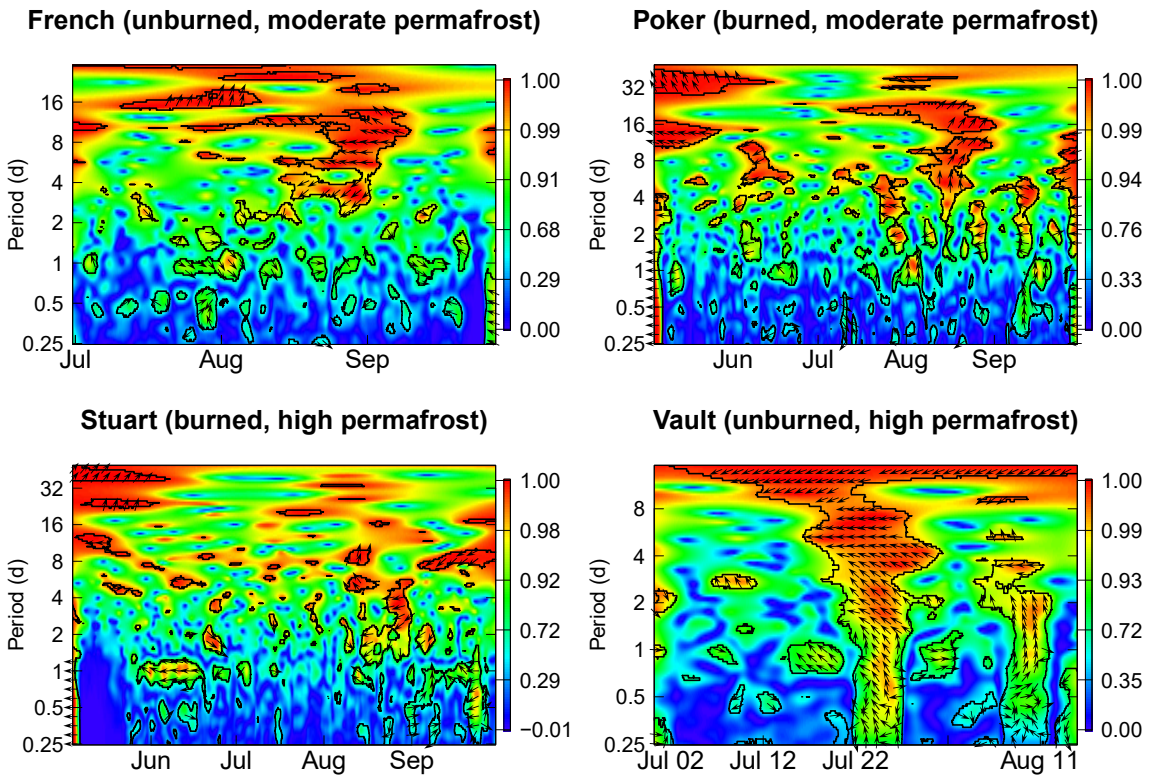


Figure A2.31. Wavelet coherence of NO_3^- concentration and discharge in 2021. Scale bar indicates coherence, with greater coherence depicted by warmer colors. Black outlines indicate times and frequencies when coherence is significantly greater than expected from an autoregressive time series. Arrows indicate the phase match when coherence is significant: → = in phase; ← = out of phase; ↖ = out of phase, NO_3^- following discharge; ↙ = out of phase, NO_3^- leading; ↗ = in phase, NO_3^- leading; ↘ = in phase, NO_3^- following. Note that the temporal extent (x axis) varies across the streams. Insufficient data form Moose Creek were available to support the analysis.

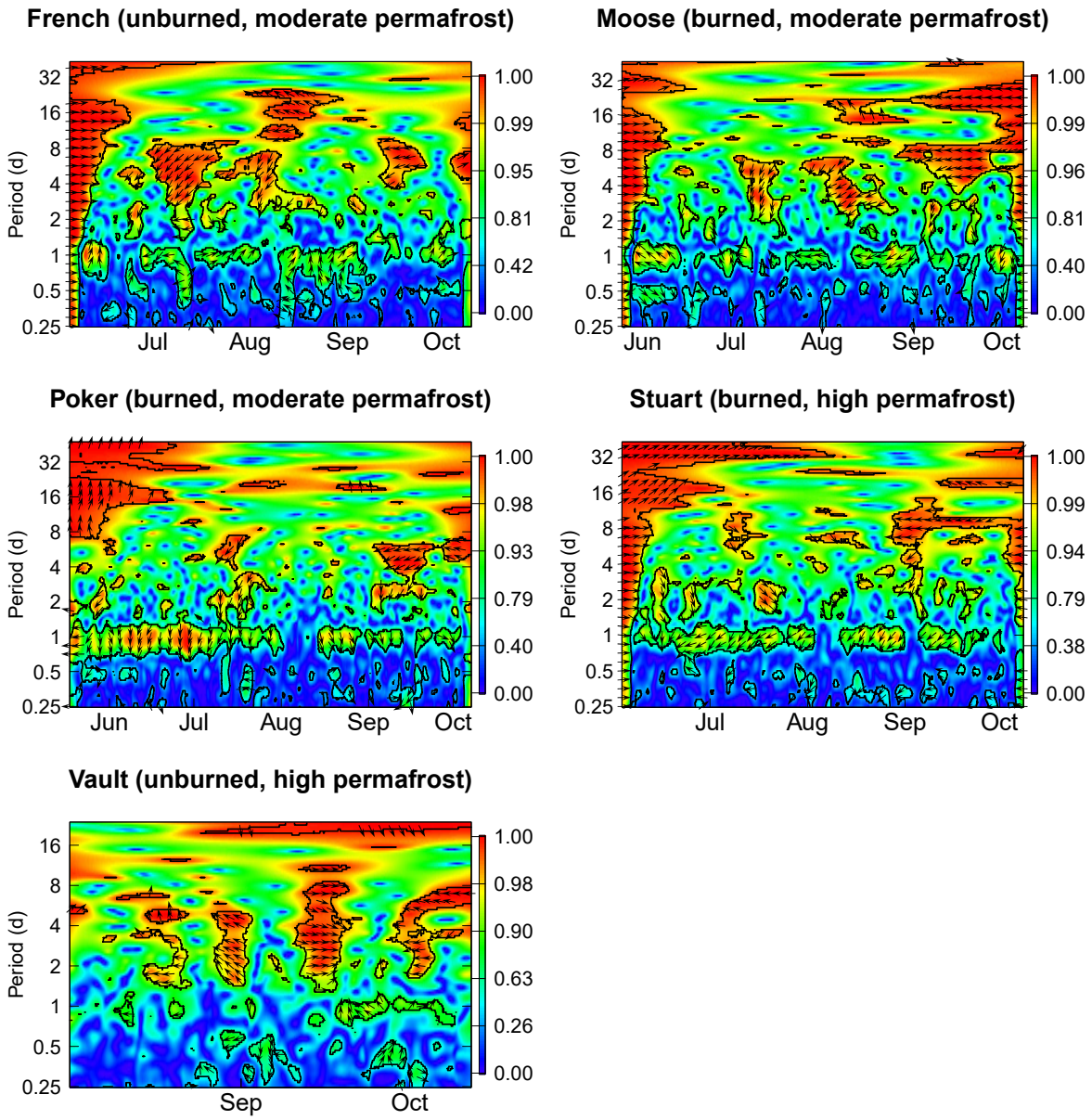


Figure A2.32. Wavelet coherence of NO_3^- concentration and discharge in 2022. Scale bar indicates coherence, with greater coherence depicted by warmer colors. Black outlines indicate times and frequencies when coherence is significantly greater than expected from an autoregressive time series. Arrows indicate the phase match when coherence is significant: → = in phase; ← = out of phase; ↖ = out of phase, NO_3^- following discharge; ↙ = out of phase, NO_3^- leading; ↗ = in phase, NO_3^- leading; ↘ = in phase, NO_3^- following. Note that the temporal extent (x axis) varies across the streams.

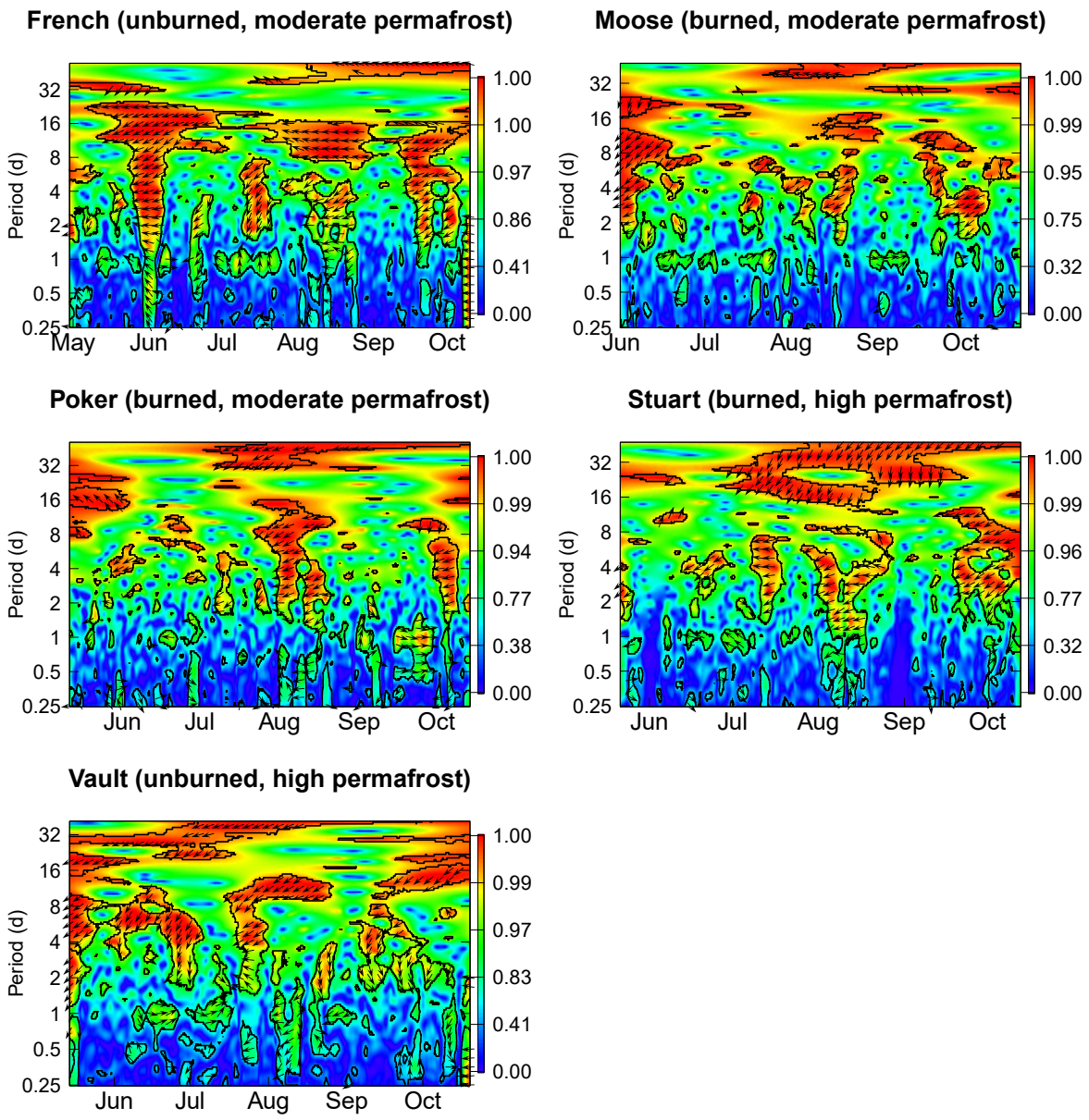


Figure A2.33. Wavelet coherence of specific conductivity (SPC) and discharge in 2019. Scale bar indicates coherence, with greater coherence depicted by warmer colors. Black outlines indicate times and frequencies when coherence is significantly greater than expected from an autoregressive time series. Arrows indicate the phase match when coherence is significant: → = in phase; ← = out of phase; ↖ = out of phase, SPC following discharge; ↙ = out of phase, SPC leading; ↗ = in phase, SPC leading; ↘ = in phase, SPC following. Note that the temporal extent (x axis) varies across the streams.

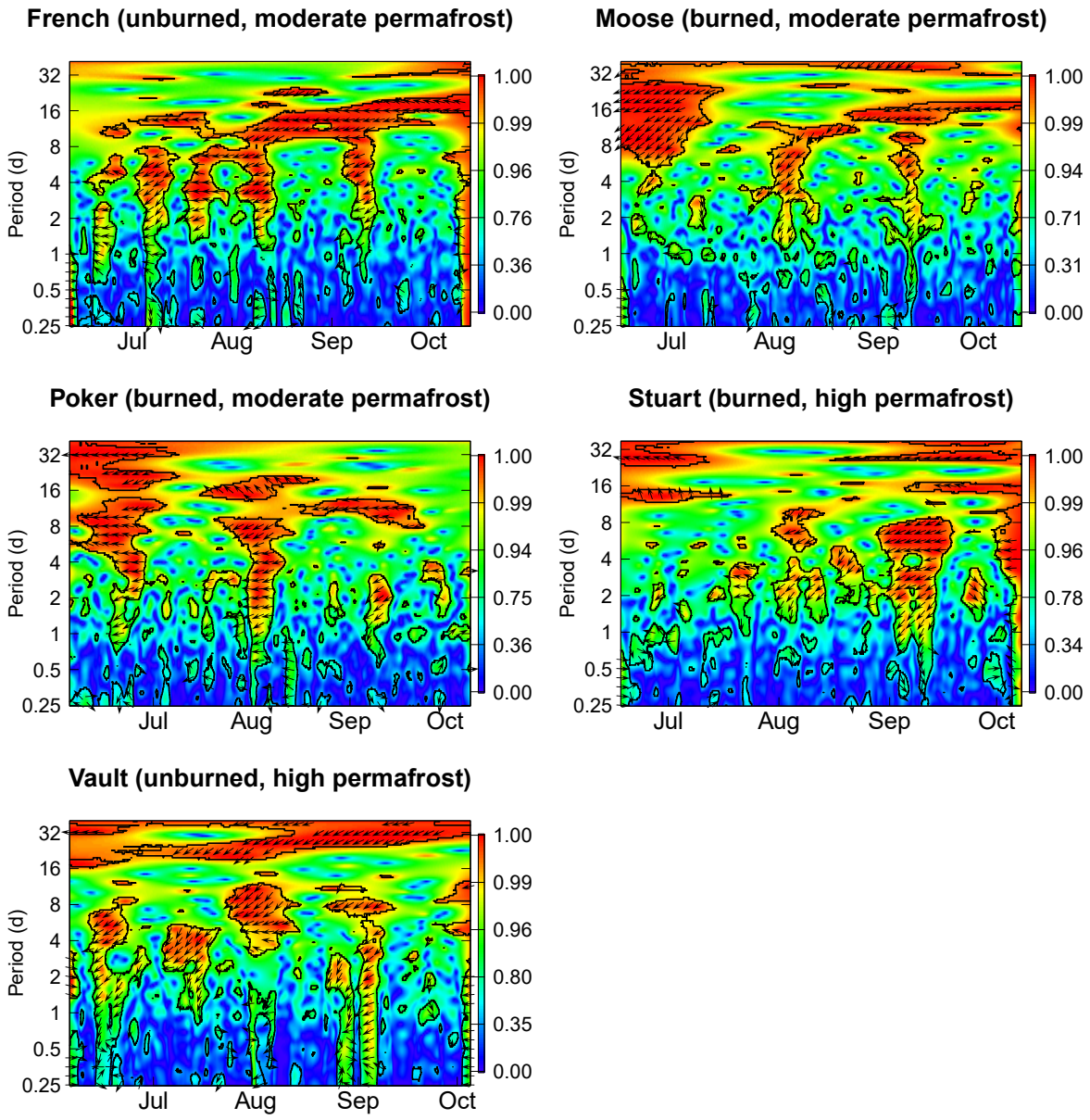


Figure A2.34. Wavelet coherence of specific conductivity (SPC) and discharge in 2020. Scale bar indicates coherence, with greater coherence depicted by warmer colors. Black outlines indicate times and frequencies when coherence is significantly greater than expected from an autoregressive time series. Arrows indicate the phase match when coherence is significant: → = in phase; ← = out of phase; ↖ = out of phase, SPC following discharge; ↙ = out of phase, SPC leading; ↗ = in phase, SPC leading; ↘ = in phase, SPC following. Note that the temporal extent (x axis) varies across the streams.

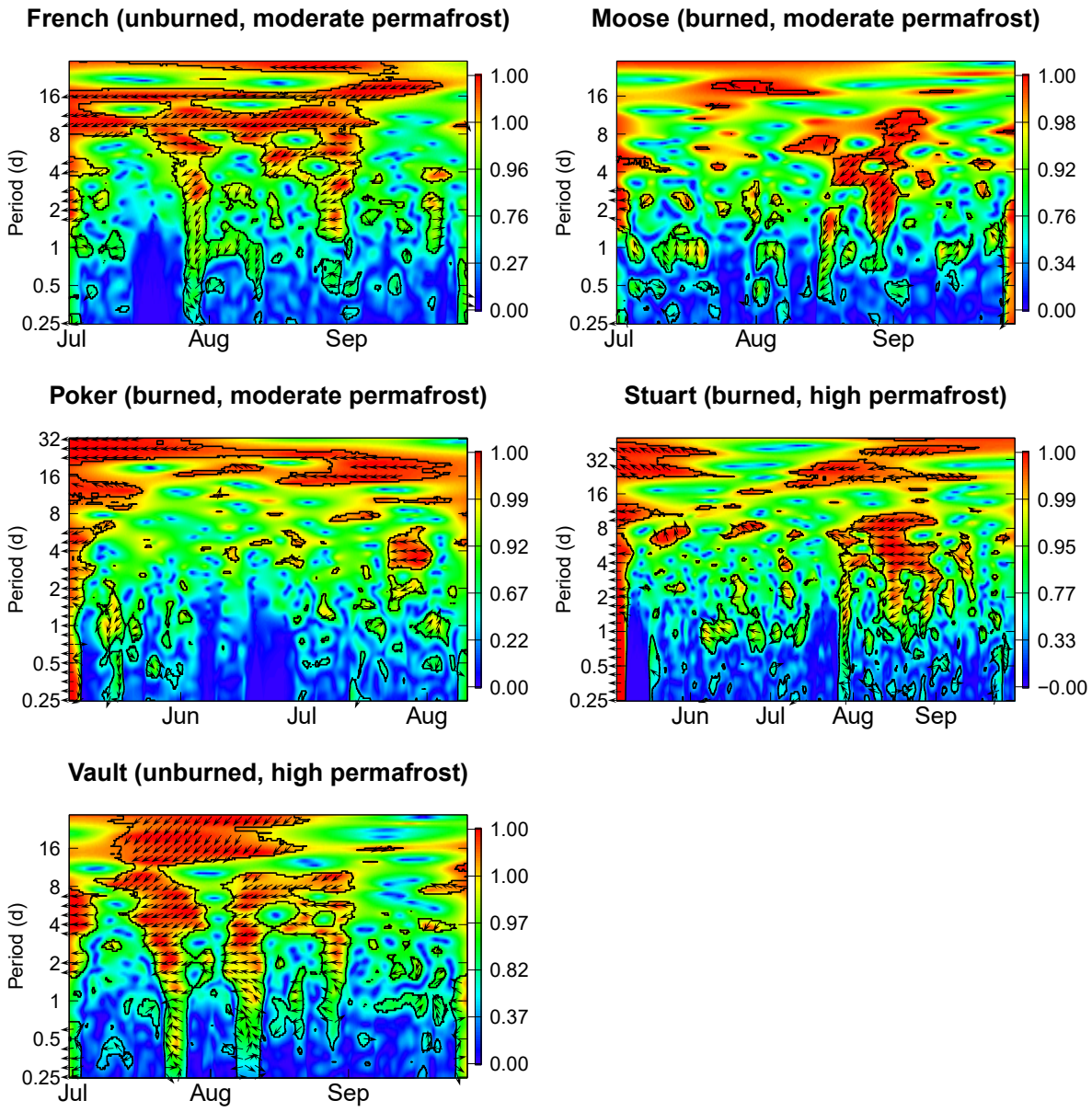


Figure A2.35. Wavelet coherence of specific conductivity (SPC) and discharge in 2021. Scale bar indicates coherence, with greater coherence depicted by warmer colors. Black outlines indicate times and frequencies when coherence is significantly greater than expected from an autoregressive time series. Arrows indicate the phase match when coherence is significant: → = in phase; ← = out of phase; ↖ = out of phase, SPC following discharge; ↙ = out of phase, SPC leading; ↗ = in phase, SPC leading; ↘ = in phase, SPC following. Note that the temporal extent (x axis) varies across the streams.

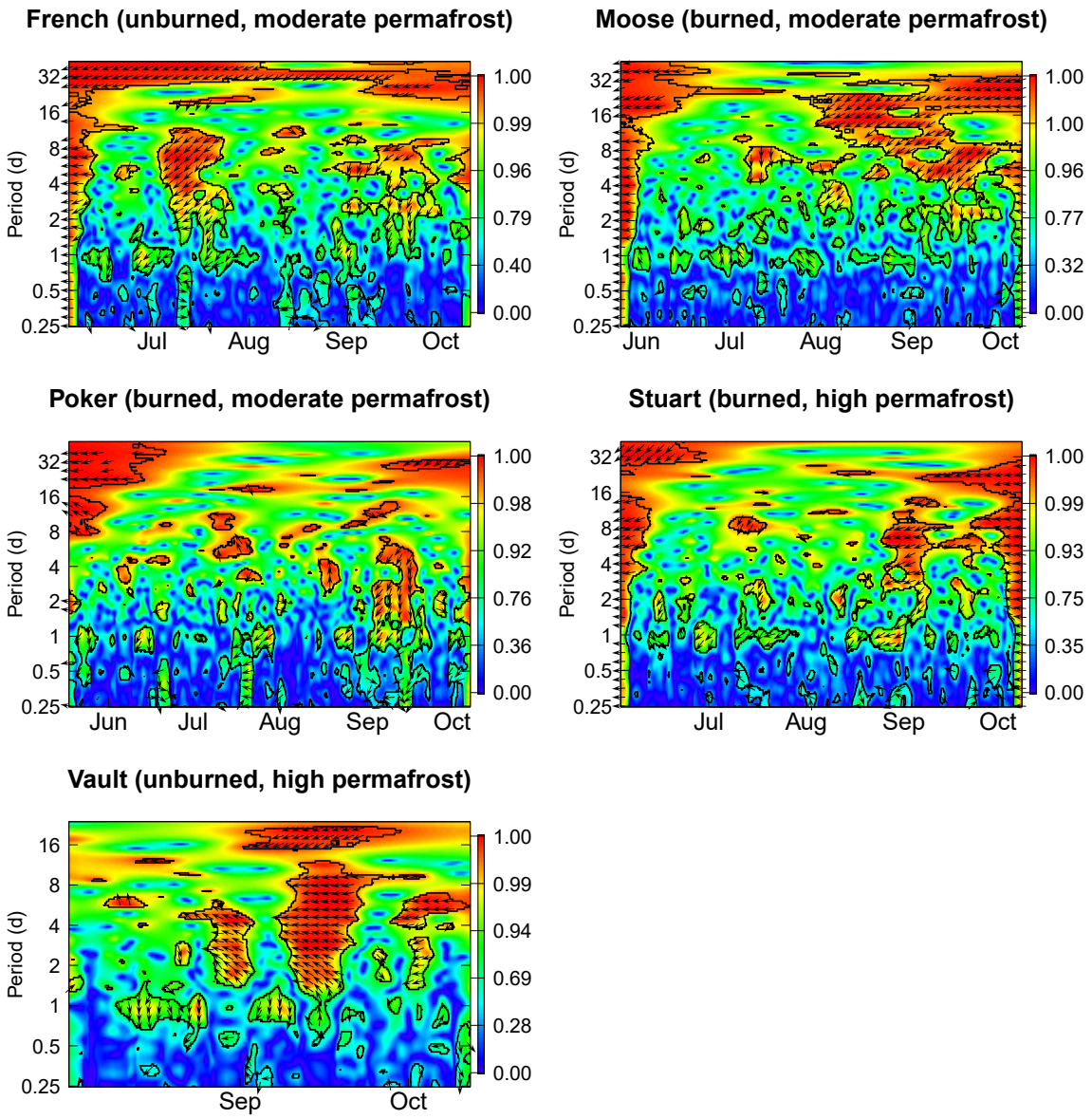


Figure A2.36. Wavelet coherence of specific conductivity (SPC) and discharge in 2022. Scale bar indicates coherence, with greater coherence depicted by warmer colors. Black outlines indicate times and frequencies when coherence is significantly greater than expected from an autoregressive time series. Arrows indicate the phase match when coherence is significant: → = in phase; ← = out of phase; ↖ = out of phase, SPC following discharge; ↙ = out of phase, SPC leading; ↗ = in phase, SPC leading; ↘ = in phase, SPC following. Note that the temporal extent (x axis) varies across the streams.

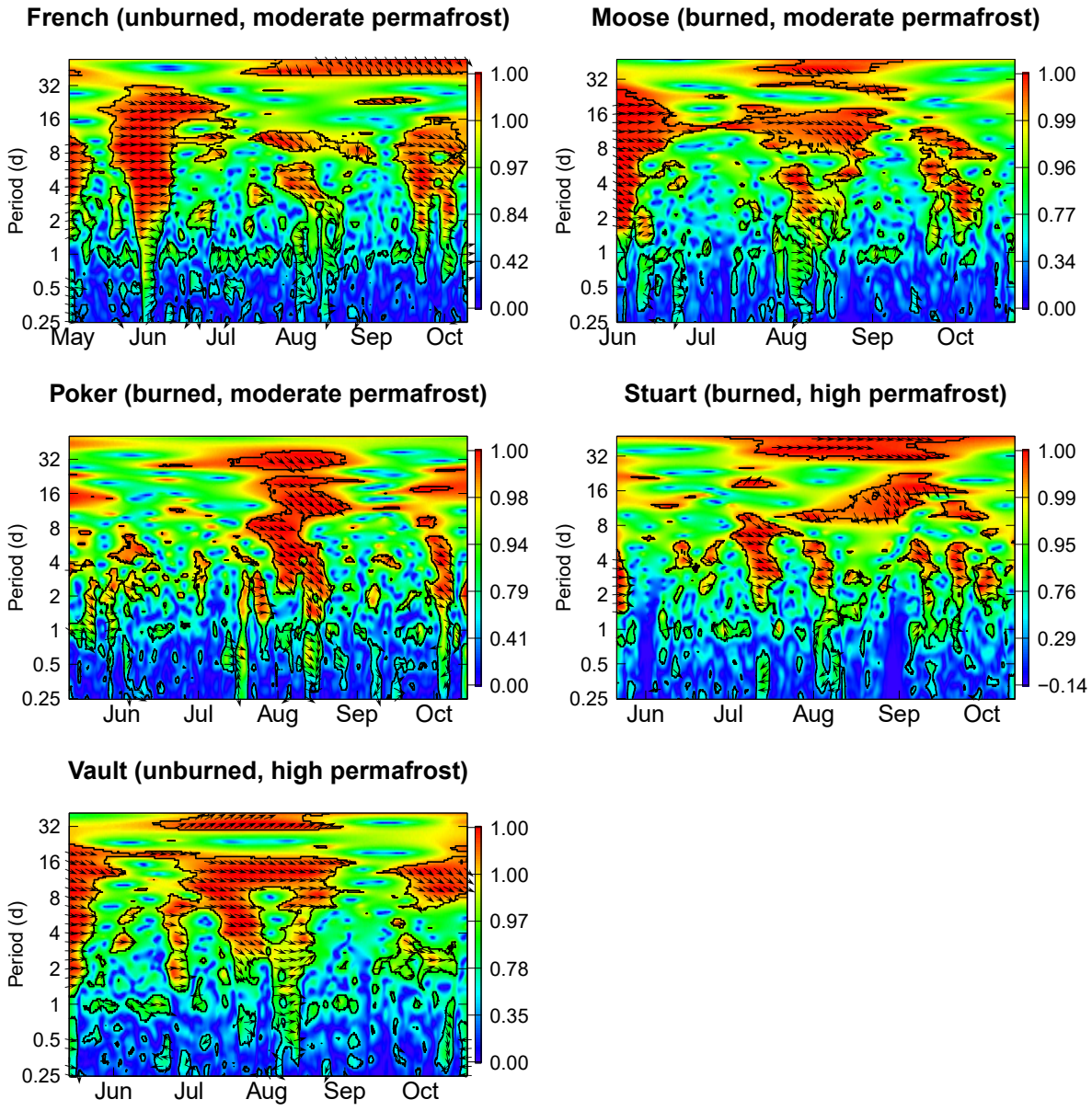


Figure A2.37. Wavelet coherence of turbidity and discharge in 2019. Scale bar indicates coherence, with greater coherence depicted by warmer colors. Black outlines indicate times and frequencies when coherence is significantly greater than expected from an autoregressive time series. Arrows indicate the phase match when coherence is significant: → = in phase; ← = out of phase; ↖ = out of phase, turbidity following discharge; ↙ = out of phase, turbidity leading; ↗ = in phase, turbidity leading; ↘ = in phase, turbidity following. Note that the temporal extent (x axis) varies across the streams.

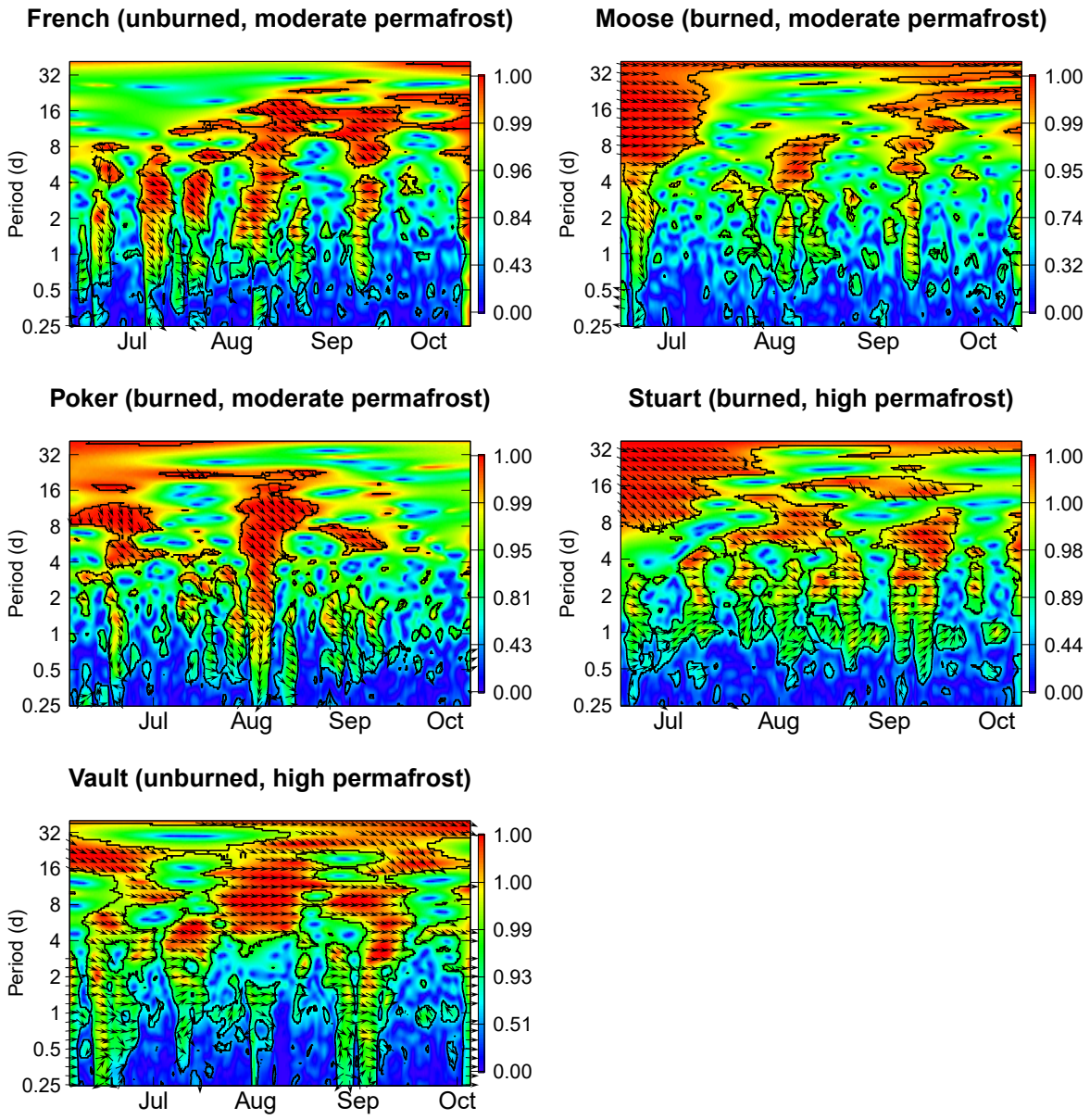


Figure A2.38. Wavelet coherence of turbidity and discharge in 2020. Scale bar indicates coherence, with greater coherence depicted by warmer colors. Black outlines indicate times and frequencies when coherence is significantly greater than expected from an autoregressive time series. Arrows indicate the phase match when coherence is significant: → = in phase; ← = out of phase; ↖ = out of phase, turbidity following discharge; ↙ = out of phase, turbidity leading; ↗ = in phase, turbidity leading; ↘ = in phase, turbidity following. Note that the temporal extent (x axis) varies across the streams.

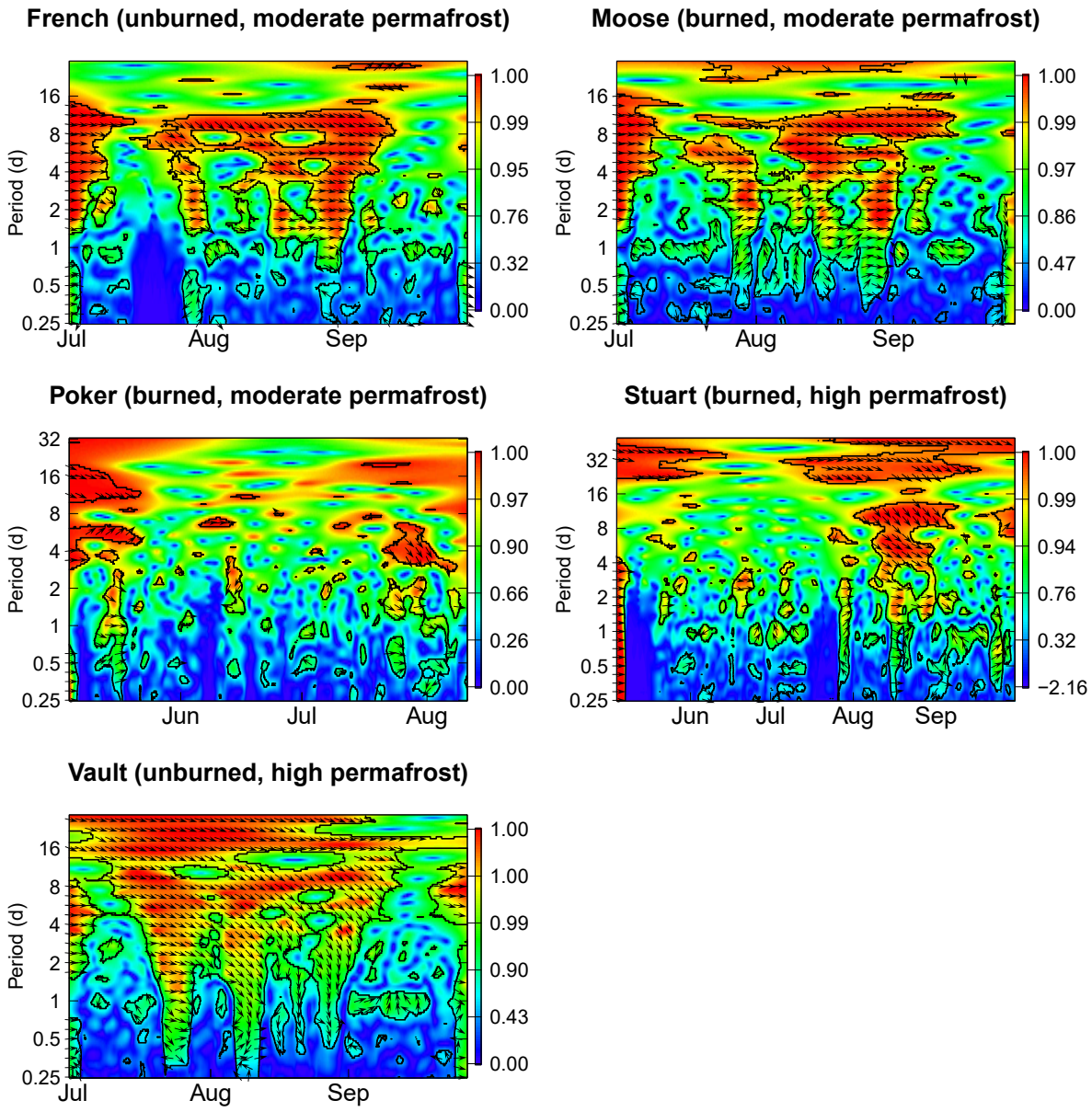


Figure A2.39. Wavelet coherence of turbidity and discharge in 2021. Scale bar indicates coherence, with greater coherence depicted by warmer colors. Black outlines indicate times and frequencies when coherence is significantly greater than expected from an autoregressive time series. Arrows indicate the phase match when coherence is significant: → = in phase; ← = out of phase; ↖ = out of phase, turbidity following discharge; ↙ = out of phase, turbidity leading; ↗ = in phase, turbidity leading; ↘ = in phase, turbidity following. Note that the temporal extent (x axis) varies across the streams.

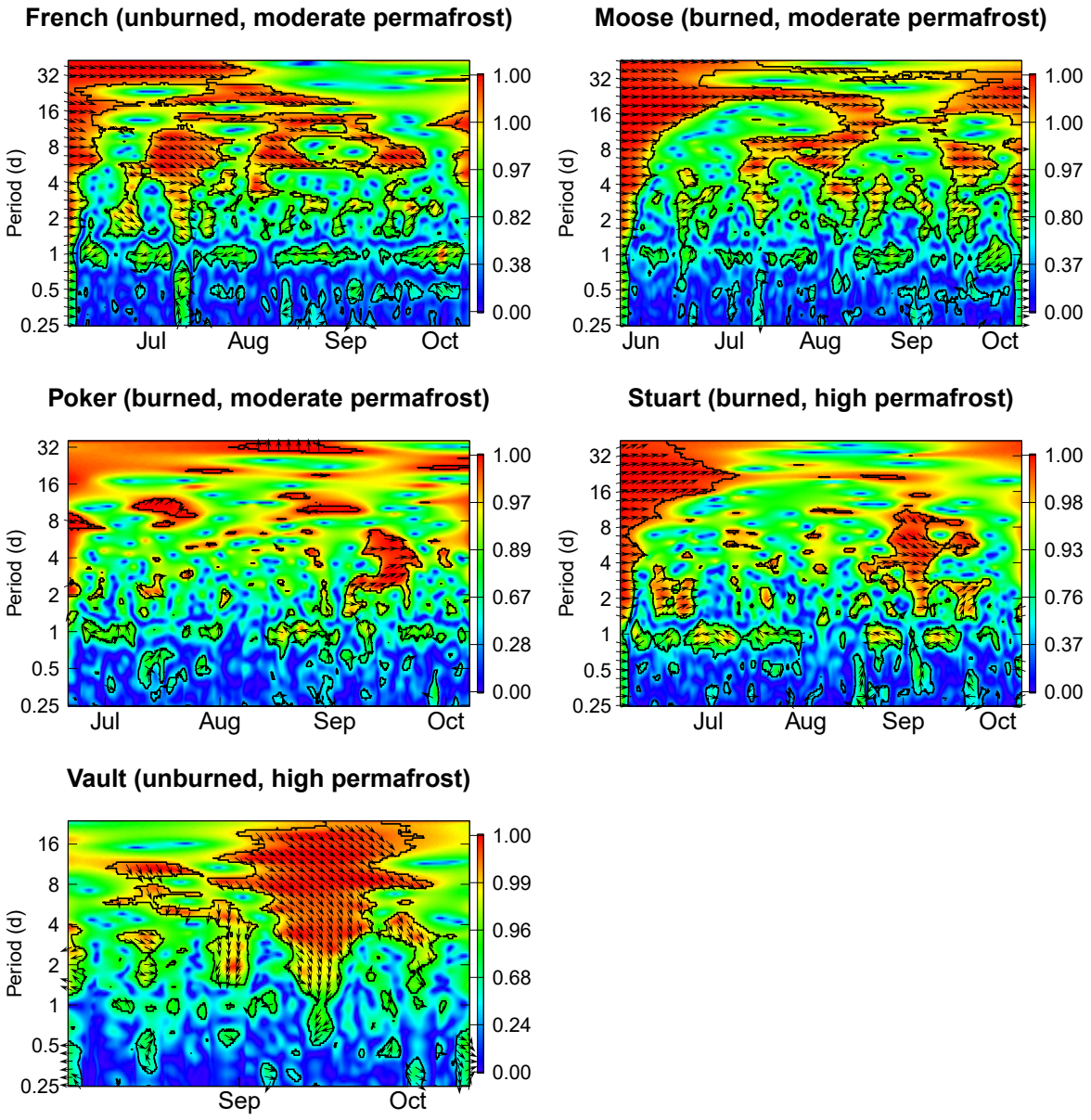


Figure A2.40. Wavelet coherence of turbidity and discharge in 2022. Scale bar indicates coherence, with greater coherence depicted by warmer colors. Black outlines indicate times and frequencies when coherence is significantly greater than expected from an autoregressive time series. Arrows indicate the phase match when coherence is significant: → = in phase; ← = out of phase; ↖ = out of phase, turbidity following discharge; ↙ = out of phase, turbidity leading; ↗ = in phase, turbidity leading; ↘ = in phase, turbidity following. Note that the temporal extent (x axis) varies across the streams.

APPENDIX B: Scientific & Technical Publications

Publications

Cavaiani, J.S., T.A. Douglas, N.J. Pastick, & T.K. Harms. Storm hydro-biogeochemistry of catchments disturbed by fire and permafrost thaw, *in preparation*

Harms, T.K., A.J. Webster, N.J. Pastick, & A. Contreras. Decadal-scale legacies of fire on fluvial export of carbon and nutrients from boreal catchments, *in preparation*

Webster, A.J., T.A. Douglas, P. Regier, M.D. Scheuerell, & T.K. Harms. 2022. Multi-scale temporal patterns in stream biogeochemistry indicate linked permafrost and ecological dynamics of boreal catchments, *Ecosystems*, doi.org/10.1007/s10021-021-00709-6

Presentations

Webster, A., A. Krehlik, & T. Harms. Time scales of variation in stream biogeochemistry across contrasts of permafrost extent, Association for the Sciences of Limnology & Oceanography, San Juan, Puerto Rico, 2/19

Harms, T., A. Webster, & T. Douglas. Linking high-frequency stream chemistry to boreal catchment resilience across contrasts of permafrost extent and fire history. Department of Defense Strategic Environmental Research and Development Program Symposium, Washington DC, 12/19

Contreras, A., A. Webster, R.L. Willis, & T. Harms. Stream chemistry indicates catchment response to disturbance and regional warming in the boreal forest. AGU, San Francisco, 12/19

Webster, A., T. Douglas, P. Regier, & T. Harms. Detecting catchment-scale permafrost degradation and biogeochemical regime change from high-frequency stream chemistry. AGU, San Francisco, 12/19

Harms, T.K. Permafrost thaw and changing cycles of the elements of life. Advanced Science Research Center, City University of New York, 3/20

Harms, T.K. Permafrost thaw and changing cycles of the elements of life. Cary Institute of Ecosystem Studies, Millbrook NY, 3/20

Harms, T & T. Douglas. Catchment biogeochemistry as an indicator of boreal ecosystem state. Strategic Environmental Research & Development Program Symposium, virtual, 11/20

Harms, T.K. High-latitude change and cycles of the elements of life. Institute of Arctic Biology, University of Alaska Fairbanks, 12/20

Harms, T., T. Douglas, J.S. Cavaiani, & A. Webster. Permafrost and legacies of fire reflected in spatial and temporal variation in stream chemistry. Department of Defense Strategic Environmental Research and Development Program Symposium, virtual, 11/21

Cavaiani, J.S. & T.K. Harms. Antecedent precipitation influence on storage and transport of nitrate and DOM in boreal catchments. AGU, New Orleans, 12/21

Harms, T.K., A.J. Webster, A. Contreras. Legacies of fire in fluvial yields of carbon and nitrogen from boreal catchments. AGU, New Orleans, 12/21

Harms, T.K., Cavaiani, J.S. & T.A. Douglas. Linking high-frequency stream chemistry to boreal catchment resilience across contrasts of permafrost extent and fire history. Strategic Environmental Research and Development Program, Arlington, VA, 12/22

APPENDIX C: Responses to Comments on the Final In-Progress Report

Comment: Address potential effects of burn intensity

Measuring burn intensity is controversial, with some scientists viewing field measurements of organic layer depth as the only reliable method for measuring intensity (e.g., Boby et al. EA) and others applying metrics based on imagery analysis (French et al. 2008). The objectives of this SERDP project addressed catchment-scale processes, and field measurements of burn intensity would not provide sufficient coverage at this scale. We characterized burn intensity of the three burned catchments included in the monitoring program using data from the Monitoring Trends in Burn Severity Program (MTBS; mtbs.gov). The MTBS estimates burn severity from a normalized burn ratio based on reflectance from Landsat imagery (Eidenshink et al. 2007).

The three burned catchments included in the intensive monitoring program encompassed similar extents of high-severity burns: 33.1% (Moose), 25.6% (Poker), and 21.5 (Stuart). Thus, comparisons between these burned catchments are relatively standardized for burn severity.

Analyses of the broad-scale survey of stream chemistry across wider gradients in spatial extent of fire and time since fire did not include burn severity. The synoptic sampling supporting this analysis included catchments that had burned at least 79 years before sampling. The MTBS analysis of burn severity begins in 1984. Thus, estimates of burn severity were not available to characterize all of the fires included in the spatial survey of stream chemistry. Though fire intensity likely explains additional variation not captured in the present analysis, we uncovered strong relationships between stream chemistry and spatial extent of fire that could be used to characterize the recovery of organic matter pools in catchments following fire.